Understanding the Catalytic Activity of Oxides through their Electronic Structure and Surface Chemistry

by

Kelsey A. Stoerzinger

B.S., Materials Science and Engineering
Northwestern University, 2010

M.Phil., Physics
University of Cambridge, 2011

Submitted to the Department of Materials Science and Engineering
in Partial Fulfillment of the Requirements for the Degree of

Doctor of Philosophy

at the

MASSACHUSETTS INSTITUTE OF TECHNOLOGY

June 2016

Author ……
Department of Materials Science and Engineering
April 25, 2016

Certified by ……
Yang Shao-Horn
W.M. Keck Professor of Energy
Thesis Supervisor

Accepted by …..…….....
Donald R. Sadoway
John F. Elliot Professor of Materials Chemistry
Chair, Department Committee on Graduate Students

Understanding the Catalytic Activity of Oxides through their Electronic Structure and Surface Chemistry

by

Kelsey A. Stoerzinger

Submitted to the Department of Materials Science and Engineering on
May 20, 2016, in partial fulfillment of the requirements for the degree of
Doctor of Philosophy

ABSTRACT

The intermittent nature of renewable energy sources requires a clean, scalable means of converting and storing energy. Water electrolysis can sustainably achieve this goal by storing energy in the bonds of oxygen and hydrogen molecules. The efficiency of this storage-conversion process is largely determined by the kinetic overpotential required for the oxygen evolution and reduction reactions (OER and ORR), respectively. This thesis focuses on transition metal oxides as alternative oxygen catalysts to costly and scarce noble metals.

In order to develop descriptors to improve catalytic activity, thus reducing material cost for commercial technologies, this work studies fundamental processes that occur on model catalyst systems. Electrochemical studies of epitaxial oxide thin films establish the intrinsic activity of oxide catalysts in a way that cannot be realized with polydisperse nanoparticle systems. This thesis has isolated the activity of the catalyst on a true surface-area basis, enabling an accurate comparison of catalyst chemistries, and also revealed how different terminations and structures affect the kinetics. These studies of epitaxial thin films are among the first to probe phenomena that are not straightforward to isolate in nanoparticles, such as the role of oxide band structure, interfacial charge transfer (the “ligand” effect), strain, and crystallographic orientation.

In addition, these well-defined surfaces allow spectroscopic examinations of their chemical speciation in an aqueous environment by using ambient pressure X-ray photoelectron spectroscopy. By quantifying the formation of hydroxyl groups, we compare the relative affinity of different surfaces for this key reaction intermediate in oxygen electrocatalysis. The strength of interaction with hydroxyls correlates inversely with activity, illustrating detrimental effects of strong water interactions at the catalyst surface. This fundamental insight brings molecular understanding to the wetting of oxide surfaces, as well as the role of hydrogen bonding in catalysis. Furthermore, understanding of the mechanisms of oxygen electrocatalysis guides the rational design of high-surface-area oxide catalysts for technical application.

Thesis Supervisor: Professor Yang Shao-Horn
Title: W.M. Keck Professor of Energy

This work is dedicated to my parents,
Rose and Glenn Stoerzinger,
for teaching me the value of hard work
and enabling me to pursue my passions.
This is but a small thank you.

Acknowledgements

The Doctoral journey that this thesis represents was made possible by the wealth of passionate and supportive people with whom I've been fortunate to interact. I here acknowledge many of them, and assure those whom I've missed that I am equally grateful for their support.

I first want to thank my adviser, Prof. Yang Shao-Horn, for her relentless support and providing me with unfathomable opportunities in terms of collaborations, research facilities and professional development. Very few students are lucky enough to have an advisor that gives them the freedom to map out their own thesis while also providing the tools to successfully execute the work of their own choosing. Prof. Shao-Horn has also shown me how to be an assertive and curious scientist, and I have greatly benefitted from being more direct and asking questions freely in the pursuit of knowledge.

Prof. Shao-Horn's driven enthusiasm and intellectual curiosity has also attracted an exceptional group of ever changing individuals who comprise her stellar research group. I am greatly indebted to all of them for everything they have taught me, in addition to their companionship on this great journey. I want to explicitly thank Jin Suntivich, Kevin May, Dr. Marcel Risch, Dr. Zhenxing Feng, Prof. Livia Giordano, Dr. Yueh-Lin Lee, Alex Han, Tom Carney, Dr. David Fenning, Dr. Alexis Grimaud, Dr. Magali Gauthier, Dr. Renshaw Wang, Dr. Nir Pour, Joe Elias, Jonathan Hwang, and Reshma Rao for all of their research help and their friendship in lab and the office. Special thanks goes to Wesley Hong, who has made (literally) thousands of hours of beamtime at the synchrotron not only scientifically productive but also fun.

I also want to thank my committee, Prof. Jeffrey Grossman and Prof. Silvija Gradecak, who always provided great insight and challenging perspectives during my too-infrequent committee meetings, and whose advice continues to aid me long after the final exam.

It has been my great fortune to work with a wide range of other researchers who have been instrumental in my research success and personal growth. Specifically, I thank Prof. Kripa Varanasi at MIT and Prof. Venky Venkatesan at NUS for their help in wetting measurements and film growth, respectively, as well as their professional guidance. Dr. Hendrik Bluhm and Dr. Ethan Crumlin have been incredible in their support of ambient pressure XPS experiments, and support of my professional growth. I would also like to thank Prof. Tom Jaramillo at Stanford, Prof. Ifan Stephens at DTU, Prof. Ib Chorkendorf at DTU, Prof. Jan Rossmeisl at DTU/Copenhagen, and Prof. Marc Koper at Leiden University for their insight and assistance in understanding electrocatalysis. Thanks go to members of MIT EEL, Dr. Weiming Lü and Changjian Li at NUS, as well as Dr. Dongkyu Lee, Dr. Ho Nyung Lee, Dr. Woo Seok Choi, Dr. Hyoungjeen Jeen, Dr. Liang Qiao and the late Dr. Mike Biegalski at ORNL for their expert film

growth. Thanks to Srinivas Subramanyam and Gisele Azimi at MIT for help with contact angle measurements. I thank Prof. Livia Giordano and Dr. Yueh-Lin Lee at MIT EEL for DFT calculations in Chapter 2, and Dr. Oscar Diaz-Morales at Leiden University for OLEMS measurements in Chapter 5.

Lastly, I cannot say enough to adequately thank my family and friends who have made my Ph.D. experience enjoyable and memorable. Thank you to all my friends who stuck with me, whether from Northwestern or as early as middle school, for your support and companionship. Thank you to all the 'other' Cambridge transplants for your friendship, scientific enthusiasm and guidance, and many a delicious cooking adventure. Thank you to my family for all your support and listening ears as you learned with me what this journey entailed. I hope I have made the most of the opportunities that you have given me through your own hard work and sacrifice. And to Rene, my partner and accomplice, thank you for being an incredible cheerleader, motivator, and teammate in every aspect of life.

Several institutions have played an enabling role in this research. I thank the National Science Foundation Graduate Research Fellowship and MRSEC Program, the Skoltech-MIT Center for Electrochemical Energy, the Eni-MIT Alliance Solar Frontiers, and the DOE Hydrogen Initiative program for funding.

Table of Contents

1. Introduction

1.1. Motivation

The intermittent nature of renewable energy sources requires a clean, scalable means of converting and storing energy. One earth abundant storage option is water electrolysis, storing energy in the bonds of O_2 and H_2 (Equation 1-1). These fuels can then be combined to form H_2O in a fuel cell[1] for on-site electricity at roughly ambient temperatures (Equation 1-2).

$$\textit{Electrolysis: } H_2O \rightarrow H_2 + \tfrac{1}{2} O_2 \qquad \textit{Equation 1-1}$$

$$\textit{Fuel cell: } H_2 + \tfrac{1}{2} O_2 \rightarrow H_2O \qquad \textit{Equation 1-2}$$

Historically speaking, the most established "low temperature" fuel cell technology is the Proton Exchange Membrane Fuel Cell (PEMFC). In such a cell, H_2 is electrochemically oxidized at the anode to yield protons and electrons (Equation 1-3), which flow across an ionically conductive membrane and electrically conductive outer circuit, respectively, to reach the cathode. Protons and electrons then react with O_2, electrochemically reducing it to form H_2O (Equation 1-4).

$$\text{Anode, PEMFC: } H_2 \rightarrow 2H^+ + 2e^- \qquad \textit{Equation 1-3}$$

$$\text{Cathode, PEMFC: } \tfrac{1}{2} O_2 + 2H^+ + 2e^- \rightarrow H_2O \qquad \textit{Equation 1-4}$$

In the case of the hydrogen oxidation reaction (HOR, Equation 1-3), only two electrons are required per mole of reactant gas, and relatively little electronic reorganization is required in the catalysis. Platinum is an excellent catalyst for this reaction, and the kinetics are so fast that the mass transport of H_2 and protons controls the reaction.[2] The case is much different for the oxygen reduction reaction (ORR), requiring four electrons per mole of O_2 and substantial reorganization in the formation of reaction intermediates. The losses in state-of-the-art, non-commercial membrane electrolyte assemblies (MEA) have been identified by Gasteiger and colleagues at General Motors to arise from ohmic, transport, and kinetic factors, of which kinetics contributes roughly 85%.[3,4] As shown in **Figure 1-1**, the potential beyond the equilibrium voltage (overpotential, η) required to drive the oxygen reaction in fuel cells and electrolyzers dominates efficiency losses. The design of effective catalyst materials for the oxygen reduction and evolution reactions is therefore a key opportunity to increase efficiencies of these renewable energy technologies.[1]

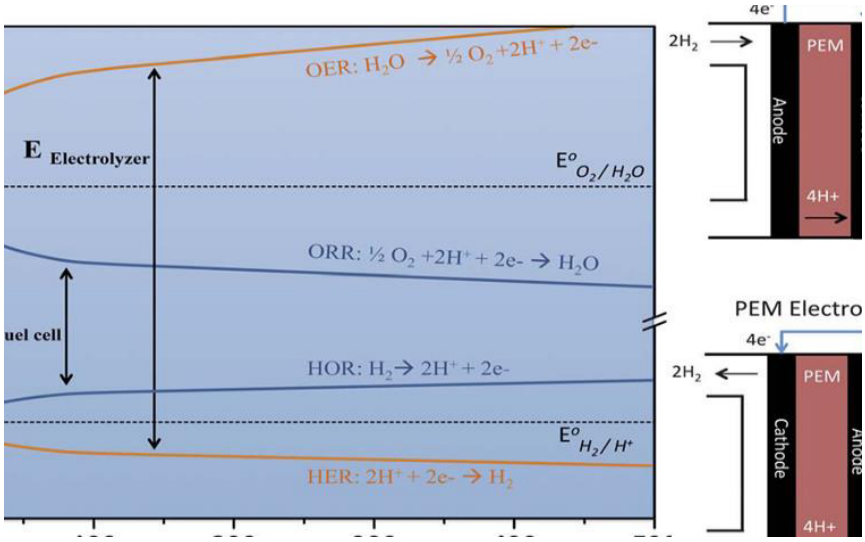

Figure 1-1. *Schematic of the potentials required to carry out oxygen and hydrogen half cell reactions, showing the large over potentials required for the ORR and oxygen evolution reaction (OER), which limit efficiencies in fuel cells and electrolyzers, respectively. Reproduced from Ref.* [4] *with permission of The Royal Society of Chemistry.*

In addition to the limitations imposed by inefficiencies, widespread implementation of PEMFCs is further hampered by the scarce nature of costly noble metals that comprise the most active known catalysts for the ORR in an acidic environment (Equation 1-4). Alkaline fuel cells (AFC), however, offer an alternative in which relatively abundant and inexpensive oxides can be comparably active[5,6] for the ORR according to Equation 1-5. Alkaline electrolysis cells (AEC) are of similar interest (Equation 1-6) due to the potential for use of abundant, transition metals as catalysts of the oxygen evolution reaction (OER).[7]

$$\text{Cathode, AFC: } O_2 + 2H_2O + 4e^- \rightarrow 4OH^- \qquad \textit{Equation 1-5}$$

$$\text{Anode, AEC: } 4OH^- \rightarrow O_2 + 2H_2O + 4e^- \qquad \textit{Equation 1-6}$$

The use of alkaline media opens up a new playing ground in which a vast array of materials can be explored for oxygen electrocatalysis. With seemingly endless permutations of the periodic table available, design principles must be developed to guide the search for highly active catalysts. This thesis is motivated by historic studies of metal catalysts in particular for the ORR, where fundamental surface science studies[8] and ab initio calculations[9] have enabled the rational design of noble metal alloy catalysts with improved activity.[10] In contrast, the study of oxides catalysts has historically been limited to pressed pellets,[11] composite electrodes,[6] and high surface area electrodeposits.[12] We therefore look to apply

surface science approaches in the study of model oxide electrodes to build fundamental understanding of ORR and OER catalysis.

1.2. Theoretical insight into the ORR mechanism

In general, an associative mechanism, in which oxygen adsorbs onto a surface without breaking the O-O bond, has been considered for the ORR on metal surfaces in acidic media. Through a combination of computational and experimental evidence,[13,14] it is understood to proceed via the following proton-coupled-electron-transfer steps (Equation 1-7 to 1-10),[15] where * represents an adsorption site:

$$* + O_2 + H^+ + e^- \rightarrow HOO* \qquad \textit{Equation 1-7}$$

$$HOO* + H^+ + e^- \rightarrow O* + H_2O \qquad \textit{Equation 1-8}$$

$$O* + H^+ + e^- \rightarrow HO* \qquad \textit{Equation 1-9}$$

$$HO* + H^+ + e^- \rightarrow H_2O + * \qquad \textit{Equation 1-10}$$

As all reaction intermediates (HOO*, O*, HO*) bind to the surface through an oxygen atom, the binding strength of oxygen has proven a useful descriptor of ORR activity.[9] Its usefulness is two-fold: first, thermodynamics can be related to kinetics through application of the Brønsted–Evans–Polanyi (BEP) relation,[16,17] thus assuming that the activation energy associated with a transition state depends linearly on the reaction energy.[18,19] Second, due to the common M-O bond of intermediates, their binding energies scale linearly with that of oxygen via so-called "scaling relationships" established computationally.[20,21] Thus, the thermodynamic calculation or measurement of a single adsorption energy—be it oxygen, hydroxyl, or oxyhydroxide—can be used to predict relative trends amongst catalyst activities.

These computed trends have roots in early studies of catalysts, where the Sabatier principle[22] established that a trade-off exists in the binding strength when optimizing catalytic activity. For materials that bind too strongly to a given reactant, desorption of products is limited and the surface is effectively poisoned. For materials that bind to weakly, interaction of the reactant with the surface is limited. This gives rise to an activity "volcano" plotted versus the descriptor of binding strength.

Such a volcano plot has been constructed from density functional theory (DFT) calculations of the strength of hydroxyl binding,[9,23] shown in **Figure 1-2** for a range of Pt-containing catalysts.[10] The location of Pt(111) on the left hand side of the volcano indicates

its activity is limited by the final step in the reaction mechanism, the reduction of *OH in its removal from the surface (Equation 1-10). In order to increase the activity, thus requiring a smaller quantity of precious metals for fuel cell applications, the binding energy of oxygen and hydroxyl groups must be made relatively weaker. We therefore must consider how to manipulate this activity descriptor to design optimal catalysts.

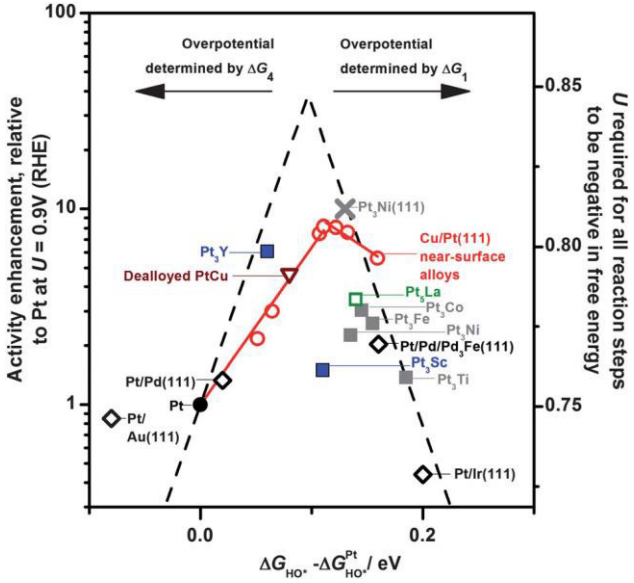

Figure 1-2. *Volcano plot for different catalysts with Pt-overlayers: experimental ORR activity enhancement as a function of hydroxyl binding energy, ΔG_{HO^*}, both relative to pure Pt. Studies consider a surface science approach for: (diamonds) Pt monolayers supported on single-crystal metal electrodes, (squares) polycrystalline alloys, (crosses) vacuum annealed $Pt_3Ni(111)$, (inverted triangles) dealloyed PtCu nanoparticles, and (red circles) Cu/Pt(111) near-surface alloys. The dashed lines are theoretical predictions, based on a simple Sabatier analysis. Reproduced from Ref.* [10] *with permission of The Royal Society of Chemistry.*

The strength of chemisorption is determined by the electronic coupling between the frontier molecular orbital levels of the adsorbate and a band of states within the catalyst:[24,25] here between the O 2*p* and transition metal *d*-band. Antibonding states are formed as a result of this coupling, and the bond becomes weaker as the antibonding states are filled (**Figure 1-3**). Thus, by manipulating the *d*-bands location, width, or filling—all of which effectively change the location of the *d*-band center relative to the Fermi level[25]—the strength of oxygen binding can be similarly manipulated.

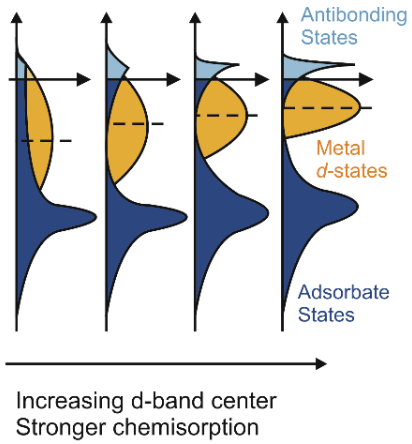

Figure 1-3. *Schematic of the local density of states projected onto an adsorbate state interacting with the d-bands at a surface. As the d-bands shift up and the width decreases, the antibonding states above E_F are emptied, and the bond becomes stronger.*[26]

The predictive power of this theory has led to the discovery of promising platinum-based catalysts for the ORR in PEMFCs.[27,28] In addition to calculations,[29] it has been shown experimentally that the *OH chemisorption energy increases as the *d*-band center moves closer to the Fermi level.[30] The expected electrocatalytic activity trends of the ORR have been subsequently shown for Pt films deposited on metal substrates in both acid[31] and base,[32] as well as Pt skin and Pt-skeleton surfaces in acid.[33] In considering materials of multiple metal centers, the *d*-band can be manipulated via both a strain and an alloy/ligand effect. The strain effect has been isolated in the study of dealloyed Cu-Pt nanoparticles,[34] while a pure alloying effect has been investigated by a study of PtCu surface alloys.[35]

1.3. Understanding catalysis of the ORR on perovskite oxides

Inspired by the understanding of the relation between the electronic structure of metal catalysts and ORR activity, there has been a renewed fervor of investigation of earth abundant oxides for catalysis of the ORR in AFCs. In an alkaline electrolyte, H_2O rather than H_3O^+ may act as the proton donor, giving an associative mechanism analogous to that in acid (Equations 1-7 to 1-10) hypothesized to occur in base (Equations 1-11 to 1-14):

$$* + O_2 + H_2O + e^- \rightarrow HOO* + OH^- \qquad \textit{Equation 1-11}$$

$$HOO* + e^- \rightarrow O* + OH^- \qquad \textit{Equation 1-12}$$

$$O* + H_2O + e^- \rightarrow HO* + OH^- \qquad \textit{Equation 1-13}$$

$$HO^* + e^- \rightarrow OH^- + * \qquad \textit{Equation 1-14}$$

Of particular interest is the perovskite family with formula $AA'BB'O_3$, where $A^{(')}$ is a Lanthanide or group II element, and $B^{(')}$ is a transition metal. The chemical flexibility of the structure and diverse range of physical-chemical and catalytic properties that result[36] make this an ideal system for systematic investigation of the electronic properties which describe ORR activity.[26] Furthermore, these materials have been shown to exhibit catalytic activity similar to that of Pt in an alkaline environment.[6]

Historically, the oxygen reduction current supported by perovskites has been reported on a geometric (projected area) basis for thin, porous electrodes.[11,37,38] Work by Motsumoto et al.[37,38] proposed that the ORR activity can be influenced by the formation and filling of a σ^* band between the e_g orbital of bulk transition-metal ions and a molecular orbital of surface oxygen. In such an experimental configuration, however, the intrinsic specific ORR activities (kinetic current densities per catalyst surface area) remain unknown, inhibiting mechanistic insight.

Recent work has implemented the use of composite thin-film rotating-disk electrodes (RDEs) with well-defined oxygen transport and much better compensated oxygen mass resistances,[6,39-41] compared to thick electrodes with high internal surface area.[11] Suntivich et al.[42] have considered perovskite oxides with various A-site and B-site substitutions in order to elucidate the descriptors of ORR activity for such a system. In contrast to prior work, their description of electronic interactions is a localized one of molecular-orbital character, favored at the surface of transition-metal oxides, as opposed to bulk itinerant electron states.[43-45]

In this framework, the transition-metal *d*-manifold is split into the antibonding e_g and t_{2g} orbitals by the ligand field of BO_6 octahedra in the perovskite structure (**Figure 1-4B,C**). Making the assumption that O_2 likely adsorbs end-on at the surface B-sites, the e_g orbital's overlap with the O-$2p_\sigma$ orbital is more strong than the t_{2g} orbital's overlap with the O-$2p_\pi$ orbital. Thus, the e_g orbital is expected to more accurately describe the strength of oxygen bonding. Experimental measurements of the intrinsic ORR activity plotted against the *d*-electron number gave an M-shaped relation, shown in **Figure 1-4A**, attributed to the spin state transition of the B-ion, while plotting the activity versus the e_g orbital occupancy yielded a volcano relation, shown in **Figure 1-4D**. Furthermore, ORR activity increased with greater hybridization of the B-O bond.

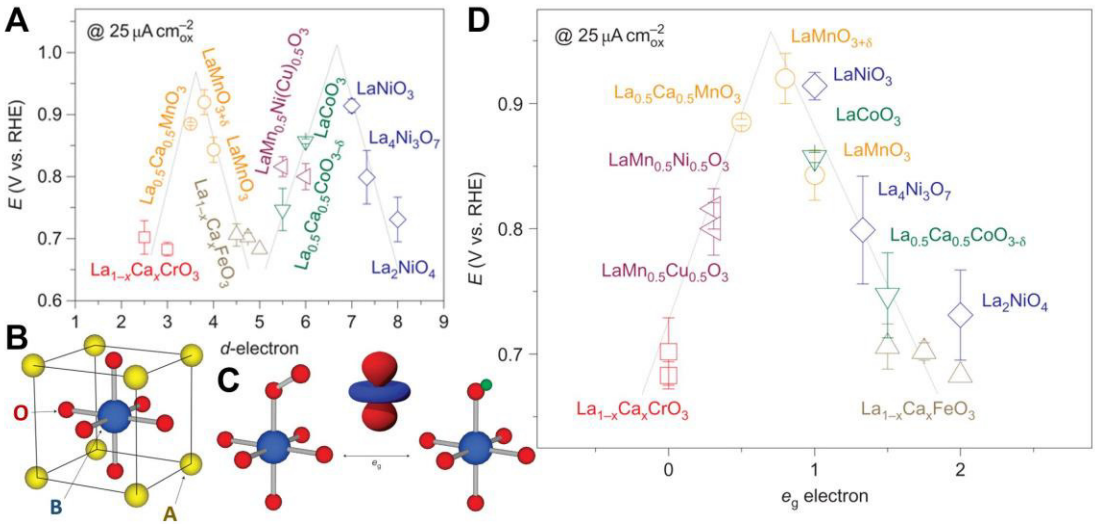

Figure 1-4. *(A) Potentials at a kinetic current of 25 μA cm$^{-2}_{ox}$ of the perovskite oxides have an M-shape relation with d-electron number. (B) ABO_3 perovskite structure. (C) The shape of the e_g orbital points directly toward the surface O atom and plays an important role during *OO^{2-}/*OH$^-$ exchange. (D) Potentials at a kinetic current of 25 μA cm$^{-2}_{ox}$ as a function of e_g orbital. Adapted by permission from Macmillan Publishers Ltd: Nature Chemistry Ref.* [42]*, copyright 2011.*

The results were interpreted in terms of a reaction mechanism analogous to the associative mechanism presented earlier, shown in **Figure 1-5** below. For materials with too little e_g filling, on the left side of the volcano of **Figure 1-4D**, the oxygen binding is too strong, and kinetics are limited by the rate of surface OH^- regeneration (4 in **Figure 1-5**). For materials with too much e_g filling, on the right of the volcano, the weak bonding of oxygen results in *OO^{2-}/*OH$^-$ exchange (1 in **Figure 1-5**) acting as the rate limiting step.

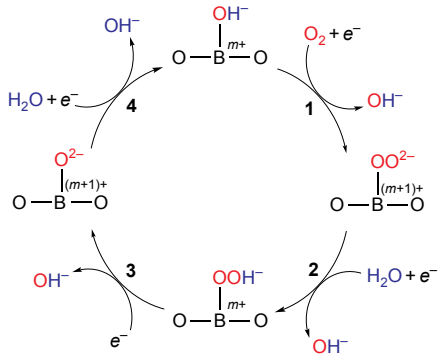

Figure 1-5. *The ORR is proposed*[14] *to proceed via four steps: 1, surface hydroxide displacement; 2, surface peroxide formation; 3, surface oxide formation; 4, surface hydroxide regeneration.*

Reprinted by permission from Macmillan Publishers Ltd: Nature Chemistry Ref. [42], copyright 2011.

Leveraging recent advances in fabricating heterojunctions and well-defined oxide surfaces can provide insights into active sites on the atomic level. Single-crystal surfaces can be produced by growing epitaxial thin films of oxides on single crystal substrates using pulsed laser deposition (PLD) or molecular beam epitaxy. Studies of such thin films and herostructures have revolutionized our understanding of oxide physics in the past decade.[46,47] Electrochemical studies of well-defined surfaces have the potential to establish the intrinsic activity of oxide catalysts in a way that cannot be realized with polydisperse nanoparticle systems. In addition to isolating the activity of the catalyst on a true surface-area basis, enabling an accurate comparison of catalyst chemistries, such studies can reveal how different terminations and structures affect the kinetics. While such effects have been demonstrated for metallic catalysts,[10] they have yet to be explored in oxide systems.

1.4. Toward understanding oxide chemistry in the ORR environment

Although e_g orbital occupancy and metal-oxygen covalency well-describe catalytic activity toward the ORR, these analytical frameworks have yet to be connected to experimental measurements of adsorbate binding energy or observation of reaction intermediates. The interaction of catalysts with water as a reactant, intermediate, or product plays a key role in the reduction of oxygen.[14] The reactivity of surfaces with water vapor or liquid dictates their hydroxylation, which changes their reactivity and adsorptive properties.[48] Furthermore, surface oxides form under the O_2-rich conditions employed in the electrochemical ORR,[49] exhibiting drastically different activities than the metallic- or bulk-terminated surface. To build an understanding of the reaction mechanism and rate-limiting steps, we require *in situ* characterization of adsorbed intermediates, such as oxygen and water.[50-52] However, at pressures approaching those of practical relevance, characterizing chemical speciation with surface science techniques is challenging. Furthermore, the study of oxide catalysts also comes with difficulty in distinguishing between different oxygen-containing species in the liquid/gas phase, adsorbed on the surface, and within the lattice.

Ambient pressure X-ray photoelectron spectroscopy (AP-XPS) is a powerful tool for

studying the surfaces of materials in environments with high pressures of gaseous species (up to a few Torr). X-ray photoelectron spectroscopy (XPS) can probe surface chemical composition at a depth of several nanometers,[53] identify oxidation states, and provide insights into the electronic structure of a catalyst.[54] XPS measures the binding energy of ejected core-level electrons, characteristic of different elements, where subtle shifts in binding energy can reflect change in the local electrical potential (e.g. due to an applied bias) or chemical shifts arising from changes in speciation or electronic structure. In AP-XPS, a high-pressure cell/chamber is separated from the electron analyzer by a differentially pumped electrostatic lens system (**Figure 1-6**),[55,56] overcoming the typical limitation of the technique to ultra-high vacuum due to the short inelastic mean free path (IMFP) of photoelectrons in condensed matter.[57] AP-XPS probes the surface chemistry of catalysts at elevated pressures,[58] identifying and quantifying adsorbates in equilibrium with the gas.

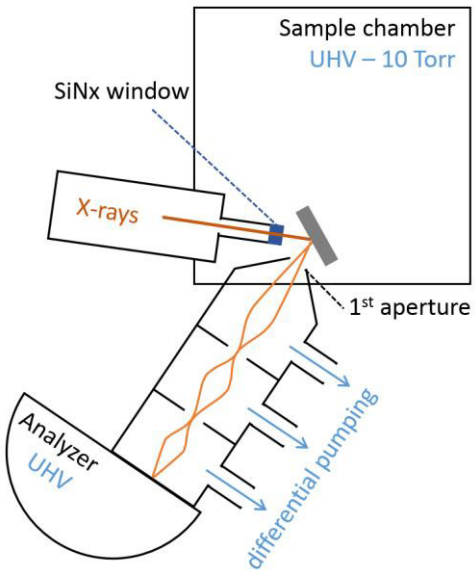

Figure 1-6. *Schematic of the ambient pressure X-ray photoelectron spectroscopy (AP-XPS) instrument at ALS beamline 11.0.2, with set of differentially pumped electrostatic lenses between the sample chamber and the electron analyzer. Figure reproduced with permission from Ref.* [59]*. Copyright 2015 American Chemical Society.*

Previously, it has been shown that the capabilities of AP-XPS allow for both qualitative and quantitative understanding of the surface species that form under different relative humidities.[60] But while the technique has been extensively used in exploring water dissociation, adsorption, and wetting of well-defined metal films as a function of relative humidity,[60] studies of oxides have only recently begun, focusing largely on binary oxides that

are inactive for the ORR/OER. For example, Yamamoto et al.[61] and Newberg et al.[62] have shown that dissociative adsorption and surface hydroxylation dominate water interactions on single crystal α-Fe_2O_3(0001) and MgO(100) thin film surfaces at low relative humidity while molecular water begins to adsorb at higher relative humidity, as shown in **Figure 1-7**. The content of hydroxyl and adsorbed H_2O was quantified using a multilayer electron attenuation model,[63] shown in **Figure 1-7B**. Understanding the degree of hydroxylation on catalytically active oxide surfaces such as perovskite surfaces could provide valuable mechanistic insights for the ORR/OER.

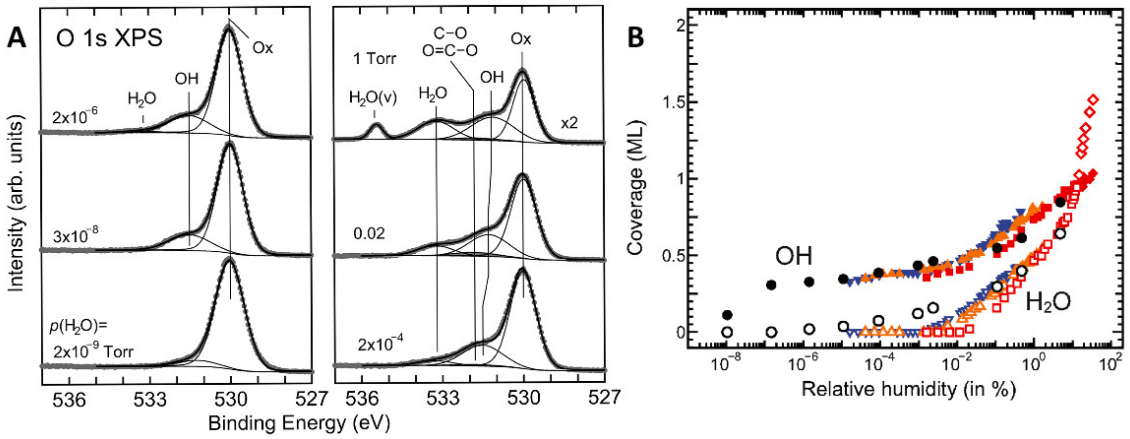

Figure 1-7. *(A) Deconvoluted O 1s XPS spectra of α-Fe_2O_3(0001) at a range of H_2O pressures. (B) Coverage of OH and H_2O at given relative humidities (RHs), calculated using a multilayer electron attenuation model.[63] The coverages of OH (filled symbols) and H_2O (open symbols) are obtained from an isotherm of T = 295 K (black) and three different isobars; p(H_2O) = 0.02 Torr (blue), 0.1 Torr (orange), 1 Torr (squares in red). The high RH data measured at p(H_2O) = 1.0-2.0 Torr and T = 280-277 K (diamonds in red) are also included. Reproduced with permission from Ref. [61]. Copyright 2010 American Chemical Society.*

1.5. Thesis scope

This thesis builds fundamental understanding of what governs catalytic activity of the ORR and OER through the study of epitaxial oxide thin-films. These studies enable quantification of intrinsic activity and the study of phenomena that are not straightforward to isolate in nanoparticles, such as the role of oxide band structure, interfacial charge transfer (the "ligand" effect), strain, and crystallographic orientation. In addition, these well-defined

surfaces allow spectroscopic examinations of their chemical speciation in an aqueous environment through the use of AP-XPS, shedding light on the reaction mechanism.

Chapter 2 establishes an experimental approach to consider the oxygen-containing surface species present on a perovskite oxide surface in a humid environment. AP-XPS is used to identify and quantifying hydroxyl groups and the adsorption of water as a function of relative humidity, in addition to considering changes in the work function or surface dipole. The relative affinity of (001)-oriented LaMO$_3$ (M = Cr–Ni) perovskite surfaces for hydroxyl species is then evaluated and compared to computational predictions.

Chapter 3 then considers implications of the hydroxyl intermediate in the activity for ORR, building understanding of the reaction mechanism and rate limiting step. This microscopic role of hydroxyls in hydrogen bonding with adsorbed water is then extended to macroscopic studies of surface wettability, and elucidation of the acid-base properties of the wetted surface.

Chapter 4 links the surface chemistry of an oxide film to its electronic structure through study of the $La_{(1-x)}Sr_xMnO_3$ system. In situ probing of the electronic structure with AP-XPS suggests a driving force for hydroxylation related to the absolute energy of occupied states relative to the water-oxygen redox level, concurrently tied to ORR activity. The electronic structure of oxide catalysts, and resultant affinity for reaction intermediates, is assessed directly regarding the activity for ORR and OER in Appendices D and E regarding the ligand effect in $LaMnO_3$ and strain in $LaCoO_3$.

Diverting from explicit assessment of hydroxyl affinity, Chapter 5 then moves to consider the role of pH and surface redox on a slightly different crystal class of oxide – the rutile structure. The terminal crystal facet of highly active IrO_2 and RuO_2 thin film catalysts is varied, establishing orientation-dependent activity for the OER. This is related to the ability of the surface to be oxidized and the pH-dependence of this process, in addition to considering the role of lattice oxygen in the process.

Finally, Chapter 6 explores the implications of the results of this doctoral work. Particular attention is given to an outlook on in operando methods of considering surface speciation on oxide electrocatalysts in aqueous environments.

References

1 Service, R. F. Hydrogen Cars: Fad or the Future? *Science* **324**, 1257-1259, (2009).

2 Marković, N. M. & Ross Jr, P. N. Surface science studies of model fuel cell electrocatalysts. *Surf. Sci. Rep.* **45**, 117-229, (2002).

3 Gasteiger, H. A., Kocha, S. S., Sompalli, B. & Wagner, F. T. Activity Benchmarks and Requirements for Pt, Pt-alloy, and Non-Pt Oxygen Reduction Catalysts for PEMFCs. *Appl. Catal., B* **56**, 9-35, (2005).

4 Greeley, J. & Markovic, N. M. The road from animal electricity to green energy: combining experiment and theory in electrocatalysis. *Energy Environ. Sci* **5**, 9246-9256, (2012).

5 Meadowcroft, D. B. Low-cost Oxygen Electrode Material. *Nature* **226**, 847-848, (1970).

6 Suntivich, J., Gasteiger, H. A., Yabuuchi, N. & Shao-Horn, Y. Electrocatalytic Measurement Methodology of Oxide Catalysts Using a Thin-Film Rotating Disk Electrode. *J. Electrochem. Soc.* **157**, B1263-B1268, (2010).

7 Suntivich, J., May, K. J., Gasteiger, H. A., Goodenough, J. B. & Shao-Horn, Y. A Perovskite Oxide Optimized for Oxygen Evolution Catalysis from Molecular Orbital Principles. *Science* **334**, 1383-1385, (2011).

8 Markovic, N. M., Gasteiger, H. A. & Ross, P. N. Oxygen Reduction on Platinum Low-Index Single-Crystal Surfaces in Sulfuric Acid Solution: Rotating Ring-Pt(hkl) Disk Studies. *J. Phys. Chem.* **99**, 3411-3415, (1995).

9 Nørskov, J. K. *et al.* Origin of the Overpotential for Oxygen Reduction at a Fuel-Cell Cathode. *J. Phys. Chem. B* **108**, 17886-17892, (2004).

10 Stephens, I. E. L., Bondarenko, A. S., Gronbjerg, U., Rossmeisl, J. & Chorkendorff, I. Understanding the electrocatalysis of oxygen reduction on platinum and its alloys. *Energy Environ. Sci* **5**, 6744-6762, (2012).

11 Bockris, J. O. & Otagawa, T. Mechanism of oxygen evolution on perovskites. *J. Phys. Chem.* **87**, 2960-2971, (1983).

12 Vigil, J. A., Lambert, T. N. & Eldred, K. Electrodeposited MnOx/PEDOT Composite Thin Films for the Oxygen Reduction Reaction. *ACS Appl. Mater. Interfaces* **7**, 22745-22750, (2015).

13 Karlberg, G. S., Rossmeisl, J. & Norskov, J. K. Estimations of electric field effects on the oxygen reduction reaction based on the density functional theory. *Phys. Chem. Chem. Phys.* **9**, 5158-5161, (2007).

14 Goodenough, J. B. & Cushing, B. L. *Handbook of Fuel Cells — Fundamentals, Technology and Applications* Vol. 2 520–533 (Wiley, 2003).

15 Koper, M. T. M. Theory of multiple proton-electron transfer reactions and its implications for electrocatalysis. *Chem. Sci.* **4**, 2710-2723, (2013).

16 Bronsted, J. N. Acid and Basic Catalysis. *Chem. Rev.* **5**, 231-338, (1928).

17 Evans, M. G. & Polanyi, M. Inertia and driving force of chemical reactions. *Transactions of the Faraday Society* **34**, 11-24, (1938).

18 Bligaard, T. *et al.* The Brønsted–Evans–Polanyi relation and the volcano curve in heterogeneous catalysis. *J. Catal.* **224**, 206-217, (2004).

19 Nørskov, J. K. *et al.* Universality in Heterogeneous Catalysis. *J. Catal.* **209**, 275-278, (2002).

20 Abild-Pedersen, F. *et al.* Scaling Properties of Adsorption Energies for Hydrogen-Containing Molecules on Transition-Metal Surfaces. *Phys. Rev. Lett.* **99**, 016105, (2007).

21 Rossmeisl, J., Logadottir, A. & Nørskov, J. K. Electrolysis of water on (oxidized) metal surfaces. *Chem. Phys.* **319**, 178-184, (2005).

22 Sabatier, P. *La catalyse en chimie organique*. (Bérange, 1920).

23 Rossmeisl, J., Qu, Z. W., Zhu, H., Kroes, G. J. & Nørskov, J. K. Electrolysis of water on oxide surfaces. *J. Electroanal. Chem.* **607**, 83-89, (2007).

24 Greeley, J., Nørskov, J. K. & Mavrikakis, M. Electronic structure and catalysis on metal surfaces. *Annu. Rev. Phys. Chem.* **53**, 319-348, (2002).

25 Hammer, B. & Nørskov, J. K. in *Adv. Catal.* Vol. Volume 45 (ed Helmut Knozinger Bruce C. Gates) 71-129 (Academic Press, 2000).

26 Hong, W. T. *et al.* Toward the Rational Design of Non-Precious Transition Metal Oxides for Oxygen Electrocatalysis. *Energy Environ. Sci*, (2015).

27 Stamenkovic, V. R. *et al.* Improved Oxygen Reduction Activity on $Pt_3Ni(111)$ via Increased Surface Site Availability. *Science* **315**, 493-497, (2007).

28 Greeley, J. *et al.* Alloys of platinum and early transition metals as oxygen reduction electrocatalysts. *Nat. Chem.* **1**, 552-556, (2009).

29 Stamenkovic, V. *et al.* Changing the Activity of Electrocatalysts for Oxygen Reduction by Tuning the Surface Electronic Structure. *Angew. Chem., Int. Ed.* **45**, 2897-2901, (2006).

30 Stamenkovic, V., Schmidt, T. J., Ross, P. N. & Marković, N. M. Surface segregation effects in electrocatalysis: kinetics of oxygen reduction reaction on polycrystalline Pt_3Ni alloy surfaces. *J. Electroanal. Chem.* **554–555**, 191-199, (2003).

31 Zhang, J., Vukmirovic, M. B., Xu, Y., Mavrikakis, M. & Adzic, R. R. Controlling the Catalytic Activity of Platinum-Monolayer Electrocatalysts for Oxygen Reduction with Different Substrates. *Angew. Chem., Int. Ed.* **44**, 2132-2135, (2005).

32 Lima, F. H. B. *et al.* Catalytic Activity−d-Band Center Correlation for the O_2 Reduction Reaction on Platinum in Alkaline Solutions. *J. Phys. Chem. C* **111**, 404-410, (2006).

33 Stamenkovic, V. R. *et al.* Trends in electrocatalysis on extended and nanoscale Pt-bimetallic alloy surfaces. *Nat. Mater.* **6**, 241-247, (2007).

34 Strasser, P. *et al.* Lattice-strain control of the activity in dealloyed core–shell fuel cell catalysts. *Nat. Chem.* **2**, 454-460, (2010).

35 Stephens, I. E. L. *et al.* Tuning the Activity of Pt(111) for Oxygen Electroreduction by Subsurface Alloying. *J. Am. Chem. Soc.* **133**, 5485-5491, (2011).

36 Peña, M. A. & Fierro, J. L. G. Chemical Structures and Performance of Perovskite Oxides. *Chem. Rev.* **101**, 1981-2018, (2001).

37 Matsumoto, Y., Yoneyama, H. & Tamura, H. Influence of the nature of the conduction band of transition metal oxides on catalytic activity for oxygen reduction. *J. Electroanal. Chem. Interfacial Electrochem.* **83**, 237-243, (1977).

38 Matsumoto, Y., Yoneyama, H. & Tamura, H. Catalytic activity for electrochemical reduction of oxygen of lanthanum nickel oxide and related oxides. *J. Electroanal. Chem. Interfacial Electrochem.* **79**, 319-326, (1977).

39 Paulus, U. A., Schmidt, T. J., Gasteiger, H. A. & Behm, R. J. Oxygen reduction on a high-surface area Pt/Vulcan carbon catalyst: a thin-film rotating ring-disk electrode study. *J. Electroanal. Chem.* **495**, 134-145, (2001).

40 Tulloch, J. & Donne, S. W. Activity of perovskite $La_{1-x}Sr_xMnO_3$ catalysts towards oxygen reduction in alkaline electrolytes. *J. Power Sources* **188**, 359-366, (2009).

41 Sunarso, J., Torriero, A. A. J., Zhou, W., Howlett, P. C. & Forsyth, M. Oxygen Reduction Reaction Activity of La-Based Perovskite Oxides in Alkaline Medium: A Thin-Film Rotating Ring-Disk Electrode Study. *J. Phys. Chem. C* **116**, 5827-5834, (2012).

42 Suntivich, J. *et al.* Design Principles for Oxygen-Reduction Activity on Perovskite Oxide Catalysts for Fuel Cells and Metal–Air Batteries. *Nat. Chem.* **3**, 546-550, (2011).

43 Morin, F. J. & Wolfram, T. Surface States and Catalysis on d-Band Perovskites. *Phys. Rev. Lett.* **30**, 1214-1217, (1973).

44 Goodenough, J. B. & Zhou, J. S. *Localized to Itinerant Electronic Transition in Perovskite Oxides*. Vol. 98 17–113 (Springer-Verlag 2001).

45 Yan, J. Q., Zhou, J. S. & Goodenough, J. B. Ferromagnetism in $LaCoO_3$. *Phys. Rev. B* **70**, 014402, (2004).

46 Mannhart, J. & Schlom, D. G. Oxide Interfaces-An Opportunity for Electronics. *Science* **327**, 1607-1611, (2010).

47 Dagotto, E. When oxides meet face to face. *Science* **318**, 1076-1077, (2007).

48 Sorescu, D. C., Lee, J., Al-Saidi, W. A. & Jordan, K. D. Coadsorption properties of CO_2 and H_2O on TiO_2 rutile (110): A dispersion-corrected DFT study. *J. Chem. Phys.* **137**, 074704, (2012).

49 Friebel, D. *et al.* In situ X-ray probing reveals fingerprints of surface platinum oxide. *Phys. Chem. Chem. Phys.* **13**, 262-266, (2011).

50 Faulkner, L. R. In Situ Characterization of Electrochemical Processes: A Recent Report from the National Research Council. *J. Electrochem. Soc.* **135**, 245C-246C, (1988).

51 Adler, S. B. Factors Governing Oxygen Reduction in Solid Oxide Fuel Cell Cathodes†. *Chem. Rev.* **104**, 4791-4844, (2004).

52 Ertl, G. Elementary Steps in Heterogeneous Catalysis. *Angew. Chem., Int. Ed. Engl.* **29**, 1219-1227, (1990).

53 Tougaard, S. & Ignatiev, A. Concentration Depth Profiles by XPS; A New Approach. *Surf. Sci.* **129**, 355-365, (1983).

54 De Groot, F. & Kotani, A. *Core level spectroscopy of solids*. (CRC press, 2008).

55 Ogletree, D. F. *et al.* A Differentially Pumped Electrostatic Lens System for Photoemission Studies in the Millibar Range. *Rev. Sci. Instrum.* **73**, 3872-3877, (2002).

56 Grass, M. E. *et al.* New Ambient Pressure Photoemission Endstation at Advanced Light Source Beamline 9.3.2. *Rev. Sci. Instrum.* **81**, 053106, (2010).

57 Seah, M. P. & Dench, W. A. Quantitative Electron Spectroscopy of Surfaces: A Standard Data Base for Electron Inelastic Mean Free Paths in Solids. *Surf. Interface Anal.* **1**, 2-11, (1979).

58 Knop-Gericke, A. *et al.* in *Adv. Catal.* Vol. 52 (eds C. Gates Bruce & Knözinger Helmut) 213-272 (Academic Press, 2009).

59 Stoerzinger, K. A., Hong, W. T., Crumlin, E. J., Bluhm, H. & Shao-Horn, Y. Insights into Electrochemical Reactions from Ambient Pressure Photoelectron Spectroscopy. *Acc. Chem. Res.* **48**, 2976-2983, (2015).

60 Bluhm, H. Photoelectron spectroscopy of surfaces under humid conditions. *J. Electron Spectrosc. Relat. Phenom.* **177**, 71-84, (2010).

61 Yamamoto, S. *et al.* Water Adsorption on α-Fe_2O_3(0001) at near Ambient Conditions. *J. Phys. Chem. C* **114**, 2256-2266, (2010).

62 Newberg, J. T. *et al.* Autocatalytic Surface Hydroxylation of MgO(100) Terrace Sites Observed under Ambient Conditions. *J. Phys. Chem. C* **115**, 12864-12872, (2011).

63 McCafferty, E. & Wightman, J. P. Determination of the Concentration of Surface Hydroxyl Groups on Metal Oxide Films by a Quantitative XPS Method. *Surf. Interface Anal.* **26**, 549-564, (1998).

2. Experimental probe of OH affinity

This chapter is adapted with permission from: Stoerzinger, K. A. et al. Water Reactivity on the $LaCoO_3$ (001) Surface: An Ambient Pressure X-ray Photoelectron Spectroscopy Study. *The Journal of Physical Chemistry C* **118**, 19733-19741, (2014). Copyright 2014 American Chemical Society. Stoerzinger, K. A. et al. Reactivity of Perovskites with Water: Role of Hydroxylation in Wetting and Implications for Oxygen Electrocatalysis. *The Journal of Physical Chemistry C* **119**, 18504-18512, (2015). Copyright 2015 American Chemical Society.

2.1. Introduction

The interaction of oxides with water plays a critical role in a large number of applications,[1-5] including water purification, gas sensing and separation, photoelectrochemistry, electrocatalysis, and wetting. The solid/liquid interface between water and oxides is one of the fundamental components in electrochemistry and electrocatalysis. The hydroxylation and binding of surface adsorbates[6,7] on oxides can greatly influence the adsorptive and wetting properties[4,5,8,9] and catalytic activity.[10-14] Changes in the surface chemistry in turn impact the surface dipole and work function,[15] surface electronic structure,[16] and the mechanisms and kinetics of surface chemical reactions.[4] For example, density functional theory studies have shown that the binding and coverage of OH species for Pt-alloys[17] and oxides[10] correlates with the activities for the oxygen reduction and evolution reactions. However, the reactivity of oxide surfaces with the environment and how oxide surface chemistry influences their functionality remains largely unexplored under *in situ* conditions.

Directly measuring hydroxylation and surface adsorbates in liquid water and correlating these species to wetting and catalytic activity is challenging – particularly for oxide systems where both the adsorbate and catalyst contain oxygen. Conventional contact angle measurements do not provide information at the molecular level on water adsorption energetics, the degree of hydroxylation, or interfacial hydration structure.[18] On the other hand, the molecular interaction of water with complex, catalytically active metal oxide surfaces has been studied using traditional surface science microscopy and spectroscopy techniques but only in ultra-high vacuum and often at cryogenic temperatures.[19-21] Here we take advantage of recent advances in ambient pressure X-ray photoelectron spectroscopy (AP-XPS)[22-24] to measure the extent of surface hydroxylation and adsorption of water on oxide surfaces.

AP-XPS[23,25] can provide novel insight into how oxide surfaces interact with water as a function of relative humidity (RH). Several studies have shown that relatively inert oxide

surfaces, such as MgO (100)[26] and α-Fe_2O_3 (0001),[27] react with water to form hydroxyl groups and molecular water on the surface. However, the reactivity of catalytically active oxide surfaces for oxygen electrocatalysis, such as perovskites (ABO_3, with rare earth metal ions on the A site and late transition metal ions on the B site), has not been studied. This is partly due to the complexity of the XPS O 1*s* spectrum present on pristine ternary oxide surfaces, which has made identification of the surface oxygen species difficult. To better understand water reactivity on perovskites, AP-XPS experiments can be used to explore surface chemistry changes and identify oxygen species based on the evolution of spectroscopic features as a function of RH.

This chapter first considers the $(001)_{pc}$ surface of epitaxial $LaCoO_3$ thin films as a model polar perovskite surface. AP-XPS experiments were performed in ultrahigh vacuum (UHV), near-ambient pressure of oxygen (~100 mTorr), as well as a range of RHs (accessed through water vapor isobaric experiments). By following changes in the surface core level features under different environments, we identify the O 1*s* contributions associated with surface hydroxyls, carbonates, adsorbed water, and a surface species we attribute to undercoordinated/surface dipole influenced oxygen species. The binding energies and full-width-half-maxima associated with fitting these features are tabulated as reference for future XPS studies on perovskite surfaces, and trends in the coverage of surface species determined from the fitted peak areas are discussed.

We then extend this approach to consider a wider range of perovskite surface chemistries (La*M*O_3, *M* = Cr to Ni) to show that increasing hydroxylation measured from AP-XPS correlates with ab initio calculations of the lower free energy for a hydroxylated surface. The extent of hydroxylation exhibits a W-shape as a function of *d* electrons, which is in agreement with computed energetics of hydroxylation on *M*O_2- and LaO-terminated surfaces from density functional theory (DFT).

2.2. Experimental methods

Thin film fabrication and characterization. Films were fabricated by pulsed laser deposition (PLD) on single crystal (001)-oriented 0.5 wt% Nb-doped $SrTiO_3$ substrates with a dimension of 10×5×0.5 mm (Crystec, GmbH). The PLD targets of $LaMnO_3$ and $LaFeO_3$ were purchased (Praxair, Inc.) for thin film deposition. The $LaCoO_3$ PLD target was synthesized using a solid-state reaction from stoichiometric mixtures of La_2O_3 and Co_3O_4 (Alfa Aesar, USA) and sintered at 1450 °C to 90% theoretical density. $LaCrO_3$ and $LaNiO_3$ PLD targets were synthesized by glycine-nitrate combustion reaction. Stoichiometric quantities of nitrate precursors – $La(NO_3)_3{\cdot}6H_2O$ (99.999% metal basis, Alfa Aesar), $Ni(NO_3)_3{\cdot}6H_2O$ (99.999% metal basis, Sigma

Aldrich) or $Cr(NO_3)_3 \cdot 9H_2O$ (99.99% metal basis, Sigma Aldrich) – were dissolved in Milli-Q water (18 MΩ•cm), to which glycine was added. The mixture was heated and allowed to slowly evaporate, then heated at 400°C under air atmosphere for 4 hours. The resulting powder was ground, pressed, and sintered at 800°C under air atmosphere for 12 hours. The resulting pellet was then re-ground, pressed, and sintered a second time at the same condition.

PLD was performed using a KrF excimer laser (λ = 248 nm) at a pulse frequency of 10 Hz and laser fluence of ~ 1.50 J cm^{-2}. ~20 nm films were deposited of $LaCrO_3$, $LaMnO_3$, $LaFeO_3$, $LaCoO_3$, and $LaNiO_3$ under the conditions shown in **Table 2-1**. Thin film X-ray diffraction (XRD) was performed using a four-circle diffractometer (Bruker D8, Germany) in normal and off-normal configurations (**Figure 2-1A,B**), with relaxed lattice parameter â (calculated assuming $\nu = 0.25$[28]) and associated strain in **Table 2-1**. The film thickness was estimated using the thickness fringes in the high-resolution θ-2θ scans of the (002) diffraction peaks ("Epitaxy" software, Panalytical).

Table 2-1. *Conditions for pulsed laser deposition of ~20 nm $LaMO_3$ films and lattice parameters and strain extracted from X-ray diffraction.*

	# Pulses	Temp (°C)	pO_2 (mTorr)	ε_{zz}	ε_{xx}	c (Å)	a (Å)	â (Å)
$LaCrO_3$	5000	650	100	-0.002	0.002	3.893	3.909	3.899
$LaMnO_3$	7500	650	200	-0.001	0.001	3.902	3.911	3.905
$LaFeO_3$	6500	650	100	0.004	-0.006	3.988	3.947	3.972
$LaCoO_3$	5000	610	50	-0.007	0.011	3.790	3.859	3.817
$LaNiO_3$	5500	650	200	-0.006	0.009	3.792	3.849	3.815

Film surface morphologies were examined by atomic force microscopy (AFM, see **Figure 2-1C-G**) (Veeco), with root-mean-square (RMS) roughness values ≤ 0.5 nm, except for $LaNiO_3$ (1.6 nm). Some particles were observed on the $LaNiO_3$ surface, the coverage of which was estimated from 100× optical microscopy images to be <3.3%. These particles are expected to be stoichiometric $LaNiO_3$ fragmented from the target during deposition,[29] and the difference in surface area compared to a flat one is <1.9%.

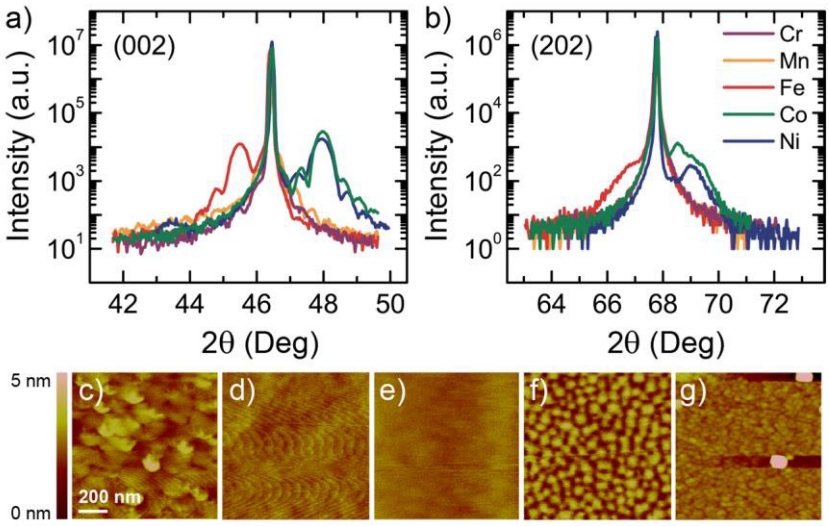

Figure 2-1. *Characterization of $LaMO_3$ films, where M = Cr (purple), Mn (orange), Fe (red), Co (green[30]), and Ni (blue). High resolution X-ray diffraction (XRD) in the a) normal configuration (002), with thickness fringes indicating high film quality, and b) off-normal configuration (202). Atomic force microscopy (AFM) of film surfaces and RMS roughness: c) $LaCrO_3$ 0.4 nm, d) $LaMnO_3$ 0.2nm, e) $LaFeO_3$ 0.2 nm, f) $LaCoO_3$ 0.5 nm,[30] g) $LaNiO_3$ 1.6 nm.*

Ambient-Pressure X-ray Photoelectron Spectroscopy (AP-XPS). AP-XPS was collected at Beamline 11.0.2[30,31] at Lawrence Berkeley National Laboratory's (LBNL) Advanced Light Source (ALS). Films were placed onto a ceramic heater,[32] with a thermocouple mounted directly onto the sample surface for temperature measurements, and isolated from the sample holder clips with an Al_2O_3 spacer. A piece of Au foil, scraped clean with a razor, was placed on top of a corner of the sample for calibration of the incident photon energy, referenced to the Au 4*f* at 84.0 eV. The binding energy (BE) of the oxide O 1*s* bulk peak was calibrated by defining the C 1*s* of adventitious carbon present on the sample prior to cleaning at 284.8 eV. All subsequent spectra are aligned relative to this O 1*s* peak.

Care was taken to reduce the beam flux so issues such as coking were not observed. This was achieved by limiting the dispersive and non-dispersive slits to 15 and 50 μm, respectively, and the X-ray beam shutter was kept closed between scans. The change in coverage of *OH for a given change of relative humidity (RH) was slightly less comparing amongst fresh regions of the sample versus comparing the change in coverage of *OH at the same location. However, coverage of *OH in both cases showed the same saturation behavior with RH.[30] We attribute the differences from beam irradiation to an increase in the dissociation constant of H_2O,[33] effectively reducing the barrier for hydroxylation. Because the irradiation was constant amongst materials and coverage of *OH shows a saturation-like behavior with RH, we do not expect adverse effects

in comparison amongst materials.

The samples were cleaned by heating to 300 °C in $p(O_2)$ of 100 mTorr (measured by a calibrated capacitance gauge) until clean of carbon (**Figure A-1**). A small amount of SO_x species were observed in the O_2 environment from displacement of residue species from the chamber walls (for an estimation of the contribution to the O 1s spectra, see **Figure A-2**), which reduced to a negligible quantity upon introduction of H_2O. After characterization of the clean surface in O_2, the chamber was evacuated to a pressure < 1.5 x 10^{-7} Torr, and $p(H_2O)$ of 100 mTorr was introduced into the chamber. The H_2O was prepared from deionized water (Millipore, >18.2 MΩ cm) and degased by several freeze-pump-thaw cycles. Contaminants in gaseous species have been previously noted to affect wetting,[34] and any possible influence from their presence has been carefully assessed. The sample was then cooled in increments of 25 °C down to a final temperature of 25 °C, keeping the chamber pressure constant at $p(H_2O)$ of 100 mTorr. At every temperature, the O 1*s* and C 1*s* core level spectra were collected, and at 100 °C increments as well as 25 °C, the La 4*d* and transition metal 3*p* core level spectra were also collected. All spectra were taken at an incident energy of 735 eV. The C/O relative sensitivity factor (RSF) was experimentally obtained by measuring the respective 1*s* core levels of 250 mTorr CO_2 gas. This provided a value of 0.86 ± 0.03:1 (O 1*s*:C 1*s*) for an incident photon energy of 735 eV. This value depends on the experimental geometry, and potentially the chamber pressure and should be measured for each experimental run.

Coverages of surface oxygenated species were estimated from the O 1*s* spectra using a multilayer electron attenuation model,[35,36] as discussed in reference [30]. This model takes as an input the oxygen atomic density, *N*, the inelastic mean free path (IMFP, λ), and the photoelectron emission angle. While the coverages of *OH and *H_2O discussed in the text give a more physical comparison amongst materials, the relative differences amongst La*M*O_3 materials can also be seen in the percent contribution of these species to the total O 1*s* counts. A small amount of adventitious carbon was also observed at lower temperatures, and is assumed to sit atop the surface uniformly and not influence the results.

Density Functional Theory Calculations. Density functional theory calculations with Hubbard U correction (DFT+U)[37,38] were carried out by Prof. Livia Giordano and Dr. Yueh-Lin Lee with a periodic approach and plane wave basis set, as implemented in the VASP code.[39,40] Core electrons were described with the Projector Augmented Wave (PAW) method,[41] and the plane wave cutoff was set to 450 eV. We used the gradient-corrected Perdew-Wang 91 (PW91) functional[42] and the optimal effective U values on the transition metal *d* electrons determined by fitting the formation enthalpies of oxides.[43,44]

Full optimizations of bulk perovskite structures for each LaMO$_3$ (M = Cr, Mn, Fe, Co, Ni) were performed using the experimental symmetry at low temperature[45-48] based on the ferromagnetic ordering in order to use a consistent and tractable set of magnetic structures, except for $LaFeO_3$, where we considered a G-type anti-ferromagnetic ordering to account for the higher Néel temperature.[45,49] Internally relaxed pseudocubic 2×2×2 perovskite supercells were then constructed with effective perovskite lattice constants obtained taking the cube root of the normalized volume (per formula unit) of the fully relaxed perovskites. The fully relaxed perovskite bulk coordinates were used as initial atomic positions and for these calculations the reciprocal space unit cell was sampled by a (2×2×2) k-point mesh. The (001) orientation of LaMO$_3$ pseudocubic perovskites is polar, and symmetric seven-layer slab models were employed in order to cancel the related dipole moment perpendicular to the surface. The (2×2) (001) LaO and MO_2-terminated slab models have been constructed using the 2×2×4 pseudocubic perovskite supercells with 10 Å vacuum space inserted between the two terminations of a (001) slab and removal of an MO_2 layer for the seven-layer (001) LaO slab (and removal of a LaO layer for the seven-layer (001) MO_2 slab). Internal relaxations of the (001) slab coordinates were performed without adsorbates. Previous work has shown that this approach gives a satisfactory description of the surface properties of these systems.[44,50] The adsorbates (dissociatively adsorbed H_2O, *OH, and *H) were then adsorbed on one side of the slab, and the adsorbate coverage varied from ¼ to 1 monolayer (ML), where 1 ML corresponds to one adsorbate per surface metal atom. The bottom two layers of the slab models were kept fixed, while the adsorbate and remaining slab coordinates were internally relaxed. A (2×2×1) k-point sampling was used for such slab models.

Stability of the (dissociatively adsorbed) H_2O, *H, and *OH at the experimental condition was estimated using the chemical potentials of H_2O, H_2 and O_2 as detailed in **Appendix A**. By setting the chemical potential of oxygen to be at the condition of T=25 °C and 1.5 x 10^{-7} Torr partial pressure of oxygen (the lowest detectable limit in the AP-XPS chamber), and the $p(H_2O)$ to be 0.1 Torr, we estimate the corresponding effective applied potential at the experimental condition to be 1.20 V relative to the standard hydrogen electrode (SHE, $a_{H^+} = 1$). This is comparable to the equilibrium potential of O_2/H_2O in O_2-saturated liquid water for ORR measurements, 1.23 V relative to the reversible hydrogen electrode. The adsorption free energies, G_{ad}, were then computed with respect to the H_2O, H_2, and O_2 chemical potential references at the effective applied potential of 1.2 V vs. SHE as detailed in **Appendix A**.

2.3. Assignment of features in core-level spectra in $LaCoO_3$ (LCO)

Significant changes in the O 1*s* and C 1*s* spectra of the LCO surface were observed with increasing RH, as shown in **Figure 2-2**. O 1*s* and C 1*s* spectra collected at select temperatures (T = 300 °C, 200 °C, 150 °C, 100 °C, 25 °C) are highlighted in shades of blue to illustrate the changes that occur with increasing RH. In contrast to the O 1*s* and C 1*s* spectra, no significant changes in the lanthanum (La 4*d*) and cobalt (Co 3*p*) spectra were observed.

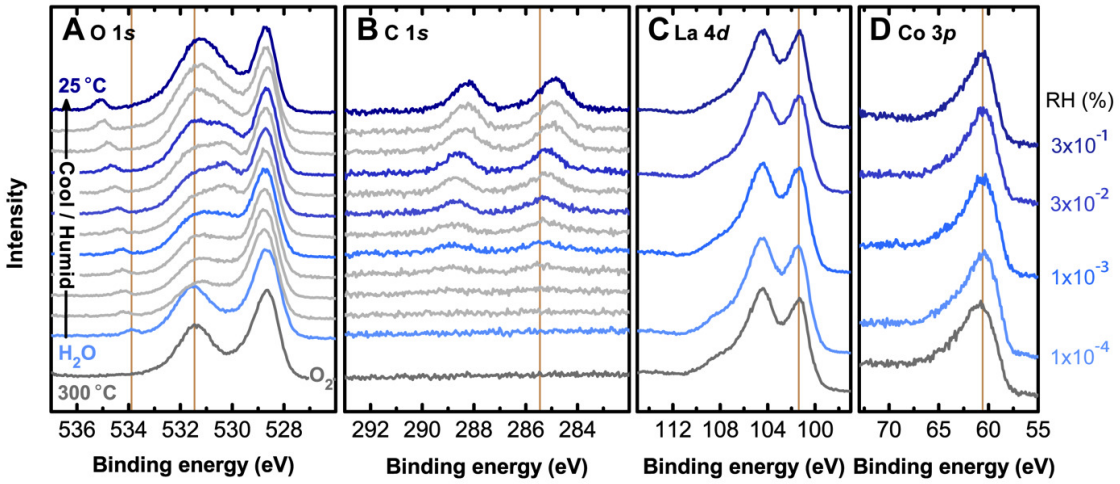

***Figure 2-2**. Spectra at 735 eV incident photon energy and fixed beam spot location. Spectra were collected for a clean film at 300 °C in 100 mTorr O_2 (bottom, dark gray) and in 100 mTorr H_2O from 300 °C (light blue) to 25 °C (dark blue) in 25°C intervals for (A) O 1s and (B) C 1s core levels. (C) La 4d and (D) Co 3p spectra were collected in 100 °C intervals. The O 1s spectra are shown normalized to the maximum intensity and all other spectra are raw intensity; all curves are offset for clarity.*

At 300 °C, the O 1*s* spectrum of the LCO surface shows two primary features at ~528.7 and ~531.5 eV. The peak at ~528.7 eV can be assigned to the bulk oxide peak (henceforth abbreviated as "Bulk"), which is consistent with those that have been reported previously.[51,52] The broad peak at higher binding energy of ~531.5 eV can be assigned to a surface species (denoted as "Surface"). It should be noted that this species is not an oxo-carbonaceous adsorbate as carbon is absent in the C 1*s* at 300 °C. The assignments of "Bulk" and "Surface" species is supported by data collected at different incident photon energies (735 eV and 1000 eV) in **Figure 2-3**, which illustrates that the relative intensity of the "Bulk" feature at the low binding energy increases at higher information depths while that of the "Surface" feature decreases. The high binding energy (significantly higher than for binary oxides) and negligible content of carbon or other impurity elements (**Appendix A, Figure A-1, A-2**) suggest that this binding energy shift results from oxygen surface species which are distinct from bulk perovskite oxide ions due to shifts in the

Madelung potential of oxygen sites on the surface[53] and/or surface electronic/structural reconstruction due to the polar nature of the oxide.[54] Undercoordinated oxygen in the crystal terminal plane or adsorbed molecularly on top would also contribute to such a surface feature.

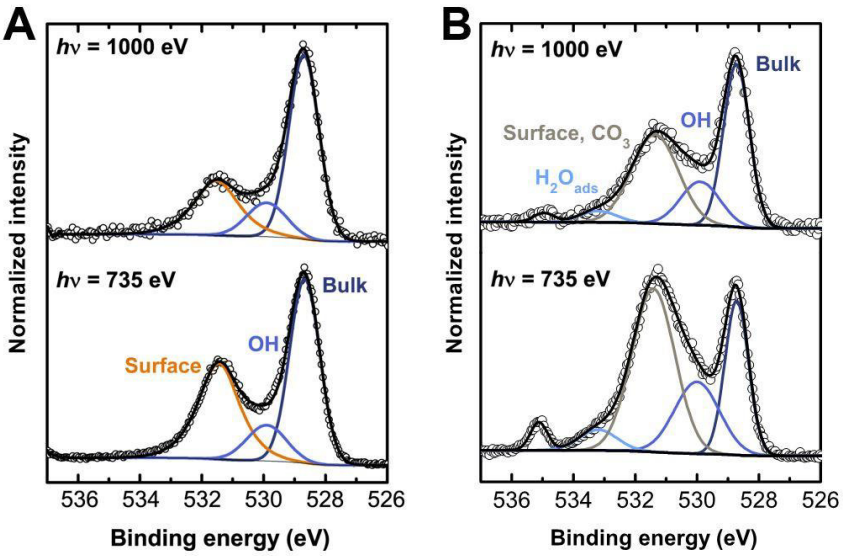

Figure 2-3. *O 1s spectra at 1000 eV and 735 eV incident photon energy and fixed beam spot. Spectra were collected for a clean film at (A) 300 °C in 100 mTorr O_2 and are shown normalized to the maximum intensity. A shallower information depth at 735 eV enhances the contribution from the surface oxidic peak ("Surface", orange) relative to the "Bulk" peak (dark blue). The nature of the central peak (OH) does not change greatly with photon energy under these conditions, however it was enhanced at shallower information depths at (B) 25 °C in 100 mTorr H_2O. In this case, the CO_3 and "Surface" oxygen are not deconvoluted separately as the RSF of O:C at 1000 eV incident photon energy was not measured.*

A peak with binding energy of ~530.5 eV (medium blue line in **Figure 2-4**) became apparent upon cooling from 300 °C in the presence of water vapor and reached maximum intensity at 150 °C. This was followed by a strong increase of a feature at higher energy (~531.5 eV, gray line in **Figure 2-4**) upon further cooling to room temperature. The intermediate binding energy peak at ~530.5 eV was found to grow with increasing RH, which can be attributed to surface hydroxylation (designated "OH"). The chemical shift of 1.8 eV observed between the hydroxyl species and "Bulk" lattice oxygen peaks (**Table 2-2**) is in good agreement with previous experimental[26,27,55] and density functional theory[55] studies on binary oxide surfaces, with reported shifts around 1.4 to 2 eV from the bulk oxide peak. This feature was present in the absence of surface carbon species and stable in the presence of water and oxygen at 300 °C (**Figure 2-4**), which is in agreement with the fact that lanthanum hydroxides are stable up to 600 °C.[56] An

increase in the high-energy O 1*s* feature with RH was coupled to the appearance of C 1*s* non-adventitious carbon species (~289 eV) on the surface, as shown in the **Figure 2-4** insets. The coupling suggests that the large increase in the feature at ~531.3 eV is due to the formation of oxo-carbonaceous species on the surface, which can occur on perovskite surfaces exposed to CO_2, even at very low pressures.[57,58] As the O 1*s* and C 1*s* binding energies of this species compares well with those of lanthanum and transition metal (bi)carbonates[59,60] but not those of other oxo-carbonaceous species,[61,62] it is assigned to surface carbonates ("CO_3"). The full-width-half-maximum (FWHM) was notably narrower for the "Bulk" peak than for the other oxygen species and remained narrow as a function of RH, similar to other metal oxides studied previously.[27] In contrast, the FWHM of all surface species were much larger but remained relatively constant as a function of RH, as shown in **Table 2-2**. Lastly, the appearance of a small shoulder on the high binding energy side of the "Surface" and (bi)carbonate feature at ~531.5 eV can be attributed to adsorbed water on the surface ("H_2O_{ads}"), where its chemical shift relative to the "Bulk" lattice oxygen peak is consistent with that seen in literature for other transition metal oxides.[27] This feature was present at only the higher RH values (> $3x10^{-2}$%, 75 °C) and increased with RH. Also present was a small peak at high binding energy associated with gas phase water (~534-535 eV).[26,27,55,63] The fitted intensities and relative contributions of these components with RH is consistent with visual inspection of the XPS spectra, where the "Bulk" peak decreased, accompanied with increasing intensities of hydroxyls, carbonates, and adsorbed water.

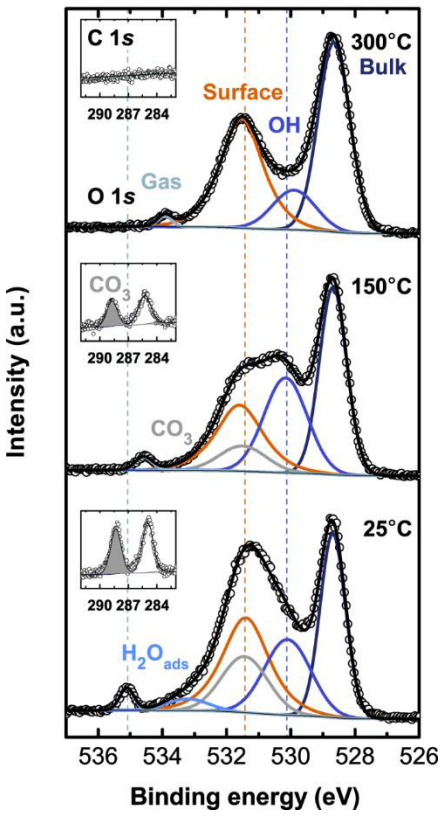

Figure 2-4. *O 1s spectra at 735 eV incident photon energy and fixed beam spot, illustrating the contribution of various surface species. Spectra were collected for an LCO film in 100 mTorr H_2O at 300 °C ($1x10^{-4}$% RH), 150 °C ($2x10^{-3}$% RH), 25 °C ($3x10^{-1}$% RH) and are shown normalized to the maximum intensity. While a clean film shows only "Bulk" oxygen (dark blue), surface oxygen ("Surface", orange), and OH (medium blue), cooling and accessing higher relative humidities results in the formation of CO_3 (light gray) and H_2O_{ads} (light blue).*

2.4. Estimation of surface adsorbate coverage on LCO

The coverage of surface adsorbates was calculated from the relative O 1*s* peak areas using a multilayer electron attenuation model,[26,64] which accounts for the number of oxygen atoms in a given adsorbate, the dimension perpendicular to the surface, and attenuation by overlaying species. The model is composed of a series of slabs, including a semi-infinite LCO crystal, a layer of "Surface" oxygen assumed to originate from the perovskite surface, a layer of co-exisiting OH and CO_3 adsorbates, and a layer of adsorbed water on top, as shown in **Figure 2-5**. It is postulated that the "Surface" oxygen layer includes perovskite CoO_2 and LaO terminations and/or reconstructed perovskite surfaces, and was treated as a slab of complete coverage but with variable thickness. OH and CO_3 were considered to co-adsorb on the film surface; although the

combined coverage was not fixed, the computed values remained less than one monolayer. Finally, adsorbed water found at low temperatures and high RHs was considered to cover the entire surface with variable thickness. Although adsorbed water likely binds preferentially to OH and less so to CO_3, our model describes adsorbed water covering both adsorbates, as it is assumed that any phase segregation of surface species such as OH and CO_3 is smaller than the area from which XPS data were collected. Additional details on the calculations and the parameters used are provided in **Appendix A** and **Table A-1**.

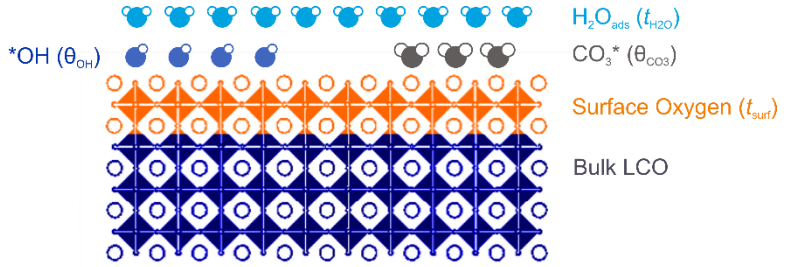

Figure 2-5. *Schematic illustration of the multilayer electron attenuation model. The computed variables of the model are listed in parentheses. The "Surface" layer of complete coverage allowed thickness t_{surf} to vary, with model parameters equal to that of the perovskite. OH and CO_3 were considered to co-adsorb with variable coverage, and adsorbed water was a uniform layer of variable thickness t_{H2O}.*

The coverage for surface adsorbates (θ_{OH}, θ_{CO3}, θ_{H2O}) on LCO as a function of temperature during the H_2O isobar experiments is shown in **Figure 2-6**. Cooling from 300 °C to 150 °C resulted in an increase of θ_{OH} from ~0.3 to ~0.85 ML, accompanied by a small amount of carbonate formation, reaching ~0.15 ML at 150 °C. This condition marks a transition point, where the combined coverage of OH and CO_3 is ~1 ML (i.e. $\theta_{OH} + \theta_{CO3} \sim 1$). Upon further cooling, the coverage of hydroxyl groups was found to decrease while the coverage of carbonates continued to increase monotonically. This observation suggests that the continued deposition of carbonaceous species on the surface comes at the expense of the hydroxyl groups. The coverage of OH and CO_3 appeared unaffected by the adsorption of water, notable at temperatures below 75 °C. The adsorption of molecular water reached ~0.1 ML at the most humid condition. The temperature-dependent surface coverage on LCO thus has three regimes: (I) predominant hydroxyl formation (300 °C < T < 150 °C); (II) predominant carbonate formation at the expense of hydroxyl groups (T < 150 °C); and (III) onset of surface wetting (T < 75 °C). Similar trends were observed during a different beamtime in which the carbonate coverage was notably higher due to residuals in the chamber from previous measurements (**Figure A-3**). The transition temperature to regime II under these conditions increased to ~200 ºC, however the corresponding

carbon coverage (θ_{CO3} ~0.2 ML) is similar to that at the transition in **Figure 2-6**.

The coverage of surface adsorbates obtained from the O 1*s* spectra collected from one fixed spot and rotating spots are compared in **Figure 2-6** as a function of temperature. While the initial OH coverage was independent of irradiation and the trends of OH, CO_3 and adsorbed water coverage as a function of RH were comparable, rotating the sample led to a lower θ_{OH} but did not affect θ_{CO3} or θ_{H2O}. The enhancement in the OH coverage by beam irradiation can be attributed to an increase in the dissociation constant of H_2O,[33] effectively reducing the barrier for hydroxylation and promoting OH binding on sites. This beam-enhanced hydroxylation was further supported by examining the coverage of OH collected from a fixed spot at 25 °C in the presence of water as a function of time. The coverage of adsorbed water remained nearly constant with time, and the slight increase in CO_3 coverage is less than the marked increase in OH coverage with 15 minutes of beam exposure, as shown in **Figure 2-6**. The linear trend in CO_3 formation both with temperature and beam exposure suggests this process is not fully equilibrated and/or reversible in the present measurements, further confirmed by a reverse isobar where the temperature was increased back to 300 ºC after cooling to 25º (**Figure A-3**).

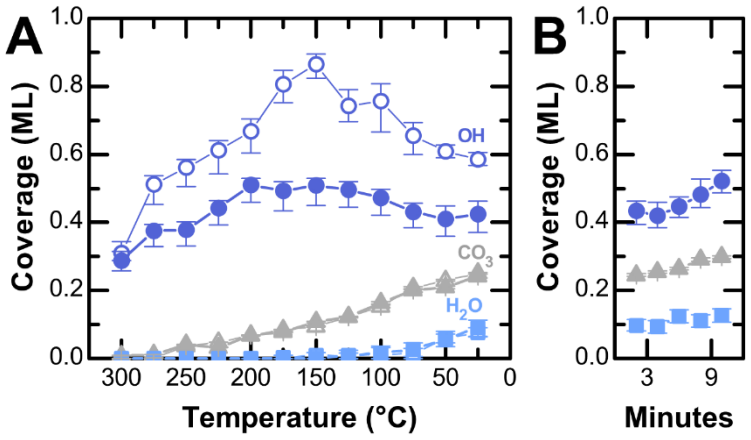

Figure 2-6. *Coverage of surface species on LCO as function of temperature (A) and time (B), comparing when the analysis area was rotated (solid) to when it was not (open): adsorbed H_2O (□, light blue), CO_3 (Δ, light gray), and OH (o, medium blue). In comparing time, the sample that was rotated during the isobar was kept at fixed position. Error bars are defined as the 95% confidence intervals estimated from Monte Carlo simulations.*

2.5. Comparison of *OH coverage across chemistries

We next examine the reactivity of water vapor on (001)-oriented La*M*O_3 film surfaces

using AP-XPS by performing water isobar experiments to deconvolute the spectra. By analyzing the evolution of the O 1*s* and C 1*s* spectra with RH, the spectra were deconvoluted into different oxygen groups on the surface (**Table 2-2**).[30] All chemistries evolve similarly with RH, with one exception in the fitting scheme in the case of $LaFeO_3$. Simple visual comparison of the spectral evolution showed that the shape of the low BE (bulk-Ox) peak widened for increasing relative humidity. Depth profiling by changing the incident photon energy showed that the low BE shoulder was bulk-like in nature (i.e. the intensity decreased for lower incident photon energy and shallower information depth; see **Figure A-4**). Thus, $LaFeO_3$ was fit with two bulk-Ox peaks, keeping the full width half maximum (FWHM) and Gaussian/Lorentzian the same, with the second located 0.8 eV higher in BE than the first. The intensity of the two bulk-Ox peaks was summed in coverage calculations.

Table 2-2. *Fitting parameters for O 1s spectra*

		Bulk-Ox	**Surface-O**	***OH**	**CO_3***	***H_2O**	**H_2O_{gas}**
$LaCrO_3$	**% Lorentzian**	10	50	0	0	0	0
	FWHM (eV)	1.0-1.3	1.5-1.7	1.5-1.7	1.5-1.7	1.4-1.5	0.5-1.0
	BE_{low} (eV)	528.7	531	530.1	531.3	533.18	533.88
	BE_{high} (eV)	528.9	531.8	530.4	531.7	533.28	535.98
$LaMnO_3$	**% Lorentzian**	10	70	0	0	0	0
	FWHM (eV)	1.0-1.3	1.5-1.7	1.5-1.7	1.5-1.7	1.4-1.5	0.5-1.0
	BE_{low} (eV)	528.92	531.3	530	531.5	533.2	533.9
	BE_{high} (eV)	528.95	531.4	530.3	531.6	533.3	535
$LaFeO_3$	**% Lorentzian**	10	50	0	0	0	0
	FWHM (eV)	1.1-1.3	1.5-1.7	1.5-1.7	1.5-1.7	1.4-1.5	0.5-1.0
	BE_{low} (eV)	528.2*	531	530.1	531.3	533.0	533.685
	BE_{high} (eV)	528.5*	531.3	530.3	531.6	533.25	534.7
$LaCoO_3$	**% Lorentzian**	10	70	0	0	0	0
	FWHM (eV)	0.9-1.2	1.5-1.7	1.5-1.7	1.5-1.7	1.4-1.5	0.5-1.0
	BE_{low} (eV)	528.6	531.4	529.9	531.2	533.2	533.9
	BE_{high} (eV)	528.8	531.7	530.2	531.7	533.3	535
$LaNiO_3$	**% Lorentzian**	10	70	0	0	0	0
	FWHM (eV)	1.0-1.3	1.5-1.7	1.5-1.7	1.5-1.7	1.4-1.5	0.5-1.0
	BE_{low} (eV)	528.2	530.9	529.4	531.3	533.02	533.7
	BE_{high} (eV)	528.3	531.3	529.7	531.5	533.12	534.8

*$LaFeO_3$ was fit with a second Bulk-Ox peak with the same peak shape and FWHM as the first Bulk-Ox peak, and located at 0.8 eV higher BE than the other bulk peak.

Quantifying by a multilayer electron attenuation model, we compare the component species

at fixed relative humidity (RH, **Figure 2-7**). The coverage of *OH and adsorbed *H_2O under the highest RH of the isobar was extracted using a multilayer model proposed above for $LaCoO_3$.[30] The *OH coverage increases in the order of Co < Mn < Ni < Fe < Cr, where a difference up to half a monolayer (ML) reflects significantly different affinities of La$M$$O_3$ toward hydroxylation and binding strengths of *OH. The coverage of *OH was also found to scale with adsorbed *H_2O, as shown in **Figure 2-7**, which suggests that water can interact strongly with hydroxyl groups on the surface.

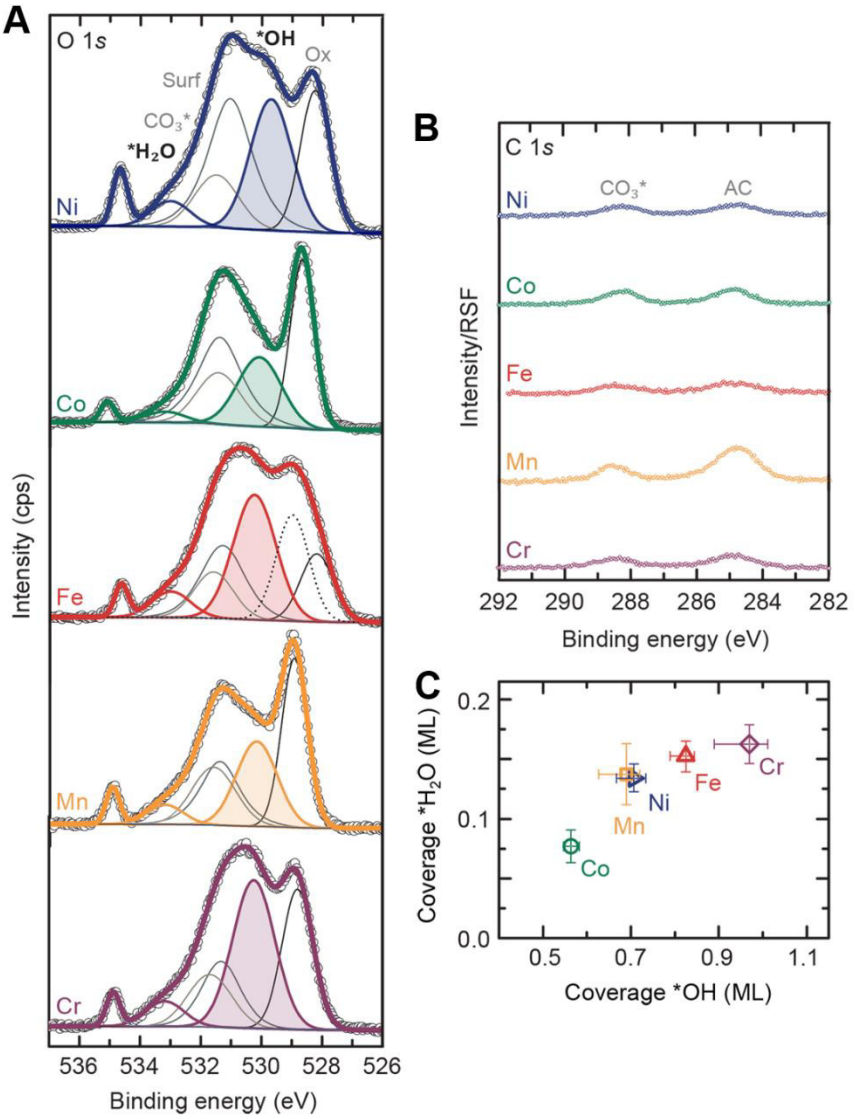

Figure 2-7. *Quantification of adsorbates by AP-XPS. (A) Fitted O 1s spectra at 25 °C in 0.1 Torr H_2O. Raw data in counts per second are shown as circles, and the envelope resulting from the fitted components in bold color; curves are offset for clarity. The *OH intensity is shaded and that of *H_2O outlined in corresponding color. (B) Corresponding C 1s spectra, with axis scale*

taken from (A), adjusted to size, and divided by the experimental O 1s:C 1s relative sensitivity factor (RSF). Shown are the CO_3 component and adventitious carbon (AC). (C) The coverage of *OH and *H_2O scale with each other, with color corresponding to that in (A). Error bars are defined as the 95% confidence intervals estimated from Monte Carlo simulations.*

To better understand the trend in hydroxyl affinity with oxide chemistry (**Figure 2-8A**), we calculated the free energy of adsorption of *OH and *H (dissociated water) on LaO and MO_2 terminations by DFT+U calculations (additional details of the thermodynamic approaches are provided in Supporting Information), corresponding to the reduction of surface energy upon hydroxylation. The stability of the different species on the two surface terminations, assuming the system is in thermodynamic equilibrium, should correspond to their relative abundance. Since the surface stability also depends on the chemical potential of metals in the bulk, such a calculation requires definition of the La and *M* chemical potentials. These metal chemical potentials are not independent variables and their sum is fixed by the condition that the system is in equilibrium with bulk $LaMO_3$. We have compared the (001) LaO and MO_2 surface energy values[65,66] obtained in both the La-rich (system in equilibrium with La_2O_3) and the *M*-rich conditions (system in equilibrium with the MO_x binary oxide compounds) (**Figure A-5**). These two conditions can be considered as the two metal potential limits where the perovskites are stable with respect to the binary oxide compounds. The relative stability of the various hydroxylated surfaces was assessed by comparing the adsorption energy on the MO_2 surface to that on the LaO surface adjusted for the difference in surface energy between the facets, both are referenced to the ideal (001) MO_2-surface at the 1.20 V vs. SHE (**Figure A-6, A-7**).

When comparing the adsorption free energy on the two surface terminations, we observe that the LaO surface has a higher affinity for water and hydroxyls groups. To gain insight into more humid environments, we then compute the free energies of the hydroxylated surface: a full monolayer of *OH and *OH + *H (dissociated water) on the LaO and MO_2 surfaces respectively (**Figure 2-8B**), both relative to the bare MO_2 surfaces. These hydroxylated surfaces are expected to better reflect the interactions between adsorbates present on a wetted surface. Both adsorption energies exhibit an inverse W-shape with the number of *d* electrons, accounting for the differences in surface energy compared to the bare MO_2 surface.

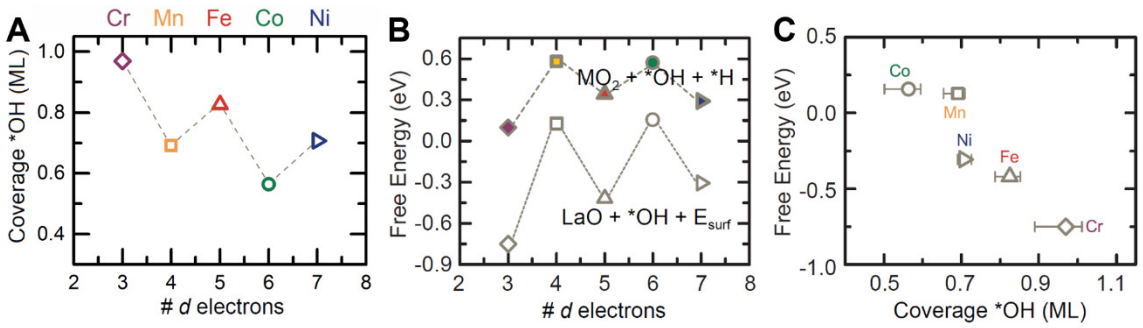

Figure 2-8. *(A) Coverage of *OH as a function of transition metal in $LaMO_3$. (B) Density Functional Theory (DFT) calculated free energies for full coverage of water dissociative adsorption on MO_2 surfaces (filled) and hydroxylation of LaO surfaces (open) relative to the bare MO_2 surface. (C) The DFT-calculated free energies for the hydroxylation of LaO surfaces correlates with the coverage measured experimentally by AP-XPS.*

The computed surface free energies of the stable hydroxylated LaO termination with 1 monolayer *OH relative to the bare MO_2 surface trends with the experimental coverage measured at 0.3% RH by AP-XPS (**Figure 2-8C**). The correlation suggests the coverage from AP-XPS experimentally assesses the relative affinity of a surface toward hydroxylation.

2.6. Chapter 2 summary

This chapter has used AP-XPS to study water reactivity with the $(100)_{pc}$ surface of LaMO$_3$ (M = Cr-Ni) films grown on Nb:SrTiO$_3$ by examining systematic changes in the core-level spectra at different RHs. Specifically, we observe that surface hydroxyl groups are the dominant adsorbate, along with minor components including (bi)carbonates, adsorbed water, and undercoordinated/surface-dipole influenced oxygen sites on the perovskite surface. The coverage of these species can be estimated using a multilayer electron attenuation model, and we report three distinct surface-water interaction regimes with increasing RH: an initial hydroxylation, followed by a saturation regime after which carbonates begin to displace hydroxyl groups, and then adsorption of water molecules. Such AP-XPS studies on well-defined oxide surfaces can provide insights into the reactivity of oxides with the environment and the chemistry of oxide surfaces, which is critical to develop functional oxides for catalysis, sensing and energy storage applications. The following chapter will consider the implications of hydroxyl affinity in the performance of perovskite catalysts for oxygen electrocatalysis and wetting on a macroscopic scale.

References

1 Brown, G. E. *et al.* Metal Oxide Surfaces and Their Interactions with Aqueous Solutions and Microbial Organisms. *Chemical Reviews* **99**, 77-174, (1998).

2 Kuhlenbeck, H., Shaikhutdinov, S. & Freund, H.-J. Well-Ordered Transition Metal Oxide Layers in Model Catalysis – A Series of Case Studies. *Chemical Reviews* **113**, 3986-4034, (2013).

3 Gray, H. B. Powering the planet with solar fuel. *Nature Chemistry* **1**, 7-7, (2009).

4 Chorkendorff, I. & Niemantsverdriet, J. W. *Concepts of Modern Catalysis and Kinetics*. (Wiley-VCH, 2003).

5 Azimi, G., Dhiman, R., Kwon, H.-M., Paxson, A. T. & Varanasi, K. K. Hydrophobicity of rare-earth oxide ceramics. *Nature Materials* **12**, 315-320, (2013).

6 Thiel, P. A. & Madey, T. E. The Interaction of Water with Solid Surfaces: Fundamental Aspects. *Surface Science Reports* **7**, 211-385, (1987).

7 Henderson, M. A. The Interaction of Water with Solid Surfaces: Fundamental Aspects Revisited. *Surface Science Reports* **46**, 1-308, (2002).

8 Giovambattista, N., Debenedetti, P. G. & Rossky, P. J. Effect of Surface Polarity on Water Contact Angle and Interfacial Hydration Structure. *The Journal of Physical Chemistry B* **111**, 9581-9587, (2007).

9 Ketteler, G. *et al.* The Nature of Water Nucleation Sites on TiO_2(110) Surfaces Revealed by Ambient Pressure X-ray Photoelectron Spectroscopy. *The Journal of Physical Chemistry C* **111**, 8278-8282, (2007).

10 Rossmeisl, J., Qu, Z. W., Zhu, H., Kroes, G. J. & Nørskov, J. K. Electrolysis of water on oxide surfaces. *Journal of Electroanalytical Chemistry* **607**, 83-89, (2007).

11 Suntivich, J. *et al.* Design Principles for Oxygen-Reduction Activity on Perovskite Oxide Catalysts for Fuel Cells and Metal–Air Batteries. *Nature Chemistry* **3**, 546-550, (2011).

12 Suntivich, J., May, K. J., Gasteiger, H. A., Goodenough, J. B. & Shao-Horn, Y. A Perovskite Oxide Optimized for Oxygen Evolution Catalysis from Molecular Orbital Principles. *Science* **334**, 1383-1385, (2011).

13 Subbaraman, R. *et al.* Trends in Activity for the Water Electrolyser Reactions on 3*d* M(Ni,Co,Fe,Mn) Hydr(oxy)oxide Catalysts. *Nature Materials* **11**, 550-557, (2012).

14 Man, I. C. *et al.* Universality in Oxygen Evolution Electrocatalysis on Oxide Surfaces. *ChemCatChem* **3**, 1159-1165, (2011).

15 Leung, T., Kao, C., Su, W., Feng, Y. & Chan, C. Relationship Between Surface Dipole, Work Function and Charge Transfer:Some Exceptions to an Established Rule. *Physical Review B* **68**, 195408, (2003).

16 Solomon, E. I., Jones, P. M. & May, J. A. Electronic Structures of Active Sites on Metal Oxide Surfaces: Definition of the Cu/ZnO Methanol Synthesis Catalyst by Photoelectron Spectroscopy. *Chemical Reviews* **93**, 2623-2644, (1993).

17 Rossmeisl, J., Karlberg, G. S., Jaramillo, T. & Norskov, J. K. Steady State Oxygen Reduction and Cyclic Voltammetry. *Faraday Discussions* **140**, 337-346, (2008).

18 Granick, S. & Bae, S. C. A Curious Antipathy for Water. *Science* **322**, 1477-1478, (2008).

19 Diebold, U., Li, S.-C. & Schmid, M. Oxide Surface Science. *Annual Review of Physical Chemistry* **61**, 129-148, (2010).

20 R. Flavell, W. *et al.* Electronic structure and surface reactivity of $La_{1-x}Sr_xCoO_3$. *Faraday Discussions* **114**, 407-420, (1999).

21 Wang, Z. *et al.* Water Adsorption at the Tetrahedral Titania Surface Layer of $SrTiO_3(110)$-(4×1). *The Journal of Physical Chemistry C* **117**, 26060-26069, (2013).

22 Ogletree, D. F. *et al.* A Differentially Pumped Electrostatic Lens System for Photoemission Studies in the Millibar Range. *Rev. Sci. Instrum.* **73**, 3872-3877, (2002).

23 Starr, D. E., Liu, Z., Havecker, M., Knop-Gericke, A. & Bluhm, H. Investigation of Solid/Vapor Interfaces Using Ambient Pressure X-ray Photoelectron Spectroscopy. *Chemical Society Reviews* **42**, 5833-5857, (2013).

24 Salmeron, M. & Schlögl, R. Ambient Pressure Photoelectron Spectroscopy: A New Tool for Surface Science and Nanotechnology. *Surface Science Reports* **63**, 169-199, (2008).

25 Ogletree, D. F., Bluhm, H., Hebenstreit, E. D. & Salmeron, M. Photoelectron Spectroscopy under Ambient Pressure and Temperature Conditions. *Nuclear Instruments & Methods in Physics Research, Section A: Accelerators, Spectrometers, Detectors, and Associated Equipment* **601**, 151-160, (2009).

26 Newberg, J. T. *et al.* Formation of Hydroxyl and Water Layers on MgO Films Studied with Ambient Pressure XPS. *Surf Sci* **605**, 89-94, (2011).

27 Yamamoto, S. *et al.* Water Adsorption on α-$Fe_2O_3(0001)$ at near Ambient Conditions. *Journal of Physical Chemistry C* **114**, 2256-2266, (2010).

28 Christen, H. M., Specht, E. D., Silliman, S. S. & Harshavardhan, K. S. Ferroelectric and antiferroelectric coupling in superlattices of paraelectric perovskites at room temperature. *Physical Review B* **68**, 020101, (2003).

29 Proyer, S., Stangl, E., Borz, M., Hellebrand, B. & Bäuerle, D. Particulates on Pulsed-Laser Deposited Y-Ba-Cu-O Films. *Physica C: Superconductivity* **257**, 1-15, (1996).

30 Stoerzinger, K. A. *et al.* Water Reactivity on the $LaCoO_3$ (001) Surface: An Ambient Pressure X-ray Photoelectron Spectroscopy Study. *The Journal of Physical Chemistry C* **118**, 19733-19741, (2014).

31 Ogletree, D. F., Bluhm, H., Hebenstreit, E. D. & Salmeron, M. Photoelectron Spectroscopy under Ambient Pressure and Temperature Conditions. *Nucl. Instrum. Methods Phys. Res., Sect. A* **601**, 151-160, (2009).

32 Whaley, J. A. *et al.* Note: Fixture for Characterizing Electrochemical Devices in-Operando in Traditional Vacuum Systems. *Review of Scientific Instruments* **81**, 086104-086103, (2010).

33 Andersson, K., Nikitin, A., Pettersson, L. G. M., Nilsson, A. & Ogasawara, H. Water Dissociation on Ru(001): An Activated Process. *Physical Review Letters* **93**, 196101, (2004).

34 Yates Jr, J. T. Photochemistry on TiO_2: Mechanisms Behind the Surface Chemistry. *Surf Sci* **603**, 1605-1612, (2009).

35 McCafferty, E. & Wightman, J. P. Determination of the Concentration of Surface Hydroxyl Groups on Metal Oxide Films by a Quantitative XPS Method. *Surface and Interface Analysis* **26**, 549-564, (1998).

36 Kurbatov, G., Darque-Ceretti, E. & Aucouturier, M. Characterization of Hydroxylated Oxide Film on Iron Surfaces and its Acid–Base Properties using XPS. *Surface and Interface Analysis* **18**, 811-820, (1992).

37 Anisimov, V. I., Aryasetiawan, F. & Lichtenstein, A. I. First-Principles Calculations of the Electronic Structure and Spectra of Strongly Correlated Systems: The LDA + U Method. *Journal of Physics: Condensed Matter* **9**, 767, (1997).

38 Dudarev, S. L., Botton, G. A., Savrasov, S. Y., Humphreys, C. J. & Sutton, A. P. Electron-Energy-Loss Spectra and the Structural Stability of Nickel Oxide:An LSDA+U Study. *Physical Review B* **57**, 1505-1509, (1998).

39 Kresse, G. & Furthmüller, J. Efficient Iterative Schemes for *Ab Initio* Total-Energy Calculations Using a Plane-Wave Basis Set. *Physical Review B* **54**, 11169-11186, (1996).

40 Kresse, G. & Hafner, J. *Ab Initio* Molecular Dynamics for Liquid Metals. *Physical Review B* **47**, 558-561, (1993).

41 Blöchl, P. E. Projector Augmented-Wave Method. *Physical Review B* **50**, 17953-17979, (1994).

42 Perdew, J. P. *et al.* Atoms, Molecules, Solids, and Surfaces: Applications of the Generalized Gradient Approximation for Exchange and Correlation. *Physical Review B* **46**, 6671-6687, (1992).

43 Wang, L., Maxisch, T. & Ceder, G. Oxidation Energies of Transition Metal Oxides within the GGA+U Framework. *Physical Review B* **73**, 195107, (2006).

44 Lee, Y.-L., Kleis, J., Rossmeisl, J. & Morgan, D. *Ab Initio* Energetics of La*B*O_3 (001) (*B* = Mn, Fe, Co, and Ni) for Solid Oxide Fuel Cell Cathodes. *Physical Review B* **80**, 224101, (2009).

45 Koehler, W. C. & Wollan, E. O. Neutron-Diffraction Study of the Magnetic Properties of Perovskite-Like Compounds $LaBO_3$. *Journal of Physics and Chemistry of Solids* **2**, 100-106, (1957).

46 Elemans, J. B. A. A., Van Laar, B., Van Der Veen, K. R. & Loopstra, B. O. The Crystallographic and Magnetic Structures of $La_{1-x}Ba_xMn_{1-x}Me_xO_3$ (Me = Mn or Ti). *Journal of Solid State Chemistry* **3**, 238-242, (1971).

47 Geller, S. & Wood, E. A. Crystallographic Studies of Perovskite-Like Compounds. I. Rare Earth Orthoferrites and $YFeO_3$, $YCrO_3$, $YAlO_3$. *Acta Crystallographica* **9**, 563-568, (1956).

48 Thornton, G., Tofield, B. C. & Hewat, A. W. A Neutron Diffraction Study of $LaCoO_3$ in the Temperature Range $4.2 < T < 1248$ K. *Journal of Solid State Chemistry* **61**, 301-307, (1986).

49 Goodenough, J. B. Localized versus Collective *d* Electrons and Néel Temperatures in Perovskite and Perovskite-Related Structures. *Physical Review* **164**, 785-789, (1967).

50 Lee, Y.-L., Kleis, J., Rossmeisl, J., Shao-Horn, Y. & Morgan, D. Prediction of Solid Oxide Fuel Cell Cathode Activity with First-Principles Descriptors. *Energy & Environmental Science* **4**, 3966-3970, (2011).

51 Gonzalez-Tejuca, L., Bell, A. T., Fierro, J. L. G. & Pena, M. A. Surface Behaviour of Reduced $LaCoO_3$ as Studied by TPD of CO, CO_2 and H_2 Probes and by XPS. *Applied Surface Science* **31**, 301-316, (1988).

52 Imamura, M., Matsubayashi, N. & Shimada, H. Catalytically Active Oxygen Species in $La_{1.x}Sr_xCoO_{3-\delta}$ Studied by XPS and XAFS Spectroscopy. *Journal of Physical Chemistry B* **104**, 7348-7353, (2000).

53 Wolfram, T., Kraut, E. & Morin, F. d-Band Surface States on Transition-Metal Perovskite Crystals: I. Qualitative Features and Application to $SrTiO_3$. *Physical Review B* **7**, 1677-1694, (1973).

54 Noguera, C. Polar Oxide Surfaces. *Journal of Physics: Condensed Matter* **12**, R367-R410, (2000).

55 Kendelewicz, T. *et al.* X-ray Photoemission and Density Functional Theory Study of the Interaction of Water Vapor with the Fe_3O_4(001) Surface at Near-Ambient Conditions. *Journal of Physical Chemistry C* **117**, 2719-2733, (2013).

56 Kohli, P. S., Kumar, M., Raina, K. K. & Singla, M. L. Mechanism for the Formation of Low Aspect Ratio of $La(OH)_3$ Nanorods in Aqueous Solution: Thermal and Frequency Dependent Behaviour. *Journal of Materials Science: Materials in Electronics* **23**, 2257-2263, (2012).

57 Tascon, J. M. D. & Tejuca, L. G. Adsorption of CO_2 on the Perovskite-Type Oxide $LaCoO_3$. *Journal of the Chemical Society, Faraday Transactions 1: Physical Chemistry in Condensed Phases* **77**, 591-602, (1981).

58 Baniecki, J. D. *et al.* Chemisorption of Water and Carbon Dioxide on Nanostructured $BaTiO_3$–$SrTiO_3$(001) surfaces. *Journal of Applied Physics* **106**, 054109, (2009).

59 Gonzalez-Elipe, A. R., Espinos, J. P., Fernandez, A. & Munuera, G. XPS Study of the Surface Carbonation/Hydroxylation State of Metal Oxides. *Applied Surface Science* **45**, 103-108, (1990).

60 Stoch, J. & Gablankowska-Kukucz, J. The Effect of Carbonate Contaminations on the XPS O 1s Band Structure in Metal Oxides. *Surface and Interface Analysis* **17**, 165-167, (1991).

61 Briggs, D. & Beamson, G. Primary and Secondary Oxygen-Induced C 1s Binding Energy Shifts in X-ray Photoelectron Spectroscopy of Polymers. *Analytical Chemistry* **64**, 1729-1736, (1992).

62 Briggs, D. & Beamson, G. XPS Studies of the Oxygen 1s and 2s Levels in a Wide Range of Functional Polymers. *Analytical Chemistry* **65**, 1517-1523, (1993).

63 Bluhm, H. Photoelectron Spectroscopy of Surfaces Under Humid Conditions. *Journal of Electron Spectroscopy and related Phenomena* **177**, 71-84, (2010).

64 McCafferty, E. & Wightman, J. P. Determination of the Concentration of Surface Hydroxyl Groups on Metal Oxide Films by a Quantitative XPS Method. *Surf. Interface Anal.* **26**, 549-564, (1998).

65 Reuter, K. & Scheffler, M. Composition, Structure, and Stability of RuO_2 (110) as a Function of Oxygen Pressure. *Physical Review B* **65**, 035406, (2001).

66 Johnston, K., Castell, M. R., Paxton, A. T. & Finnis, M. W. $SrTiO_3$ (001) (2x1) Reconstructions:First-Principles Calculations of Surface Energy and Atomic Structure

Compared with Scanning Tunneling Microscopy Images. *Physical Review B* **70**, 085415, (2004).

3. Implications of *OH on ORR and macroscopic wetting

3.1. Introduction

An assessment of the surface species present under humid conditions and different surface's affinity for them can build understanding of the reaction mechanism in oxygen electrocatalysis. For example, computational approaches have shown that the binding and coverage of *OH species for Pt-alloys[1] correlates with the activities for the oxygen reduction and evolution reactions. This has been corroborated by experimental assessment of OH affinity through features in cyclic voltammetry (CV).[2] Such studies have established the binding strength of *OH as an activity descriptor, which has enabled the rational design of more active Pt-containing catalysts.[3]

In Chapter 2, we established AP-XPS as an experimental approach to quantify the affinity of perovskite surfaces for hydroxyl formation. Specifically, the coverage at a fixed chemical potential of water (i.e. relative humidity, RH) scales with the stability of hydroxylated surfaces calculated by density functional theory (DFT).[4] We will now use this experimental value of coverage as a proxy for OH affinity, trending with numerous parameters expected to impact the catalytic reactivity and wettability, including M-OH bond strength and length in addition to electron density on the adsorbed OH group.[5,6]

Having established correlation in adsorbed *OH and *H_2O coverage using AP-XPS in Chapter 2, we now further consider the role of H-bonding in the oxygen reduction reaction (ORR) and wetting on a macroscopic scale. Specifically, we employ contact angle measurements on epitaxial films—minimizing extrinsic variables such as grain boundaries, roughness, and exposure of multiple crystal facets[7]—to consider the intrinsic wettability of oxide surfaces. The resultant angle reflects a balance of apolar, electron donating, and electron accepting forces between the probe liquid and the surface,[8] and therefore can establish the acid/base properties[9] of the wetted (and hydroxylated) oxide surface.

We then consider the implications of surface speciation and polarity in oxygen electrocatalysis. In Chapter 1, a reaction mechanism for the ORR was proposed, in which *OH served as a key reaction intermediate. Work by Suntivich et al.[10] proposed the activity volcano

resulting using the antibonding orbital occupancy of e_g electrons in composite powder-based electrons resulted from a tradeoff in rate-limiting steps. For strong interactions, the final reprotonation of adsorbed *O to reinstate the resting *OH state was assumed rate limiting, in contrast to weaker interactions, when the displacement of *OH by reactant O_2 was assumed limiting. This Chapter therefore considers the affinity for *OH across La*M*O_3 (*M* = Cr-Ni) films in relation to their activity for the ORR in order to assess the validity of the proposed mechanism.

3.2. Experimental

*Details of film fabrication and quantification of *OH and *H_2O coverage with AP-XPS are provided in Chapter 2.*

Contact Angle Measurements. Contact angles for the three probe liquids of diiodomethane (DIM, Alfa Aesar), ethylene glycol (EG, Alfa Aesar), and deionized water (18 MΩ-cm, Millipore) were measured using a Ramé-Hart M500-advanced goniometer. The advancing and receding contact angles were measured by adding/removing water from a 5 µl droplet on the surface at the rate of 0.2 µl/sec. This ensures that the capillary number is always low enough for accurate measurements. A smaller droplet volume was used with other probe liquids due to the lower contact angle and small sample size. Measurements on a second $LaMnO_3$ film yielded a water advancing angle within 2° and a receding angle within 5° of that measured on the first film. Repeat measurements on the first film after drying yielded values within the same range.

For interactions between a solid *S* and a liquid *L*, the change in free energy can be considered as the sum of that arising from apolar Lifshitz-van der Waals interactions, ΔG_{SL}^{LW}, and from polar acid-base interactions, ΔG_{SL}^{AB}:

$$\Delta G_{SL} = \Delta G_{SL}^{LW} + \Delta G_{SL}^{AB} \qquad \textit{Equation 3-1}$$

The apolar interactions depend only on the apolar free energy, γ^{LW}, of the solid and liquid:[11]

$$\Delta G_{SL}^{LW} = -2\sqrt{\gamma_S^{LW}\gamma_L^{LW}} \qquad \textit{Equation 3-2}$$

Whereas the polar interactions depend on the electron accepting, γ^+, and electron donating, γ^-, contributions from both surface and probe liquid:[9,12,13]

$$\Delta G_{SL}^{AB} = -2\sqrt{\gamma_S^+\gamma_L^-} - 2\sqrt{\gamma_S^-\gamma_L^+} \qquad \textit{Equation 3-3}$$

Thus by measuring the contact angle, θ, with three probe liquids of known $\gamma_{L,i}^{LW}$, $\gamma_{L,i}^{+}$, $\gamma_{L,i}^{-}$, and surface tension $\gamma_{L,i}$, all components of surface energy can be quantified using the van Oss-Chaudhury-Good approach:[9,14]

$$\gamma_{L,i}(1+\cos\theta_i) = 2\left(\sqrt{\gamma_S^{LW}\gamma_{L,i}^{LW}} + \sqrt{\gamma_S^{+}\gamma_{L,i}^{-}} + \sqrt{\gamma_S^{-}\gamma_{L,i}^{+}}\right) \quad \textit{Equation 3-4}$$

Error bars were determined from the spread in calculated γ^- resulting from duplicate measurements on the same film. The surface components of select probe liquids are shown below in **Table 3-1**.[15]

Table 3-1. *Components of surface free energy for the three probe liquids used*[15]

	γ (mJ m^{-2})	γ^{LW} (mJ m^{-2})	γ^{+} (mJ m^{-2})	γ^{-} (mJ m^{-2})
Water	72.8	21.8	25.5	25.5
Ethylene glycol (EG)	48	29	1.92	47
Diiodomethane (DIM)	50.8	50.8	0	0

The Gibb's Adsorption equation relates the surface free energy of a solid to its chemical potential, which when in equilibrium with a liquid can in turn be related to the pressure difference across the air-liquid interface. The pressure can be expressed in terms of the contact angle and curvature; comparing advancing (θ_a) and receding angles (θ_r), the contact line remains pinned, and the free energy of hysteresis, Δg, can be expressed solely in terms of contact angles:[16,17]

$$\Delta g = -(RT/A)ln(\sin\theta_r / \sin\theta_a) \quad \textit{Equation 3-5}$$

where A is the molar surface area. As all LaMO$_3$ films show negligible roughness via AFM, with the projected surface area being within 1% of the true surface area, we will neglect this areal term and compare molar free energies, ΔG. The free energy of hysteresis is plotted in **Figure 3-3** versus the transition metal *d*-filling. The trends observed are similar to that intuited from looking at the difference in advancing and receding angles in **Figure 3-1**, but considering ΔG enables a direct comparison of the magnitude of hysteresis.

The magnitudes of ΔG observed for the polar probe molecules EG and H_2O is large. While there are few studies of the surface chemistry of oxides in relation to wetting, polymers containing numerous functional groups have been extensively investigated. Relatively nonpolar polymers (such as polyethylene) have molar free energies corresponding to the strength of van der Waals bonds, less than1 kJ/mol[18]. In contrast, polar polymers are characterized by ΔG ~ 1-4 kJ/mol, which has been attributed to conformational changes in polar groups[19] and/or strong interactions such as hydrogen bonding.[20]

Electrochemical Measurements. Electrical contacts were applied to the back of the

conductive Nb-doped $SrTiO_3$ substrate, as reported previously.[21] Gallium–indium eutectic (Sigma-Aldrich, 99.99%) was scratched into the Nb-doped $SrTiO_3$, and a Ti wire (Sigma-Aldrich, 99.99%) was affixed with silver paint (Ted Pella, Leitsilber 200). The back and sides of the electrode, as well as the wire, were covered with a non-conductive, chemically resistant epoxy (Omegabond 101), so only the catalyst surface was exposed to the electrolyte.

Electrochemical measurements were conducted with a Biologic SP-300 potentiostat in an ~120 mL solution of 0.1 M KOH, prepared from deionized water (Millipore, >18.2 MΩ cm) and KOH pellets (Sigma-Aldrich, 99.99%). Potentials were referenced to a saturated Ag/AgCl electrode (Pine), calibrated to the reversible hydrogen electrode (RHE) scale in 0.1 M KOH. Oxygen reduction reaction (ORR) measurements were carried out in an electrolyte pre-saturated by bubbling O_2 for at least 45 minutes and under continuous O_2 bubbling (Airgas, ultrahigh-grade purity). ORR cyclic voltammetry (CV) at a scan rate of 10 mV s^{-1} is plotted corrected for capacitance by averaging the forward and backward sweeps. Electrical impedance spectroscopy (EIS) was performed at the open circuit voltage with an amplitude of 10 mV. Potentials were corrected for the electrolyte/cell resistance from the high frequency intercept of the real impedance (45 Ω).

3.3. Influence of *OH on macroscopic wetting

We first show that the receding contact angle of water in macroscopic wetting trends with the surface coverage of *OH groups on La$M$$O_3$ measured by AP-XPS. The macroscopic interaction of La$M$$O_3$ film surfaces with water was measured by the advancing and receding contact angle. Wetting hysteresis can provide insights into the chemical nature of the water/oxide interface as the contact line experiences different interactions during advancing and receding motion.[16]

All surfaces were moderately hydrophobic in contact with water with advancing angles of ~90°, with the exception of $LaCrO_3$ ~70° (**Figure 3-1A**). We attribute the difference in wettability to the presence of Cr^{6+} when exposed to O_2 gas and its readiness to reduce to Cr^{3+} upon wetting (**Figure 3-2**). This is in contrast to other transition metals in the form of La$M$$O_3$, which remain nominally in the 3+ valence state upon exposure to O_2 gas, and are more resistant to oxidation. The higher oxidation state of Cr leads to a more electronegative transition metal center (higher reduction potential), promoting electron transfer upon interaction with H_2O and expected to wet more readily than other La$M$$O_3$ surfaces, where M retains the 3+ valence state on the surface. The oxidized $LaCrO_3$ surface can also be considered more acidic,[22] which promotes wetting.[23]

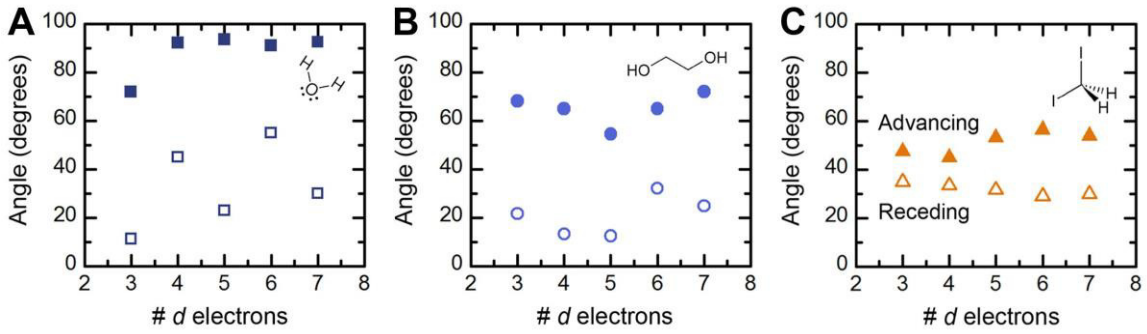

Figure 3-1. *Advancing (solid) and receding (open) contact angles on $LaMO_3$ surfaces, with M of different d-electron number. The probe liquid was (A) dipolar water, dark blue, (B) monopolar ethylene glycol, medium blue, or (C) apolar diiodomethane, orange.*

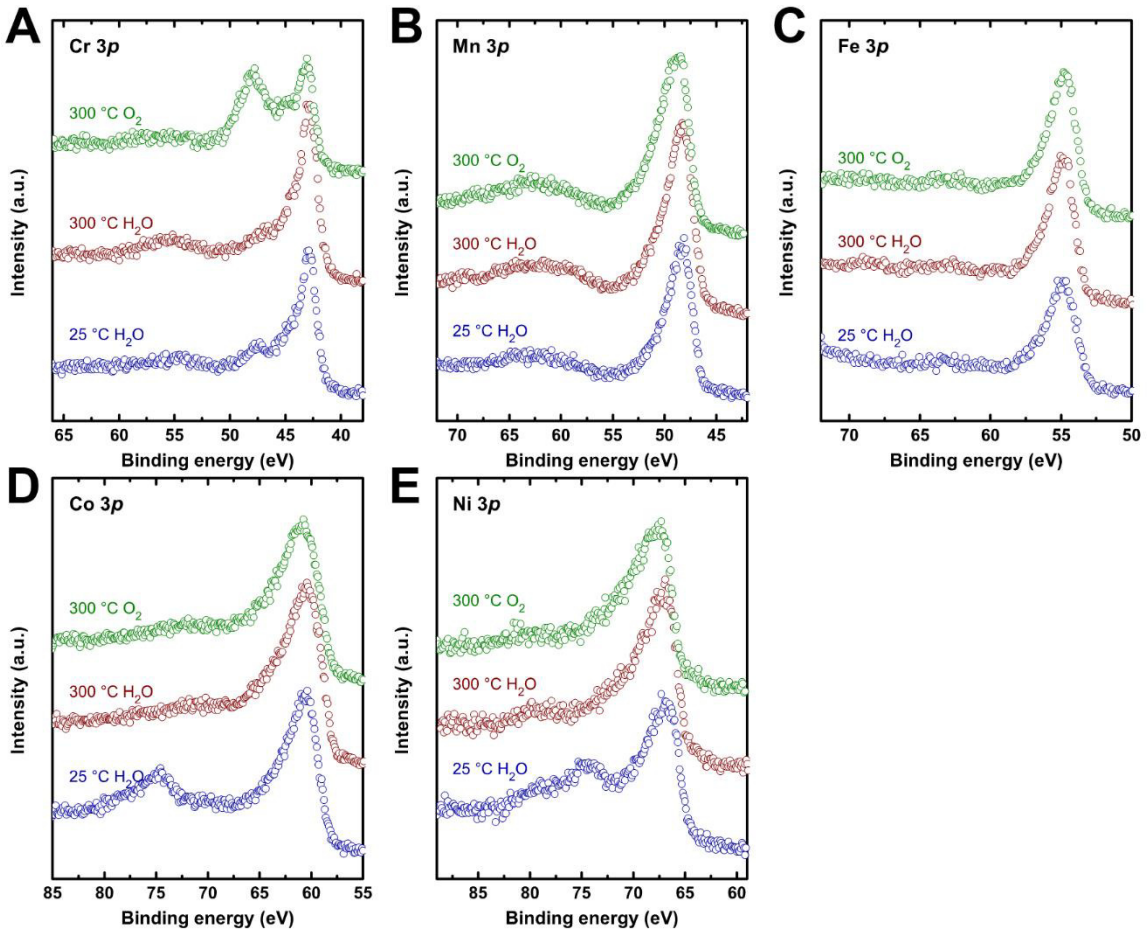

Figure 3-2. *M 3p spectra at an incident energy of 735 eV of $LaMO_3$ in $p(O_2)$ = 0.1 Torr at 300 °C (top, green) and $p(H_2O)$ = 0.1 Torr at 300 °C (middle, red), and 25 °C (blue, bottom). (A) M = Cr easily oxidizes from 3+ to 6+ in O_2 (seen by the peak at ~47 eV) but is reduced upon introduction of H_2O into the chamber, suggesting the high electronegativity of surface Cr^{6+} promotes electron transfer to water and thus wetting. This is in contrast to M = (B) Mn (C) Fe*

(D) Co and (E) Ni, which show no change in M 3p in an O_2 vs an H_2O environment. The peak at 75 eV in the Co and Ni spectra are also observed for the other $LaMO_3$ materials under the same conditions, and is attributed to a small amount of Al, however Al_2O_3 is not notable in the O 1s spectrum (binding energy 532.8-536.6 eV[24]).

In contrast to the advancing angles, the receding contact angles of all LaMO$_3$ were notably lower and strongly dependent on the transition metal. Although the difference in the advancing and receding angle is not fully understood at the molecular scale, it is postulated that receding water must break the H-bonds[16] that have formed between surface polar groups and water, thus leading to stronger interaction with water and a lower receding angle[25] than advancing. To assess this hypothesis, we consider the polar contributions of the oxide surface to dewetting.

For interactions between a solid and a liquid, the change in free energy can be considered as the sum of that arising from apolar Lifshitz-van der Waals (γ^{LW}) interactions and from polar acid-base interactions. The polar interactions depend on the electron-accepting (γ^+) and electron-donating (γ^-) contributions from both surface and probe liquid.[9,12,13] Thus by measuring the contact angle with three probe liquids of known apolar and polar components and surface tension, all components of surface energy can be quantified using the van Oss-Chaudhury-Good approach.[9,14] The resultant contact angles for each liquid are shown in **Figure 3-1**. The advancing angle was highest for polar liquids and depended weakly on the transition metal of LaMO$_3$ surfaces. In contrast, the receding contact angle varied notably with M for a polar probe, but remained approximately constant for all surfaces probed with apolar DIM. Notable hysteresis was seen in the contact angle of polar H_2O and EG, in contrast to that of DIM.

The associated free energy of hysteresis in wetting enables a direct experimental comparison of the strength of interaction between the surface and probe liquids of different polar character. The free energy of hysteresis for apolar DIM is ~1 kJ/mol and varies little with *d*-electron number, while for polar EG and H_2O spans from ~1 to 4 kJ/mol (**Figure 3-3**). This range is comparable to that attributed to conformational changes in polar groups[19] and/or strong interactions such as hydrogen bonding.[20] Thus, the large free energy of hysteresis can be attributed to oxygen-containing groups[26] and hydroxyl species.[27] We propose that the large hysteresis observed upon wetting with a polar solvent arises from polar groups at the LaMO$_3$ surface. The LaMO$_3$ (001) surface itself is polar, with alternating planes of LaO (+1 charge) and MO$_2$ (-1 charge). In contact with the atmosphere, it may compensate for the net surface dipole through numerous mechanisms – including the adsorption of surface species, surface reconstruction, and charge redistribution.[28,29] Upon changing the environment from ambient air

(or DIM) to that of a polar medium, the surface compensation will change dramatically due to interaction with this dielectric, giving rise to a large free energy of hysteresis. We hypothesize a change in the polarity of the oxide surface upon wetting can be achieved by orientation of polar *OH groups such that electron-rich oxygen interacts with the positive dipole of the water molecule, yielding low receding contact angle.

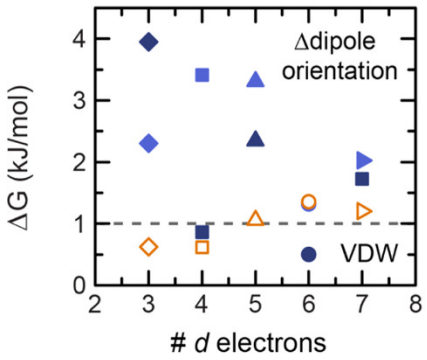

Figure 3-3. *The free energy of hysteresis, ΔG, obtained from the advancing and receding angle of each liquid in corresponding color, is large in magnitude (≥ 1 kJ/mol) for polar solvents, indicative of reorientation of polar surface groups.*

The γ^{LW} and γ^{+} components were roughly constant for all La*M*O_3 surfaces for both advancing (**Figure 3-4A**) and receding (**Figure 3-4B**) contact angles. In contrast, the γ^{-} component, roughly zero for the advancing angle, was found to be much larger and strongly dependent on the transition metal for the receding contact angle, and linearly increases with *OH coverage (**Figure 3-4C**). These observations indicate that strong H-bonding interactions at the oxide/water interface leads to lower receding contact angles (**Figure 3-4D**). Although lanthanide-containing perovskites are known to have high affinities for carbonate formation,[30] the correlation of receding angle with *OH coverage and measurement of surface energy using carbon-containing probe liquids suggests the receding contact angle reflects strong interactions with polar hydroxyl groups on the surface.

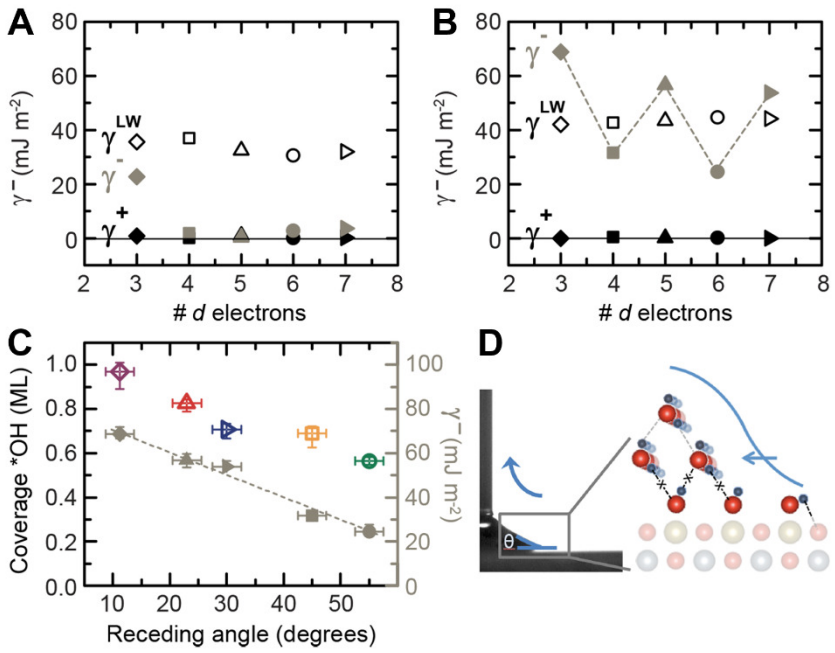

Figure 3-4. *Molecular insight into dewetting and contact angle hysteresis. (A) The apolar (γ^{LW}), electron-accepting (γ^{+}), and electron-donating component (γ^{-}) to the advancing contact angle and (B) the receding angle. (C) The receding contact angle is lowest for the surface with the highest coverage of *OH from AP-XPS, and reflects H-bonding by electron-donating surface groups, γ^{-}. (D) Schematic for the receding contact angle, where surface *OH groups can reorient in the polar liquid medium and interact strongly with water. The need to break H-bonds is indicated with an "x".*

Both hydroxyl and water coverage (see Chapter 2) and electron-donating polarity (**Figure 3-4B**) exhibit a W-shape trend with transition metal *d*-electron number. Inverse W-like trends have been reported among catalytic studies of perovskites such as O_2 adsorption and hydrocarbon oxidation,[31] as well as ORR.[10] Here we propose that the polarity of the water/oxide interface can be influenced by the coverage of polar species on the surface and/or the charge distribution of the surface hydroxyl groups. This hypothesis is supported by the fact that decreasing receding angle correlates with increasing both the electron-donating polar contribution to the oxide surface free energy in dewetting and coverage of *OH on La*M*O_3 measured from AP-XPS (**Figure 3-4C**). The trend in the reduction of surface energy upon hydroxylation calculated from density functional theory (DFT) in Chapter 2 (**Figure 2-8**) is reflected in the ease of removing a macroscopic droplet of water. The physical origin to different receding angles therefore resides in the transition-metal-dependent affinities toward hydroxyl formation and electron-donating polarity (γ^{-}) on La*M*O_3 surfaces.

3.4. Implications of *OH on the oxygen reduction reaction

Looking forward to the potential implications of the interaction between *OH and H_2O in designing functional chemistry, we examine these La*M*O_3 films for aqueous oxygen electrocatalysis and we report that ORR activity trends inversely with *OH coverage measured under humid conditions. The interaction between *OH and water on the La*M*O_3 surface can bridge the wetting behavior with their ORR catalytic activity. In basic solution, ORR proceeds on hydroxylated oxide surfaces with a proposed mechanism shown in **Figure 3-5**.[10,32] O_2 displaces *OH (step 1), and subsequent reduction leads to a final step, where water re-protonates the surface (step 4), thus the binding and coverage of *OH can play an important role in the ORR activity.[33]

We measured the intrinsic activity of the (001)-oriented perovskite films toward the ORR (**Figure 3-5**) using methods established recently,[21] where carbon and binder additives used for oxide powder measurements were not needed. The overpotential, η, (kinetic loss) to provide intrinsic ORR current of 40 μA cm^{-2}_{ox} was found to increase from *M* = Co, Mn to Ni. For the inactive *M* = Fe and Cr, meaningful current densities could not be obtained without potential reduction of the oxide due to the lack of carbon ORR current. The ORR activity trends inversely with the coverage of *OH measured by AP-XPS, where the most active catalyst $LaCoO_3$ has the smallest amount of *OH (**Figure 3-5C**). Although the absolute coverage of *OH depends on pH,[34,35] this trend of *OH on La*M*O_3 measured in water vapor gauges the relative affinity of these surfaces toward hydroxylation, established by their correlation to the DFT calculations in Chapter 2. Greater *OH coverage, indicative of an increased binding strength of *OH, can hinder the displacement of *OH by molecular oxygen (step 1 in **Figure 3-5A**), which is considered to be rate-limiting for ORR,[10] and lower ORR activity.

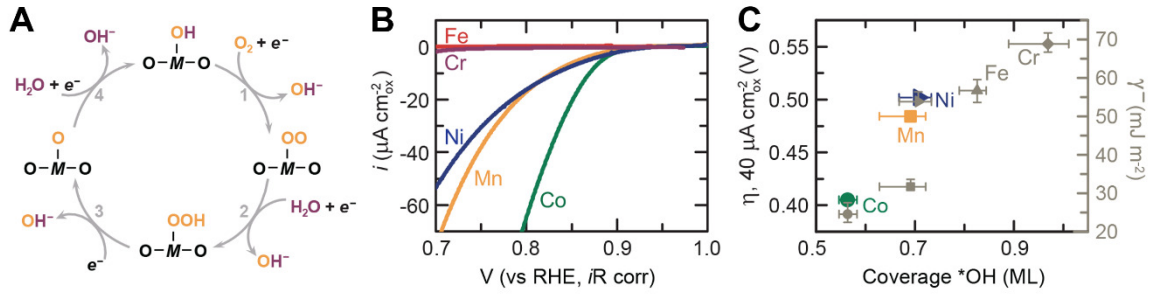

Figure 3-5. *Affinity toward hydroxylation describes ORR and wetting. (A) Schematic of the mechanism for the oxygen reduction reaction (ORR) proposed by Suntivich et al.*[10] *and Goodenough et al.,*[32] *noting the *OH species between step 4 and 1. (B) Capacitance-corrected cyclic voltammetry at 10 mV/s in O_2-saturated 0.1 M KOH. (C) The overpotential (η) required to achieve a given ORR current, extracted from CVs, correlates with the coverage of *OH (left axis), where an inactive surface is more hydroxylated, with a higher electron-donating component (γ^-) to dewetting (right axis).*

3.5. Conclusions

This chapter has established the molecular descriptor of *OH coverage for both the receding contact angle and ORR activity. Increasing *OH coverage on perovskites correlates with lower receding contact angle, greater electron-donor character of the surface and lower ORR activity. These measurements demonstrate for the first time that the tendency of a polar LaMO$_3$ surface toward hydroxylation can influence macroscopic wetting properties and oxygen electrocatalysis. We note that extension of these trends to broader classes of surfaces and ranges of hydroxyl affinity requires further investigation, however current understanding suggests that the design of highly active ORR catalysts should consider the intrinsic hydrophobicity of oxide chemistries and their tendency to hydroxylate. Thus, this study opens a new door to study and exploit hydrogen-bonding on polar surfaces to design functionality at the solid/water interface.

References

1 Rossmeisl, J., Karlberg, G. S., Jaramillo, T. & Norskov, J. K. Steady State Oxygen Reduction and Cyclic Voltammetry. *Faraday Discussions* **140**, 337-346, (2008).

2 Stephens, I. E. L. *et al.* Tuning the Activity of Pt(111) for Oxygen Electroreduction by Subsurface Alloying. *Journal of the American Chemical Society* **133**, 5485-5491, (2011).

3 Stephens, I. E. L., Bondarenko, A. S., Gronbjerg, U., Rossmeisl, J. & Chorkendorff, I. Understanding the electrocatalysis of oxygen reduction on platinum and its alloys. *Energy & Environmental Science* **5**, 6744-6762, (2012).

4 Stoerzinger, K. A. *et al.* Reactivity of Perovskites with Water: Role of Hydroxylation in Wetting and Implications for Oxygen Electrocatalysis. *The Journal of Physical Chemistry C* **119**, 18504-18512, (2015).

5 Karp, E. M., Campbell, C. T., Studt, F., Abild-Pedersen, F. & Nørskov, J. K. Energetics of Oxygen Adatoms, Hydroxyl Species and Water Dissociation on Pt(111). *The Journal of Physical Chemistry C* **116**, 25772-25776, (2012).

6 Cappus, D. *et al.* Hydroxyl groups on oxide surfaces: NiO(100), NiO(111) and Cr2O3(111). *Chemical Physics* **177**, 533-546, (1993).

7 Granick, S. & Bae, S. C. A Curious Antipathy for Water. *Science* **322**, 1477-1478, (2008).

8 Azimi, G., Dhiman, R., Kwon, H.-M., Paxson, A. T. & Varanasi, K. K. Hydrophobicity of rare-earth oxide ceramics. *Nat Mater* **12**, 315-320, (2013).

9 Van Oss, C. J., Ju, L., Chaudhury, M. K. & Good, R. J. Estimation of the Polar Parameters of the Surface Tension of Liquids by Contact Angle Measurements on Gels. *Journal of Colloid and Interface Science* **128**, 313-319, (1989).

10 Suntivich, J. *et al.* Design Principles for Oxygen-Reduction Activity on Perovskite Oxide Catalysts for Fuel Cells and Metal–Air Batteries. *Nature Chemistry* **3**, 546-550, (2011).

11 Fowkes, F. M. Determination of Interfacial Tensions, Contact Angles, and Dispersion Forces in Surfaces by Assuming Additivity of Intermolecular Interactions in Surfaces. *The Journal of Physical Chemistry* **66**, 382-382, (1962).

12 van Oss, C. J., Chaudhury, M. K. & Good, R. J. Monopolar surfaces. *Advances in Colloid and Interface Science* **28**, 35-64, (1987).

13 Van Oss, C. J., Good, R. J. & Chaudhury, M. K. The role of van der Waals forces and hydrogen bonds in "hydrophobic interactions" between biopolymers and low energy surfaces. *Journal of Colloid and Interface Science* **111**, 378-390, (1986).

14 Good, R. J. Contact Angle, Wetting, and Adhesion: A Critical Review. *Journal of Adhesion Science and Technology* **6**, 1269-1302, (1992).

15 Van Oss, C. J. *Interfacial forces in aqueous media*. (Marcel Dekker, 1994).

16 Extrand, C. W. Contact Angles and Their Hysteresis as a Measure of Liquid−Solid Adhesion. *Langmuir* **20**, 4017-4021, (2004).

17 Extrand, C. W. & Kumagai, Y. An Experimental Study of Contact Angle Hysteresis. *Journal of Colloid and Interface Science* **191**, 378-383, (1997).

18 Israelachvili, J. N. *Intermolecular and Surface Forces*. 2 edn, (Academic Press, 1992).

19 Volkenstein, M. V. *Configurational statistics of polymeric chains*. (Wiley, 1963).

20 Fowkes, F. *Surface and Interfacial Aspects of Biomedical Polymers*. 337-372 (Springer, 1985).

21 Stoerzinger, K. A. *et al.* Oxygen Electrocatalysis on (001)-Oriented Manganese Perovskite Films: Mn Valency and Charge Transfer at the Nanoscale. *Energy & Environmental Science* **6**, 1582-1588, (2013).

22 Connell, G. & Dumesic, J. A. Acidic Properties of Binary Oxide Catalysts: I. Mössbauer Spectroscopy and Pyridine Adsorption for Iron Supported on Silica. *Journal of Catalysis* **101**, 103-113, (1986).

23 Lee, T. R., Carey, R. I., Biebuyck, H. A. & Whitesides, G. M. The Wetting of Monolayer Films Exposing Ionizable Acids and Bases. *Langmuir* **10**, 741-749, (1994).

24 Deng, X., Herranz, T., Weis, C., Bluhm, H. & Salmeron, M. Adsorption of Water on Cu_2O and Al_2O_3 Thin Films. *The Journal of Physical Chemistry C* **112**, 9668-9672, (2008).

25 de Gennes, P.-G., Brochard-Wyart, F. & Quéré, D. in *Capillarity and Wetting Phenomena* Ch. 7, 153-190 (Springer New York, 2004).

26 Morra, M., Occhiello, E. & Garbassi, F. Contact Angle Hysteresis on Oxygen Plasma Treated Polypropylene Surfaces. *Journal of Colloid and Interface Science* **132**, 504-508, (1989).

27 Bain, C. D., Evall, J. & Whitesides, G. M. Formation of Monolayers by the Coadsorption of Thiols on Gold: Variation in the Head Group, Tail Group, and Solvent. *Journal of the American Chemical Society* **111**, 7155-7164, (1989).

28 Noguera, C. Polar Oxide Surfaces. *Journal of Physics: Condensed Matter* **12**, R367, (2000).

29 Tasker, P. W. The Stability of Ionic Crystal Surfaces. *Journal of Physics C: Solid State Physics* **12**, 4977, (1979).

30 Tascon, J. M. D. & Tejuca, L. G. Adsorption of CO_2 on the Perovskite-Type Oxide $LaCoO_3$. *Journal of the Chemical Society, Faraday Transactions 1: Physical Chemistry in Condensed Phases* **77**, 591-602, (1981).

31 Kremenic, G., Nieto, J. M. L., Tascon, J. M. D. & Tejuca, L. G. Chemisorption and Catalysis on $LaMO_3$ Oxides. *Journal of the Chemical Society, Faraday Transactions 1: Physical Chemistry in Condensed Phases* **81**, 939-949, (1985).

32 Goodenough, J. B., Manoharan, R. & Paranthaman, M. Surface Protonation and Electrochemical Activity of Oxides in Aqueous Solution. *Journal of the American Chemical Society* **112**, 2076-2082, (1990).

33 Man, I. C. *et al.* Universality in Oxygen Evolution Electrocatalysis on Oxide Surfaces. *ChemCatChem* **3**, 1159-1165, (2011).

34 Boehm, H. P. Acidic and Basic Properties of Hydroxylated Metal Oxide Surfaces. *Discussions of the Faraday Society* **52**, 264-275, (1971).

35 Brown, G. E. *et al.* Metal Oxide Surfaces and Their Interactions with Aqueous Solutions and Microbial Organisms. *Chemical Reviews* **99**, 77-174, (1998).

4. Electronic origins of wetting and ORR activity

This chapter is reproduced in part with permission from: Stoerzinger, K. A. et al. Highly Active Epitaxial $La_{(1-x)}Sr_xMnO_3$ Surfaces for the Oxygen Reduction Reaction: Role of Charge Transfer. *The Journal of Physical Chemistry Letters* **6**, 1435-1440, (2015).

4.1. Introduction

The previous chapters have established an experimental probe of hydroxyl affinity, and related this to the performance in applications of electrocatalysis and wetting. Missing, however, is an understanding of what intrinsic properties of the oxide electronic structure dictate interactions at the solid/liquid interface. This is in part limited by a lack of understanding in how the energy levels of an oxide interact with that of an aqueous solution, which impacts charge transfer at the surface.[1] It is further hindered by the difficulty in directly measuring surface speciation, such as hydroxyl formation, when the solid, adsorbate, and liquid all contain oxygen. This chapter further leverages recent advances in ambient pressure X-ray photoelectron spectroscopy (AP-XPS)[2-4] to measure the extent of surface hydroxylation and adsorption of water on oxide surfaces and relate this to changes in the electronic structure.

Manganese oxides are abundant, inexpensive, and nontoxic with rich oxide chemistry, of interest for oxygen electrocatalysis[5,6] and important in determining groundwater chemistry.[7] The electronic structure and conductivity of manganese oxides, which may greatly influence the reactivity with water, can be tuned in $AMnO_3$ of the perovskite family. For example, the electronic structure and conductivity can be modified drastically by the substitution of A-site cations, such as altering Mn valence via substituting some portion of A-site commonly from the lanthanide (A^{3+}) group for an alkaline earth (A^{2+}) element[8] or changing the ionic radius of the lanthanide element.[9,10] The increased conductivity in the case of $La_{(1-x)}Sr_xMnO_3$ compositions with moderate Sr content has been well studied in the solid state physics community. Incorporation of Sr^{2+} can lead to oxygen nonstoichiometry,[11] but charge compensation also results in the incorporation of ligand holes and Mn^{4+}.[12] Oxygen *p*-metal *d* coupling causes materials with Sr = 0.2-0.6 to become ferromagnetic metals,[12] with compositions of Sr = 0.3-0.4 exhibiting maximum conductivity.[13-15] In addition to the conductivity that results from Mn^{4+} incorporation, ORR studies on MnO_x materials have found that the presence of both valence states is beneficial to catalytic activity,[16] which has been attributed to their acting as an oxygen acceptor/donor mediator.[17,18] In the $La_{(1-x)}A_xMnO_3$ system, the inclusion of Ca^{2+} or Sr^{2+} has been reported to

increase ORR activity, as well as introduce oxygen nonstoichiometry via cation vacancies[19] in $La_{(0.6-x)}Ca_{0.4}MnO_3$ and rhombohedral $La_{(1-x)}Mn_{(1-y)}O_3$, referred to historically as $LaMnO_{3+\delta}$.[20] In a rotating ring disk electrode experiment by Tulloch et al.,[21] $La_{0.4}Sr_{0.6}MnO_3$, characterized by the smallest crystallite size in the series Sr = 0, 0.2, 0.4, 0.6, 0.8, and 1, had the highest ORR activity and smallest production of peroxide in 1 M KOH. Missing, however, are studies which compare the role of valence and charge transport in the absence of grain boundaries[22] in the ORR catalysis.

The surface electronic conductivity at the $AMnO_3$/electrolyte interface is little understood,[8,23-25] which leads to ambiguities in the role of charge transfer on the ORR kinetics. Conventional electrodes consist of oxide particles dispersed with electronically conductive carbon powder, which can dominate electronic conduction in the electrodes,[26,27] and influence electrode ORR currents as carbon is highly active to reduce oxygen to peroxide.[25] The study of thin-film single-crystal surfaces can eliminate the use of carbon,[24,28] and provide precise control of the surface area and crystallographic orientation, which allows the measurement of charge transfer kinetics at the oxide/electrolyte interface, intrinsic ORR activity and insights into the mechanism of oxygen electrocatalysis.[29]

This chapter considers (001)-oriented epitaxial films of $La_{(1-x)}Sr_xMnO_3$ (LSMO) to systematically tune the conductivity and valence state of Mn and elucidate the effects in ORR catalysis and surface speciation in an aqueous environment. Comparing amongst chemistries, we show that hydroxylation measured from AP-XPS is related to the relative location of the oxide valence band and Fermi level. Interaction with water leads to a hydroxyl feature in the valence band, and a raising of the Fermi level and shift in A-site core levels. Furthermore, this molecular hydroxylation is reflected in the surface electron-donating character of a wetted surface, with implications on the activity for oxygen electrocatalysis in alkaline solution. We find that the ORR activity trends with the ability to transfer charge, measured both by in-plane conductivity and in situ via a facile redox couple, where metallic-like LSMO with 33% Sr is most active. This observation corroborates findings on binary metal oxides,[17,18] which suggest that a mixture of $Mn^{3+/4+}$ valence states aids in charge transfer to and adsorption of oxygen. For highly active chemistries with 33% and 50% Sr, the ORR activity at pH 13 is comparable for the (001), (110), and (111) pseudo-cubic (pc) orientations, attributable to either a lack of structural sensitivity in the reaction mechanism or reconstruction of the surface under ORR conditions, meriting further study.

4.2. Experimental methods

Film Fabrication and Characterization. High quality $La_{(1-x)}Sr_xMnO_3$ (LSMO) thin films were fabricated by using pulsed laser deposition (PLD) on 0.5 wt% Nb-doped $SrTiO_3$ (NSTO) substrates of (001), (110), or (111) orientation (Crystech). The substrates were pretreated by etching in HF and annealing at 950 °C for 2 hours to produce a uniform, terraced surface. PLD was performed using a KrF excimer laser (λ = 248 nm) with a laser fluence of ~1.6 J/cm^2 at a repetition rate of 5 Hz. Sintered LSMO targets were used for ablation. The films were fabricated at 750 °C in different oxygen partial pressures from 75 mTorr ($LaMnO_3$) to 500 mTorr ($SrMnO_3$). The 15 nm thickness of the manganite film was carefully controlled by growth time, and subsequently the samples were cooled to room temperature under the growth condition.

The crystal structure of the films was examined using X-ray diffraction (XRD) (Bruker). Film surface morphologies were examined by atomic force microscopy (AFM) in tapping mode (Nanoscope IV, Veeco Metrology). The root mean square (RMS) roughness was ~1 nm, projected to modulate the surface area by <1 %. Characterization is provided in in **Figure B-1** and **B-2**. The in-plane resistivity was measured by a four-point probe station integrated with Keithley source-meter 2400 and multi-meter 2002 at room temperature for LSMO films grown on insulating $SrTiO_3$.

Ambient-Pressure X-ray Photoelectron Spectroscopy (AP-XPS). AP-XPS was collected at Beamline 9.3.2 at Lawrence Berkeley National Laboratory's (LBNL) Advanced Light Source (ALS). Films were placed onto a ceramic heater, with a thermocouple mounted directly onto the sample surface for temperature measurements, and isolated from the sample holder clips with an Al_2O_3 spacer. Three different alignment schemes are used to better observe specific trends. (1) The work function of the analyzer was determined by defining the C 1*s* of adventitious carbon present on each sample prior to cleaning at 284.8 eV, thus defining the binding energy (BE) scale. This is referred to as aligning to the Fermi level. (2) To simplify fitting of the O 1*s* spectra in a uniform way across Sr compositions, other chemistries are plotted relative to the LMO by fixing the La 4*d* binding energy at 735 eV incident photon energy, in effect fixing the chemical potential of La under each condition. (3) To consider the valence bands on a common energy scale, the La 4*d* was fixed to that of LMO using the same incident photon energy of 350 eV. To ensure the trends presented here are not artifacts of ionizing radiation, we checked that the O 1*s* spectra was the same between a spot irradiated for ~30 minutes and that of fresh spots that had not been exposed to the X-ray beam prior to a quick acquisition (**Figure B-3**).

The samples were cleaned by heating to 300 °C in $p(O_2)$ of 100 mTorr (measured by a calibrated capacitance gauge) until clean of carbon. After characterization of the clean surface in O_2, the chamber was evacuated to a pressure < 1.5 x 10^{-7} Torr, and $p(H_2O)$ of 100 mTorr was

introduced into the chamber. The H_2O was prepared from deionized water (Millipore, >18.2 MΩ cm) and degased by several freeze-pump-thaw cycles. The sample was then cooled in increments of 25 °C down to a final temperature of 25 °C, keeping the chamber pressure constant at $p(H_2O)$ of 100 mTorr. At every temperature, the O 1*s* and C 1*s* core level spectra were collected, and at 100 °C increments as well as 25 °C, the La 4*d* and transition metal 3*p* core level spectra were also collected. All spectra were taken at an incident energy of 735 eV for the water isobar. Additional spectra were collected at lower incident photon energy of 350 eV to tune the cross section and information depth at 300 °C in O_2 and H_2O, as well as at 25 °C in H_2O following the isobar. In determining the location of components and differences between them, an estimation of error was obtained through standard deviations from Monte Carlo simulations of spectral noise and fit with the constraints in **Table B-1 to B-3**, which are smaller than the data points.

Electrochemical Measurements. Electrochemical measurements were performed on a duplicate set of films as those used for AP-XPS. In order to affix electrical contacts, gallium–indium eutectic (Sigma-Aldrich, 99.99%) was scratched into the NSTO substrate, and a Ti wire (Sigma-Aldrich, 99.99%) was affixed with silver paint (Ted Pella, Leitsilber 200). The back and sides of the electrode, as well as the wire, were covered with a non-conductive, chemically resistant epoxy (Omegabond 101), so only the catalyst surface was exposed to the electrolyte.

Electrochemical measurements were conducted with a Biologic SP-300 potentiostat in an ~120 mL solution of 0.1 M KOH, prepared from deionized water (Millipore, >18.2 MΩ cm) and KOH pellets (Sigma-Aldrich, 99.99%). Potentials were referenced to a saturated Ag/AgCl or saturated calomel electrode (Pine), both calibrated to the reversible hydrogen electrode (RHE) scale in 0.1 M KOH. Electrical impedance spectroscopy (EIS) was performed at the open circuit voltage with an amplitude of 10 mV. Potentials were corrected for the electrolyte/cell resistance from the high frequency intercept of the real impedance (~45 Ω).

Measurements of the oxygen reduction reaction (ORR) were carried out in 0.1 M KOH electrolyte pre-saturated by bubbling O_2 for ~30 minutes and under continuous O_2 bubbling (Airgas, ultrahigh-grade purity) to fix the equilibrium potential. Cyclic voltammetry (CV) scans were performed at a sweep rate of 10 mV/s, starting and finishing at open circuit voltage, sweeping from 1.0 down to 0.7 V vs RHE. Discrete points on the Tafel plot were obtained from chronoamperometry (applying constant potential).

After all measurements in O_2-saturated KOH were completed, measurements of the $[Fe(CN)_6]^{3-/4-}$ reaction were carried out in an Ar-saturated (Airgas, ultrahigh-grade purity) solution of 0.1 M KOH, to which 5 mM each of $K_4Fe(CN)_6$-$3H_2O$ (Sigma-Aldrich, 99.99%) and

$K_3Fe(CN)_6$ (Sigma-Aldrich, 99%) were added. The potential was swept from 0.7 to 1.55 or 1.6 V vs. RHE at a rate of 10 mV/s, starting and finishing at open circuit voltage.

Contact Angle Measurements. Contact angles for the three probe liquids of diiodomethane (DIM, Alfa Aesar), ethylene glycol (EG, Alfa Aesar), and deionized water (18 MΩ-cm, Millipore) were measured using a Ramé-Hart M500-advanced goniometer. Separate duplicate films were used for DIM and EG. The advancing and receding contact angles were measured by adding/removing water from a 5 µl droplet on the surface at the rate of 0.2 µl/sec. This ensures that the capillary number is always low enough for accurate measurements. A smaller droplet volume was used with other probe liquids due to the lower contact angle and small sample size. Measurements on a second $LaMnO_3$ film yielded a water advancing angle within 2° and a receding angle within 5° of that measured on the first film. Repeat measurements on the first film after drying yielded values within the same range.

4.3. Measuring *OH with AP-XPS

As in Chapter 2, the reactivity of water vapor on the film surfaces was evaluated using AP-XPS by performing water isobar experiments to deconvolve the spectra.[30,31] The surfaces were cleaned *in situ* by heating in O_2 before exposure to water vapor (**Figure B-4**). Care was taken to ensure no change in the ratio of Sr species was observed to result from this treatment (**Figure B-5**), as cation segregation is known to occur at higher temperatures and pressures in the solid oxide fuel cell community.[32] Water isobar measurements (pH_2O = 100 mTorr) were performed by cooling, reaching a final relative humidity (RH) of ~0.3% at 25 °C. We note no appreciable change in surface cation stoichiometry was observed during this process (**Figure B-4**). The O 1*s* spectra of all LSMO films showed similar features (**Figure 4-1**), and the intensities varied with RH, aiding in the deconvolution into different oxygen groups on the surface (**Table 4-1**).[30] This fit varies some from that presented in Chapter 2 due to the lower energy resolution of beamline 9.3.2, the inability to quantify $*CO_3$ (discussed in more detail below), and the desire to have a common fit across Sr contents to aid in comparison of *OH affinity. The spectral evolution with RH has been discussed in great detail in Chapter 2,[31] and we here only compare the speciation at a fixed final RH of ~0.3% at 25 °C.

Table 4-1. *Fitting constraints for O 1s spectra at 735 eV, calibrated to La 4d at 735 eV of $LaMnO_3$ for consistency of fit. The 1.3 eV offset between OH and bulk was determined by*

conditions with 70% Sr LSMO where 3 distinct maxima are observed. The 2.6 eV offset between surface and bulk was determined by fitting at high RH for all chemistries.

	Bulk-Ox	**Surface-O**	***OH**	***H_2O**	**H_2O_{gas}**
% Lorentzian	10	70	0	0	0
FWHM (eV)	<1.8	<1.8	<1.8	1.4-1.5	<2
BE_{low} (eV)	(free)	Bulk+2.6	Bulk+1.3	533.2	533.85
BE_{high} (eV)	(free)	Bulk+2.6	Bulk+1.3	533.3	-

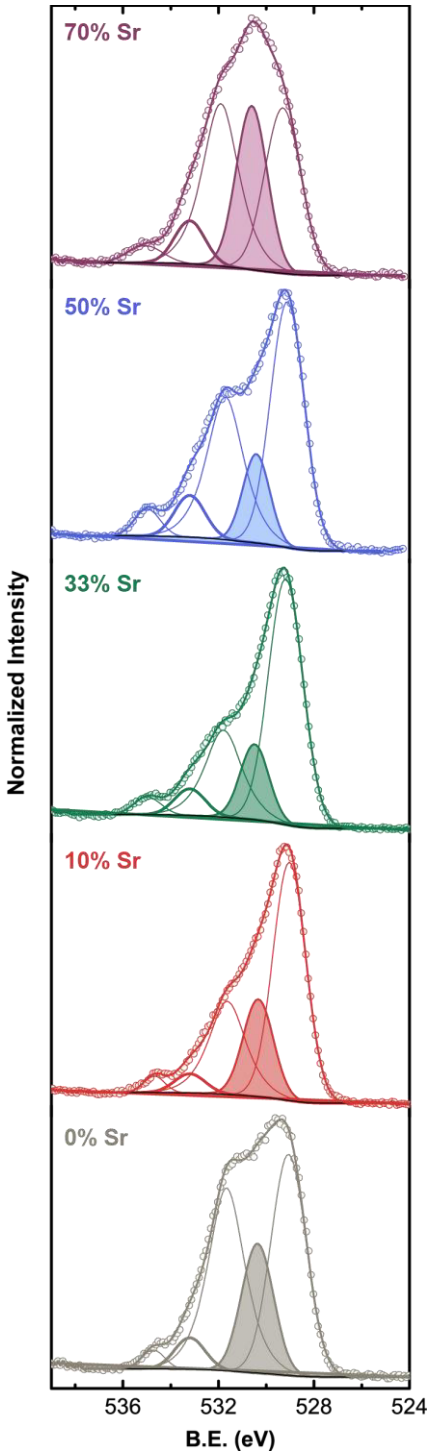

Figure 4-1. *Fitted O 1s spectra at 25 °C in 0.1 Torr H_2O, probed with an incident photon energy of 735 eV. Raw data in counts per second are shown as circles, and the envelope resulting from the fitted components in bold color; curves are offset for clarity. The *OH intensity is shaded; its relative intensity varies notably with Sr content.*

The lowest O 1*s* binding energy (BE) is characteristic of oxygen in bulk coordination, while that at ~2.8 eV higher BE was shown by depth profiling (**Figure 4-2**, ref. [30,31]) to be located at the surface. As we fixed the incident photon energy to obtain greater accuracy in determining binding energy shifts during the water isobar, the low cross section of carbon on beamline 9.3.2 (in contrast to measurements on 11.0.2 presented in Chapter 2) prohibited us from quantifying whether this surface feature contains a small contribution from carbonate species, known to be located at similar binding energies.[33] However, we expect a carbonate coverage comparable to that observed for La*M*O_3 films of ~0.3 ML over the course of an isobar measurement.[30] At intermediate BE ~1.3 eV higher than the bulk is a feature attributable to *OH species. The intensity of *OH increased as the sample was cooled to access higher RH, further supporting the peak assignment (**Figure 4-2**). At high RH, water adsorbed on the surface, *H_2O, with a BE at ~533.3 eV.[34,35] In addition, the gas phase H_2O peak is observed at a water partial pressure of 0.1 Torr.

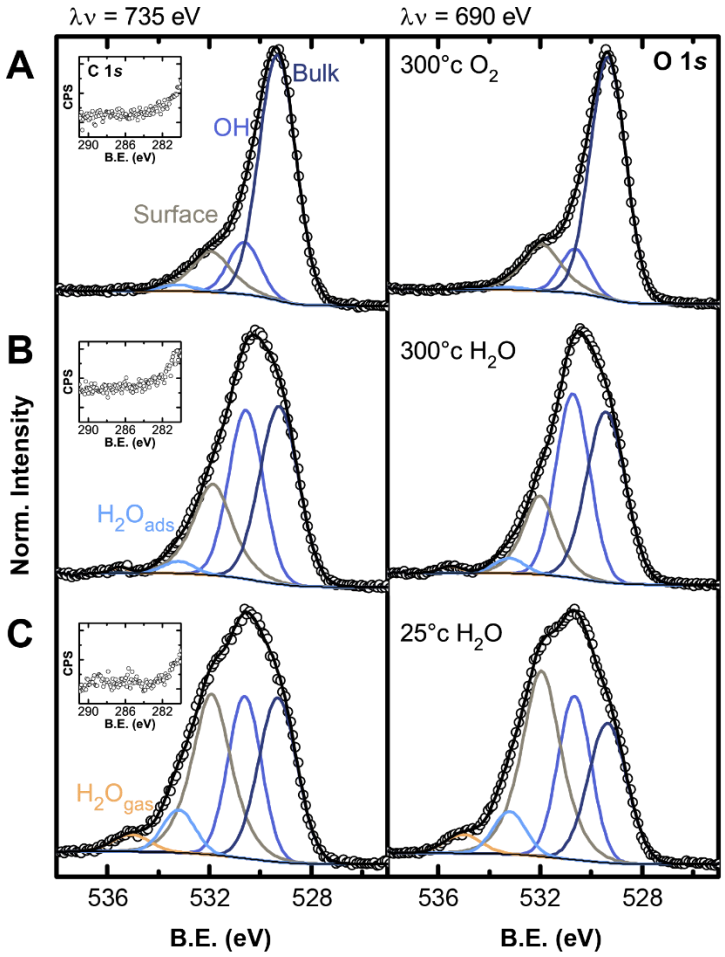

Figure 4-2. *Selected O 1s and C 1s (inset) spectra for 70% Sr LSMO illustrating the evolution of surface species with increasing RH (going down) at an incident photon energy of 735 eV (left),*

and a shallower probing 690 eV (right). (A) 300 °C in 0.1 Torr O_2: the O 1s spectrum of a carbon-free surface requires 3 peaks (bulk, dark blue; OH, medium blue; surface, gray) to fit. (B) 300 °C in 0.1 Torr H_2O: the OH component dramatically increases upon introduction of water into the chamber, and the increase in the surface peak likely occurs from some formation of CO_3 species below the detection limit given the low C 1s cross section. Depending on the Sr concentration, some adsorbed water (H_2O_{ads}, light blue) may also be observed at this point. (C) 25 °C in 0.1 Torr H_2O: further increasing RH, H_2O_{ads} increases and a gas phase water (H_2O_{gas}, light blue) is apparent.

The perovskite surfaces react with water to form hydroxyl groups, which is evidenced by notable *OH contribution in the O 1*s* spectra with increasing RH. Previous studies of La*M*O_3 films, where *M* is a transition metal Cr-Ni, have shown a correlation of the *OH coverage measured from AP-XPS with the stability of hydroxylated surfaces calculated by density functional theory, illustrating the technique serves as an experimental probe of hydroxyl affinity.[30] The degree of hydroxylation on the LSMO perovskite surface is dependent on the composition of the film, illustrated by the %OH intensity (shown for La*M*O_3 films to scale with the coverage of *OH in cases where *CO_3 was explicitly isolated)[30] of the total O 1*s* intensity in **Figure 4-3**.

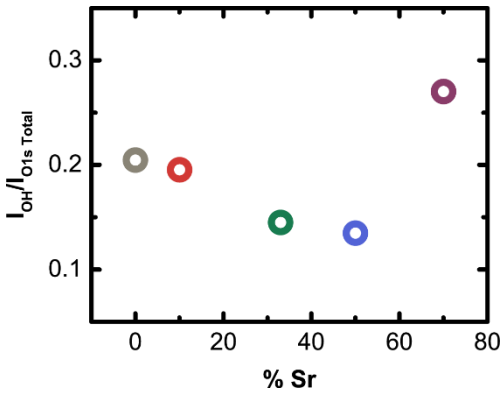

Figure 4-3. *The degree of hydroxylation, quantified by the intensity relative to the total O 1s spectum (excluding gas phase water) at 25 °C in 0.1 Torr H_2O, varies with the %Sr in LSMO. The propogated errors in $I_{OH}/I_{O1s\ Total}$ from standard deviations in each component, obtained by Monte Carlo simulations of spectral noise and fit with the constraints in Table S1, are smaller than the data points.*

4.4. Linking surface speciation to electronic structure

In order to relate the surface speciation to the electronic structure of the materials, we consider first ex situ measurement of the in-plane conductivity by four-point-probe.[36] These measurements are in general agreement with studies of the influence of Sr content on conductivity in the solid state physics community,[8,13-15] which provided motivation for this work. Films with lower resistivity, such as 33% Sr LSMO, show a lower propensity to form hydroxyl species (**Figure 4-4**). However, such a technique lacks information about the relative energy levels and the nature of charge-transfer, hindering a mechanistic understanding of surface hydroxylation and wetting.

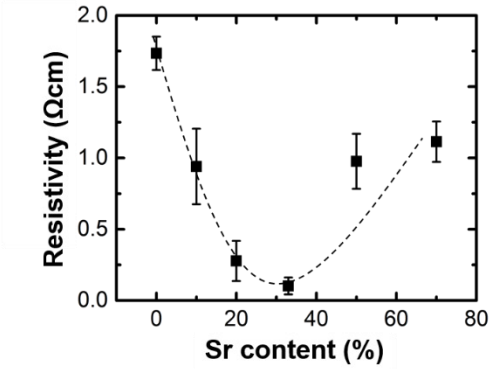

Figure 4-4. *Resistivity measured by four-point-probe for LSMO films grown on insulating STO substrate. Error bars are from measurements on five duplicate films.*

To understand how the valence band position of LSMO films relates to the redox levels of oxygen and water, key players in dictating the speciation of oxide surfaces in ambient conditions and aqueous environments,[1] we turn to electrochemistry. Specifically, we consider a facile redox couple with reversible kinetics having a reversible potential equal to that of sluggish oxygen redox (whose irreversible kinetics hinder understanding of charge transfer). With the $[Fe(CN)_6]^{3-/4-}$ equilibrium potential at 1.2 V vs. RHE in pH 13, the ability of the LSMO surface to donate and accept electrons near the O_2/OH^- redox couple at 1.23 V was probed, effectively measuring the available charge in situ. This measurement captures the energetics of charge carriers, in contrast to the transport information obtained from 4-point probe, critical to assess charge-transfer properties of (semi)conductor catalysts. As shown in **Figure 4-5**, the shape of the redox peaks varies notably with Sr content. For the highly conductive LSMO with 33% Sr, a classic duckbill shape is observed with two closely spaced redox peaks. Considering the other chemistries, these peaks spread away from the equilibrium redox potential, characteristic of a resistance to charge transfer and less available free charge at the electrode surface. The ease of charge-transfer kinetics for films of intermediate Sr content clearly illustrates that LSMO with

mixed $Mn^{3+/4+}$ easily donates and accepts electrons near the equilibrium potential of O_2/OH^- redox.

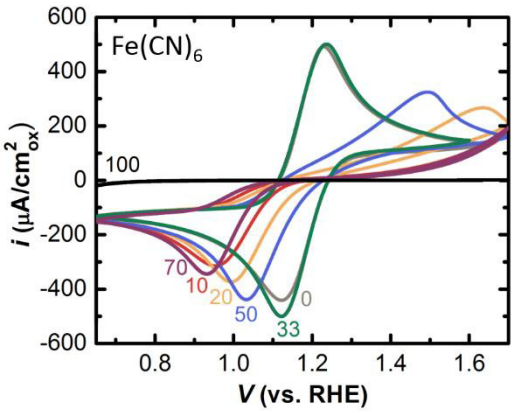

Figure 4-5. *Cyclic voltammetry (CV) at 10 mV/s on LSMO films for 10 mM $[Fe(CN)_6]^{3-/4-}$ in Ar-saturated 0.1 M KOH. The shift in the maximum reduction current away from the equilibrium voltage of 1.2 V vs. RHE indicates fewer available electrons and a barrier to their transfer, reflected in the ORR activity of the films.*

Measurement of the kinetics for an outer sphere redox couple effectively locates the valence band relative to the redox potential in situ. The results show that the valence band of 70% Sr LSMO are located lower in energy than oxygen redox, compared to the more conductive e.g. 33% Sr LSMO film, with available states close to this potential. Thus, a difference in the surface speciation resulting from equilibration with an aqueous environment is expected.

We next relate the surface speciation to the electronic structure directly as a function of RH, during the hydroxylation process. The valence band exhibits notable changes comparing a clean surface in oxygen to one in low RH and high RH (**Figure B-6**), where this change is most prominent for the 70% Sr film (**Figure 4-6**), which exhibits a high propensity for hydroxylation. For all chemistries, the VB in an oxygen (dry) environment is characterized by two features at ~2 and ~6 eV BE, characteristic of primarily Mn and O character, respectively. With increased humidity, a new feature increases between these two at ~4.5 eV, with its intensity being greatest for 70% Sr LSMO, followed by 0 and 10%. This trends with the hydroxyl intensity measured from the O 1*s* core level, and we therefore attribute the increased intensity at ~4.5 eV to hydroxyl formation.

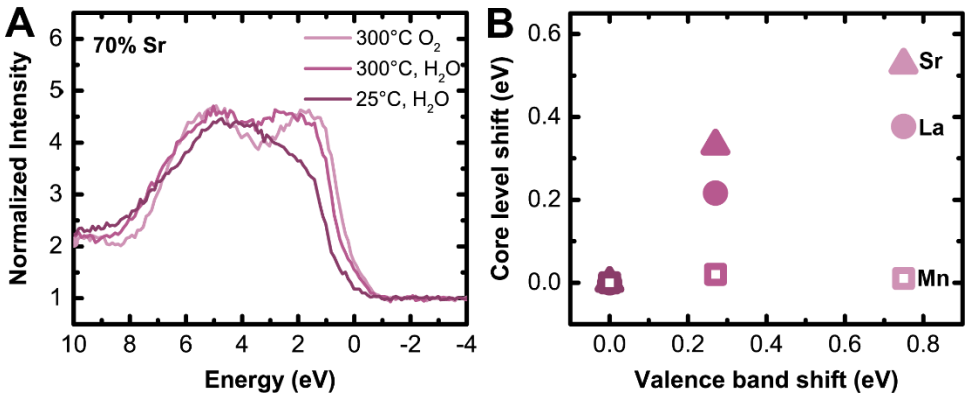

Figure 4-6. *Valence band (A) and core level shifts (B) of 70% Sr LSMO probed at an incident photon energy of 350 eV calibrated to the Fermi level of the as-prepared film via adventitious carbon. (B) The relative shift in valence band edge trends with an increase in the principle binding energy feature of the Sr 3d (triangle) and La 4d (circle), but the Mn 3p (square) remains unshifted.*

Of further note is the shift in energy of the valence band edge when the BE scale is common across RH (aligned to the Fermi level of the as-prepared sample via adventitious carbon), shown in **Figure 4-6** for the 70% Sr case. This implies a raising of the Fermi level relative to the valence band edge with hydroxylation. Considering the metal core levels of comparable photoelectron kinetic energy (350 eV, in order to fix the information volume), the shift in valence band edge mirrors that of the La 4*d* and Sr 3*d* core levels, while the Mn 3*p* core level remains unchanged (**Figure B-7**). Assuming a constant work function for the analyzer with RH, this suggests a chemical shift resulting from hydroxylation of La and Sr sites and a raising of the Fermi level due to the presence of surface adsorbates. Hydroxylation of La is further supported by an increase in the ionicity of the La-O bond (**Figure B-8**), probed via hydridization features in the La 4*d* core level.[37]

In an effort to compare the energy levels of LSMO on absolute scales, we fix the chemical potential of lanthanum via the La 4*d* core level BE. This was chosen as lanthanum will remain fixed in the 3+ valence state, is present in all samples, and is probed at a similar length scale due to the comparable kinetic energies from ejected La core level electrons and those from the valence band. A comparison of the valence bands under dry conditions (100 mTorr O_2, 300 °C) is shown in **Figure 4-7**. The metallic-like 33% Sr LSMO has a high valence band edge (BE close to 0), as does 10% Sr, followed by 50% Sr. The band edges of 0% (LMO) and 70% Sr are located lower yet in energy (higher BE). These findings agree well with electrochemical measurements of the relative location of the LSMO available electrons in 0.1 M KOH electrolyte,

probed by a facile redox reaction $[Fe(CN)_6]^{3-/4-}$, with redox potential at 1.2 V vs the reversible hydrogen electrode (RHE), close to that of oxygen redox at 1.23 V vs. RHE.[29] Comparing the relative locations of the band edges to the observed OH intensity, materials with a lower valence band show a higher propensity to hydroxylate. Considering electrochemical measurements, we propose this arises from a driving force to raise the Fermi level to equilibrate with the aqueous electrolyte, in part achieved through the adsorption of hydroxyl species.

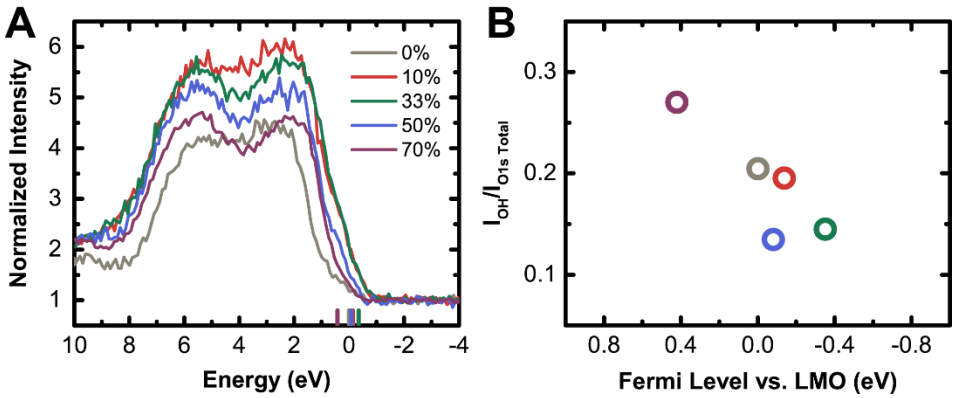

Figure 4-7. *(A) Comparison of valence bands for different %Sr in LSMO probed at 350 eV in 100 mTorr O_2 at 300 °C (dry conditions). To provide a common energy scale, the BE of the La 4d was fixed to that of 0% Sr LSMO. The location of 0 (Fermi level) prior to BE scale alignment is illustrated as a hash in corresponding color, and (B) shown versus the degree of hydroxylation, quantified by the ratio of the total O 1s spectum (excluding gas phase water) at 25 °C in 100 mTorr H_2O.*

4.5. Relating electronic structure to surface polarity and electrocatalytic activity

We next characterize the electron donor/acceptor nature of the wetted surface by receding contact angle measurements with liquids of different known acid-base character.[38,39] As seen previously for La*M*O_3 films,[30] the extent of hydroxylation generally trends with an increase in the electron donating nature of the surface free energy, which scales directly with the receding contact angle (**Figure 4-8**). The polar nature of the wetted surface is in agreement with the accumulation of elecron-rich hyrodyxl groups, observed from the shifts in valence band and core level BE in AP-XPS.

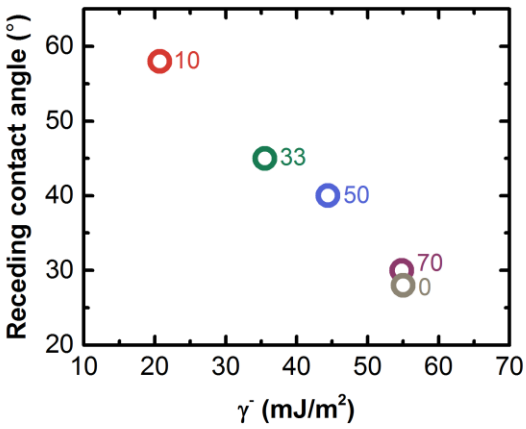

Figure 4-8. *The receding water contact angle is determined by the electron donor nature (γ^-) of the LSMO films, which generally trends with the affinity for OH except for 10% Sr, likely due to minor Al contamination (Figure B-3).*

The substitution of a moderate amount of Sr (33%-50%) replacing La was found to notably enhance ORR activity in comparison to $LaMnO_3$ (LMO) or $SrMnO_3$ end members containing purely Mn^{3+} and Mn^{4+}, respectively. The ORR activities of the $(001)_{pc}$ surfaces were measured by cyclic voltammetry (CV) (**Figure 4-9A**) and chronoamperometry (**Figure 4-9B**, **B-9**) in a standard 3-electrode setup in O_2-saturated 0.1 M KOH (Experimental Methods), with negligible background measured in Argon-saturated solution (**Figure B-10**). With the exception of LMO, the activities of LSMO surfaces were comparable measured by initial CV or subsequent chronoamperometry measurements of ORR kinetics (**Figure B-11**). The ORR activities remained largely unchanged after sweeping to the region of oxygen evolution (up to 1.7 V vs. RHE) for compositions with 10, 20, and 33 % Sr, but increased slightly for 50 % and 70 % Sr (**Figure B-11**). Comparing chemistries, the activity increases with Sr substitution of La to reach a maximum at Sr = 33%, beyond which the ORR activity decreases to an immeasurable value on $SrMnO_3$. In addition, both CV and chronoamperometry measurements show that the Tafel slope decreases with increasing activity (**Figure 4-9**), in the range from ~130 to ~50 mV/decade (**Figure B-12**). This observation suggests that more active surfaces are accompanied with a shallower slope and thus higher oxygen reduction currents for a given change in overpotential, indicating that charge transfer may play an important role in ORR kinetics.

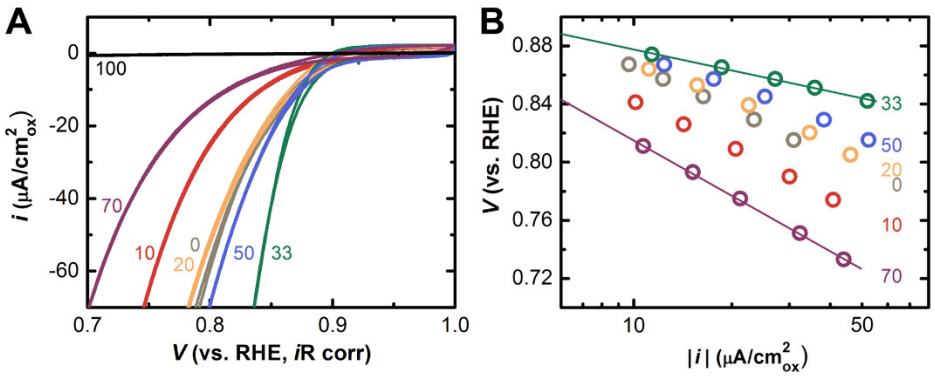

Figure 4-9. *ORR activity of LSMO films in O_2–saturated 0.1 M KOH. (A) Cyclic voltammetry (CV) at a scan rate of 10 mV/s showing the ORR current per surface area (i) vs. the ohmic corrected applied voltage (V-iR). (B) Tafel plot obtained from chronoamperometry (constant applied voltage) showing V-iR vs. |i| on a logarithmic scale. Lines guide the eye.*

The presence of electron-rich surface species on perovskite surfaces has also been observed to affect their performance as catalysts for the oxygen reduction reaction (ORR).[30] In agreement with previous measurements of LaMO$_3$ films, we find LSMO films with a lower hydroxyl affinity are more active for ORR (**Figure 4-10**). New, however, is an understanding of how this hydroxyl affinity is dictated by the electronic structure of the catalyst, specifically the relative location of the valence band and Fermi level. This suggests that materials with available electrons (reflected in the valence band density of states) near the Fermi level when in equilibrium with an aqeous electrolyte are more active for ORR due to their low propensity to form hydroxyl species.

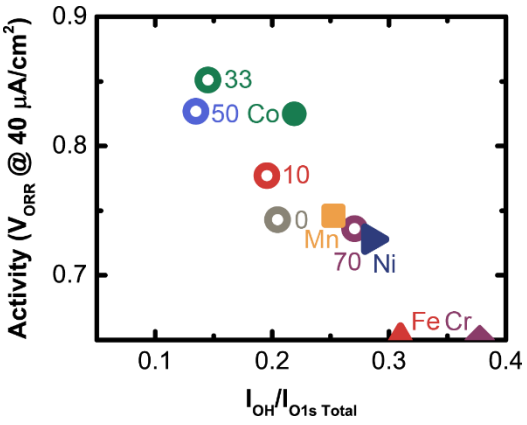

Figure 4-10. *The voltage required to achieve a given ORR current, extracted from CVs in reference [36] and [30], correlates with the relative affinity for *OH, quantified by the ratio of *OH to the total O 1s intensity (without gas phase water) for the LSMO series (open, denoted by percent*

Sr concentration and collected at an angle of 90°) and $LaMO_3$ series (closed, denoted by transition metal and collected at an angle of 42° [30]).

We next take a step back to connect ORR activity to the availability of electrons, measured by ex situ four-point-probe and in situ by a fast redox reaction. Lower resistivity was correlated with more active surfaces for the ORR, where the most active Sr concentration of 33% exhibited a minimum resistivity of 0.11 Ωcm (**Figure 4-11**). This result is in contrast to previous ORR studies of composite LSMO powder and carbon electrodes,[21] where conductivity measurements on pressed LSMO pellets did not correlate notably with activity. These previous results of oxide conductivity may have been convoluted with the effect of grain boundaries on the conductivity measurements of pellets, where the highest surface-area $La_{0.6}Sr_{0.4}MnO_3$ (9.6 m^2/g) had the lowest conductivity (0.009 Scm^{-1}) and the lowest surface-area $SrMnO_3$ (1.7 m^2/g) had the highest conductivity (0.284 Scm^{-1}). This hypothesis is further supported by increased resistivity from 0.01 to 0.06 Ωcm for $La_{0.8}Sr_{0.2}MnO_3$ when the grain size was reduced from 2.8 to 0.6 μm.[22]

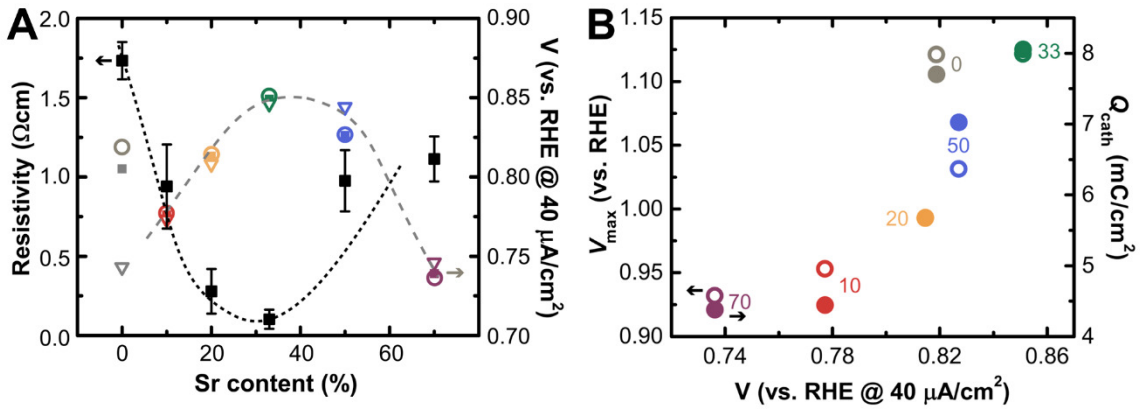

Figure 4-11. *(A) (Right axis, color) ORR activity measured by the voltage to achieve 40 μA/cm² of capacitance-corrected current from the 5th cycle of initial CV measurements (open circle), subsequent chronoamperometry (CA, solid squares), and CV measurements following sweeping to oxidative potentials (open triangles). A similar trend is observed at 10 μA/cm² (Figure B-13). The activity exhibits a maximum at Sr = 33%, the opposite trend of resistivity (left axis, black squares), which is minimum for this composition. Dashed lines are guides to the eye. (B) The ease of charge-transfer kinetics (Figure B-14), measured by the voltage of maximum cathodic current, V_{max} (open, left axis) and available electrons for $[Fe(CN)_6]^{3-}$ reduction, Q_{cath} (solid, right axis), trends with the voltage to achieve 40 μA/cm² ORR in O_2–saturated 0.1 M KOH.*

Considering explicitly the availability of electrons near oxygen redox, probed via the location and integrated current density of the reduction peak for $[Fe(CN)_6]^{3-}$, we find even

stronger ties to the ORR activity. At potentials exceeding the onset of the ORR, all films can pass current densities in 10 mM $[Fe(CN)_6]^{3-/4-}$ roughly an order of magnitude greater than the current density used to quantify the specific ORR activity (**Figure 4-9**, where the solubility of O_2 in 0.1 M KOH is ~1 mM[40]). Nevertheless, faster charge transfer for $[Fe(CN)_6]^{3-/4-}$ redox clearly scales with increasing ORR activity of LMO and LSMO, where the high ORR activity of LMO is better reflected by its facile $[Fe(CN)_6]^{3-/4-}$ redox kinetics than in-plane electronic conductivity from ex situ four-point-probe measurements. This finding connects the charge-transfer properties of semiconductor catalysts to their ORR activity, where the nature of conduction (electron, hole, mixed) and the energy levels of charge carriers are critical. The metallic-like 33% Sr LSMO is amongst the most active oxide catalysts measured to date (**Figure B-15**).

An extension considering the ORR activity of (110) and (111) orientations of 33% and 50% Sr LSMO is presented in **Appendix B-3**, **Figures B-16** to **B-18**. In short, no notable differences in ORR activity or the availability of electrons were observed as a function or orientation, meriting further study.

4.6. Conclusion

This chapter has related the electronic structure of LSMO films to their hydroxylation, ORR activity, and wettability. Specifically, we used AP-XPS to monitor changes in the valence band and Fermi level as a function of relative humidity, observing an increase in the work function and formation of new states in the valence band as a result of *OH formation. This chemical shift is specific to La and Sr, with the Mn 3*p* core level remaining unchanged. Comparing the valence band and Fermi level across the LSMO series, the driving force for hydroxylation was established to be the relative location of the Fermi level and valence band, where a deeper energies (lower relative to vacuum) drive *OH formation. This can be considered as the equilibration of the LSMO energy levels with that of the electrolyte. Films with available states near the Fermi level and with a smaller work function show a lower propensity to hydroxylate, improved charge transfer for the ORR, and higher catalytic activity.

References

1 Chakrapani, V. *et al.* Charge Transfer Equilibria Between Diamond and an Aqueous Oxygen Electrochemical Redox Couple. *Science* **318**, 1424-1430, (2007).

2 Starr, D. E., Liu, Z., Havecker, M., Knop-Gericke, A. & Bluhm, H. Investigation of Solid/Vapor Interfaces Using Ambient Pressure X-ray Photoelectron Spectroscopy. *Chemical Society Reviews* **42**, 5833-5857, (2013).

3 Salmeron, M. & Schlogl, R. Ambient pressure photoelectron spectroscopy: a new tool for surface science and nanotechnology. *Journal Name: Surface Science Reports; Journal Volume: 63*, Medium: ED, (2008).

4 Stoerzinger, K. A., Hong, W. T., Crumlin, E. J., Bluhm, H. & Shao-Horn, Y. Insights into Electrochemical Reactions from Ambient Pressure Photoelectron Spectroscopy. *Accounts of Chemical Research* **48**, 2976-2983, (2015).

5 Stoerzinger, K. A., Risch, M., Han, B. & Shao-Horn, Y. Recent Insights into Manganese Oxides in Catalyzing Oxygen Reduction Kinetics. *ACS Catalysis* **5**, 6021-6031, (2015).

6 Huynh, M., Bediako, D. K. & Nocera, D. G. A Functionally Stable Manganese Oxide Oxygen Evolution Catalyst in Acid. *Journal of the American Chemical Society* **136**, 6002-6010, (2014).

7 Post, J. E. Manganese oxide minerals: Crystal structures and economic and environmental significance. *Proceedings of the National Academy of Sciences* **96**, 3447-3454, (1999).

8 Matsumoto, Y., Yoneyama, H. & Tamura, H. Dependence of the Exchange Current Density of Oxygen Reduction on the Resistivities of $La_{1-x}Sr_xMnO_3$ and $LaNi_{1-x}M_xO_3$ Electrodes. *Journal of Electroanalytical Chemistry and Interfacial Electrochemistry* **83**, 245-249, (1977).

9 Sakaguchi, M., Uematsu, K., Sakata, A. & Sato, M. Electrocatalytic Activity and Oxygen Adsorption Property of Perovskite-Type Oxides, $LnMnO_3$ (Ln: Rare Earth). *Electrochimica Acta* **35**, 65-67, (1990).

10 Hyodo, T., Hayashi, M., Miura, N. & Yamazoe, N. Catalytic Activities of Rare-Earth Manganites for Cathodic Reduction of Oxygen in Alkaline Solution. *Journal of the Electrochemical Society* **143**, L266-L267, (1996).

11 Gaudon, M., Laberty-Robert, C., Ansart, F., Stevens, P. & Rousset, A. Preparation and Characterization of $La_{1-x}Sr_xMnO_{3+\delta}$ ($0 \leq x \leq 0.6$) Powder by Sol–Gel Processing. *Solid State Sciences* **4**, 125-133, (2002).

12 Saitoh, T. *et al.* Electronic Structure of $La_{1-x}Sr_xMnO_3$ Studied by Photoemission and X-Ray-Absorption Spectroscopy. *Physical Review B* **51**, 13942-13951, (1995).

13 Urushibara, A. *et al.* Insulator-Metal Transition and Giant Magnetoresistance in $La_{1-x}Sr_xMnO_3$. *Physical Review B* **51**, 14103-14109, (1995).

14 Ju, H. L., Sohn, H. C. & Krishnan, K. M. Evidence for O_{2p} Hole-Driven Conductivity in $La_{1-x}Sr_xMnO_3$ ($0 \leq x \leq 0.7$) and $La_{0.7}Sr_{0.3}MnO_z$ Thin Films. *Physical Review Letters* **79**, 3230-3233, (1997).

15 Hishida, T., Ohbayashi, K. & Saitoh, T. Hidden Relationship Between the Electrical Conductivity and the Mn 2*p* Core-Level Photoemission Spectra in $La_{1-x}Sr_xMnO_3$. *Journal of Applied Physics* **113**, 043710, (2013).

16 Lima, F. H. B., Calegaro, M. L. & Ticianelli, E. A. Investigations of the Catalytic Properties of Manganese Oxides for the Oxygen Reduction Reaction in Alkaline Media. *Journal of Electroanalytical Chemistry* **590**, 152-160, (2006).

17 Roche, I., Chaînet, E., Chatenet, M. & Vondrák, J. Carbon-Supported Manganese Oxide Nanoparticles as Electrocatalysts for the Oxygen Reduction Reaction (ORR) in Alkaline Medium: Physical Characterizations and ORR Mechanism. *The Journal of Physical Chemistry C* **111**, 1434-1443, (2006).

18 Vondrak, J. *et al.* Electrochemical Activity of Manganese Oxide/Carbon-Based Electrocatalysts. *Journal of New Materials for Electrochemical Systems* **8**, 209-212, (2005).

19 Yuan, X.-Z., Li, X., Qu, W., Ivey, D. G. & Wang, H. Electrocatalytic Activity of Non-Stoichiometric Perovskites toward Oxygen Reduction Reaction in Alkaline Electrolytes. *ECS Transactions* **35**, 11-20, (2011).

20 Suntivich, J. *et al.* Design Principles for Oxygen-Reduction Activity on Perovskite Oxide Catalysts for Fuel Cells and Metal–Air Batteries. *Nature Chemistry* **3**, 546-550, (2011).

21 Tulloch, J. & Donne, S. W. Activity of Perovskite $La_{1-x}Sr_xMnO_3$ Catalysts Towards Oxygen Reduction in Alkaline Electrolytes. *Journal of Power Sources* **188**, 359-366, (2009).

22 Kameli, P., Salamati, H. & Aezami, A. Influence of Grain Size on Magnetic and Transport Properties of Polycrystalline $La_{0.8}Sr_{0.2}MnO_3$ Manganites. *Journal of Alloys and Compounds* **450**, 7-11, (2008).

23 Matsumoto, Y., Yoneyama, H. & Tamura, H. Influence of the Nature of the Conduction Band of Transition Metal Oxides on Catalytic Activity for Oxygen Reduction. *Journal of Electroanalytical Chemistry and Interfacial Electrochemistry* **83**, 237-243, (1977).

24 Miyahara, Y., Miyazaki, K., Fukutsuka, T. & Abe, T. Catalytic Roles of Perovskite Oxides in Electrochemical Oxygen Reactions in Alkaline Media. *Journal of the Electrochemical Society* **161**, F694-F697, (2014).

25 Poux, T. *et al.* Dual Role of Carbon in the Catalytic Layers of Perovskite/Carbon Composites for the Electrocatalytic Oxygen Reduction Reaction. *Catalysis Today* **189**, 83-92, (2012).

26 Fabbri, E. *et al.* Composite Electrode Boosts the Activity of $Ba_{0.5}Sr_{0.5}Co_{0.8}Fe_{0.2}O_{3-\delta}$ Perovskite and Carbon toward Oxygen Reduction in Alkaline Media. *ACS Catalysis* **4**, 1061-1070, (2014).

27 Suntivich, J., Gasteiger, H. A., Yabuuchi, N. & Shao-Horn, Y. Electrocatalytic Measurement Methodology of Oxide Catalysts Using a Thin-Film Rotating Disk Electrode. *Journal of the Electrochemical Society* **157**, B1263-B1268, (2010).

28 Komo, M., Hagiwara, A., Taminato, S., Hirayama, M. & Kanno, R. Oxygen Evolution and Reduction Reactions on $La_{0.8}Sr_{0.2}CoO_3$ (001), (110), and (111) Surfaces in an Alkaline Solution. *Electrochemistry* **80**, 834-838, (2012).

29 Stoerzinger, K. A. *et al.* Oxygen Electrocatalysis on (001)-Oriented Manganese Perovskite Films: Mn Valency and Charge Transfer at the Nanoscale. *Energy & Environmental Science* **6**, 1582-1588, (2013).

30 Stoerzinger, K. A. *et al.* Reactivity of Perovskites with Water: Role of Hydroxylation in Wetting and Implications for Oxygen Electrocatalysis. *The Journal of Physical Chemistry C* **119**, 18504-18512, (2015).

31 Stoerzinger, K. A. *et al.* Water Reactivity on the $LaCoO_3$ (001) Surface: An Ambient Pressure X-ray Photoelectron Spectroscopy Study. *The Journal of Physical Chemistry C* **118**, 19733-19741, (2014).

32 Orikasa, Y. *et al.* Surface Strontium Segregation of Solid Oxide Fuel Cell Cathodes Proved by In Situ Depth-Resolved X-ray Absorption Spectroscopy. *ECS Electrochemistry Letters* **3**, F23-F26, (2014).

33 Gonzalez-Elipe, A. R., Espinos, J. P., Fernandez, A. & Munuera, G. XPS study of the surface carbonation/hydroxylation state of metal oxides. *Applied Surface Science* **45**, 103-108, (1990).

34 Ketteler, G. *et al.* The Nature of Water Nucleation Sites on TiO_2(110) Surfaces Revealed by Ambient Pressure X-ray Photoelectron Spectroscopy. *The Journal of Physical Chemistry C* **111**, 8278-8282, (2007).

35 Yamamoto, S. *et al.* Water Adsorption on α-Fe_2O_3(0001) at near Ambient Conditions. *The Journal of Physical Chemistry C* **114**, 2256-2266, (2010).

36 Stoerzinger, K. A. *et al.* Highly Active Epitaxial $La_{(1-x)}Sr_xMnO_3$ Surfaces for the Oxygen Reduction Reaction: Role of Charge Transfer. *The Journal of Physical Chemistry Letters* **6**, 1435-1440, (2015).

37 Sunding, M. F. *et al.* XPS characterisation of *in situ* treated lanthanum oxide and hydroxide using tailored charge referencing and peak fitting procedures. *Journal of Electron Spectroscopy and related Phenomena* **184**, 399-409, (2011).

38 Van Oss, C. J., Ju, L., Chaudhury, M. K. & Good, R. J. Estimation of the polar parameters of the surface tension of liquids by contact angle measurements on gels. *Journal of Colloid and Interface Science* **128**, 313-319, (1989).

39 Good, R. J. Contact angle, wetting, and adhesion: a critical review. *Journal of Adhesion Science and Technology* **6**, 1269-1302, (1992).

40 Davis, R. E., Horvath, G. L. & Tobias, C. W. The Solubility and Diffusion Coefficient of Oxygen in Potassium Hydroxide Solutions. *Electrochimica Acta* **12**, 287-297, (1967).

5. OER activity of RuO_2 and IrO_2: orientation and pH dependence

This chapter is adapted with permission from: Stoerzinger, K. A., Qiao, L., Biegalski, M. D. & Shao-Horn, Y. Orientation-Dependent Oxygen Evolution Activities of Rutile IrO_2 and RuO_2. *The Journal of Physical Chemistry Letters* **5**, 1636-1641, (2014).

5.1. Introduction

Having established the role of hydroxylation in ORR activity and its electronic origins, we now consider other means to impact activity: specifically the ability of a surface to become 'activated' by a redox process. At the same time, we reverse the process of oxygen electrocatalysis: taking oxygen in its reduced form (H_2O, OH^-) and oxidizing it to generate a chemical fuel. The storage of renewable energy using hydrogen 'fuel' is hampered by the slow kinetics of this oxygen evolution reaction (OER),[1-4] and the development of highly active OER catalysts is critical to develop efficient storage technologies.[5-8] IrO_2 and RuO_2 are highly active to promote OER kinetics, and are often considered as the gold standards for OER catalysts.[5,9-11] Unfortunately, the intrinsic OER activities of different surface orientations have not been reported from well-defined surface terminations of RuO_2 and IrO_2, which limits the design of highly active nanoscale catalysts, especially crucial for practical applications considering their high cost and low elemental abundance.[12] Moreover, it is not straightforward to extract such information from the reported OER results of IrO_2 and RuO_2 particles, which contain different degrees of crystallinity,[13,14] degrees of hydration (as $IrO_2 \cdot xH_2O$[15,16] or $RuO_2 \cdot xH_2O$[16,17]) and surface crystallographic texture.[18]

Despite notable work on RuO_2 ranging from nanoparticles[11] to single crystals,[19] experimental to theoretical,[9,20] the actual mechanism of OER remains poorly understood. Four types of mechanisms have been suggested in the literature: (1) four concerted proton-electron transfers occurring on a single (undercoordinated Ru) site,[9] (2) a sequence of two electrochemical steps followed by two chemical steps between neighboring Ru sites,[21] (3) decomposition of higher valent Ru oxides,[1,22] and (4) one involving the exchange of oxygen with the oxide itself, more qualitative in nature.[23,24] These mechanisms differ in both the number of active sites involved and also the role of lattice oxygen, where these aspects bear important ramifications in the rational design of catalysts with improved OER activity.

Recent studies have highlighted the exchange of lattice oxygen, or anion redox, in the alkaline OER for Co-containing perovskites when the Fermi level becomes pinned at the top of

the O 2*p* band.[25] Previous studies of RuO_2 nanoparticles[24] and RF sputtered films[23] have also demonstrated oxygen exchange during the acidic OER by ^{18}O labelling experiments, coupled with online electrochemical mass spectrometry (OLEMS) to measure products as a function of applied potential. However, the geometry of the RuO_2 electrode in these studies is characterized by a degree of surface roughness and porosity, which can potentially trap isotopically labelled water during the exchange experiment, convoluting results. Furthermore, aspects well-known to impact OER activity, including the extent of crystallinity,[21,26] crystallographic orientation,[27] and surface area,[21] are challenging to quantify and control in previously-studied electrode geometries. Therefore an open question remains in regard to what extent oxygen exchange during OER takes place, and whether the mechanism depends on the surface crystallinity.

This chapter presents the activity of five crystallographic orientations of RuO_2 and IrO_2 in both acidic and basic environments, where OER activity depends on both orientation and pH. Of significance, RuO_2 (100) has an intrinsic activity an order of magnitude greater than nanoparticles with predominant surfaces of (110) and (101).[11] Employing ^{18}O-labelling and OLEMS, we report that for dense RuO_2 films, oxygen exchange is in fact *not* observed to coincide with the OER. This suggests that the origin of this secondary mechanism for the OER are grain boundaries or defects. These observations point to distinct design principles for maximizing the activity of single- and polycrystalline RuO_2.

5.2. Experimental methods

Film Fabrication and Characterization. Films were fabricated by pulsed laser deposition (PLD) on single crystal (001)-oriented $SrTiO_3$ or MgO substrates (from CrysTec GmbH and MTI Corp.) or (101), (111) or (001) TiO_2 from a ceramic RuO_2 and an Ir metal target. The $SrTiO_3$ substrates were treated with HF-etch and annealed to obtain an atomic-flat surface. The MgO substrates were not subject to pre-treatment but annealed at growth temperature for ~30 minutes. PLD was performed using a KrF excimer laser (λ = 248 nm) to obtain films of at least 25 nm thickness, which were deposited at the oxygen pressure of 200 mTorr and substrate temperature of 750 °C for IrO_2, 50 mTorr at 400 °C for RuO_2, and cooled to room temperature under 200 Torr oxygen. For the IrO_2 film grown on MgO, a 2 nm buffer layer of $BaTiO_3$ was used to prevent the formation of IrMg intermetallics.

Thin film X-ray diffraction (XRD) was performed using a four-circle diffractometer (X'Pert PRO, PANalytical) in normal and off-normal configurations (**Figure C-1, C-2**). The (110)-oriented IrO_2 film also has <0.3% (100)-orientation on the surface that could not be avoided. As evidenced from the in-plane (φ) scan of the (100)-oriented films, both exhibit

oriented twin domains.

Film surface morphologies were examined by atomic force microscopy (AFM, see **Figure 5-1, Figure C-1**) (Dimension Icon, Bruker). The root mean square (RMS) roughness was ~6 nm for IrO_2 films, and ~1 nm for RuO_2 films (**Table C-1**) measured before electrochemistry. Changes in roughness were examined after all electrochemistry measurements were performed (**Table C-1**).

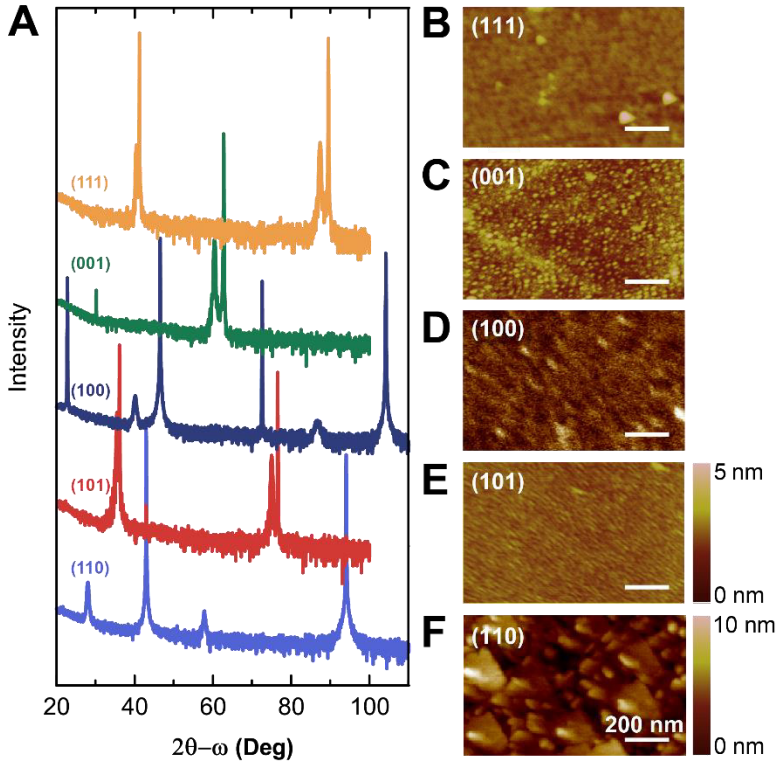

Figure 5-1. *Characterization of RuO_2 films. (A) Normal 2θ−ω scan of films with noted orientation, where (110) and (100) are grown on (001) MgO and $SrTiO_3$, with all others grown on TiO_2 of corresponding rutile orientation. Intensity is on a logarithmic scale, with curves offset for clarity. (B-F) Atomic force microscopy (AFM) image of representative samples after deposition. (B) (111), (C) (001), (D) (100), (E) (101), (F) (110) RuO_2. The scale bar is 200 nm for all images, and contrast scale is 0 to 5 nm for (B-E).*

Electrochemical Measurements. Electrical contacts were applied to the front of the conductive IrO_2 or RuO_2 film. Gallium–indium eutectic (Sigma-Aldrich, 99.99%) was scratched into a small corner, and a Ti wire (Sigma-Aldrich, 99.99%) was affixed with silver paint (Ted Pella, Leitsilber 200). The back and sides of the electrode, as well as the wire, were covered with a non-conductive, chemically resistant epoxy (Omegabond 101), so only the catalyst surface was exposed to the electrolyte.

Electrochemical measurements were conducted with a Biologic SP-300 potentiostat in an ~120 mL solution of 0.1 M KOH, prepared from deionized water (Millipore, >18.2 MΩ cm) and KOH pellets (Sigma-Aldrich, 99.99%). Potentials were referenced to a saturated Ag/AgCl electrode (Pine) for measurements of the oxygen evolution reaction (OER), and a saturated calomel electrode (Pine) for q^* measurements, both calibrated to the reversible hydrogen electrode (RHE) scale in 0.1 M KOH. Electrical impedance spectroscopy (EIS) was performed at the open circuit voltage with an amplitude of 10 mV. Potentials were corrected for the electrolyte/cell resistance from the high frequency intercept of the real impedance (~45 Ω).

OER measurements were carried out in 0.1 M KOH or 0.1 M $HClO_4$ electrolyte pre-saturated by bubbling O_2 for ~30 minutes and under continuous O_2 bubbling (Airgas, ultrahigh-grade purity) to fix the equilibrium potential. Cyclic voltammetry (CV) scans were performed at a sweep rate of 10 mV/s, starting and finishing at open circuit voltage, and sweeping between 1.1 and 1.7 V vs. RHE. Discrete points on the Tafel plot were obtained from galvanostatic measurements (applying constant potential). Lines on the Tafel plot were obtained from the capacitance-corrected CV, where the forward and reverse scans were averaged. The largest source of likely error in specific current of the IrO_2 (100) film is the 10% change in surface area with cycling. For other films, error is likely dominated by uncertainty in voltage (vs. RHE) from electrolyte preparation; an estimated variation of 0.05 pH units yields a ~3mV shift in potential, which can be related to OER current using the reported Tafel slopes.

Measurements of q^* were carried out after performing OER, in an Ar-saturated (Airgas, ultrahigh-grade purity) solution of 0.1 M KOH. The potential was swept from 0.3 to 1.25 V vs. RHE at a rate of 50 mV/s, starting and finishing at open circuit voltage. The order of measurements for RuO_2 was OER and q^* in KOH, followed by OER and q^* in $HClO_4$. The order for IrO_2 started with $HClO_4$ (first OER, then q^*) and then KOH, due to roughening observed in initial measurements in KOH.

Online electrochemical mass spectrometry. OLEMS experiments[28] were performed using an EvoLution mass spectrometer system (European Spectrometry systems Ltd.). The setup has a mass detector (Prisma QMS200, Pfeiffer), which was brought to vacuum using both a turbo molecular pump (TMH-071P, Pfeiffer, flow rate 60 L s−1) and a rotary vane pump (Duo 2.5, Pfeiffer; flow rate 2.5 $m^3\ h^{-1}$). During measurements, the pressure inside the mass detector chamber was around 10^{-6} mbar. Volatile reaction products were collected from the electrode interface by a small inlet tip positioned close (~10 μm) to the electrode surface using a micrometric screw system and a camera. The electrochemical cell used for these experiments is a two-compartment cell with three electrodes, using a gold wire as counter electrode and a

reversible hydrogen electrode as reference electrode. Electrodes were galvanostatically labeled with ^{18}O in 0.1 H_2SO_4 solution made with ^{18}O-labeled water by drawing 10 μA for 30 minutes. Electrodes were then rinsed with ^{16}O water to remove $H_2{}^{18}O$ and measured in 0.1 M H_2SO_4 solution of $H_2{}^{16}O$ at 2 mV/s for 2 cycles. Following this, 1.7 V vs. RHE was applied for 10 min to remove ^{18}O, then following a 2-5 minute hold at 1.0 V, a background was collected at 2 mV/s in 0.1 M H_2SO_4 made with DI water. This labeling at 10 μA, OLEMS measurement, 1.7 V polarization, and subsequent OLEMS background measurement was then repeated in 0.1 M KOH.

5.3. OER of (110), (100) RuO_2, IrO_2 in 0.1 M KOH

We begin by considering the activity of two relatively low-energy facets: the (100) and (110) of both RuO_2 and IrO_2. The (100) orientation was found notably more active than the (110) surface for both chemistries, as indicated by lower potentials for the onset of OER current of the (100) surfaces in **Figure 5-2**. The activity measured for the RuO_2 (110)-oriented surface is consistent with that reported for a single-crystal in 0.5 M H_2SO_4.[19] For the (100) surfaces, we provide the first report of enhanced activity relative to the (110) surface: by 2.8 times in the case of RuO_2 having 182 $\mu A/cm^2_{oxide}$ for (100) and 65 $\mu A/cm^2_{oxide}$ for (110), and 6 times in the case of IrO_2 having 3 $\mu A/cm^2_{oxide}$ for (100) and 0.5 $\mu A/cm^2_{oxide}$ for (110), at an overpotential of 0.3 V (1.53 V vs. the reversible hydrogen electrode, RHE). In addition, RuO_2 (100) and (110) surfaces were found to be more active than those of IrO_2 by an order of magnitude. This observation is in agreement with previous density functional theory (DFT) findings[9] and previously reported activities of RuO_2 and IrO_2 nanoparticles.[11] The intrinsic OER activity of RuO_2 (100) was found markedly higher than that of RuO_2 nanoparticles reported previously[11] with predominant (101) and (110) facets. In contrast, the intrinsic OER activities of IrO_2 (100) after ten cycles were less active than reported IrO_2 nanoparticles[11] with noted (101) and (110) faceting.

No significant change was found in the OER activity of RuO_2 (100) during cyclic voltammetry (CV) while the OER activity of RuO_2 (110) increased from the first to the second cycle and reached steady state after the second cycle. The greater stability of RuO_2 (100) is interesting as DFT calculations have reported RuO_2 (110) as the lowest energy surface.[29] We note that the increase in current at oxygen evolving potentials did not coincide with any significant change in capacitive current at potentials <1.5 V vs. RHE or surface roughness (**Figure 5-2**, **Table C-1**), and elucidating any resultant structural changes requires further study. In contrast, the OER activity of IrO_2 (100) was found to increase considerably with cycling and reached

steady state after ten cycles (**Figure 5-2D**). This is in agreement with the increased roughness of the IrO_2 (100) surface measured after electrochemical cycling (**Table C-1, Figure C-3**). Similarly the OER activity of IrO_2 (110) increased continuously with cycling, and yet further increased in the constant potential measurements after CV cycling, as shown in **Figure 5-2B**. The increased OER activities of IrO_2 (100) and (110) can be in part attributed to the formation of an amorphous layer on the outermost surface as suggested previously.[30] This hypothesis is supported by the observation that both oxidative features[22,31] found in the first cycle became absent upon subsequent cycling (**Figure 5-2C**).

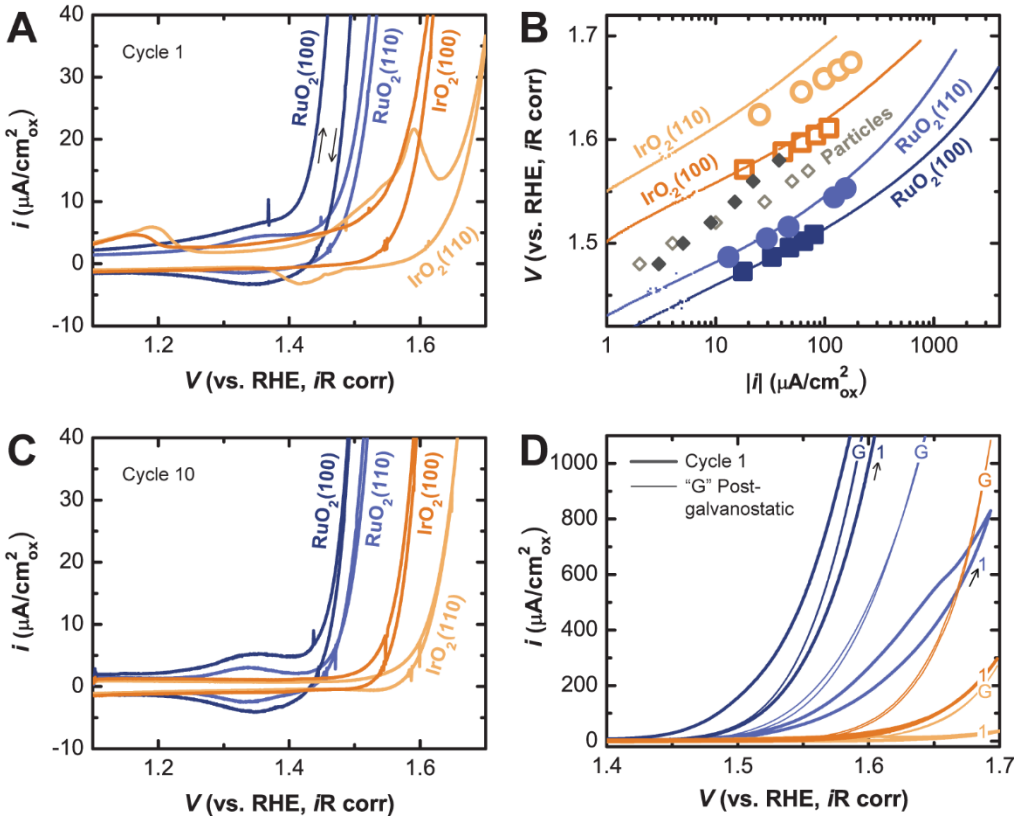

Figure 5-2. *(A) Cyclic voltammetry (CV) at 10 mV/s in 0.1 M KOH showing the 1st cycle vs. the ohmic-corrected applied voltage (E-iR) for RuO_2 (blue) and IrO_2 (orange). The oxidative peak at 1.2 V vs. RHE has been attributed to the oxidation of Ir(III) to Ir(IV),[31] and the peak at 1.4/1.6 V vs. RHE for IrO_2 (110) to the Ir(IV/VI) redox couple.[22] The redox peak of RuO_2 at ~1.35 V vs. RHE has been attributed to the Ru(VI/VII) couple.[22] (B) Tafel plot from galvanostatic measurements (points) showing E-iR vs. |i| on a logarithmic scale. Solid lines correspond to CVs of the 10th OER cycle (C) that proceeded galvanostatic measurements, averaging forward and reverse sweeps to correct for capacitance. Data for particles of RuO_2 (dark gray, filled) and IrO_2 (light gray, open) were extracted from ref. [11]. (C) 10th cycle CV measurement. (D) Overlay of 1st*

cycle (thick, "1") and the 2nd cycle following galvanostatic measurements (thin, "G"). The scanning direction is noted with a forward arrow.

RuO_2 and IrO_2 surfaces were found to exhibit dissimilar Tafel slopes at high overpotentials, which indicates changes in the reaction mechanism as a function of applied potential (**Figure 5-2**) as suggested previously.[19,22,32,33] At low overpotentials (<0.3 V), the Tafel slopes of all four surfaces were comparable (~60 mV/decade) (**Figure C-4, Table C-2**). In contrast, at high overpotentials (>0.4 V), the Tafel slopes were considerably greater (140 mV/decade for RuO_2 vs. ~90 mV/decade for IrO_2). The kink in Tafel slope for the RuO_2 (110) surface may correspond to a change in the electrochemically stable surface from an OH/O mixed phase to one of pure O termination at potentials greater than 1.58 V vs. RHE as reported previously.[33] A lesser difference in Tafel slope was observed for IrO_2 (100) and (110) surfaces in this study, which might be related to requiring greater potentials to stabilize the OH/O mixed phase compared to RuO_2. This hypothesis is supported by recent DFT findings on the RuO_2 and IrO_2 (110) surfaces.[33]

The higher OER activities on the (100) surface of IrO_2 and RuO_2 can be in part attributed to the higher atomic densities of electrochemically active Ir/Ru than on the (110) surface, termed coordinatively undersaturated sites (Ir_{cus}/Ru_{cus}).[34-36] The atomic arrangements on the (100) and (110) surfaces are shown in **Figure 5-3A,B** respectively. The nominal metal site density of Ir_{cus}/Ru_{cus} atoms on the (100) surface is ~7.2 M_{cus}/nm^2, ~1.4 times larger than that on the (110) surface, ~5.1 M_{cus}/nm^2. The difference in the electrochemically active metal site density on the surface was examined by analyzing the cathodic pseudocapacitive charge ($q^*_{cathodic}$) measured in Ar-saturated electrolyte,[32,37] as shown in **Figure 5-3C,D**. The charge density for the (100) surface was similarly ~1.4 times higher than the (110) surface for both IrO_2 and RuO_2, as shown in **Table 5-1**. Thus, the ratio of charge between orientations reflects the density of undercoordinated metal sites on the surface. Normalizing by the charge of one electron, $q^*_{cathodic}$ corresponds to redox of approximately the expected density of M_{cus} exposed on each facet, reported as M_{q^*} in **Table 5-1**, although we note other processes may contribute in the pseudocapacitive region.

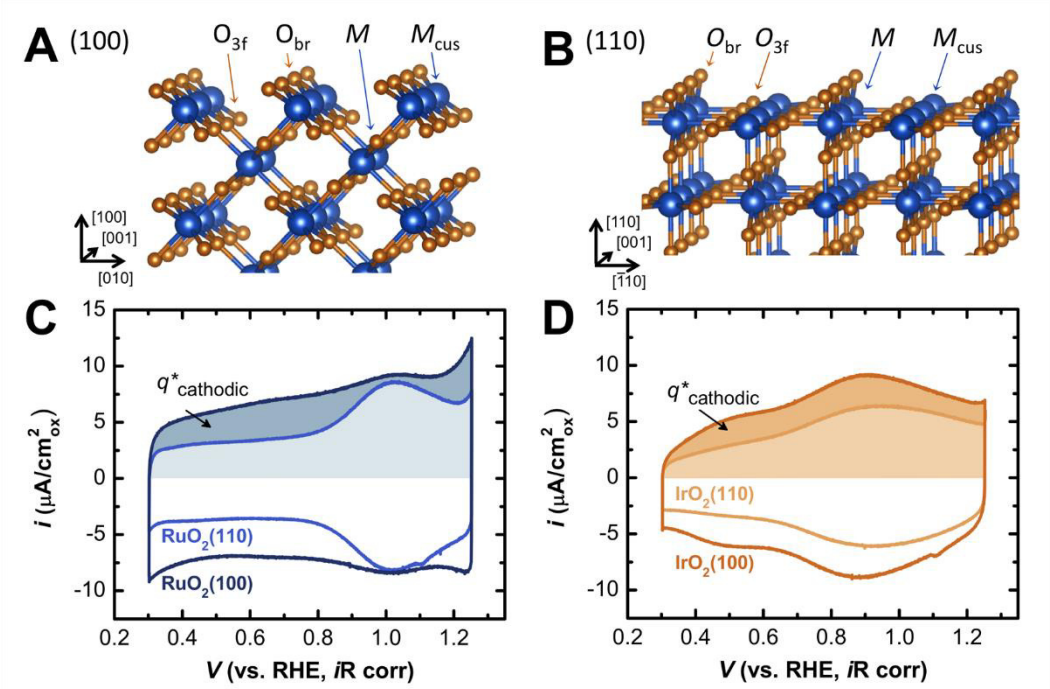

Figure 5-3. *Schematic projection of the (A) (100)-oriented surface and (B) (110)-oriented surface, with unit cell dimensions and surface projections given in Figure C-5. Species unique to the surface are annotated, including coordinatively undersaturated sites (M_{cus}, M = Ir or Ru, blue), bridging oxygen (O_{br}, orange), and 3-fold coordinated oxygen (O_{3f}, orange), in addition to fully coordinated metal sites (M, blue). Note that for the (110) surface, the fully coordinated metal site in the terminal plane was not included in the site density calculation of M_{cus}. (C) Charge passed from RuO_2 (100) and (110) and (D) charge passed from IrO_2 (100) and (110) in Ar-saturated 0.1 M KOH at 50 mV/s in the voltage window from 0.3 to 1.25 V vs. RHE, as suggested by previous work[37] to determine the charge density, $q^*_{cathodic}$.*

Table 5-1. *Comparison of charge density and metal redox to OER current density.*

	M_{cus} density [#/nm^2]	$q^*_{cathodic}$ [μC/cm^2]	M_{q^*} density [#/nm^2]	q_{O2+KOH} [μC/cm^2]	i_{OER} @ 1.53 V [μA/cm^2]
IrO_2 (100)	7.0	130	8.1	-	3
IrO_2 (110)	5.0	90	5.6	-	0.5
RuO_2 (100)	7.2	140	8.7	31.5	182
RuO_2 (110)	5.1	100	6.2	13.1	65

$q^*_{cathodic}$ was measured in Ar-saturated KOH, and includes double layer capacitance

M_{q^*} density is the associated electron density from $q^*_{cathodic}$, assuming 1 e^- transfer

q_{O2+KOH} is anodic charge discernable from the double layer capacitance

i_{OER} is obtained from the 10th cycle of a capacitance corrected CV

The correspondence between the charge ratio and that of M_{cus} density between facets is not preserved, however, when the RuO_2 films are polarized to more oxidative potentials in O_2-saturated electrolyte. The charge density of the cathodic peak associated with the Ru(VI/VII) couple[38] for the (100) surface corresponded to an atomic density of 1.97 M_{cus}/nm^2 assuming 1 electron transfer, while that on the (110) corresponded to 0.82 M_{cus}/nm^2 (**Table 5-1** and **Figure 5-4**), associated with redox of 27% and 16% of the total M_{cus} on each facet respectively. The 2.4 times greater extent of Ru(VI/VII) redox on the (100) vs. (110) surface is comparable to the difference in the OER currents at 1.53 V of these two orientations. This suggests a higher utilization of undersaturated Ru-sites on the (100) surface at oxidizing potentials, which are active for the OER. Thus, the structural sensitivity of the OER can be attributed to a greater ease of oxidation of the more open (100) surface, as has been noted in the study of vicinal RuO_2 surfaces for chlorine evolution.[39] We note that this increased utilization is reversible, in that the pseudocapacitive charge of **Figure 5-3**, which yields the expected ratio of M_{cus} density between the orientations, was measured following the OER.

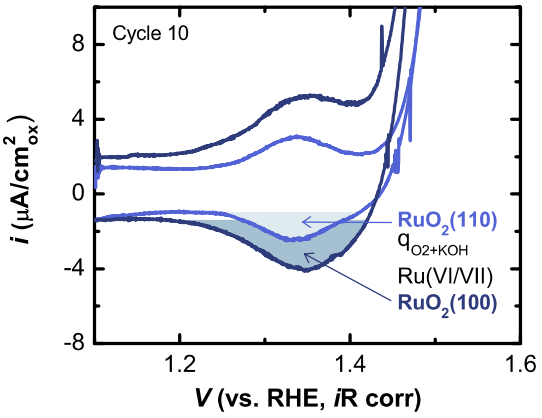

Figure 5-4. *Schematic of the determination of q_{O2+KOH}, the anodic charge discernable from the double layer capacitance from the Ru(VI/VII) redox. Cyclic voltammetry (CV) at a scan rate of 10 mV/s in O_2-saturated 0.1 M KOH, showing the current per surface area (i) for the noted cycle vs. the ohmic-corrected applied voltage (E-iR).*

One possible explanation of the discrepancy between the difference in nominal Ru_{cus} site density on each orientation and that measured in the Ru(VI/VII) redox could be faceting of the (110)-oriented surface and/or reconstruction including the (100) c(2×2) phase.[36,40] This phase has been reported inactive for CO oxidation,[40] and would likely have lower metal site-density. It is

also possible that the orientation of M_{cus} on the surface and its proximity to the bridging oxygen on the neighboring surface site may play an important role in site accessibility and catalysis of the OER. Thus, complex multi-site interactions with the catalyst surface may give rise to the structural sensitivity of the OER. The interaction between surface species and the influence of given reconstructions on oxygen electrocatalysis is an interesting avenue for future study.

5.4. pH dependence in OER activity of RuO_2

Having established the importance of Ru oxidation in OER by the correlation between activity and integrated charge of the Ru(VI/VII) redox peak, we now consider the ease of oxidation across a broader range of orientations and in different pH electrolytes. As we now consider facets of higher surface energy, we first seek to evaluate whether their surface reflects that of the desired crystallographic orientation. To do so, we evaluate the active metal site density of each RuO_2 orientation by analyzing the cathodic pseudocapacitive charge ($q^*_{cathodic}$) measured in Ar-saturated electrolyte.[32,37] The capacitive features differ notably for each orientation (**Figure 5-5, 5-6**) in both 0.1 M KOH and 0.1 M $HClO_4$, and demonstrate pH-dependent shifts in the location of redox features (**Figure 5-7**) on the reversible hydrogen electrode (RHE) scale.[41] The charge density for the lowest surface energy facets[42]—(110), (100), and (101)—scales with the nominal site density of 5-fold coordinatively undersaturated Ru sites (Ru_{cus}), as shown in **Table C-2**. Assuming a 1 e^- process, the measured number of Ru_{cus} sites agrees well with the ideal structure (**Figure 5-6**). For the higher surface energy (111) and (001) facets, the ideal truncation contains 4-fold coordinated Ru sites, which may give rise to their higher capacitance than expected assuming a 1 e^- process. However, we note that reconstruction to expose a greater number of surface Ru-atoms cannot be excluded. As $q^*_{cathodic}$ has been found to increase directly with surface area,[21] its agreement with that expected from a flat surface leads us to conclude that the thin films are not only smooth but also dense, lacking the porosity and corresponding defects associated with polycrystalline films or nanoparticles.

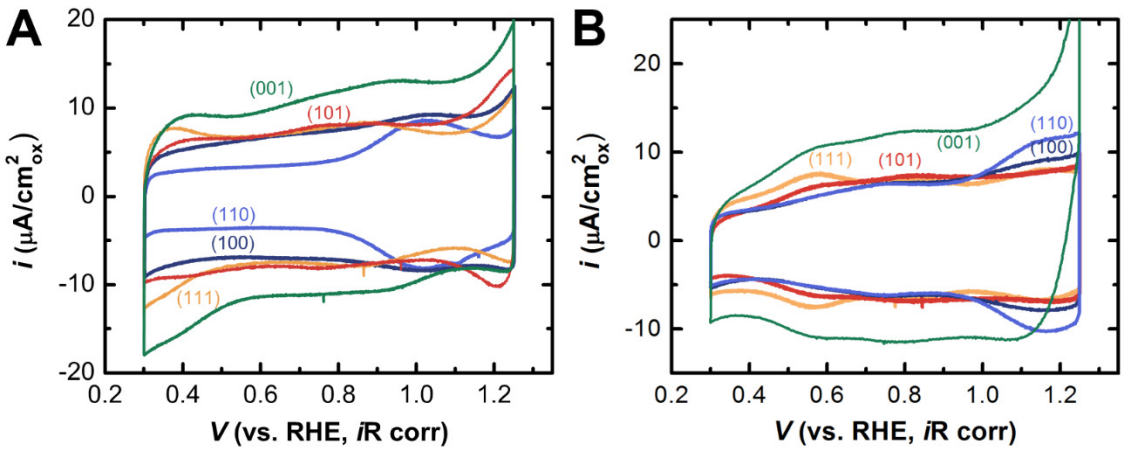

Figure 5-5. *Charge passed from RuO_2 of noted orientation in corresponding color in Ar-saturated (A) 0.1 M KOH and (B) 0.1 M $HClO_4$ at 50 mV/s in the voltage window from 0.3 to 1.25 V versus RHE, as suggested by previous work[37] to determine the charge density, $q^*_{cathodic}$.*

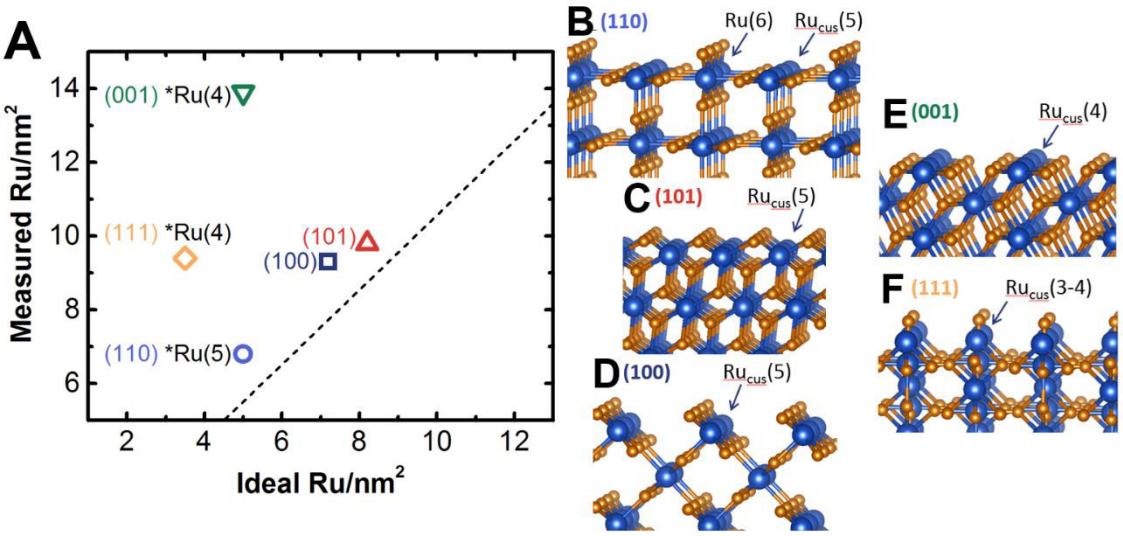

Figure 5-6. *(A) Measured Ru/nm² calculated from $q^*_{cathodic}$, assuming a 1 e^- process. The ideal undercoordinated Ru density was calculated from slices of the crystal structure: (B-F) Schematic of ideal slices on noted crystallographic facets, noting the coordination of Ru sites (blue) to oxygen (orange) at the surface, where Ru is 6-fold coordinated in the bulk rutile structure. For top-down projections, see ref.* [43].

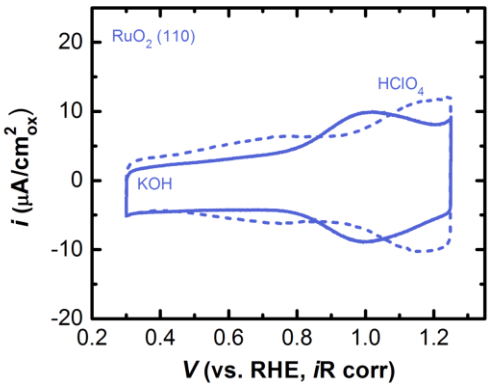

Figure 5-7. *CV of (110)-oriented RuO_2 film at 50 mV/s in Ar-saturated 0.1 M KOH (solid) and 0.1 M $HClO_4$ (dashed) on the RHE scale. The shift in the redox peaks (~15 mV/pH) demonstrates super-Nernstian behavior.*

The specific OER activities (normalized by surface area) of the different crystal orientations differ notably, with (100) and (001) being the most active in 0.1 M KOH. The OER activities measured by cyclic voltammetry (CV) and galvanostatic measurements (see Experimental Methods) provide comparable results (**Figure 5-8**). The differences in activity between surfaces can be understood in part by examining the Ru redox feature at ~1.35 V vs. RHE, attributed to the Ru(VI/VII) couple in the literature,[38] which directly precedes the onset of OER. The activity scales with the integrated anodic charge (**Figure 5-6B**), however the site utilization, extracted by converting this charge to a number of Ru-sites for a 1 e^- process, differs between surfaces. In contrast to the lower energy (101) and (110) face, which utilize ~15% of the Ru_{cus} sites, the higher energy (100) and (001) facet utilize ~25% and 50% of the Ru_{cus} sites, respectively (**Table 5-2**).

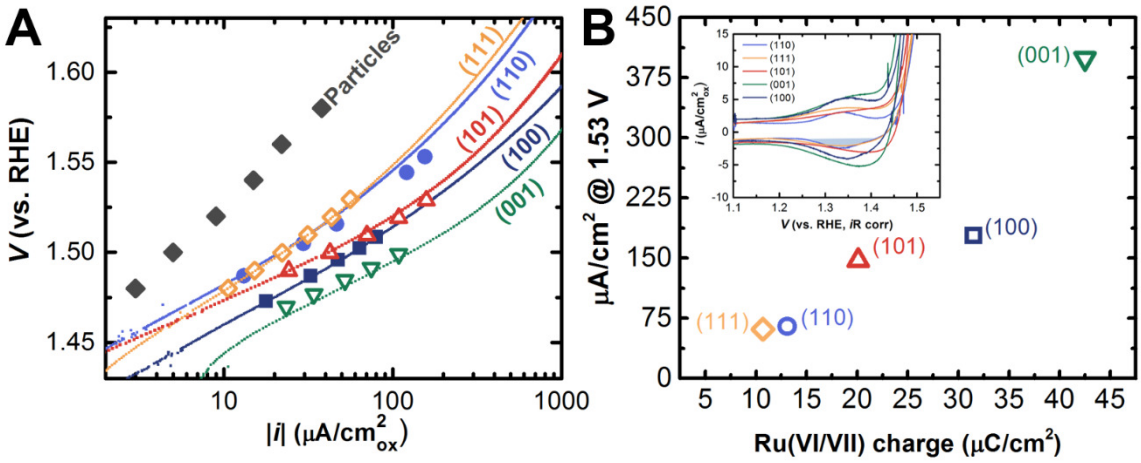

Figure 5-8. *(A) Tafel plot from galvanostatic measurements (constant applied voltage, points) showing E-iR versus |i| on a logarithmic scale. Solid lines correspond to CVs of the 10th OER cycle that proceeded galvanostatic measurements, averaging forward and reverse sweeps to correct for capacitance. Data for particles of RuO_2 (dark gray, filled) were extracted from ref.* [11]*. (B) OER activity, given as the current density at 1.53 V vs. RHE (0.3 V overpotential), scales with the anodic charge of the redox peak attributed in literature to Ru(VI/VII),*[38] *shown in the inset at 10 mV/s in O_2-saturated 0.1 M KOH, illustrating the integrated anodic charge schematically shaded for the (110) film.*

Table 5-2. *Charge associated with the Ru(VI/VII) anodic wave, schematically shown in the inset of Figure 5-8, and corresponding utilization of Ru_{cus} sites (assuming 1 e^- and the ideal number of Ru_{cus}/nm^2 as given in Table C-3.*

	(110)	**(100)**	**(101)**	**(111)**	**(001)**
Charge in μC/cm²	13.1	31.5	20.1	10.7	42.5
Utilization of Ru_{cus}	16%	27%	15%	19%	53%

The non-Nernstian behavior of the Ru redox peaks, which shift ~15 mV/pH (**Figure 5-7**) suggests that pH may play some role in the activity and/or mechanism of OER on RuO_2. In acidic environments, the activity of the (100) and (111) oriented RuO_2 films are comparable (**Figure 5-9**). However for the most stable (110) facet, an increase in activity is observed in 0.1 M $HClO_4$, similar to that previously reported for nanoparticles.[11] A slight increase in the activities with cycling or potential holding, however, suggested potential instability. AFM performed post cycling illustrated that while the (110) film remains smooth after measurements in 0.1 M KOH,

pitting is present after cycling in 0.1 M $HClO_4$ (**Figure C-6**). Such roughening was not observed on any other orientation. Further studies are required to deduce whether this is a result of intrinsic instability at defects in the (110) facet or from pinholes to the MgO substrate.

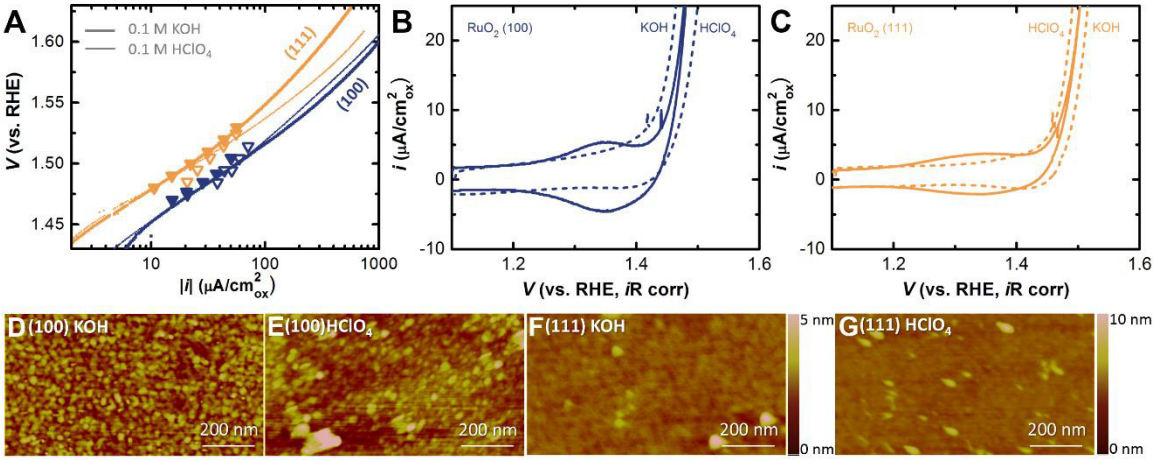

Figure 5-9. *(A) Tafel plot from galvanostatic measurements (constant applied voltage, points) showing E-iR versus |i| on a logarithmic scale for (111)-oriented RuO_2 (orange) and (100)-oriented RuO_2 (dark blue). Solid lines correspond to CVs of the 10th OER cycle (B,C) that proceeded galvanostatic measurements, averaging forward and reverse sweeps to correct for capacitance. Thick lines/solid points correspond measurements in O_2-saturated 0.1 M KOH (measured first) and thin lines/open points correspond measurements in O_2-saturated 0.1 M $HClO_4$ (measured second). (D) AFM image taken of (100)-oriented film after cycling in 0.1 M KOH or (E) 0.1 M $HClO_4$ bears no notable signs of corrosion. (F) AFM image taken of (111)-oriented film after cycling in 0.1 M KOH or (G) 0.1 M $HClO_4$ bears no notable signs of corrosion.*

For the (101) and (001) facet, the activity is slightly lower in acid compared to in base, shown in **Figure 5-10**. We note the attributed Ru(VI/VII) redox peaks are at higher potential in 0.1 M KOH compared to the OER pH-independent (100) surface. Assuming this redox couple is a precursor to OER, the non-Nernstian shift would then lead to a higher overpotential for the (101) and (001) fact, in agreement with the lower activity in 0.1 M $HClO_4$.

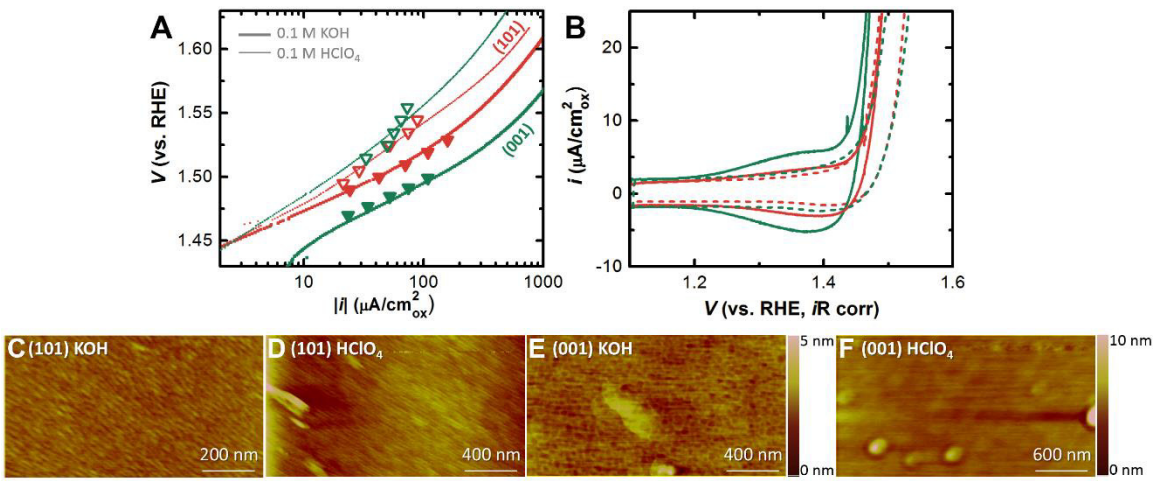

Figure 5-10. *(A) Tafel plot from galvanostatic measurements (constant applied voltage, points) showing E-iR versus |i| on a logarithmic scale for (101)-oriented RuO_2 (red) and (001)-oriented RuO_2 (green). Solid lines correspond to CVs of the 10th OER cycle (B) that proceeded galvanostatic measurements, averaging forward and reverse sweeps to correct for capacitance. Thick lines/solid points correspond measurements in O_2-saturated 0.1 M KOH (measured first) and thin lines/open points correspond measurements in O_2-saturated 0.1 M $HClO_4$ (measured second). (C) AFM image taken of (101)-oriented film after cycling in 0.1 M KOH or (D) 0.1 M $HClO_4$ bears no notable signs of corrosion. (E) AFM image taken of (001)-oriented film after cycling in 0.1 M KOH or (F) 0.1 M $HClO_4$ bears no notable signs of corrosion.*

5.5. Insight into reaction mechanism on RuO_2

We next assess the potential involvement of lattice oxygen by online electrochemical mass spectrometry (OLEMS) measurements.[28] The films were held galvanostatically at high current densities in 0.1 M H_2SO_4 or KOH, where the electrolyte was prepared with ^{18}O-labeled water. After rinsing and replacing the electrolyte with that prepared from DI water (^{16}O), the masses of evolved oxygen were measured during OER.

Motivated by historic studies reporting oxygen exchange during OER on RuO_2,[23,24] one might expect the extent of lattice oxygen involvement to depend of the structure of the terminating crystal facet, as does OER activity.[27] Furthermore, the non-Nernstian behavior of Ru redox motivates the study of lattice oxygen involvement at both acidic and basic pH. Surprisingly, while we observe notable $^{32}O_2$ (^{16}O + ^{16}O) gas evolved during OER, we observe negligible formation of $^{34}O_2$ (^{18}O + ^{16}O), and no formation of $^{36}O_2$ (^{18}O + ^{18}O) (**Figure 5-11**). To assess whether the $^{34}O_2$ arises from a mechanism where one ^{18}O from the lattice interacts with a ^{16}O from the electrolyte, or is a simply a product of the natural isotopic abundance of ^{18}O (0.2%),

we take the ratio of $^{34}O_2$ to $^{32}O_2$ evolved as a function of applied potential (**Figure 5-11**). This ratio is voltage independent, and identical to that of the background obtained after passing extensive OER current to remove any ^{18}O. This clearly indicates that within the timeframe of measurements and sensitivity of the instrument (previously demonstrated to detect oxygen exchange on a polycrystalline gold disk[44]), oxygen is not exchanged with the lattice during OER on oriented RuO_2 films.

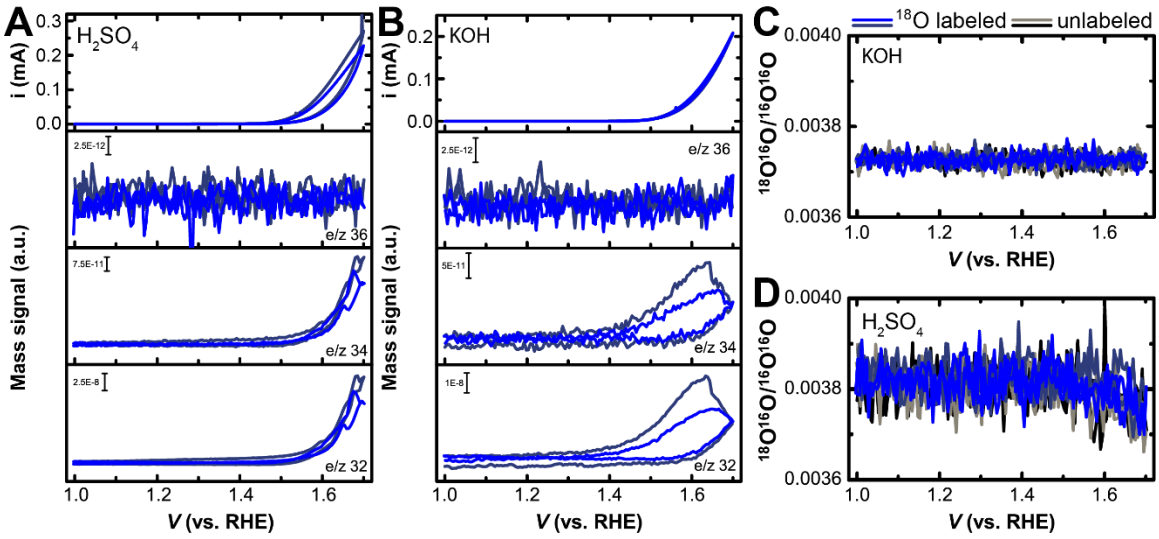

Figure 5-11. *(A) Representative online electrochemical mass spectrometry (OLEMS) measurements on ^{18}O labeled (100)-oriented RuO_2 (see method section for details). Shown is the current as a function of applied voltage, along with the mass signals collected in parallel for $^{36}O_2$, $^{34}O_2$, and $^{32}O_2$. (B) $^{34}O_2$ / $^{32}O_2$ signal ratio, which is independent of applied potential and overtop the same ratio measured after aggressive polarization to remove any exchanged oxygen, indicating it arises from background $^{34}O_2$. Measurements provided by Oscar Diaz-Morales at Leiden University.*

The lack of oxygen exchange on RuO_2 films of high surface energy orientation, in either basic or acidic environments, gives rise to the question of what prompted the observation of lattice involvement in previous studies. Given exchange was observed on polycrystalline RuO_2 RF sputtered onto a membrane[23] and nanocrystalline particles,[24] we hypothesize that a mechanism involving lattice oxygen proceeds at defects or grain boundaries, while a different mechanism prevails on the crystallographic facets. It is likely low-coordinated surface sites in less-crystalline catalysts of nominally "RuO_2" stoichiometry which are electrochemically active and exhibit exchange. Fortunately, such exchange is not necessary to achieve high catalytic activity and oriented films display excellent activity and stability in a range of pH environments.

5.6. Conclusions

This chapter has considered the orientation-dependent activity of rutile oxides RuO_2 and IrO_2 for the OER. Explicitly, the more open (100) facet was found more active than the (110), attributed to a greater ease of oxidation of surface Ru_{cus} sites, probed via Ru redox. Consideration of higher surface area facets also found that the OER activity trends with not the nominal Ru_{cus} site density on each crystallographic projection, but the number of these sites which are oxidized prior to the onset of OER.

These redox features exhibit non-Nernstian behavior, resulting in a pH-dependent shift on the RHE scale. For orientations with a higher potential for the Ru redox peak in pH 13, the activity is decreased in acidic electrolyte, presumably because of the shift of Ru redox to higher potentials. This is in contrast to orientations with a lower potential for Ru redox, where the OER activity is independent of pH.

Online mass spectrometry measurements of ^{18}O labeled RuO_2 do not provide evidence for lattice oxygen involvement at appreciable scales, in contrast to literature reports on nanocrystalline material and RF sputtered films. This suggests that the reaction mechanism on dense, oriented facets does not involve lattice oxygen, however such a mechanism may be involved in more disordered materials.

References

1 Lyons, M. E. G. & Burke, L. D. Mechanism of Oxygen Reactions at Porous Oxide Electrodes. Part 1.-Oxygen Evolution at RuO_2 and $Ru_xSn_{1-x}O_2$ Electrodes in Alkaline Solution Under Vigorous Electrolysis Conditions. *Journal of the Chemical Society, Faraday Transactions 1: Physical Chemistry in Condensed Phases* **83**, 299-321, (1987).

2 Gray, H. B. Powering the Planet with Solar Fuel. *Nature Chemistry* **1**, 7-7, (2009).

3 Walter, M. G. *et al.* Solar Water Splitting Cells. *Chemical Reviews* **110**, 6446-6473, (2010).

4 Cook, T. R. *et al.* Solar Energy Supply and Storage for the Legacy and Nonlegacy Worlds. *Chemical Reviews* **110**, 6474-6502, (2010).

5 Trasatti, S. Electrocatalysis by Oxides — Attempt at a Unifying Approach. *Journal of Electroanalytical Chemistry and Interfacial Electrochemistry* **111**, 125-131, (1980).

6 Suntivich, J., May, K. J., Gasteiger, H. A., Goodenough, J. B. & Shao-Horn, Y. A Perovskite Oxide Optimized for Oxygen Evolution Catalysis from Molecular Orbital Principles. *Science* **334**, 1383-1385, (2011).

7 Kanan, M. W. & Nocera, D. G. In Situ Formation of an Oxygen-Evolving Catalyst in Neutral Water Containing Phosphate and Co^{2+}. *Science* **321**, 1072-1075, (2008).

8 Duan, L. *et al.* A Molecular Ruthenium Catalyst with Water-oxidation Activity Comparable to that of Photosystem II. *Nature Chemistry* **4**, 418-423, (2012).

9 Rossmeisl, J., Qu, Z. W., Zhu, H., Kroes, G. J. & Nørskov, J. K. Electrolysis of Water on Oxide Surfaces. *Journal of Electroanalytical Chemistry* **607**, 83-89, (2007).

10 McCrory, C. C. L., Jung, S., Peters, J. C. & Jaramillo, T. F. Benchmarking Heterogeneous Electrocatalysts for the Oxygen Evolution Reaction. *Journal of the American Chemical Society* **135**, 16977-16987, (2013).

11 Lee, Y., Suntivich, J., May, K. J., Perry, E. E. & Shao-Horn, Y. Synthesis and Activities of Rutile IrO_2 and RuO_2 Nanoparticles for Oxygen Evolution in Acid and Alkaline Solutions. *The Journal of Physical Chemistry Letters* **3**, 399-404, (2012).

12 Vesborg, P. C. K. & Jaramillo, T. F. Addressing the Terawatt Challenge: Scalability in the Supply of Chemical Elements for Renewable Energy. *RSC Advances* **2**, 7933-7947, (2012).

13 Tsuji, E., Imanishi, A., Fukui, K.-i. & Nakato, Y. Electrocatalytic Activity of Amorphous RuO_2 Electrode for Oxygen Evolution in an Aqueous Solution. *Electrochimica Acta* **56**, 2009-2016, (2011).

14 Rasten, E., Hagen, G. & Tunold, R. Electrocatalysis in Water Electrolysis with Solid Polymer Electrolyte. *Electrochimica Acta* **48**, 3945-3952, (2003).

15 Burke, L. Electrochrornic Iridium Oxides. *Platinum Metals Review* **28**, 56-61, (1984).

16 Trasatti, S. Physical Electrochemistry of Ceramic Oxides. *Electrochimica Acta* **36**, 225-241, (1991).

17 Dmowski, W., Egami, T., Swider-Lyons, K. E., Love, C. T. & Rolison, D. R. Local Atomic Structure and Conduction Mechanism of Nanocrystalline Hydrous RuO_2 from X-ray Scattering. *The Journal of Physical Chemistry B* **106**, 12677-12683, (2002).

18 Hu, J.-M. *et al.* Effect of Crystallite Orientation of IrO_2 Rutile on the Corrosion Characteristics of IrO_2+Ta_2O_5 Oxide Coatings. *Journal of Materials Science Letters* **20**, 1353-1355, (2001).

19 Castelli, P., Trasatti, S., Pollak, F. H. & O'Grady, W. E. Single Crystals as Model Electrocatalysts: Oxygen Evolution on RuO_2 (110). *Journal of Electroanalytical Chemistry and Interfacial Electrochemistry* **210**, 189-194, (1986).

20 Man, I. C. *et al.* Universality in Oxygen Evolution Electrocatalysis on Oxide Surfaces. *ChemCatChem* **3**, 1159-1165, (2011).

21 Lodi, G., Sivieri, E., Battisti, A. & Trasatti, S. Ruthenium dioxide-based film electrodes. *Journal of Applied Electrochemistry* **8**, 135-143, (1978).

22 Lyons, M. E. G. & Floquet, S. Mechanism of Oxygen Reactions at Porous Oxide Electrodes. Part 2-Oxygen Evolution at RuO_2, IrO_2 and $Ir_xRu_{1-x}O_2$ Electrodes in Aqueous Acid and Alkaline Solution. *Physical Chemistry Chemical Physics* **13**, 5314-5335, (2011).

23 Wohlfahrt-Mehrens, M. & Heitbaum, J. Oxygen evolution on Ru and RuO_2 electrodes studied using isotope labelling and on-line mass spectrometry. *Journal of Electroanalytical Chemistry and Interfacial Electrochemistry* **237**, 251-260, (1987).

24 Macounova, K., Makarova, M. & Krtil, P. Oxygen evolution on nanocrystalline RuO_2 and $Ru_{0.9}Ni_{0.1}O_{2-\delta}$ electrodes – DEMS approach to reaction mechanism determination. *Electrochemistry Communications* **11**, 1865-1868, (2009).

25 Grimaud, A., Hong, W. T., Shao-Horn, Y. & Tarascon, J. M. Anionic redox processes for electrochemical devices. *Nat Mater* **15**, 121-126, (2016).

26 Paoli, E. A. *et al.* Oxygen evolution on well-characterized mass-selected Ru and RuO_2 nanoparticles. *Chemical Science* **6**, 190-196, (2015).

27 Stoerzinger, K. A., Qiao, L., Biegalski, M. D. & Shao-Horn, Y. Orientation-Dependent Oxygen Evolution Activities of Rutile IrO_2 and RuO_2. *The Journal of Physical Chemistry Letters* **5**, 1636-1641, (2014).

28 Wonders, A. H., Housmans, T. H. M., Rosca, V. & Koper, M. T. M. On-line mass spectrometry system for measurements at single-crystal electrodes in hanging meniscus configuration. *Journal of Applied Electrochemistry* **36**, 1215-1221, (2006).

29 Novell-Leruth, G., Carchini, G. & López, N. On the Properties of Binary Rutile MO_2 Compounds, M = Ir, Ru, Sn, and Ti: A DFT Study. *The Journal of Chemical Physics* **138**, 194706-194701-194706-194710, (2013).

30 Slavcheva, E., Radev, I., Topalov, G. & Budevski, E. Sputtered Electrocatalysts for PEM Electrochemical Energy Converters. *Electrochimica Acta* **53**, 362-368, (2007).

31 Kötz, R. & Stucki, S. Oxygen Evolution and Corrosion on Ruthenium-Iridium Alloys. *Journal of the Electrochemical Society* **132**, 103-107, (1985).

32 Guerrini, E., Chen, H. & Trasatti, S. Oxygen Evolution on Aged IrO_x /Ti Electrodes in Alkaline Solutions. *J Solid State Electrochem* **11**, 939-945, (2007).

33 Fang, Y.-H. & Liu, Z.-P. Mechanism and Tafel Lines of Electro-Oxidation of Water to Oxygen on RuO_2(110). *Journal of the American Chemical Society* **132**, 18214-18222, (2010).

34 Kim, Y. D., Schwegmann, S., Seitsonen, A. P. & Over, H. Epitaxial Growth of RuO_2(100) on Ru(10$\bar{1}$0): Surface Structure and Other Properties. *The Journal of Physical Chemistry B* **105**, 2205-2211, (2001).

35 Knapp, M., Seitsonen, A. P., Kim, Y. D. & Over, H. Catalytic Activity of the RuO_2(100) Surface in the Oxidation of CO†. *The Journal of Physical Chemistry B* **108**, 14392-14397, (2004).

36 Assmann, J. *et al.* Heterogeneous Oxidation Catalysis on Ruthenium: Bridging the Pressure and Materials Gaps and Beyond. *Journal of Physics: Condensed Matter* **20**, 184017, (2008).

37 Burke, L. D. & Murphy, O. J. Cyclic Voltammetry as a Technique for Determining the Surface Area of RuO_2 Electrodes. *Journal of Electroanalytical Chemistry and Interfacial Electrochemistry* **96**, 19-27, (1979).

38 Trasatti, S. Electrocatalysis in the Anodic Evolution of Oxygen and Chlorine. *Electrochimica Acta* **29**, 1503-1512, (1984).

39 Guerrini, E. & Trasatti, S. Recent developments in understanding factors of electrocatalysis. *Russ J Electrochem* **42**, 1017-1025, (2006).

40 Aßmann, J. *et al.* Understanding the Structural Deactivation of Ruthenium Catalysts on an Atomic Scale under both Oxidizing and Reducing Conditions. *Angewandte Chemie International Edition* **44**, 917-920, (2005).

41 Giordano, L. *et al.* pH dependence of OER activity of oxides: Current and future perspectives. *Catalysis Today* **262**, 2-10, (2016).

42 Xu, C. *et al.* Prediction on the Surface Phase Diagram and Growth Morphology of Nanocrystal Ruthenium Dioxide. *Journal of the American Ceramic Society* **97**, 3702-3709, (2014).

43 Hepel, T., Pollak, F. H. & O'Grady, W. E. Effect of Crystallographic Orientation of Single-Crystal RuO_2 Electrodes on the Hydrogen Adsorption Reactions. *Journal of the Electrochemical Society* **131**, 2094-2100, (1984).

44 Diaz-Morales, O., Calle-Vallejo, F., de Munck, C. & Koper, M. T. M. Electrochemical water splitting by gold: evidence for an oxide decomposition mechanism. *Chemical Science* **4**, 2334-2343, (2013).

6. Conclusions and outlook

6.1. Summary

In this thesis, we have presented studies of model transition metal oxide systems, of interest as more abundant alternatives in oxygen electrocatalysis compared to precious metal industry standards. Specifically, we considered well-defined surfaces of epitaxial thin films, on which electrochemical studies establish the intrinsic activity of oxide catalysts in a way that cannot be realized with polydisperse nanoparticle systems. This thesis has isolated the activity of the catalyst on a true surface-area basis, enabling an accurate comparison of catalyst chemistries, and also revealed how different terminations and structures affect the kinetics.

Our studies have primarily focused on the crystal class of the perovskite oxide due to its ability to incorporate a wide range of the periodic table, with resulting breath of electronic structure and chemical reactivity. Many of these oxide chemistries have been previously considered as catalysts for the oxygen reduction and oxygen evolution reaction (ORR, OER) as micron-sized powders, either pressed into a pellet or mixed with conductive carbon in composite electrodes. This has hindered understanding of the intrinsic activity and its relation to adsorbed reaction intermediates, which have been challenging to probe and especially quantify by surface sensitive spectroscopic approaches.

This thesis has employed ambient pressure X-ray photoelectron spectroscopy to probe the surface species present in environments approaching that of fuel cell/electrolyzer operation, bridging the pressure gap between surface science and application. The interaction of catalysts with water as a reactant, intermediate, or product is expected to play a key role in the reduction and evolution of oxygen, however the nature of this interaction has not been well-understood. We investigated the adsorption of water on well-defined thin film surfaces at a range of relative humidities, establishing the oxygen speciation and quantifying its dependence on the chemical potential of water (Chapter 2). We found that the strength of interaction with hydroxyls correlates strongly with catalytic ORR activity, with more active catalysts having a lower tendency to hydroxylate. Furthermore, this thesis sought to bridge wetting and activity for oxygen electrocatalysis in aqueous solutions by measuring the intrinsic wettability of catalyst surfaces, as well as obtain complimentary microscopic chemical understanding of how the interaction with water influences the reactivity (Chapter 3). This fundamental insight brought molecular understanding to the wetting of oxide surfaces, as well as the role of hydrogen bonding in catalysis. We further explored the changes in oxide electronic structure with the hydroxylation

and wetting of the surface, establishing that materials with a lower Fermi level and valence band showed a higher tendency to hydroxylate (Chapter 4).

Studies of thin films also enable investigation of the phenomena that are not straightforward to isolate in nanoparticles, such as the role of oxide band structure, interfacial charge transfer (the "ligand" effect), strain, and crystallographic orientation. This thesis has gone beyond considering electronic conductivity in order to directly relate the availability of electrons of a given energy to activity for the ORR (Chapter 4). Furthermore, we have considered the role of crystallographic orientation in the oxidation of transition metals, which is a prerequisite for catalysis of the oxygen evolution reaction (OER) on ruthenium dioxide (Chapter 5). A more open structure promotes site utilization and higher activity. The oxidation of transition metal in this system displays a non-Nernstian behavior with respect to pH, where this pushes the surface oxidation of Ru atoms to higher potentials on the reversible hydrogen electrode scale in acidic environments, in some cases then reducing the OER activity. Despite this pH-dependent behavior, no lattice involvement or exchange of oxygen atoms between the surface and electrolyte is observed, contrary to historic reports and suggesting well-defined crystal facets support OER only on the transition metal (Chapter 5). We also present an investigation of the ligand effect by changing film thickness (Appendix D) and a first investigation of the role of epitaxial strain in the perovskite oxide system (Appendix E).

6.2. Outlook

This thesis shows it is possible to experimentally probe the relative affinity across different surfaces for a reaction intermediate, such as OH. The spectral deconvolution provided at a range of relative humidities bridges the pressure gap, bringing surface science approaches closer to realistic applications. This has set the stage for considering oxide surfaces in even higher humidities, and even—given appropriate probes—in liquid medium.

We have recently moved toward *in operando* spectroscopy by two different approaches: one which probes the surface through a thin liquid layer, collecting photoelectrons excited by a "tender" X-ray source, and one which probes the solid/liquid interface by penetrating through the solid, collecting the electron yield current or fluorescence that arises from soft X-ray spectroscopy. Initial efforts in each approach are discussed below.

This thesis has worked to bridge the pressure gap, which limits understanding of application-relevant surfaces, by increasing the pressure of surface science techniques. In doing so, we have considered model systems to enable quantification of activity and speciation, which

points to another potential limitation in understanding: the "materials gap". Increasing the complexity of surfaces through controlled introduction and characterization of defects will build further understanding of more realistic catalysts.

6.2.1. In operando XPS

The ambient pressure XPS presented within the previous chapters was probed with soft X-rays, limiting the inelastic mean free path of ejected photoelectrons to below ~2 nm. This prohibits consideration of a condensed liquid layer greater than a few monolayers due to significant attenuation of the desired signal from the solid/liquid interface, where the measured signal is dominated by the liquid/gas interface instead. With the development of hard (>7 keV) and "tender" (2-7 keV) X-ray photoelectron endstations,[1] it will be possible to probe buried interfaces in the near future.[2] Hard/tender X-rays will further provide information on the electrochemical double layer that forms at solid/liquid interfaces, recently demonstrated by observing the oxidation of platinum in KF/H_2O[1] and Ni in a KOH electrolyte[3] *in situ* by the hanging meniscus method.

We have recently made initial measurements using such a setup at beamline 9.3.1 at the Advanced Light Source. Building upon our extensive consideration of (001)-oriented $LaCoO_3$ in a humid environment (Chapter 2), as well as initial measurements of $La_{(1-x)}Sr_xCoO_3$ surfaces, we carried out a preliminary study of such surfaces in operando in 0.1 M KOH. The speciation at the solid/liquid interface under ~20 nm of electrolyte meniscus was considered as a function of applied potential, including both the ORR and OER range. Of interest is comparing the surface band bending between semiconducting and metallic oxides,[4] as well as the speciation present under electrocatalytically active conditions. Comparison of some preliminary data is presented in **Figure 6-1**.

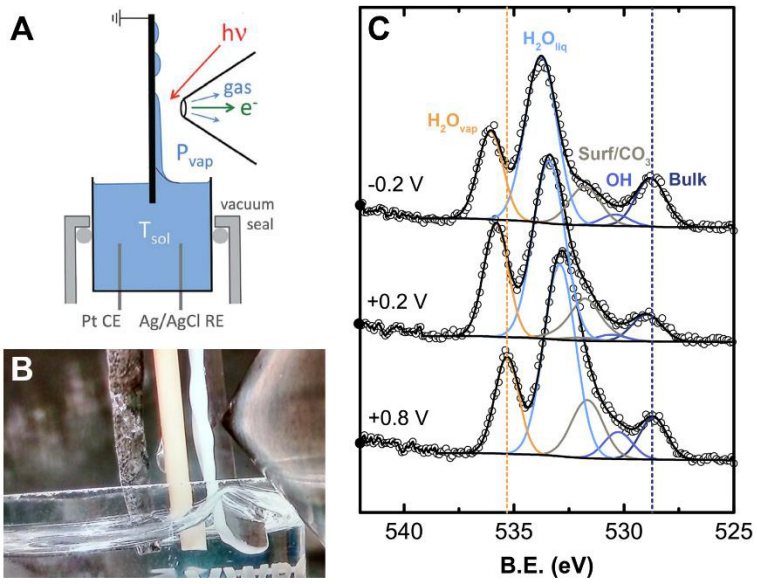

Figure 6-1. *(A) Schematic of meniscus formed above an electrolyte well, where tender X-rays and associated photoelectrons can penetrate through the ~20 nm thick liquid layer to obtain information about the solid/liquid interface. Reproduced from Ref.* [3] *with permission of The Royal Society of Chemistry. (B) Photograph showing, from left to right, the Pt foil counter electrode, Ag/AgCl reference electrode, epitaxial* $La_{0.6}Sr_{0.4}CoO_3$ *catalyst film, and the nose cone with aperture limiting the pressure entering the differential pumping system. (C) O 1s spectra at different polarizations in a 2-electrode configuration. The shift of the gas phase peak scales with the applied potential.*

6.2.2. In situ and in operando XAS

Complementing the information regarding occupied states that is obtained from XPS, information regarding the unoccupied states can be obtained from XAS. The physics of the technique involves the excitation of a core level electron to allowed unoccupied states, which in the case of soft X-ray transitions must then be measured by something proportional to this process (as a transmission measurement—the method used for hard X-rays—is prohibited by the short mean free path). Measurement modes therefore include florescence detection (>100 nm information depth),[5] collection of the grounding current resulting from photo- and Auger electron processes (<10 nm information depth),[6] and collection of photoelectrons with a chosen kinetic energy (tunable information depth ~2 nm).[7]

It is desirable to obtain information about the unoccupied states in a humid environment, as well as in liquid electrolyte, in order to probe the oxidation state of the transition metal under

reaction conditions and changes in the metal-oxygen covalency during oxygen reduction and evolution. We have made initial strides in both regimes. Using the ambient pressure XPS equipment, we have measured the O K-edge and transition metal L-edge of perovskite oxides in a range of relative humidities in partial electron yield mode. Comparison of some preliminary data is presented in **Figure 6-2**. Understanding differences in spectral features when integrating select photoelectron kinetic energies, as opposed to measuring grounding current, is still underway.

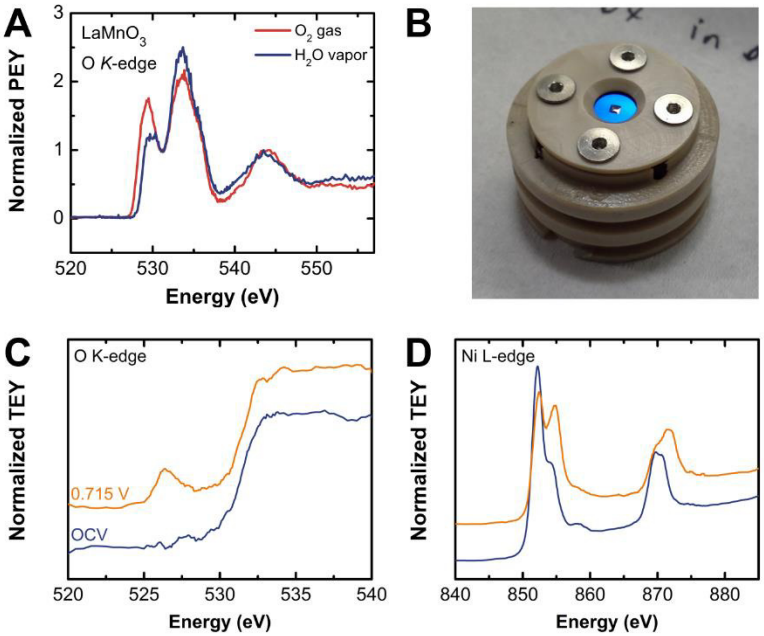

Figure 6-2. *(A) O K-edge spectrum of $LaMnO_3$ epitaxial film in a dry environment (O_2 gas) and a humid one (H_2O vapor). (B) Photograph of a static-volume electrochemical cell for in operando XAS on ALS beamline 6.3.1.2. (C) O K-edge spectrum of Ni-oxide electrodeposited catalyst at OCV and near the onset of OER (0.715 V). (D) Ni L-edge under the same conditions illustrating Ni-oxyhydroxide formation.*

We have also made initial attempts to employ an in situ cell containing liquid electrolyte for in operando measurements of catalyst electronic structure. This requires fabrication of a thin (~20 nm) catalyst layer and current collector (~10 nm Au or C) on an X-ray transparent window (100 nm thick Si_3N_4 windows, with dimensions of 1 mm x 0.5 mm in a 5 x 5 mm Si frame). We have found that supported particles tend to delaminate from the window due to the mechanical flexing that results from the large pressure gradient, however electrodeposited films or those made by pulsed laser deposition are mechanically robust. Initial measurements on an electrodeposited film illustrate changes in transition metal valence state and covalency when going toward OER-relevant conditions (**Figure 6-2**). However, measurement by fluorescence

yield mode is often dominated by signal from the electrolyte, making it challenging to extract meaningful information about the oxide surface. Greater surface sensitivity can be obtained using total electron yield mode. Because the current measured at the Au collector will include both XAS and faradaic current in an electrochemical cell, we must chop the incident X-rays and use a lock-in amplifier to isolate these contributions, which after much optimization of numerous experimental challenges has illustrated increased surface sensitivity promising for future experiments.

6.2.3. Bridging the materials gap

As discussed in the study of RuO_2 in Chapter 5, discrepancies exist between the oxygen exchange results on oriented films presented in this thesis and those reported in literature on polycrystalline films and nanoparticles.[8,9] This suggests that defect sites, such as grain boundaries or step edges, may support a different reaction mechanism. Work is underway to explicitly consider the activity of polycrystalline RuO_2 films on the same OLEMS setup with identical procedures to assess the role of grain boundaries. The crystallinity of this film can be further tuned by annealing temperature, as well as electrochemically inducing film defects.

It is of further interest to introduce defects in the perovskite films presented in this thesis. Although the coincident activity of e.g. $LaCoO_3$ epitaxial films with that of micron sized powders normalized to the oxide surface area suggests grain boundaries do not play a large role, other defects such as oxygen vacancies may be critical in determining the surface electronic structure, speciation, and activity. This can be controlled to some extent by growth or post-growth annealing in oxygen rich or poor atmospheres, however vacancy content is challenging to probe for thin films. Approaches common in powder materials, such as titration, do not work well with such small surface areas. Rutherford backscattering (RBS) can help in quantifying oxygen stoichiometry, although this is challenging in ternary oxides including heavy elements. Spectroscopic approaches may be promising in at least a relative comparison. The presence of oxygen vacancies may also play a large role in dictating the hydroxylation of oxide surfaces, due to the ability for water to fill the vacancy with a hydroxyl and protonate a nearby site in some chemistries. Step edges can be another source of reactive undercoordinated sites in realistic catalysts. Their density can be controlled in epitaxial films through choice of substrates with different degrees of miscut, which may provide more information regarding the nature of different active sites.

References

1 Axnanda, S. *et al.* Using "Tender" X-ray Ambient Pressure X-Ray Photoelectron Spectroscopy as A Direct Probe of Solid-Liquid Interface. *Sci. Rep.* **5**, 9788, (2015).

2 Stoerzinger, K. A., Hong, W. T., Crumlin, E. J., Bluhm, H. & Shao-Horn, Y. Insights into Electrochemical Reactions from Ambient Pressure Photoelectron Spectroscopy. *Accounts of Chemical Research* **48**, 2976-2983, (2015).

3 Karsloglu, O. *et al.* Aqueous Solution/Metal Interfaces Investigated in operando by Photoelectron Spectroscopy. *Faraday Discussions*, (2015).

4 Lichterman, M. F. *et al.* An Electrochemical, Microtopographical and Ambient Pressure X-Ray Photoelectron Spectroscopic Investigation of Si/TiO_2/Ni/Electrolyte Interfaces. *Journal of The Electrochemical Society* **163**, H139-H146, (2016).

5 Braun, A. *et al.* Direct Observation of Two Electron Holes in a Hematite Photoanode during Photoelectrochemical Water Splitting. *The Journal of Physical Chemistry C* **116**, 16870-16875, (2012).

6 Velasco-Velez, J.-J. *et al.* The structure of interfacial water on gold electrodes studied by x-ray absorption spectroscopy. *Science* **346**, 831-834, (2014).

7 Mueller, D. N., Machala, M. L., Bluhm, H. & Chueh, W. C. Redox activity of surface oxygen anions in oxygen-deficient perovskite oxides during electrochemical reactions. *Nat Commun* **6**, (2015).

8 Wohlfahrt-Mehrens, M. & Heitbaum, J. Oxygen evolution on Ru and RuO_2 electrodes studied using isotope labelling and on-line mass spectrometry. *Journal of Electroanalytical Chemistry and Interfacial Electrochemistry* **237**, 251-260, (1987).

9 Macounova, K., Makarova, M. & Krtil, P. Oxygen evolution on nanocrystalline RuO_2 and $Ru_{0.9}Ni_{0.1}O_{2-\delta}$ electrodes – DEMS approach to reaction mechanism determination. *Electrochemistry Communications* **11**, 1865-1868, (2009).

A. Additional information for Chapter 2

A.1. Additional figures regarding surface speciation

Survey spectra are presented for $LaCoO_3$ (LCO) in **Figure A-1**. Only expected elements (La, Co, O) are observed when cleaning in O_2, except for sulfur, which is known to bind strongly to perovskites in such conditions.[1] No sulfur was observed in films prior to cleaning, and the amount decreased upon changing the environment from O_2 to H_2O, as well as reducing the temperature. The potential contribution of sulfate to the O 1*s* is discussed in **Figure A-2**. In order to estimate the maximum potential contribution of sulfate to the O 1*s*, the S 2*p* intensity was scaled by the ratio of the tabulated cross sections of C 1*s* at 735 eV to S 2*p* at 350 eV ($\sigma_S = 0.1339\ \sigma_{C1s}$)[2,3] the measured RSF of O 1*s* to C 1*s* at 735 eV (RSF = 0.83), and the oxygen stoichiometry of sulfate (O:S = 4:1). At 25 °C in water, carbon is present, but sulfur is negligible. A small peak at 75 eV appeared after the isobar experiments at 25 °C in water, which is consistent with the Al 2*p* core level. However, no features in the O 1*s* spectra were consistent with the hydroxylation (534.6 eV) and wetting (536.6 eV) of Al_2O_3.[4]

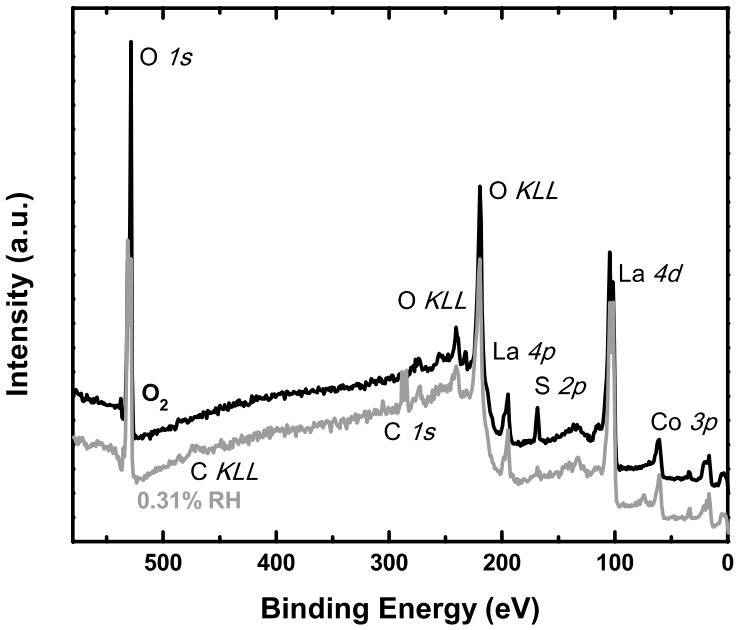

Figure A-1. *Survey spectra at 735 eV incident energy, at 300 °C in O_2 (black, top) and 25 °C in H_2O (gray, bottom).*

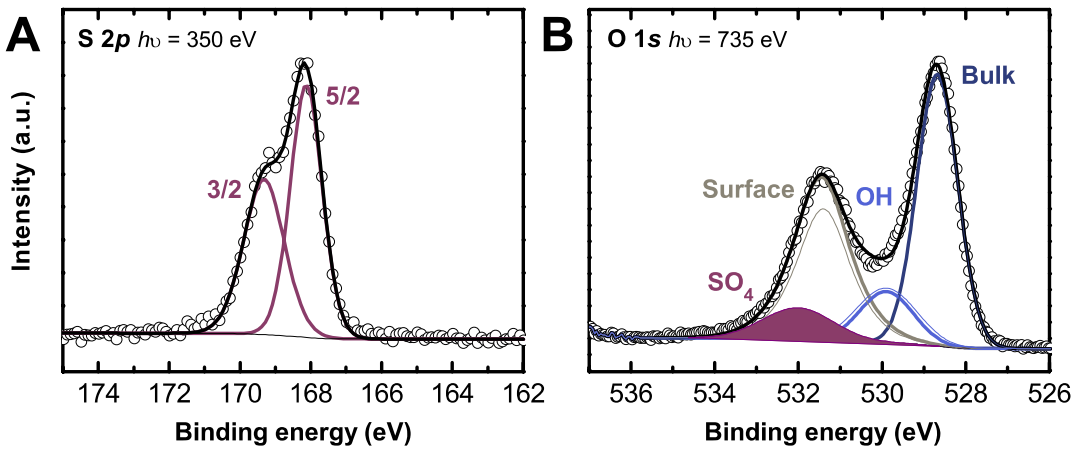

Figure A-2. *Sulfur was observed when the LCO was heated to 300 °C in O_2. (A) S 2p core level at an incident photon energy of 350 eV, with binding energy typical of that for lanthanum and transition metal sulfates.[1] The sulfate O 1s binding energy is 532-533 eV.[1] (B) Including possible sulfate contribution (purple) reduces the quantity of the surface oxygen species (thin gray line), but only by ~20%.*

Figure A-3 presents additional measurements performed at ALS 11.0.2 under two-bunch operation – which can be compared with **Figure 2-6** in Chapter 2, measured under multi-bunch operation during a different beamtime. Similar trends in the evolution of surface species were observed: an initial growth of OH, CO_3 formation at the expense of OH coverage, and H_2O adsorption at high relative humidity/low temperature, with greater θ_{CO3} in **Figure A-3** resulting from higher residual carbon in the XPS chamber from previous measurements. In the subsequent heating (solid points), H_2O adsorption/desorption appeared to be largely reversible. Similarly, the trend in θ_{CO3} qualitatively suggests that its adsorption/desorption is reversible, but this cannot be quantitatively evaluated because measurements were performed out of equilibrium with the intent of minimizing CO_3 coverage. In contrast, OH adsorption/desorption was not reversible, and θ_{OH} was found to increase upon heating. The coverage was much greater returning to 300 °C than that initially obtained introducing H_2O into the chamber with the O_2-cleaned surface at 300 °C, which is in agreement with strongly-bound OH sites observed even in oxidative environments.

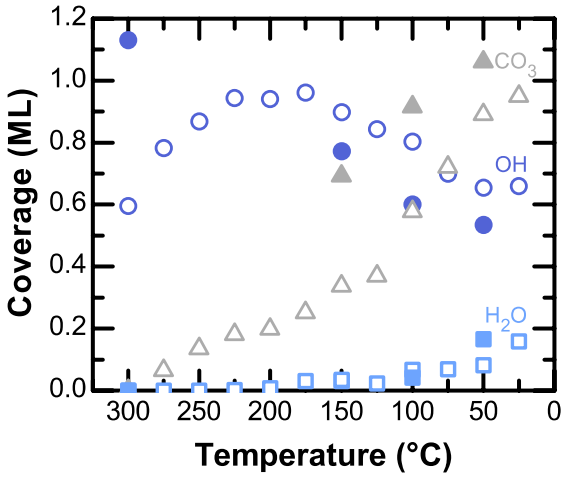

Figure A-3. *Coverage of surface species on LCO as a function of temperature in 100 mTorr H_2O: adsorbed H_2O (□, light blue), CO_3 (Δ, gray), and OH (O, medium blue). Open circles indicate coverage from measurements performed as a function of decreasing temperature, and filled circles indicate measurements testing for reversibility by increasing the temperature from 25 °C to 300 °C.*

Figure A-4 presents depth profiling of $LaFeO_3$ in humid conditions, illustrating change in the low binding energy feature(s) not observed for other perovskite chemistries. The gas phase H_2O (light blue), H_2O_{ads} (light orange), CO_3 (gray), surface-O (medium blue), and OH (dark orange) are all more pronounced for shallower information depths; thus, they are located spatially above above the species fit by two bulk-Ox peaks (dark blue dashed and solid). Fitting the $LaFeO_3$ spectra with only one bulk-Ox peak, as done for other La*M*O_3 samples, would result in a worse fit and require the FWHM to increase notably with relative humidity. Thus, two bulk-Ox peaks were used, and their intensity summed in coverage calculations.

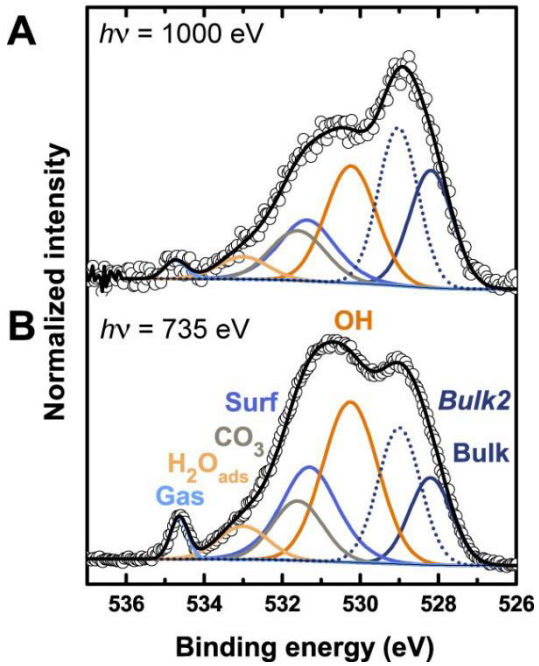

Figure A-4. *O 1s spectra of $LaFeO_3$ in p(H_2O) = 0.1 Torr at 25 °C, with intensity normalized to the envelope maximum, and curves offset for clarity. (A) An incident energy of 1000 eV has a deeper information depth compared to (B) an incident energy of 735 eV.*

A.2. Details of surface adsorbate coverage calculations

Our model treats each species as a continuum slab in a multilayer configuration, characterized by its oxygen atomic density (N), photoionization cross section (σ), thickness (t), coverage (θ), and inelastic mean free path (λ'). OH and CO_3 were considered to co-adsorb on the film surface, with component thickness fixed at t_{OH} = 3.0 Å based on $Co(OH)_2$[5] and t_{CO3} = 4.5 Å based on $La_2(CO_3)_3 \cdot 8H_2O$[6] (**Table A-1**). Although the combined coverage was allowed to vary, the computed values remained less than one monolayer. The XPS intensities (I) of all components in the model were expressed as below, where λ is defined as the mean free path component along the surface normal, accounting for the emission angle of photoelectrons from the surface normal (42° in the current setup), i.e. $\lambda = \lambda' \cos(42°)$. N was determined from the density and oxygen stoichiometry of reference compounds (**Table A-1**), and σ assumed to vary little in the < 5 eV binding energy difference from bulk oxygen to adsorbed water.

$$I_{H_2O} \sim N_{H_2O}\, \sigma_{H_2O}\, \lambda_{H_2O} \left[1 - exp\left(-\frac{t_{H_2O}}{\lambda_{H_2O}}\right)\right] \qquad \textit{Equation A-1}$$

$$I_{OH} \sim N_{OH}\, \sigma_{OH}\, \lambda_{OH}\, \theta_{OH}\, exp\left(-\frac{t_{H_2O}}{\lambda_{H_2O}}\right)\left[1 - exp\left(-\frac{t_{OH}}{\lambda_{OH}}\right)\right] \qquad \textit{Equation A-2}$$

$$I_{CO_3} \sim N_{CO_3}\,\sigma_{CO_3}\,\lambda_{CO_3}\,\theta_{CO_3}\,exp\left(-\frac{t_{H_2O}}{\lambda_{H_2O}}\right)\left[1-exp\left(-\frac{t_{CO_3}}{\lambda_{CO_3}}\right)\right] \qquad \textit{Equation A-3}$$

$$I_{surf} \sim N_{surf}\,\sigma_{surf}\,\lambda_{surf}\;exp\left(-\frac{t_{H_2O}}{\lambda_{H_2O}}\right)\left[\theta_{OH}\,exp\left(-\frac{t_{OH}}{\lambda_{OH}}\right)+\theta_{CO_3}\,exp\left(-\frac{t_{CO_3}}{\lambda_{CO_3}}\right)+\left(1-\theta_{OH}-\theta_{CO_3}\right)\right]\left[1-exp\left(-\frac{t_{surf}}{\lambda_{surf}}\right)\right] \qquad \textit{Equation A-4}$$

$$I_{ox} \sim N_{ox}\,\sigma_{ox}\,\lambda_{ox}\;exp\left(-\frac{t_{H_2O}}{\lambda_{H_2O}}\right)\left[\theta_{OH}\,exp\left(-\frac{t_{OH}}{\lambda_{OH}}\right)+\theta_{CO_3}\,exp\left(-\frac{t_{CO_3}}{\lambda_{CO_3}}\right)+\left(1-\theta_{OH}-\theta_{CO_3}\right)\right]exp\left(-\frac{t_{surf}}{\lambda_{surf}}\right) \qquad \textit{Equation A-5}$$

By taking the intensity ratios, the variables t_{surf}, θ_{OH}, θ_{CO3} and t_{H2O} are uniquely determined:

$$t_{surf} = \lambda_{surf}\,ln\left(1+R_{ox}^{surf}\right) \qquad \textit{Equation A-6}$$

where $R_j^i \equiv \frac{I_i}{I_j}\left(\frac{N_j\sigma_j\lambda_j}{N_i\sigma_i\lambda_i}\right)$

$$\begin{bmatrix} \frac{exp\left(\frac{t_{surf}}{\lambda_{surf}}\right)}{R_{ox}^{OH}}+a_{OH}^{*}-a_{OH}^{OH} & a_{OH}^{*}-a_{OH}^{CO_3} \\ a_{CO_3}^{*}-a_{CO_3}^{OH} & \frac{exp\left(\frac{t_{surf}}{\lambda_{surf}}\right)}{R_{ox}^{CO_3}}+a_{CO_3}^{*}-a_{CO_3}^{CO_3} \end{bmatrix}\begin{bmatrix}\theta_{OH}\\ \theta_{CO_3}\end{bmatrix}=\begin{bmatrix}a_{OH}^{*}\\ a_{CO_3}^{*}\end{bmatrix} \qquad \textit{Equation A-7}$$

where $a_j^* \equiv \frac{1}{1-\exp\left(-\frac{t_j}{\lambda_j}\right)}$; $a_j^i \equiv a_j^*\exp\left(-\frac{t_i}{\lambda_i}\right)$

$$t_{H_2O} = \lambda_{H_2O}\,ln\left(\frac{1+b_{H_2O}}{b_{H_2O}}\right) \qquad \textit{Equation A-8}$$

where $b_{H_2O} \equiv \left\{R_{ox}^{H_2O}\left[\theta_{OH}\exp\left(-\frac{t_{OH}}{\lambda_{OH}}\right)+\theta_{CO_3}\exp\left(-\frac{t_{CO_3}}{\lambda_{CO_3}}\right)+\left(1-\theta_{OH}-\theta_{CO_3}\right)\right]\exp\left(-\frac{t_{surf}}{\lambda_{surf}}\right)\right\}^{-1}$

Finally, the thickness of the water layer (t_{H2O}) was used to estimate the water surface coverage θ_{H2O} by normalizing to the size of the water molecule ($\theta_{H_2O} = \frac{t_{H_2O}}{3.1\ \text{Å}}$)[7]. It is noted that the fitted thickness of the surface oxygen layer is on the order of a few atomic layers, which is consistent with the length-scale of a reconstructed surface, and it did not change significantly as a function of RH. **Table A-1** provides the constants used in the electron attenuation model.

Table A-1. *Constants used in the multilayer electron attenuation model. The inelastic mean free paths were calculated using the Gries inelastic scattering model and predictive equation with the density of reference compounds.[8] Inelastic mean free paths (λ) and oxygen atomic densities (N) for the OH and CO_3 layers were taken as the average of the transition metal and lanthanide reference compounds in order to account for the ambiguity of the surface termination.*

	ρ [g cm^{-3}]	λ [Å]	N [cm^{-3}]	λ_{ave} [Å]	N_{ave} [cm^{-3}]
H_2O	0.997 [9]	14.39	3.336×10^{22}		
$La(OH)_3$	4.445 [10]	8.63	4.226×10^{22}		
$La_2(CO_3)_3$	2.6 [5]	14.13	3.078×10^{22}		
$Cr(OH)_3$	3.11	7.77	5.454×10^{22}	8.2	4.840×10^{22}
$Mn(CO_3)$*	3.7	7.5	5.815×10^{22}	10.815	4.447×10^{22}
$LaCrO_3$	6.77 [11]	6.48	5.120×10^{22}		
$Mn(OH)_2$	3.3 [5]	8.19	4.468×10^{22}	8.41	4.347×10^{22}
$Mn(CO_3)$	3.7	7.5	5.815×10^{22}	10.815	4.447×10^{22}
$LaMnO_3$	6.57 [12]	6.73	4.908×10^{22}		
$Fe(OH)_2$	3.4 [5]	7.97	4.557×10^{22}	8.3	4.392×10^{22}
$Fe(CO_3)$	3.944 [13]	7.04	6.150×10^{22}	10.585	4.614×10^{22}
$LaFeO_3$	6.63 [14]	6.66	4.934×10^{22}		
$Co(OH)_2$	3.6 [5]	7.72	4.662×10^{22}	8.175	4.444×10^{22}
$Co(CO_3)$	4.13 [5]	6.86	6.270×10^{22}	10.495	4.674×10^{22}
$LaCoO_3$	7.29 [15]	6.11	5.358×10^{22}		
$Ni(OH)_2$	4.1 [16]	6.71	5.326×10^{22}	6.71	4.776×10^{22}
$Ni(CO_3)$	4.39	6.41	6.681×10^{22}	10.27	4.880×10^{22}
$LaNiO_3$	7.22 [17]	6.13	5.311×10^{22}		

*No report was found for the density for Cr carbonate; $Mn(CO_3)$ was used as a substitute.

A.3. Density functional theory calculations

Stability of the (dissociatively adsorbed) H_2O, *H, and *OH at the experimental condition was estimated using the chemical potentials of H_2O, H_2 and O_2 (*i.e.*, $\mu_{H_2O(g)}$, $\mu_{H_2(g)}$, and $\mu_{O_2(g)}$) set by the following equations[18,19]:

$$\mu_{H_2O(g)}\left(=\mu_{H_2O(l)}\right)=\mu^0_{H_2O(g)}+k_BT\cdot ln\left(\frac{p(H_2O)}{p^*(H_2O)}\right) \quad \text{Equation A-9}$$

$$\mu_{H_2(g)} = \mu^0_{H_2(g)} - 2eU_{eff} + 2k_B T \cdot ln(a_{H^+})$$ Equation A-10

$$\mu_{O_2(g)} = \mu^0_{O_2(g)} + k_B T \cdot ln\left(\frac{p(O_2)}{p^0(O_2)}\right)$$ Equation A-11

where $\mu^0_{H_2O(g)}$, $\mu^0_{H_2(g)}$, and $\mu^0_{O_2(g)}$ are the chemical potentials of H_2O, H_2 and O_2 at the standard condition and can be defined as the following $\mu^0_{H_2O(g)} = E^{DFT}_{H_2O(g)} + ZPE_{H_2O(g)} - TS^0_{H_2O(g)}(0.035\text{ bar})$, $\mu^0_{H_2(g)} = E^{DFT}_{H_2(g)} + ZPE_{H_2(g)} - TS^0_{H_2(g)}$, and $\mu^0_{O_2(g)} = 4.92\ eV + 2\mu^0_{H_2O(l)} - 2\mu^0_{H_2(g)}$, with $E^{DFT}_{H_2O(g)}$ and $E^{DFT}_{H_2(g)}$ being the computed DFT energies of H_2O and H_2 gas molecules, $ZPE_{H_2O(g)}$, $ZPE_{H_2(g)}$, and $ZPE_{O_2(g)}$ being the zero point energies, and $S^0_{H_2O(g)}(0.035\text{ bar})$ and $S^0_{H_2(g)}$ being the entropy of the gas phase H_2O at pressure of 0.035 bar and the standard entropy of H_2. The zero point energy and standard entropy terms were taken from Table 3 of Ref. [18]. T is temperature, $p^*(H_2O)$ is the pressure of the gas phase H_2O in equilibrium with liquid water at T=300 K (*i.e.*, 0.035 bar), $p^0(O_2)$ is 1 atm or 760 Torr oxygen partial pressure, eU_{eff} is the corresponding shift in electron energy or the effective applied potential at the experimental condition, and a_{H^+} is the proton activity.

The adsorption free energies, G_{ad}, were then computed with respect to the H_2O, H_2, and O_2 chemical potential references at the effective applied potential of 1.2 V vs. the standard hydrogen electrode (SHE) from Equation A-9, A-10, and A-11, respectively according to the formula: $G_{ad} = (E^{DFT}(n*X/LaMO_3) - E^{DFT}(LaMO_3) - n(\mu(X) - ZPE(*X) + TS(*X))/n$, where $E(LaMO_3)$ and $E(n*X/LaMO_3)$, are the DFT total energies of the bare $LaMO_3$ surface and of the combined system (with adsorbed *X), respectively, and n is the number of adsorbed species on (2×2) (001) surfaces, $\mu(X)$ is the chemical potential reference of H, OH, and H_2O at 1.2 V vs. SHE ($\mu(H) = {}^1/_2\,\mu_{H_2(g)}$, $\mu(OH) = \mu_{H_2O(g)} - {}^1/_2\,\mu_{H_2(g)}$, and $\mu(O) = {}^1/_2\,\mu_{O_2(g)}$), and $ZPE(*X)$ and $TS(*X)$ are the zero point energy and the entropic term of the adsorbed species *X (*X=*H, *OH), respectively, as also provided in Table 3 of Ref.[18].

We have thus computed the surface energies of the (001) LaO and MO_2-terminated surfaces based on the following equations[20,21]:

$$E^{LaO}_{surf} = E^{LaO\text{-}slab}_{DFT} - N^{LaO\text{-}slab}_{O} \cdot \mu_O - N^{LaO\text{-}slab}_{La} \cdot \mu_{La} - N^{LaO\text{-}slab}_{M} \cdot \mu_M$$ Equation A-12

$$E^{MO_2}_{surf} = E^{MO_2\text{-}slab}_{DFT} - N^{MO_2\text{-}slab}_{O} \cdot \mu_O - N^{MO_2\text{-}slab}_{La} \cdot \mu_{La} - N^{MO_2\text{-}slab}_{M} \cdot \mu_M$$ Equation A-13

where E^{LaO}_{surf} ($E^{MO_2}_{surf}$) is the surface energy of the (001) LaO (MO_2) –termination, $E^{LaO\text{-}slab}_{DFT}$($E^{MO_2-slab}_{DFT}$), is the calculated DFT total energy of the (001) 7-layer LaO slab (7-layer MO_2 slab), $N^{LaO\text{-}slab}_{O}$, $N^{LaO\text{-}slab}_{La}$, and $N^{LaO\text{-}slab}_{M}$ ($N^{MO_2\text{-}slab}_{O}$, $N^{MO_2\text{-}slab}_{La}$, and $N^{MO_2\text{-}slab}_{M}$) correspond to the number of the O, La, and M atoms in the (001) 7-layer LaO (MO_2) slab, and μ_O, μ_{La}, and μ_M

are the chemical potential of O, La, *M* in the bulk La*M*O_3 (*i.e.* $3\mu_O+\mu_{La}+\mu_M = E^{DFT}$ (La*M*O_3), where E^{DFT} (La*M*O_3) is the DFT total energy of La*M*O_3 normalized as per formula unit, and μ_O $=1/2\ \mu_{O_2(g)}$ at equilibrium with the O_2 gas phase).

We have compared the (001) LaO and MO_2 surface energy values obtained in both the La-rich (system in equilibrium with La_2O_3 at the 1.20 V vs. SHE) and the *M*-rich conditions (system in equilibrium with MO_x, where the chemical potentials of Cr, Mn, Fe, Co, and Ni are obtained based on the calculated DFT total energies of the most stable transition metal binary oxides among the investigated compounds at various oxidation states under the μ_O condition i.e. CrO_2 among Cr_2O_3, CrO_2, and CrO_3; Mn_2O_3 among MnO, Mn_3O_4, Mn_2O_3, and MnO_2; Fe_2O_3 among FeO, Fe_3O_4, Fe_2O_3, and FeO_2; Co_3O_4 among CoO, Co_3O_4, and Co_2O_3; and NiO, respectively). Further increasing the chemical potential of La above the La_2O_3 limit will lead to precipitation of La_2O_3, and increasing the chemical potential of *M* above the MO_x limit will lead to precipitation of MO_x. Thus perovskites are not stable outside these metal chemical potential conditions. Refinement of metal chemical potential limits for the perovskite stability region can be further performed although the stability region will be mainly narrowed within the defined metal chemical potential limits in this work if other more stable phases exist.

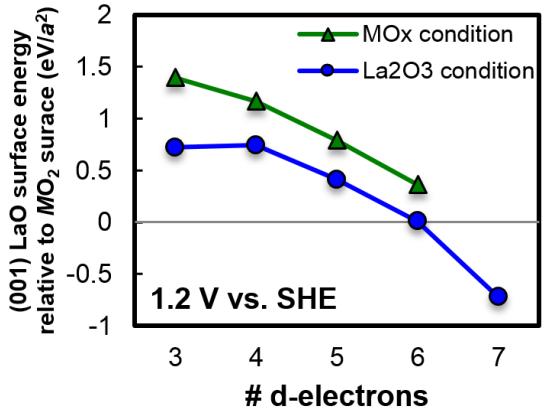

Figure A-5. *Surface energy (per unit cell area) of the LaO-termination relative to the MO_2-termination at the MO_x condition (green triangles) and at the La_2O_3 condition (blue circles). a is the lattice constant of the pseudocubic perovskite $LaMO_3$. The surface energy of the (001) LaO termination of $LaNiO_3$ at the MO_x (NiO) condition is found to be negative, indicating that the bulk is unstable relative to the LaO surface at such condition.*

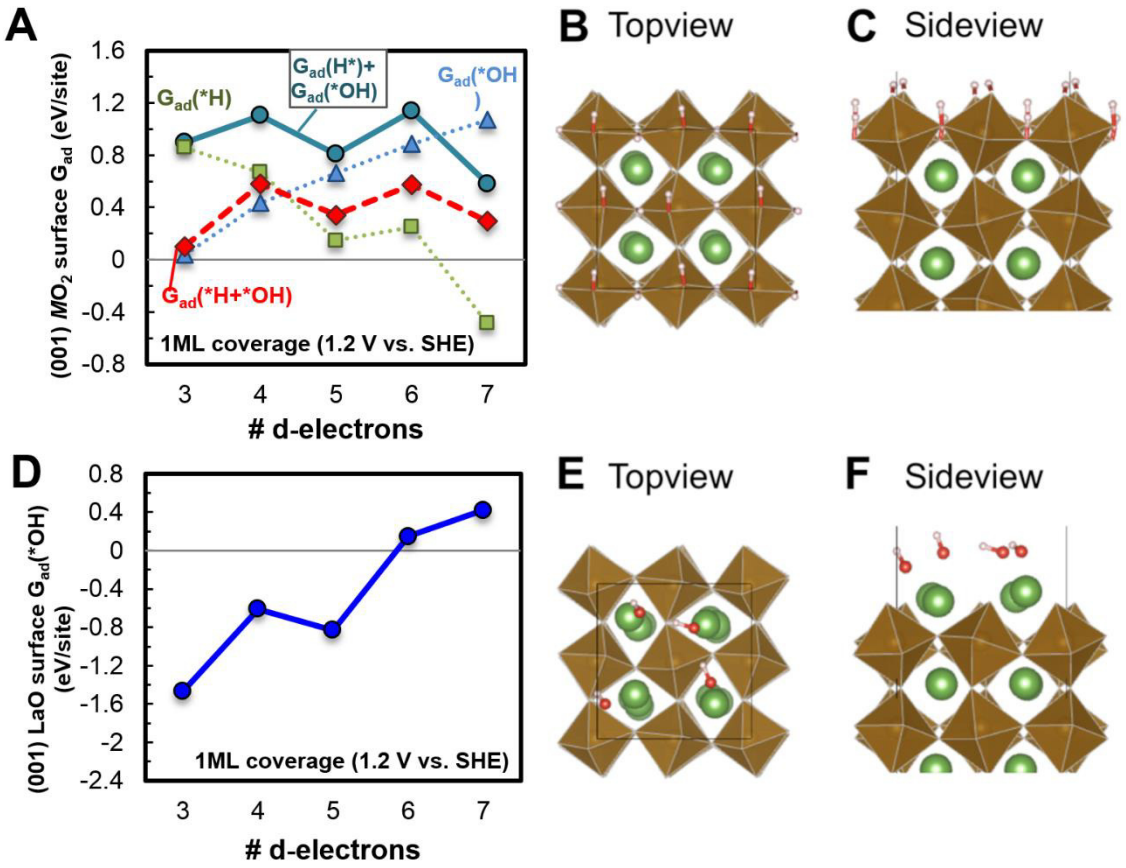

Figure A-6. *(A) Computed adsorption properties for *H_2O (dissociative adsorption) – red diamond, *OH – light blue triangle, and *H – green square at full coverage vs. the number of M d-electrons for $LaMO_3$ (001) MO_2 surfaces at 1.2 V vs. SHE (the effective applied potential vs. SHE that corresponds to the pressures relevant to NAP-XPS). The sum of *H and *OH adsorption free energies, which is also included in the plot as represented by the teal circles, shows a similar trend as the dissociative *H_2O adsorption free energies (i.e., G_{ad}(*H+*OH)) vs. the number of M d-electrons for $LaMO_3$. (B) Optimized geometries on $LaFeO_3$ for dissociated water on the MO_2-terminated surface, viewed from the top and (C) side. Pink sphere represents H, red sphere represents adsorbed O, brown polyhedral represents Fe-O local environment, green sphere represents La; OH bonds are shown with the pink-red rods. (D) Computed adsorption properties for *OH on the LaO-terminated surface. (E) Optimized geometries on $LaFeO_3$ for *OH on the LaO terminated surface, viewed from the top and (F) side, with colors as in (B,C).*

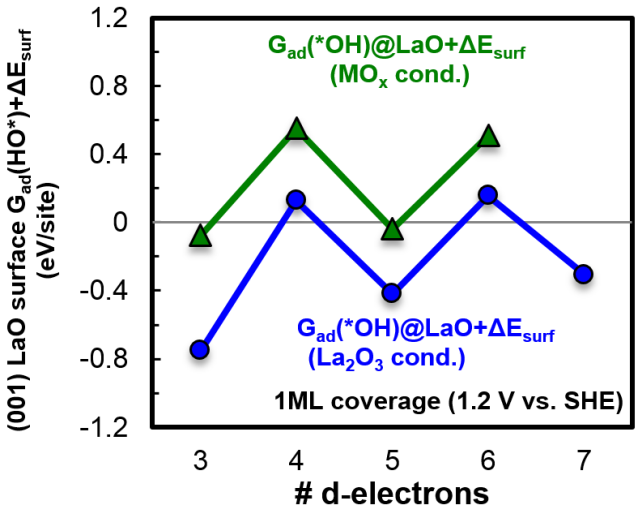

Figure A-7. *$LaMO_3$ (001) LaO G_{ad}(*OH)+ ΔE_{surf} (LaO relative to the MO_2, Figure A-5). The y=0 corresponds to the ideal, bare (001) MO_2 surface energy per unit cell area. The $LaNiO_3$ (001) LaO surface energy at the condition of NiO limit is found to be negative (i.e. $LaNiO_3$ bulk is not stable and will decompose to form the (001) LaO surface), and therefore the (001) LaO surface energy at the condition of NiO limit for $LaNiO_3$ is not included in the plot (green triangle points).*

References

1 Liang, J.-J. & Weng, H.-S. XPS Analysis for the SO_2 Poisoning of Mn- and Co-series Perovskite Catalysts Used in Toluene Oxidation. *J. Environ. Eng. Manage.* **17**, (2007).

2 Yeh, J. J. (Gordon and Breach Science Publishers, Langhorne, PE (USA), 1993).

3 Yeh, J. J. & Lindau, I. Atomic Data and Nuclear Data Tables. **32**, 1-155, (1985).

4 Deng, X., Herranz, T., Weis, C., Bluhm, H. & Salmeron, M. Adsorption of Water on Cu_2O and Al_2O_3 Thin Films. *J. Phys. Chem. C* **112**, 9668-9672, (2008).

5 Perry, D. L. *Handbook of Inorganic Compounds*. 2 edn, (CRC Press, 2011).

6 Shinn, D. B. & Eick, H. A. The Crystal Structure of Lanthanum Carbonate Octahydrate. *Inorg. Chem.* **7**, 1340-1342, (1968).

7 Tîmneanu, N., Caleman, C., Hajdu, J. & van der Spoel, D. Auger Electron Cascades in Water and Ice. *Chem. Phys.* **299**, 277-283, (2004).

8 Gries, W. H. A Universal Predictive Equation for the Inelastic Mean Free Pathlengths of X-ray Photoelectrons and Auger Electrons. *Surf. Interface Anal.* **24**, 38-50, (1996).

9 Tîmneanu, N., Caleman, C., Hajdu, J. & van der Spoel, D. Auger electron cascades in water and ice. *Chem. Phys.* **299**, 277-283, (2004).

10 Shannon, R. D. Dielectric polarizabilities of ions in oxides and fluorides. *J. Appl. Phys.* **73**, 348-366, (1993).

11 Furusaki, A., Konno, H. & Furuichi, R. Pyrolytic process of La(III) Cr(VI) precursor for the perovskite type lanthanum chromium oxide. *Thermochim. Acta* **253**, 253-264, (1995).

12 Van Roosmalen, J. A. M. & Cordfunke, E. H. P. The Defect Chemistry of $LaMnO_{3\pm\delta}$: 3. The Density of (La,*A*)$MnO_{3+\delta}$ (*A* = Ca, Sr, Ba). *J. Solid State Chem.* **110**, 106-108, (1994).

13 Robie, R. A., Bethke, P. M. & Beardsley, K. M. *Selected X-ray crystallographic data, molar volumes, and densities of minerals and related substances*. (U.S. Govt. Print. Off. , 1967).

14 Robbins, M., Pierce, R. D. & Wolfe, R. Magnetic properties of fluoride substituted orthoferrites. *J. Phys. Chem. Solids* **32**, 1789-1796, (1971).

15 Pathak, S., Kuebler, J., Payzant, A. & Orlovskaya, N. Mechanical behavior and electrical conductivity of $La_{1-x}Ca_xCoO_3$ (x = 0, 0.2, 0.4, 0.55) perovskites. *J. Power Sources* **195**, 3612-3620, (2010).

16 Ke, K., Zhang, X. Y. & Du, Y. L. A New Electrochemical Sensor for Monitoring Mobile Atomic Hydrogen in Metals. *Corrosion* **57**, 353-359, (2001).

17 Galal, A., Atta, N. F. & Ali, S. M. Optimization of the synthesis conditions for $LaNiO_3$ catalyst by microwave assisted citrate method for hydrogen production. *Applied Catalysis A: General* **409–410**, 202-208, (2011).

18 Nørskov, J. K. *et al.* Origin of the Overpotential for Oxygen Reduction at a Fuel-Cell Cathode. *J. Phys. Chem. B* **108**, 17886-17892, (2004).

19 Man, I. C. *et al.* Universality in Oxygen Evolution Electrocatalysis on Oxide Surfaces. *ChemCatChem* **3**, 1159-1165, (2011).

20 Reuter, K. & Scheffler, M. Composition, structure, and stability of RuO_2 (110) as a function of oxygen pressure. *Phys. Rev. B* **65**, 035406, (2001).

21 Johnston, K., Castell, M. R., Paxton, A. T. & Finnis, M. W. $SrTiO_3$ (001) (2x1) reconstructions: First-principles calculations of surface energy and atomic structure compared with scanning tunneling microscopy images. *Phys. Rev. B* **70**, 085415, (2004).

B. Additional information for Chapter 4

B.1. Additional figures and tables regarding fabrication and AP-XPS

XRD of the LSMO films (**Figure B-1**) indicate epitaxy with the (001) orientation. AFM illustrates the films are atomically smooth, exhibiting terraces separated by steps of unit cell height (**Figure B-1, B-2**).

Figure B-3 illustrates the lack of beam-induced effects over the course of measurement. The survey spectra (**Figure B-4**) after cleaning in the AP-XPS chamber indicate that for 33% Sr LSMO, a small amount of Au foil used for calibration was within the collection window. Given the large cross section for the Au 4*f* (1.6 at 735 eV compared to 0.4 for La 4*d*) and small intensity (4x smaller than La), we do not expect any notable effect on the valence band. For 10% Sr LMSO, a small amount of Al is present, however, none is notable in the O 1*s* spectra (532.8-536.6 eV[1]) and we therefore do not expect any influence on the discussed trends.

The region ratios (Sr, **Figure B-5A**, Mn, **Figure B-5B**) remain roughly constant for each condition. In comparing the Mn ratio for different chemistries, note the cross section of the La 4*d* is greater than that of Sr 3*d* at this incident photon energy, and that changes in the bulk composition can also impact the IMFP.

Changes in the valence band calibrated to the initial Fermi level, expected to remain calibrated to the Fermi level under each condition baring a change in the work function of the analyzer, are shown as a function of Sr content in **Figure B-6**. **Figure B-7** plots the locations of the principle component (see **Tables B-1** to **B-3** for fitting parameters) of the cation core levels versus the valence band edge fit with a step down function, calibrated to the Fermi level. The La and Sr core levels shift with the valence band, in contrast to the Mn core levels, which remain relatively unchanged. This indicates a chemical process occurring as a result of the hydroxylation process that raises the Fermi level.

Chemical changes in the La are corroborated by differences in the La-O ionicity, quantified as the intensity of main peaks in La 4*d* relative to the total (main+satellite) intensity,[2] as a function of information depth and relative humidity (**Figure B-8**). LSMO chemistries with the greatest tendency to hydroxylate (70% Sr, 0% Sr) show the largest increase in iconicity with RH. Comparing chemistries using a long information depth ($\lambda\nu$ = 735 eV), ionicity decreases with increased Sr content as expected from trends in metal-oxygen covalency.[3] At the surface ($\lambda\nu$ = 350 eV), the ionicity increases due to the presence of adsorbates like OH.

Fitting parameters are tabulated for the La 4*d* (**Table B-1**), Sr 3*d* (**Table B-2**), and Mn 3*p* (**Table B-3**).

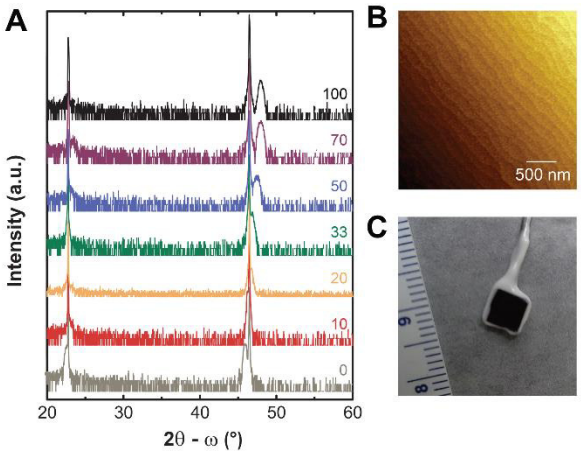

Figure B-1. *Characterization of LSMO films, with the number representing the Sr percentage. (A) X-ray diffraction showing normal 2θ-ω scan of the* $(001)_{pc}$ *and* $(002)_{pc}$ *reflections. (B) Exemplary atomic force microscopy of* $La_{0.67}Sr_{0.33}MnO_3$ *films, with a vertical contrast scale of 7.8 nm. (C) Photograph of a film sample prepared for electrochemical measurements.*

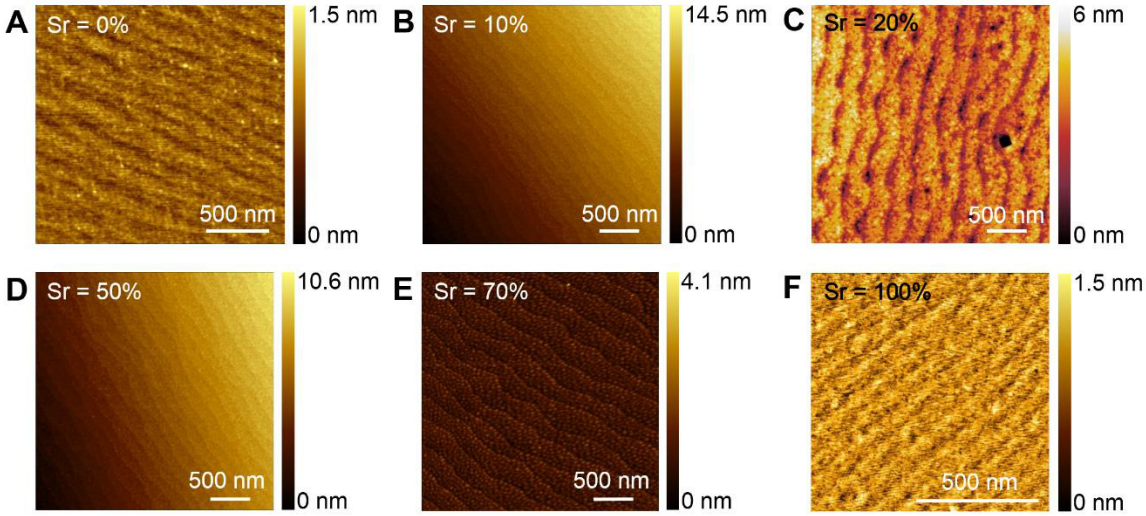

Figure B-2. *Atomic force microscopy (AFM) of* $La_{(1-x)}Sr_xMnO_3$ *films of noted % Sr in the A-site. Sr = (A) 0%, (B) 10%, (C) 20%, (D) 50%, (E) 70%, and (F) 100%. See Figure B-1 for Sr = 33%. All surfaces showed comparably low root mean squared roughness.*

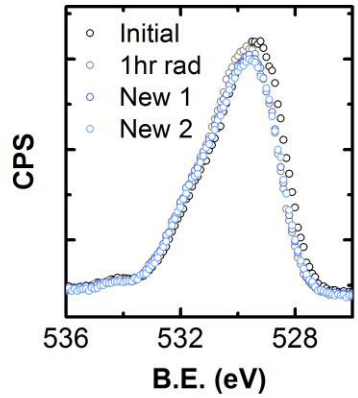

Figure B-3. *The O 1s spectra are comparable for a sample measured initially and after 1 hour of radiation in 100 mTorr of H_2O, and also comparable at two fresh spots that were previously unexposed to radiation (New 1, New 2), indicating no beam-induced effects during the acquisition time.*

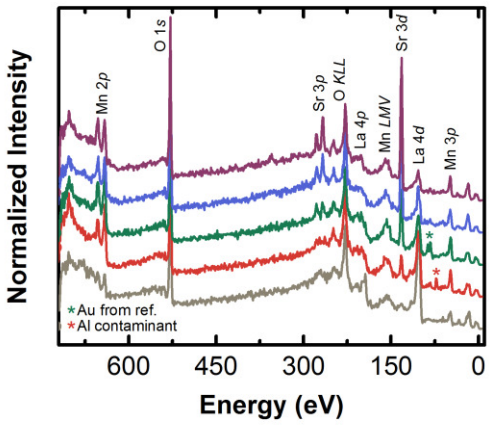

Figure B-4. *Survey spectra after cleaning for 0% Sr (LMO, gray), 10% (red), 33% (green), 50% (blue), and 70% Sr (purple) LSMO films.*

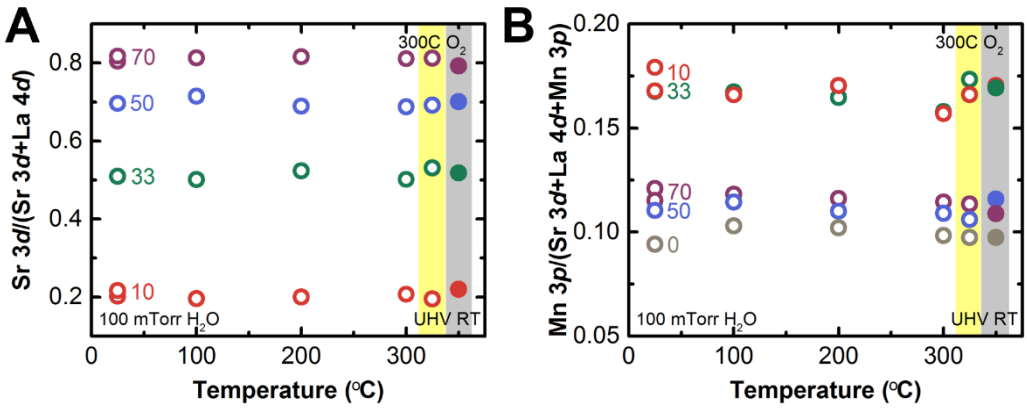

Figure B-5. *Cation ratio as a function of temperature in 100 mTorr H_2O (open circles, white background), 300 °C in 100 mTorr O_2 (open circles, yellow background), and in UHV at room temperature (RT) prior to cleaning (solid circles, gray background). Sr contents are distinguished by color, and all measurements performed with an incident energy of 735 eV. (A) Sr 3d/(Sr 3d + La 4d) and (B) Mn 3p/(Mn 3p + Sr 3d + La 4d) both roughly constant across conditions.*

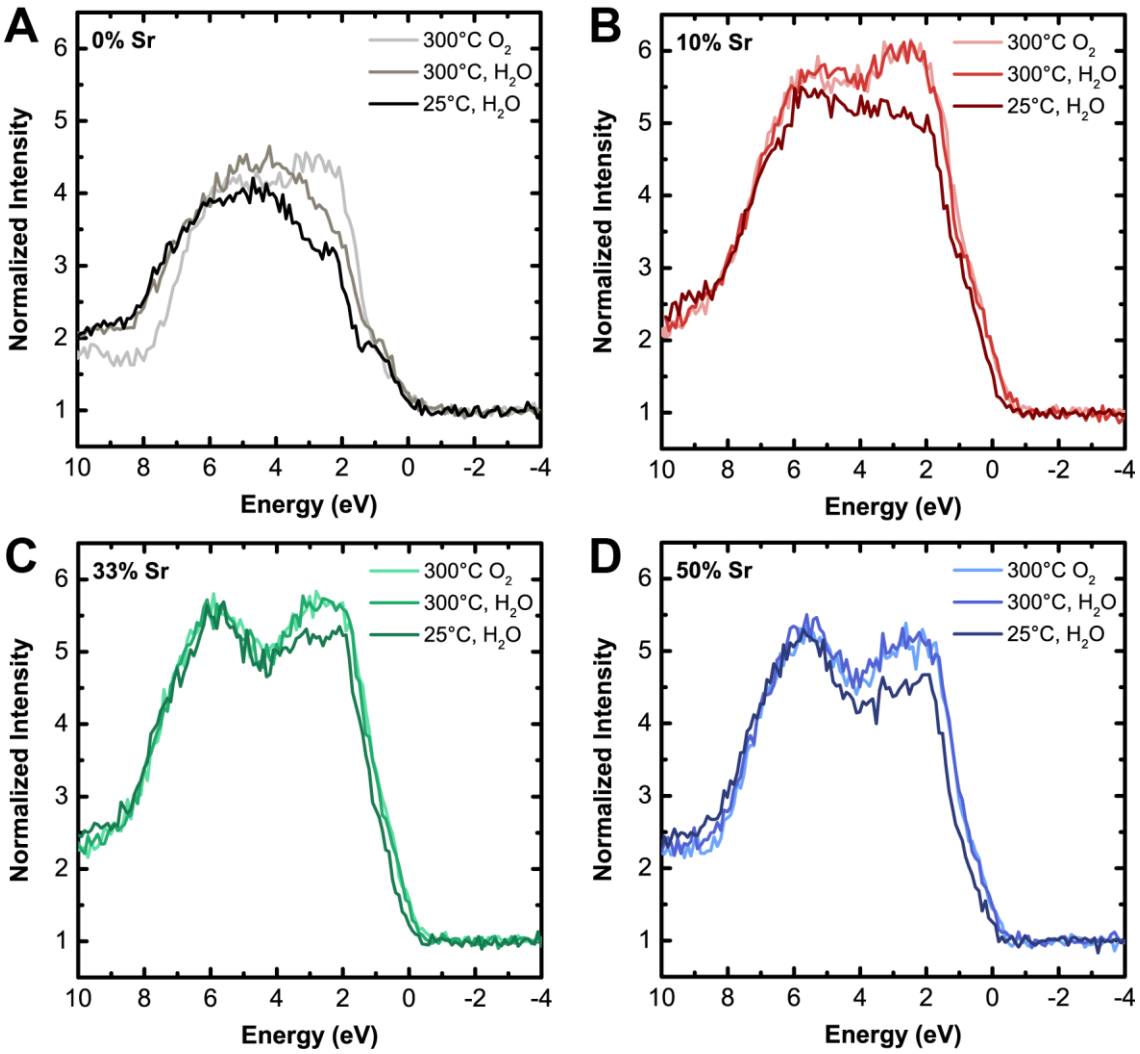

Figure B-6. *Valence band calibrated to the initial Fermi level. The color saturation increases with RH, and the valence band shifts to higher BE, indicating an increase in the Fermi level. Films are denoted by percent Sr (A) 0%, (B) 10%, (C) 33%, (D) 50%, with 70% shown in Figure 4-6.*

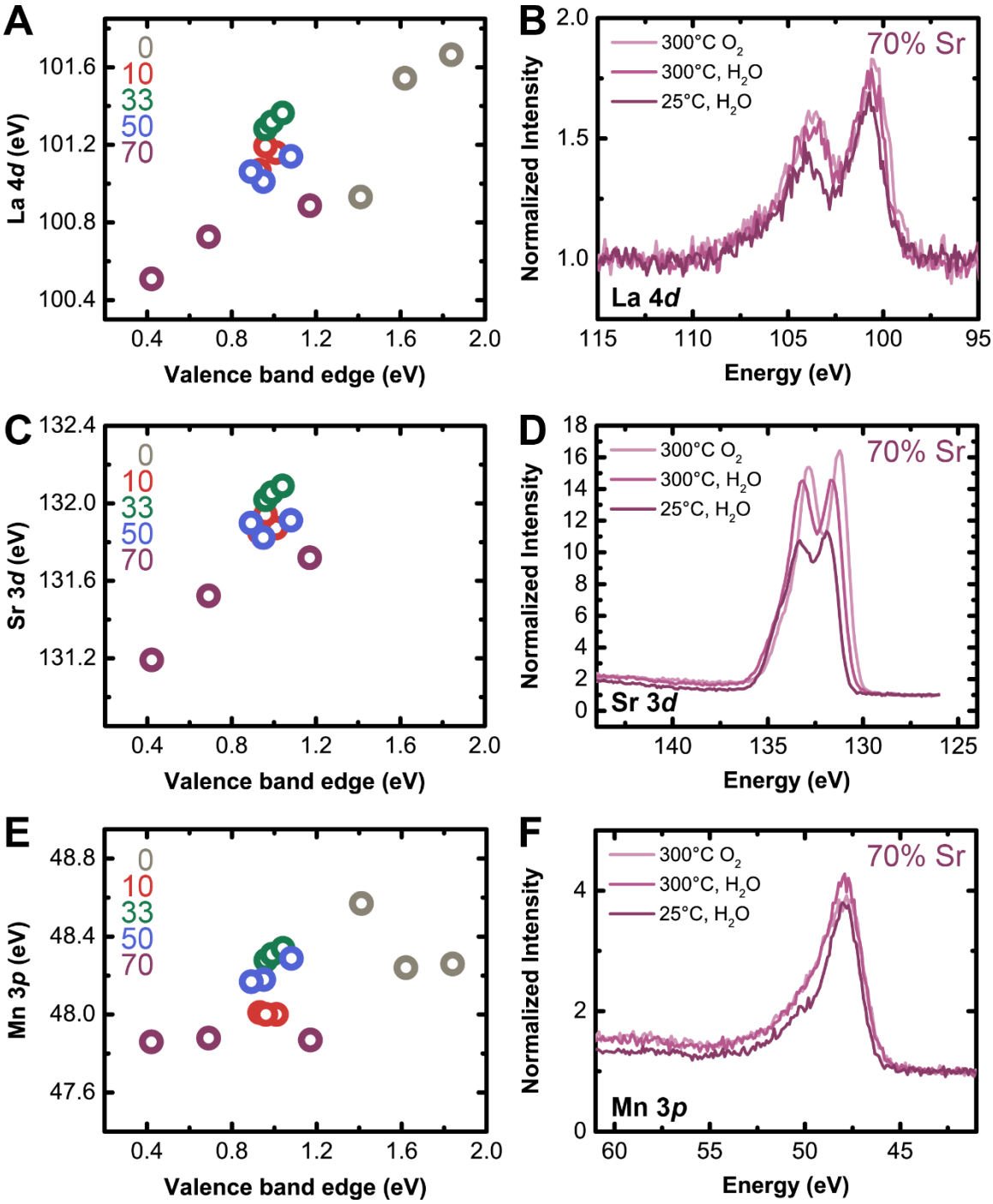

Figure B-7. *Locations of the principle component (see Tables B-1 to B-3 for fitting parameters) of the (A) La 4d, (C) Sr 3d, (E) Mn 3p core levels versus the valence band edge fit with a step down function, calibrated to the Fermi level. Individual points correspond to different RH, shown for the 70% Sr case for the (B) La 4d, (D) Sr 3d, and (F) Mn 3p.*

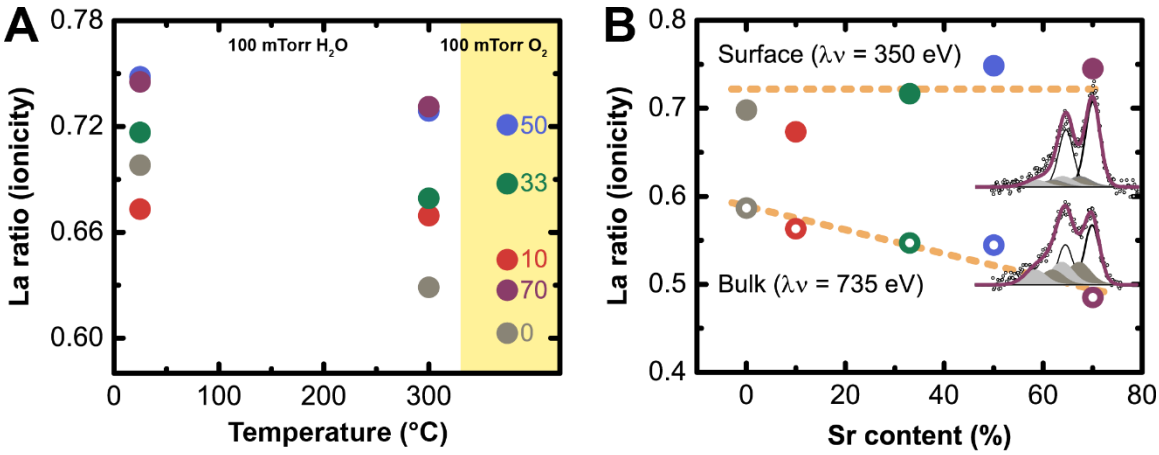

Figure B-8. *(A) La-O ionicity, quantified as the intensity of main peaks in La 4d relative to the total (main+satellite) intensity[2] probed at an incident photon energy of 350 eV. (B) La-O ionicity at 25 °C in 100 mTorr H_2O probed at different incident photon energies. In the bulk (λν = 735 eV), ionicity decreases with increased Sr content as expected from trends in metal-oxygen covalency.[3] At the surface (λν = 350 eV), the ionicity increases due to the presence of adsorbates like OH. Fitting parameters are shown in Table B-1.*

Table B-1. *Fitting constraints for La 4d[2] from which the principle component (greatest intensity at lowest binding energy, $Main_{5/2}$) was used in quantifying shifts in Figure B-6.*

La 4*d*	**$Main_{5/2}$**	**$Main_{3/2}$**	**Anti-$bonding_{5/2}$**	**Anti-$bonding_{3/2}$**	**$Bonding_{5/2}$**	**$Bonding_{3/2}$**
% Lorentzian	30	30	30	30	30	30
FWHM (eV)	(free)	$Main_{5/2}$	<3	Anti-$bonding_{5/2}$	Anti-$bonding_{5/2}$	Anti-$bonding_{5/2}$
Intensity	(free)	2/3*$Main_{5/2}$	(free)	2/3*Anti-$bonding_{5/2}$	Anti-$bonding_{5/2}$	2/3*Anti-$bonding_{5/2}$
BE (eV)	(free)	$Main_{5/2}$+3.1	$Main_{5/2}$+1.5	$Main_{5/2}$+4.6	$Main_{5/2}$+3.5	$Main_{5/2}$+6.6

Table B-2. *Fitting constraints for Sr 3d[4] from which the principle component (greatest intensity at lowest binding energy, $Bulk_{5/2}$) was used in quantifying shifts in Figure B-6.*

Sr 3*d*	**$Bulk_{5/2}$**	**$Bulk_{3/2}$**	**$Surface_{5/2}$**	**$Surface_{3/2}$**
% Lorentzian	30	30	30	30
FWHM (eV)	1-2	$Bulk_{5/2}$	<2	$Surface_{5/2}$
Intensity	(free)	$Bulk_{5/2}$*2/3	(free)	$Surface_{5/2}$*2/3
BE (eV)	(free)	$Bulk_{5/2}$+1.8	(free)	$Surface_{5/2}$+1.8

Table B-3. *Fitting constraints for Mn $3p^5$ from which the binding energy was used in quantifying shifts in Figure B-6.*

Mn 3*p*	**Main**
% Lorentzian	30
CasaXPS Asymmetry parameters	0.2, 1, 0

B.2. Additional figures regarding electrochemical cycling

ORR measurements by chronoamperometry are shown in **Figure B-9**. For 0% Sr (LMO), the current visibly decreased with time, and the voltage to achieve 40 $\mu A/cm^2$ from chronoamperometry was extrapolated with the Tafel slope. CVs in Ar-saturated 0.1 M KOH (**Figure B-10**) illustrate featureless capacitance and a lack of parasitic current for all stoichiometries, measured on a second set of films. Thus the current measured in O_2-saturated 0.1 M KOH is ORR current.

Some aging behavior in ORR activity was observed for films with 0% and 50% Sr, shown in **Figure B-11**. Although the 0% Sr film activity decreased with time, deviation from what would be expected with a linear trend from the initial 3 measures of ORR shows measurement of OER has additional effect on activity.

Figure B-12 shows a correlation between ORR activity and Tafel slope obtained from chronoamperometry. An assessment of activity at lower current densities in **Figure B-13** confirms the absence of spurious effects from mass transport in comparing ORR activities. Previous work on films of comparable geometry and activity[2] has shown that ORR currents are not affected by the rate of O_2 bubbling or electrolyte stirring for currents <40 $\mu A/cm^2$, which thus are governed by kinetics and not affected by diffusion in O_2-saturated solution.

An illustration of the integrated cathodic charge (Q_{cath}), maximum absolute current (i_{max}), and voltage at which the maximum current is reached (V_{max}) is provided in **Figure B-14**. The reduction in available electrons, the similar shift in V_{max} away from the 1.2 V vs. RHE equilibrium potential, and the lower i_{max} is reflected in reduced ORR activity of the films, measured by the voltage to achieve 40 $\mu A/cm^2$ in O_2–saturated 0.1 M KOH.

Figure B-15 compares the activity of LSMO films to those in literature.

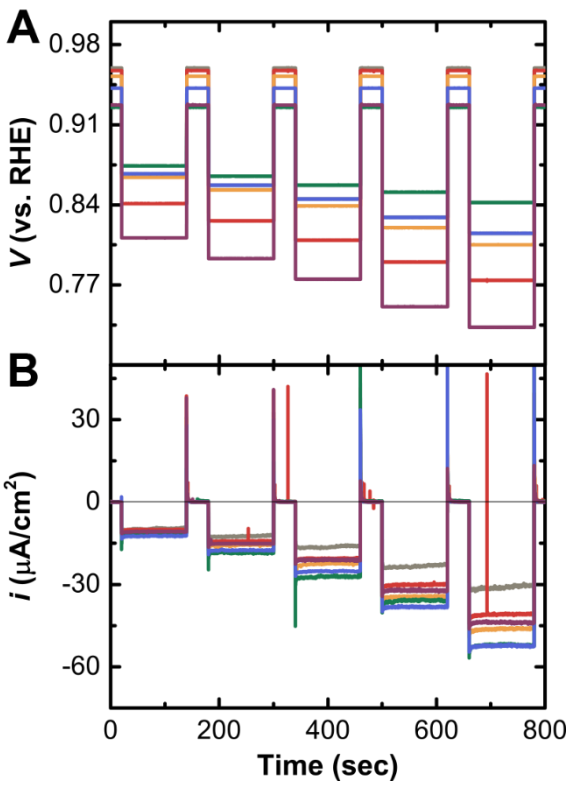

Figure B-9. *Measurement of ORR activity by chronoamperometry, showing (A) applied voltage and (B) measured current versus time, with color as in the main text: 0% (gray), 10% (red), 20% (yellow), 33% (green), 50% (blue), and 70% (purple).*

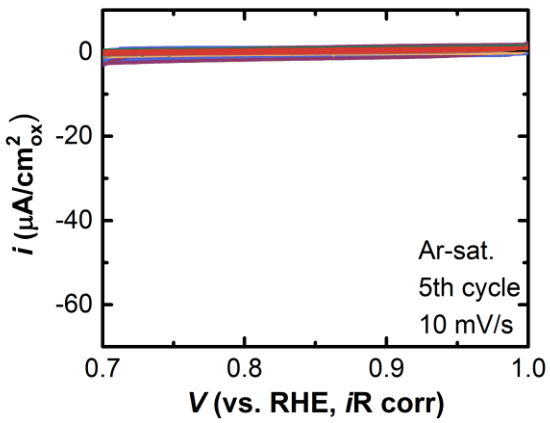

Figure B-10. *The 5th cycle of cyclic voltammetry (CV) at a scan rate of 10 mV/s showing the current per surface area (i) vs. the ohmic corrected applied voltage (V-iR) measured in Argon-saturated 0.1 M KOH. The color as in the main text: 0% (gray), 10% (red), 20% (yellow), 33% (green), 50% (blue), and 70% (purple).*

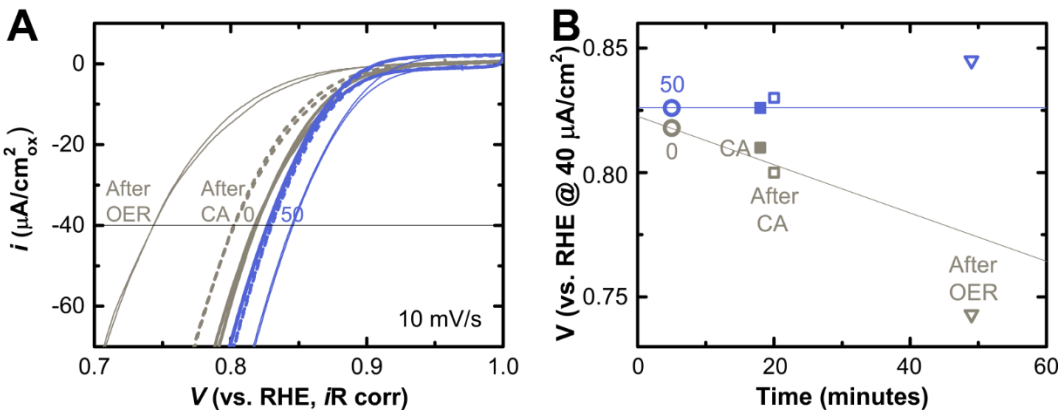

Figure B-11. *Different aging behaviors for the ORR activity of LSMO films, where 0% Sr (gray) decreased with cycling and 50% Sr (blue) increased slightly after measurement up to 1.7 V vs. RHE (oxygen evolution conditions, OER). (A) CVs of the 5th initial cycle (thick, solid), 2nd cycle after CA (dashed), and 2nd cycle after OER (thin solid). (B) Voltage required to achieve 40 μA/cm^2 versus the total measurement time. A line guides the eye of what would be expected with a linear trend from the initial 3 measures of ORR.*

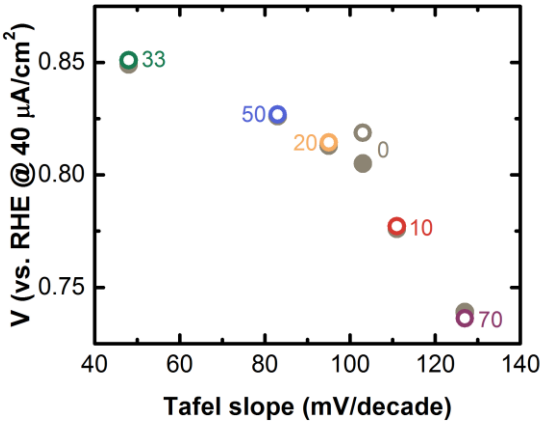

Figure B-12. *Correlation between ORR activity and Tafel slope, obtained from chronoamperometry. Activity is measured by the voltage to achieve 40 μA/cm^2 of capacitance corrected current from CV (open circle) and also chronoamperometry (solid), in which the activity of $LaMnO_3$ (Sr = 0%) decreased slightly.*

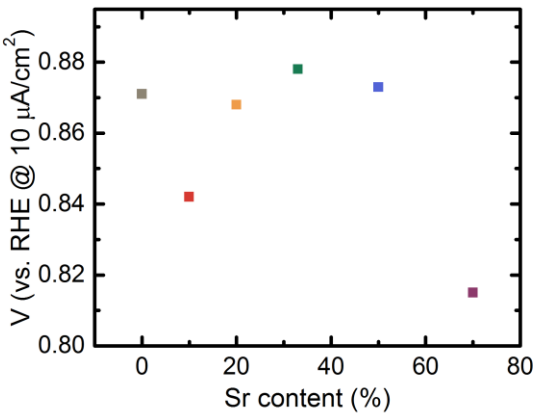

Figure B-13. *ORR activity measured by the voltage to achieve 10 μA/cm^2 of capacitance-corrected current from the 5th cycle of initial CV measurements.*

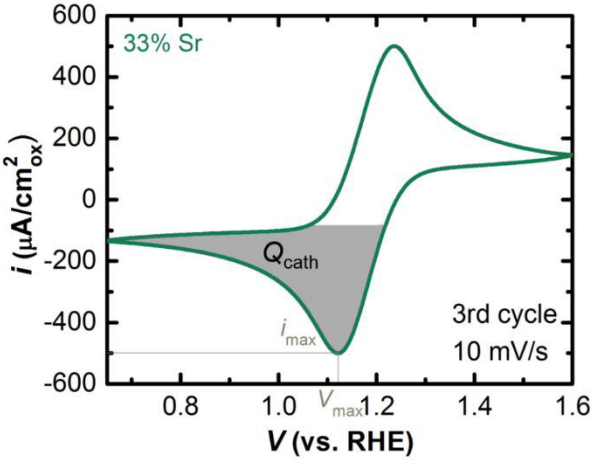

Figure B-14. *CV at 10 mV/s for 10 mM $[Fe(CN)_6]^{3-/4-}$ in Ar-saturated 0.1 M KOH illustrating the integrated cathodic charge (Q_{cath}), maximum absolute current (i_{max}), and voltage at which the maximum current is reached (V_{max}).*

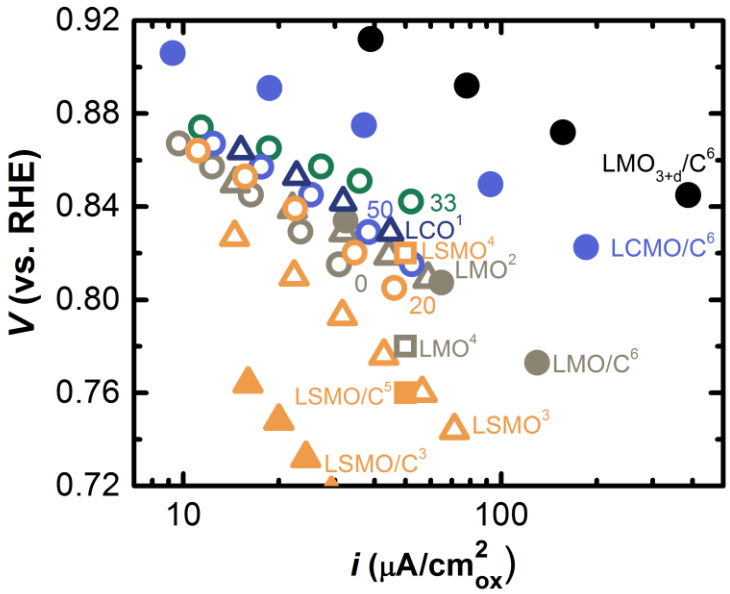

Figure B-15. *ORR activity of LSMO and related chemistries comparing the current study to those in literature. Measurements were made in O_2–saturated 0.1 M KOH unless otherwise noted. The percent substitution at the A-site is indicated by different colors: pure $LaMnO_3$ (gray), 20% Sr (yellow), 33% Sr(green), 50% Sr or Ca (blue), and cation deficient (black). A $LaCoO_3$ (LCO) film epitaxially strained to LSAT is included to reference a different highly-active transition metal chemistry (navy blue).*[6] *Films (open symbols) are from the present work (15-nm thick, circles), a previous work (10-nm thick, triangles),*[7] *Risch et al. (16-nm thick, triangles),*[8] *and Miyahara et al. (200-nm thick polycrystalline, 1 M KOH, squares).*[9] *Particles on a glassy carbon disk (filled symbols) are from Risch et al. (0.25 mg/cm$^2_{disk}$ LSMO + 0.05 mg/cm$^2_{disk}$ carbon, triangles),*[8] *Tulloch and Donne (0.021 mg/cm$^2_{disk}$ LSMO, 1 M KOH, squares),*[10] *and Suntivich et al. (0.25 mg/cm$^2_{disk}$ L(C)MO + 0.05 mg/cm$^2_{disk}$ carbon, circles).*[11]

B.3. Additional figures on different LSMO orientations

Figure B-16 presents characterization of LSMO films with Sr = 33% and 50% in the (110) and (111) orientation. **Figure B-17** characterizes the surface stoichiometry by XPS, normalizing the Sr 3*d* core level intensity by the relative sensitivity factor (RSF) tabulated for the instrument, and given on the basis of total A-site including the La 4*d*. Cycling behavior for the ORR and $[Fe(CN)_6]^{3-/4-}$ is presented in **Figure B-18**.

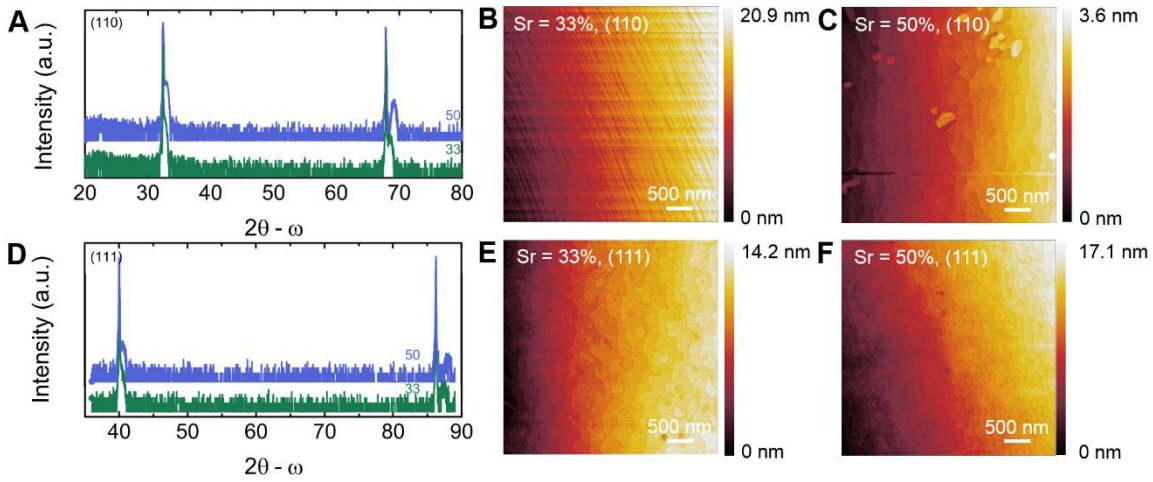

Figure B-16. *Characterization of LSMO films with Sr = 33% (green) and 50% (blue). (A) X-ray diffraction showing normal 2θ-ω scan of the $(110)_{pc}$ and $(220)_{pc}$ reflections. (B) AFM of (110) oriented film for Sr = 33% and (C) 50%. (D) X-ray diffraction showing normal 2θ-ω scan of the $(111)_{pc}$ and $(222)_{pc}$ reflections. (E) AFM of (111) oriented film for Sr = 33% and (F) 50%.*

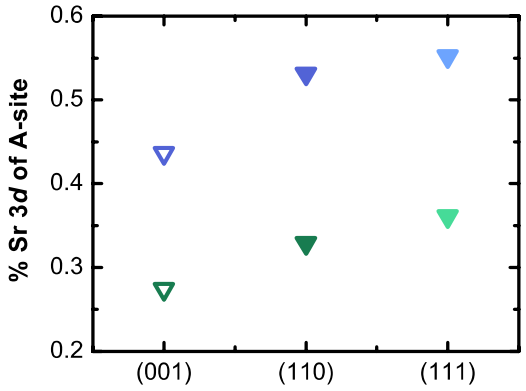

Figure B-17. *X-ray photoelectron spectroscopy of $La_{(1-x)}Sr_xMnO_3$ films of nominal 33% (green) and 50% (blue) Sr in the A-site from the target stoichiometry. The core level intensities are normalized by the relative sensitivity factor (RSF) tabulated for the instrument, and given on the basis of total A-site including the La 4d.*

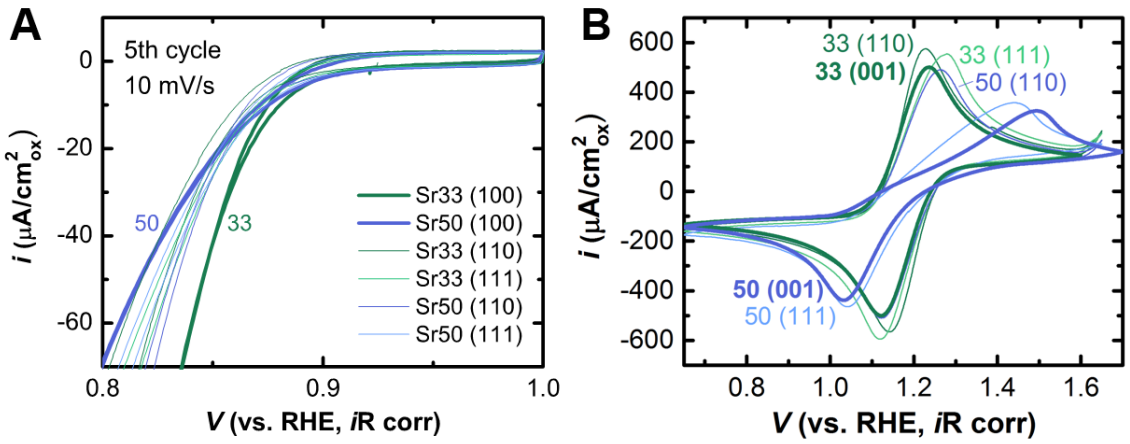

Figure B-18. *Cyclic voltammetry (CV) at 10 mV/s on LSMO films for Sr = 33% (green) and 50% (blue) in 0.1 M KOH (A) O_2-saturated for ORR and (B) Ar-saturated with 10 mM $[Fe(CN)_6]^{3-/4-}$. Films of different orientation exhibit comparable ORR activity and charge-transfer properties.*

References

1 Deng, X., Herranz, T., Weis, C., Bluhm, H. & Salmeron, M. Adsorption of Water on Cu_2O and Al_2O_3 Thin Films. *The Journal of Physical Chemistry C* **112**, 9668-9672, (2008).

2 Sunding, M. F. *et al.* XPS characterisation of in situ treated lanthanum oxide and hydroxide using tailored charge referencing and peak fitting procedures. *Journal of Electron Spectroscopy and Related Phenomena* **184**, 399-409, (2011).

3 Suntivich, J. *et al.* Estimating Hybridization of Transition Metal and Oxygen States in Perovskites from O K-edge X-ray Absorption Spectroscopy. *The Journal of Physical Chemistry C* **118**, 1856-1863, (2014).

4 Crumlin, E. J. *et al.* In Situ Ambient Pressure X-ray Photoelectron Spectroscopy of Cobalt Perovskite Surfaces under Cathodic Polarization at High Temperatures. *The Journal of Physical Chemistry C* **117**, 16087-16094, (2013).

5 Cerrato, J. M., Hochella, M. F., Knocke, W. R., Dietrich, A. M. & Cromer, T. F. Use of XPS to Identify the Oxidation State of Mn in Solid Surfaces of Filtration Media Oxide Samples from Drinking Water Treatment Plants. *Environmental Science & Technology* **44**, 5881-5886, (2010).

6 Stoerzinger, K. A., Choi, W. S., Jeen, H., Lee, H. N. & Shao-Horn, Y. Role of Strain and Conductivity in Oxygen Electrocatalysis on $LaCoO_3$ Thin Films. *The Journal of Physical Chemistry Letters*, 487-492, (2015).

7 Stoerzinger, K. A. *et al.* Oxygen Electrocatalysis on (001)-Oriented Manganese Perovskite Films: Mn Valency and Charge Transfer at the Nanoscale. *Energy & Environmental Science* **6**, 1582-1588, (2013).

8 Risch, M. *et al.* $La_{0.8}Sr_{0.2}MnO_{3-\delta}$ Decorated with $Ba_{0.5}Sr_{0.5}Co_{0.8}Fe_{0.2}O_{3-\delta}$: A Bifunctional Surface for Oxygen Electrocatalysis with Enhanced Stability and Activity. *Journal of the American Chemical Society* **136**, 5229-5232, (2014).

9 Miyahara, Y., Miyazaki, K., Fukutsuka, T. & Abe, T. Catalytic Roles of Perovskite Oxides in Electrochemical Oxygen Reactions in Alkaline Media. *Journal of the Electrochemical Society* **161**, F694-F697, (2014).

10 Tulloch, J. & Donne, S. W. Activity of Perovskite $La_{1-x}Sr_xMnO_3$ Catalysts Towards Oxygen Reduction in Alkaline Electrolytes. *Journal of Power Sources* **188**, 359-366, (2009).

11 Suntivich, J. *et al.* Design Principles for Oxygen-Reduction Activity on Perovskite Oxide Catalysts for Fuel Cells and Metal–Air Batteries. *Nature Chemistry* **3**, 546-550, (2011).

C. Additional information for Chapter 5

C.1. Additional figures and tables regarding fabrication

Characterization of the IrO_2 films by XRD and AFM is presented in **Figure C-1**. (110)- and (100)-oriented films are grown on (001) MgO and $SrTiO_3$, with all others grown on TiO_2 of corresponding rutile orientation. Roughness values for both RuO_2 and IrO_2 before and after cycling are quantified in **Table C-1**. In plane characterization of is presented in **Figure C-2**. AFM after cycling for the (100) and (110) orientation after cycling in KOH is shown in **Figure C-3**.

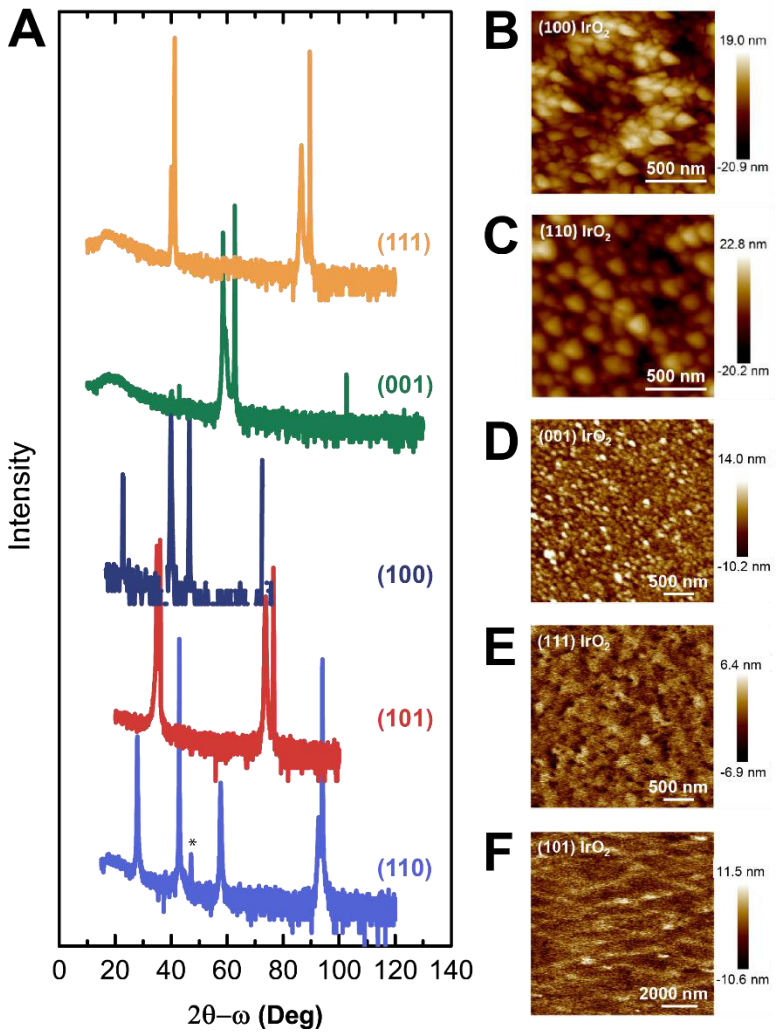

***Figure C-1**. (A) Normal 2θ−ω scan of films with noted orientation. Intensity is on a logarithmic scale, with curves offset for clarity. The asterix marks an impurity of <0.3% (100) orientation in the film. (B-F) Atomic force microscopy (AFM) image of representative samples after deposition. (B) (100), (C) (110), (D) (001), (E) (111), (F) (101) IrO_2.*

Table C-1. *Root mean square (RMS) roughness from AFM before any electrochemistry measurements and after all electrochemistry.*

Film	RMS roughness (nm) Before	RMS roughness (nm) After KOH	RMS roughness (nm) After $HClO_4$
IrO_2 (100)	5.97	18.76	2.35
IrO_2 (110)	6.20	6.37	2.755
IrO_2 (001)	3.22	n/a	2.911
IrO_2 (111)	1.87	n/a	2.56
IrO_2 (101)	3.15	2.075	1.931
RuO_2 (100)	0.66	0.74	0.582
RuO_2 (110)	1.57	1.12	-
RuO_2 (001)	0.771	0.584	0.782
RuO_2 (101)	0.429	0.223	0.509
RuO_2 (111)	0.27	0.327	0.734

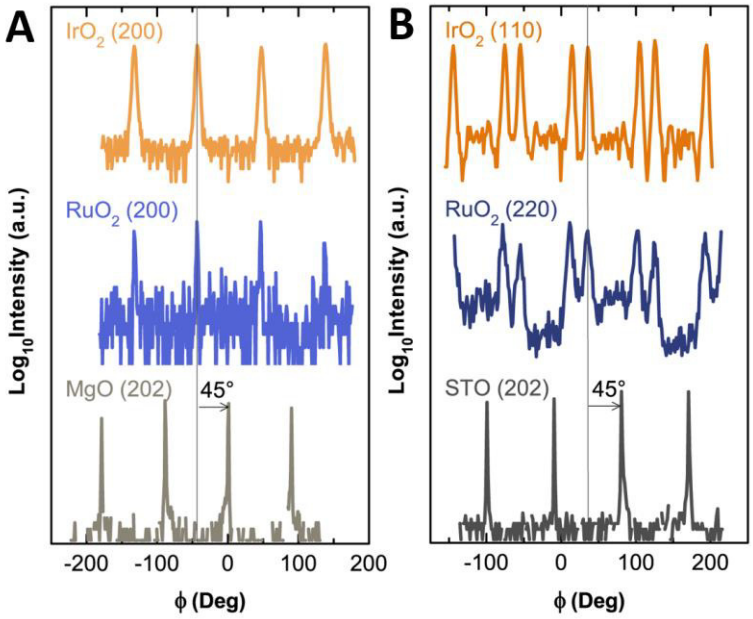

Figure C-2*. (A) Phi scans in-plane, aligned to the noted reflections for films grown on MgO. Films orient 45° to the substrate; scans were shifted to plot on a common axis for easy viewing. (C) Phi scans in-plane, aligned to the noted reflections for films grown on $SrTiO_3$ (STO). Films orient 45° to the substrate; scans were shifted to plot on a common axis for easy viewing.*

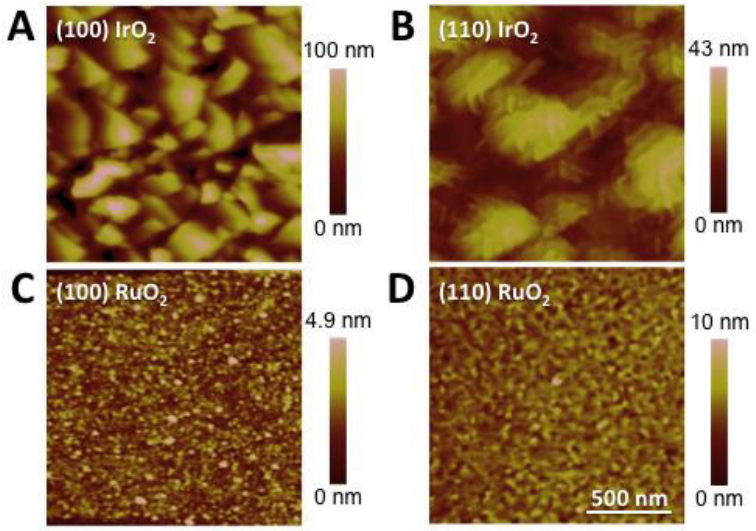

Figure C-3. *Atomic force microscopy (AFM) of film surfaces after all electrochemistry measurements; the 500 nm scale bar is the same for all images. (A) (100)-oriented IrO_2, (B) (110)-oriented IrO_2, (C) (100)-oriented RuO_2, and (D) (110)-oriented RuO_2. Corresponding roughness factors can be found in Table C-1.*

C.2. Additional figures regarding activity of the (110), (100)

The Tafel plot shown in **Figure C-4** illustrates fits to slopes in the regions noted in the footnotes of **Table C-2**. Schematic projections of the (100) and (110) orientation are shown in **Figure C-5**.

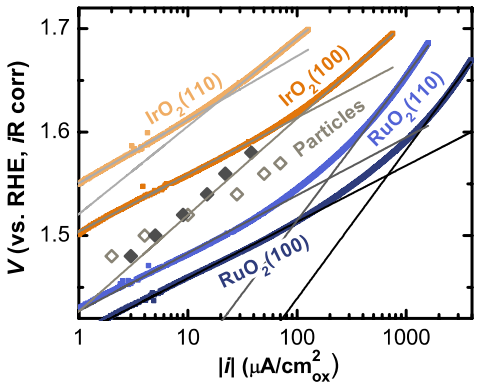

Figure C-4. *Tafel plot showing E-iR vs. |i| on a logarithmic scale. Colored lines correspond to CVs of the 10th OER cycle, averaging forward and reverse sweeps to correct for capacitance. Data for particles of RuO_2 (dark gray, filled) and IrO_2 (light gray, open) were extracted from [1]. The fit lines to determine the Tafel slopes in Table C-2 are shown in shades of gray.*

Table C-2. *Comparison of Tafel slopes.*

	low **[mV/decade]**	***high*** **[mV/decade]**
IrO_2 (100)*	55	93
IrO_2 (110)*	61	85
RuO_2 (100)**	54	144
RuO_2 (110)**	56	141

* Tafel slope fitting for IrO_2 films was between 1.55-1.6 V vs. RHE (low) and 1.65-1.7 V (high).

** Tafel slope fitting for RuO_2 films was between 1.4-1.5 V vs. RHE (low) and 1.61-1.7 V (high).

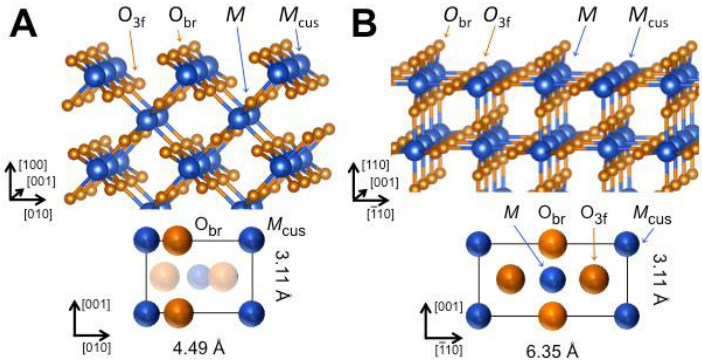

Figure C-5. *Schematic projection of (A) (100)-oriented surface and (B) (110)-oriented surface, with unit cell dimensions given for RuO_2[2] (IrO_2 a = 4.51 Å, c = 3.16 Å)*[3]*. Species unique to the surface are annotated, including coordinatively undersaturated sites (M_{cus}, M = Ir, Ru, blue), bridging oxygen (O_{br}, orange), and 3-fold coordinated oxygen (O_{3f}, orange), in addition to fully coordinated metal sites (M, blue).*

C.3. Additional data for pH, orientation dependence of RuO_2

Cathodic charges obtained by cycling in Ar-saturated electrolyte (q*) are quantified in **Table C-3** and compared to the ideal case. **Figure C-6** presents a Tafel plot from galvanostatic measurements (constant applied voltage, points) for (110)-oriented RuO_2 in 0.1 M KOH (measured first) and 0.1 M $HClO_4$ (measured second). While AFM images taken after cycling in KOH bears no notable signs of corrosion, after cycling in 0.1 M $HClO_4$ square concave features illustrate pitting on large length scales.

Table C-3. *Cathodic charge density in Ar-saturated electrolyte, $q^*_{cathodic}$, and its correspondence to the measured number of Ru atoms/nm^2 (assuming 1 e^- passed per Ru-site), compared to the ideal case calculated from Figure 5-6.*

	$q^*_{cathodic}$ (μC/cm^2)			# Ru/nm^2 (assume 1 e^-/Ru)			Ru_{cus}/nm^2
	KOH[†]	$HClO_4$	H_2SO_4[a]	KOH[†]	$HClO_4$	H_2SO_4[a]	Ru_{cus}/nm^2
(110)	104	125	160	6.3	7.8	10	5
(100)	146	117	113.6	8.8	7.3	7.1	7.2
(101)	149	119	131.2	9.3	7.4	8.2	8.2
(001)	216	209*	80	13.4	13.1	5	5
(111)	143	125	56.8	8.9	7.8	3.55	3.5

[†]$q^*_{cathodic}$ was measured first in 0.1 M KOH, and second in 0.1 M $HClO_4$ on the same film

[a]Literature reference for "$Q_{Ru\text{-}H2}$" on single crystals RuO_2 facets in 0.5 M H_2SO_4,[2] with corresponding number of electrons passed, calculated as for the films in this work

*Average of cathodic and anodic q^*, due to asymmetry

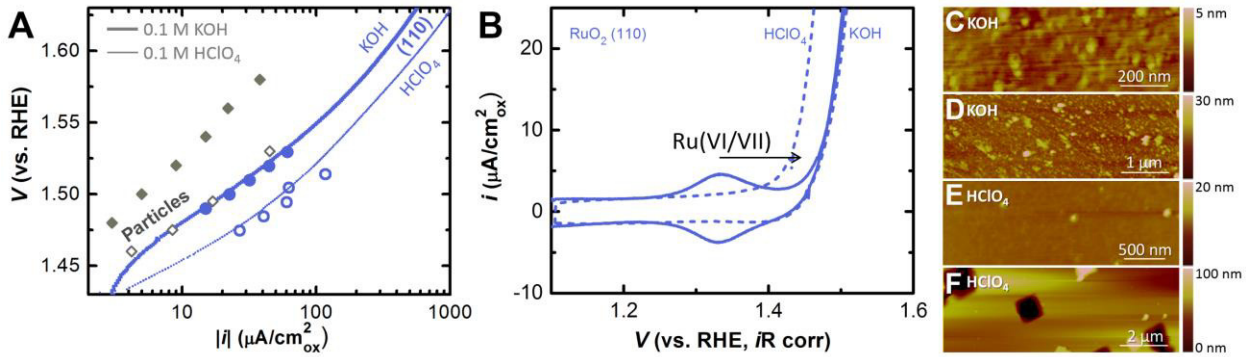

Figure C-6. *(A) Tafel plot from galvanostatic measurements (points) showing E-iR versus |i| on a logarithmic scale for (110)-oriented RuO_2. Solid lines correspond to averaged forward/back CVs of the 10th OER cycle (B, unaveraged) that proceeded galvanostatic measurements. Thick lines/solid points correspond measurements in O_2-saturated 0.1 M KOH (measured first) and thin lines/open points in 0.1 M $HClO_4$ (measured second). Data for particles of RuO_2 (dark gray, filled KOH, open $HClO_4$) were extracted from ref. [1]. (C,D) AFM image taken after cycling in KOH bears no notable signs of corrosion, however (E,F) AFM taken after cycling in 0.1 M $HClO_4$ illustrate pitting on large length scales.*

References

1 Lee, Y., Suntivich, J., May, K. J., Perry, E. E. & Shao-Horn, Y. Synthesis and Activities of Rutile IrO_2 and RuO_2 Nanoparticles for Oxygen Evolution in Acid and Alkaline Solutions. *The Journal of Physical Chemistry Letters* **3**, 399-404, (2012).

2 Hepel, T., Pollak, F. H. & O'Grady, W. E. Effect of Crystallographic Orientation of Single-Crystal RuO_2 Electrodes on the Hydrogen Adsorption Reactions. *Journal of the Electrochemical Society* **131**, 2094-2100, (1984).

3 Bolzan, A. A., Fong, C., Kennedy, B. J. & Howard, C. J. Structural Studies of Rutile-Type Metal Dioxides. *Acta Crystallographica Section B* **53**, 373-380, (1997).

D. The ligand effect: changing $LaMnO_3$ film thickness on Nb-$SrTiO_3$

This chapter is reproduced in part with permission from: Stoerzinger, K. A. *et al.* Oxygen electrocatalysis on (001)-oriented manganese perovskite films: Mn valency and charge transfer at the nanoscale. *Energy Environ. Sci.* **6**, 1582-1588, (2013). Reproduced by permission of The Royal Society of Chemistry.

D.1. Introduction

Notable progress in identifying "activity descriptors" for the ORR on oxide catalysts based on studies of oxide catalysts supported on high surface area carbon to eliminate issues related to electrode conductivity has been reported.[1-3] For example, Suntivich et al.[4] have recently reported that near-unity occupancy of the e_g orbital of transition-metal ions at the active B-site[5] of perovskite oxides having a formula of ABO_3 is an essential ingredient for developing highly active ORR oxide catalysts. In their study, $LaMnO_3$-based (LMO) oxides were found to be among the most active for the ORR with activities comparable to that of Pt.[1] However, ambiguity exists in which Mn valence state on the surface is responsible for the high ORR activity since manganese oxides with very different Mn valence states[6-12] have been reported "active" for the ORR. In many cases the presence of surface defects has been cited as a key factor in determining activity,[7,12,13] but the lack of morphological control in particles and electrodeposited films makes the identification of the active Mn valence state on the surface challenging. A recent study of cobalt perovskite thin films suggests the promise of studying more well-defined surfaces.[14]

Herein, we investigate the ORR activities of single-crystal Mn(III,IV) perovskite oxide nanometer-thin films grown epitaxially on electron-conductive substrates. Using such well-defined surfaces, without the influence of carbon additive and uncertainty in estimation of the electrochemical surface area of oxide powders, allows us to better measure the intrinsic ORR activities of these oxide surfaces. In addition, the nominal valence state of Mn in our LMO films can be tuned from 3+ to 4+ by A-site substitution, from which we find that the Mn^{3+} oxidation state is responsible for high ORR activity. Moreover, as single-crystal oxide thin films and superlattices can have physical properties drastically different from surfaces of bulk materials, such as enhanced ferroelectricity[15] and oxygen ion conductivity,[16] we investigate whether the ORR activities of surfaces of very thin, epitaxial films are different from that of bulk powder. We show that LMO epitaxial films with thicknesses from 1 to 10 nm can have drastically different ORR activity from bulk, which can be attributed to the barrier associated with interfacial band bending that impedes electron transfer to the electrolyte and the reduction of Mn^{3+} to Mn^{2+} associated with charge transfer from an electron-rich substrate to LMO. This hypothesis is

supported by potential shifts observed for the reduction wave of the $[Fe(CN)_6]^{3-/4-}$ redox couple and X-ray absorption spectroscopy studies of the Mn valence state.

D.2. Experimental

Film Fabrication. $CaMnO_3$ (CMO), $La_{0.67}Sr_{0.33}MnO_3$ (LSMO), and $LaMnO_3$ (LMO) used for electrochemical measurements and characterized by atomic force microscopy (AFM) in **Figures D-6, D-7, D-11, D-13, D-15** and X-ray photoemission spectroscopy (XPS) were grown by pulsed laser deposition (PLD) on 0.5wt% Nb-doped $SrTiO_3$ (NSTO) substrates with (001)-orientation (CrysTec). The manganite targets for PLD were made by conventional solid phase sintering using commercial powders of lanthanum oxide, strontium carbonate, and manganese oxide (Alfa Aesar, 99.99 %). PLD was performed at 750 ^oC in an oxygen atmosphere of 600 mTorr for CMO and LSMO, and 75 mTorr for LMO at the National University of Singapore. The thickness of the manganite film was carefully controlled by growth time, and following, the samples were cooled to room temperature under the growth condition. Surface morphologies were examined by AFM (Veeco Metrology Nanoscope IV) in tapping mode. The surface morphology of the LMO (**Figure D-1**), CMO and LSMO (**Figure D-2**) films were studied via AFM, suggesting complete coverage. The consistent maximum height difference and the root-mean-squared (RMS) roughness across film thicknesses are indicative of uniform coverage and wetting of the NSTO substrate, as opposed to particle growth (**Table D-1**).

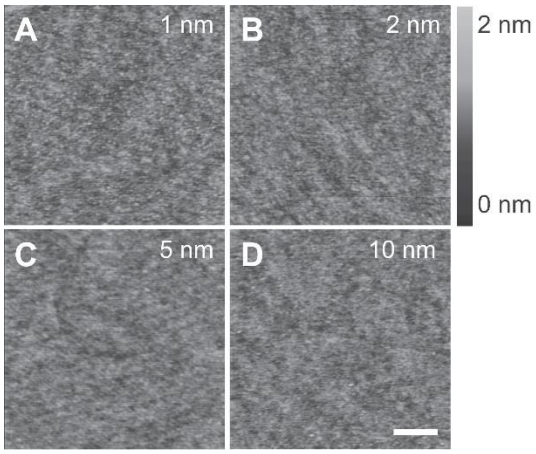

Figure D-1. *Atomic force microscopy (AFM) images in tapping mode of $LaMnO_3$ (LMO) films (A) 1, (B) 2, (C) 5, and (D) 10 nm in thickness. The scale bar is the same for all images and is 200 nm in length; the brightness scale bar is 0–2 nm.*

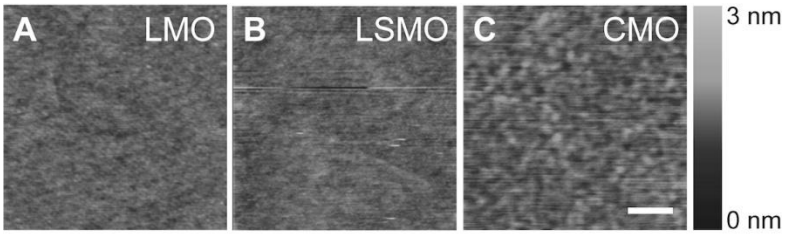

Figure D-2. *Atomic force microscopy (AFM) images in tapping mode of 5 nm films of (A) $LaMnO_3$ (LMO), (B) $La_{0.67}Sr_{0.33}MnO_3$ (LSMO), and (C) $CaMnO_3$ (CMO). The scale bar is the same for all figures and is 200 nm in length. The brightness scale bar is 0–3 nm.*

Table D-1. *Quantification of topography from AFM of LMO, LSMO, and CMO films of noted thickness.*

Material	Maximum height (nm)	RMS roughness (nm)
5 nm LMO	1.55	0.13
5 nm LSMO	3.29	0.17
5 nm CMO	1.83	0.20
NSTO (bare)	1.17	0.16
1 nm LMO	1.47	0.16
2 nm LMO	1.45	0.15
5 nm LMO	1.55	0.13
10 nm LMO	1.90	0.15

Elemental composition was probed using XPS (Physical Electronics PHI Versaprobe II) with an Aluminum K-alpha source. Samples were affixed with conductive carbon tape, and the binding energy scale was calibrated by defining the fitted C 1s peak for adventitious carbon at 285 eV.[17] XPS confirms the intended composition of the films (**Figure D-3**). Some signal from the substrate is observed for all films, which is not surprising considering the inelastic mean free path for a band gap ~1 eV (bulk LMO) [18] and an incident energy of 1.5 keV is nearly 3 nm. The consistent ratio of Sr:Ti measured confirms no preferential segregation from the substrate during deposition.

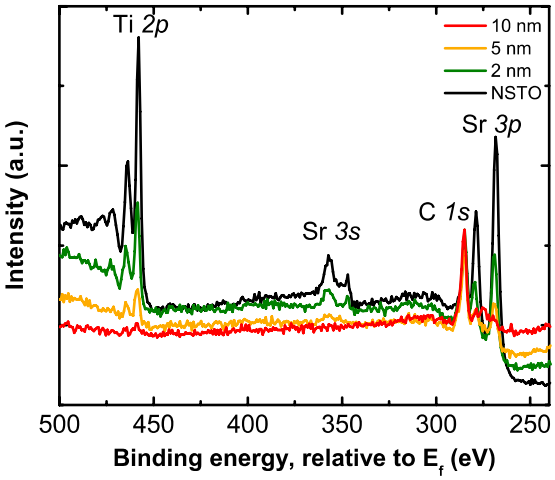

Figure D-3. *X-ray photoemission spectroscopy (XPS) of LMO films of 2 (green), 5 (orange), and 10 nm (red) thickness, as well as a blank NSTO substrate (black).*

Structural Characterization. Thin film XRD was performed using a four-circle diffractometer (Bruker D8, Germany) in normal and off-normal configurations. Films characterized by X-ray absorption spectroscopy (XAS)—the electrochemical measurements and X-ray diffraction (XRD) of which are provided in **Figure D-4**—were grown on 0.7 wt% Nb-doped $SrTiO_3$ (MTI) in 200 mTorr oxygen at the Center for Nanophase Materials Sciences. For these films, the target was pressed from LMO powder synthesized by nitrate combustion. XRD shows good epitaxial growth, with no detectable strains beyond experimental uncertainty in the case of LMO due to near lattice matching (3.92 Å pseudo-cubic LMO[4] on 3.91 Å NSTO[19]).

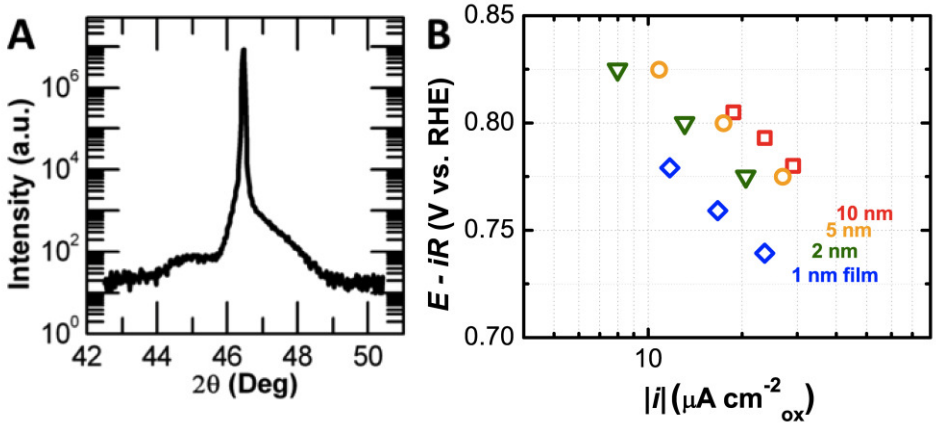

Figure D-4. *(A) Thin film X-ray diffraction (XRD) in a coupled 2θ-ω configuration around the (002) Bragg peak of the Nb-doped $SrTiO_3$ (NSTO) substrate for a 5 nm LMO film. (B) ORR activity of the set of LMO films deposited at Oak Ridge National Labs, including the 5 nm film from panel (A). A Tafel plot from chronoamperometry shows the ohmic corrected applied voltage (E-iR) vs. current (|i|) on a logarithmic scale. The trend of decreasing activity with thickness is*

consistent with that of the films grown at the National University of Singapore, presented in Figure D-11.

X-ray Absorption Spectroscopy. XAS at the Mn L-edge was collected in electron yield mode at the Canadian Light Source for MnO powder and LMO films, and at the Advanced Light Source for $Sr_4Mn_2CoO_9$ (comparable to a hexagonal perovskite with only Mn in the B-site, **Figure D-5A**) and $LaMnO_3$ powder. The energy scale was aligned for a 100 nm LMO film to that of LMO powder (**Figure D-5B**). The spectra were normalized by subtraction of a constant before the L_3-edge, then division by a constant after the L_2-edge. The large intensity ratio of $I(L_3)/I(L_2)$ establishes clearly that Mn^{3+} is predominantly in the high spin state.[20,21]

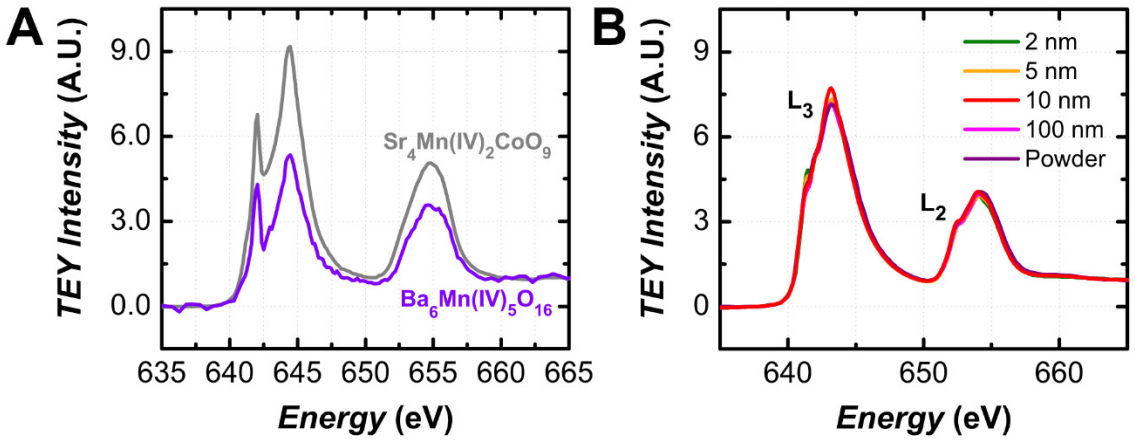

Figure D-5. *X-ray absorption spectra (XAS) acquired in total electron yield (TEY) mode at Mn L-edges. (A) Comparable Mn^{4+} spectra are measured for for $Sr_4Mn(IV)_2CoO_9$ (gray), known to charge disproportionate into Mn^{4+} and Co^{2+},[22] and $Ba_6Mn(IV)_5O_{16}$ (purple). (B) Comparable Mn^{3+} spectra for a 100 nm LMO film (pink) and LMO powder (red), used to align the energy scale at the ALS to that of the CLS in order to compare with a Mn^{4+} reference. LMO films of 2 (green), 5 (orange), and 10 nm (red) thickness show predominately Mn^{3+} character.*

Electrochemical Measurements. Electrical contacts were applied to the back of the NSTO substrate. Gallium-Indium eutectic (Sigma-Aldrich, 99.99%) was scratched into the NSTO, and a Ti wire (Sigma-Aldrich, 99.99 %) was affixed with silver paint (Ted Pella, Leitsilber 200). The back and sides of the electrode, as well as the wire, were covered with a non-conductive, chemically resistant epoxy (Omegabond 101), so only the catalyst surface was exposed to electrolyte.

Electrochemical measurements were conducted with a Biologic SP-300 potentiostat in an ~120 ml solution of 0.1 M KOH, prepared from Milli-Q water (18 MΩ cm) and KOH pellets

(Sigma-Aldrich, 99.99%). Potentials were referenced to a saturated Ag/AgCl electrode (Pine), calibrated to the reversible hydrogen electrode (RHE) scale in 0.1 M KOH. ORR measurements were carried out in an electrolyte pre-saturated by bubbling O_2 at least 45 minutes and under continuous O_2 bubbling (Airgas, ultrahigh-grade purity). ORR cyclic voltammetry plots (CVs) were capacitance corrected by averaging the forward and backward sweeps. Tafel plots present chronoamperometry measurements (applying constant potential). Measurements of the $[Fe(CN)_6]^{3-/4-}$ reaction were carried out in an Ar-saturated (Airgas, ultrahigh-grade purity) solution of 0.1 M KOH, to which 5 mM each of $K_4Fe(CN)_6$-$3H_2O$ (Sigma-Aldrich, 99.99%) and $K_3Fe(CN)_6$ (Sigma-Aldrich, 99%) were added. All CV scans were carried out at 10 mV/s, and electrical impedance spectroscopy (EIS) was performed at the open circuit voltage with an amplitude of 10 mV. Potentials were corrected for the electrolyte/cell resistance from the high frequency intercept of the real impedance (45 Ω).

D.3. Results and discussion

Films of LMO, CMO, and LSMO with thicknesses in the range from 1 to 10 nm were grown on (001)-oriented NSTO by PLD. The electrochemical behavior of films was measured in a standard 3-electrode setup in O_2-saturated 0.1 M KOH, where reduction of oxygen is defined as negative current. The working electrode was contacted via the back of the NSTO substrate, and all but the active film area (front face) was covered with a chemically resistant epoxy. The ORR currents of the films were measured by CVs (**Figure D-6A**), and chronoamperometry (**Figure D-6B**); both methods yielded comparable ORR activities (**Figure D-6B, D-7**).

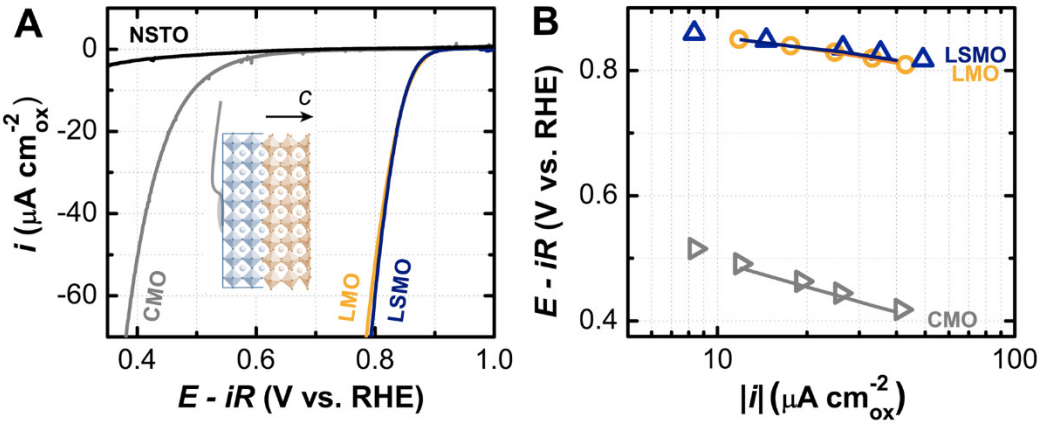

Figure D-6. *ORR activity in O_2-saturated 0.1 M KOH. (A) Cyclic voltammetry (CV) at a scan rate of 10 mV/s showing the capacitance-corrected (average of the forward and back sweep) ORR current per surface area (i) vs. the ohmic corrected applied voltage (E-iR) for a blank*

NSTO substrate and 5 nm films of CMO, LSMO, and LMO. (B) Tafel plot from chronoamperometry showing E-iR vs. |i| on a logarithmic scale. Solid lines correspond to data from the CVs shown in (A).

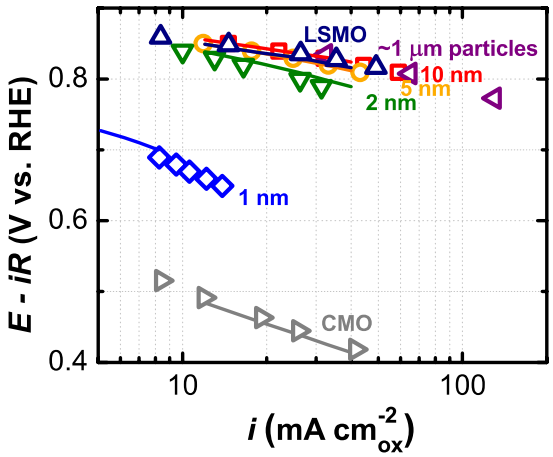

Figure D-7. *Tafel plot comparing measurements from current-voltage (CV) scans at 10 mV/s (lines) to those from chronoamperometry (points), showing ohmic-corrected applied voltage vs. absolute current on a logarithmic scale. Films are 5 nm CMO, 5 nm LSMO, and LMO of 1, 2, 5, and 10 nm thickness, comparing to previously reported LMO micron-sized powder.*[4]

In order to ensure that the ORR current was not limited by diffusion of the reactants, **Figure D-8** shows the current measured for an electrode under different applied potentials, where stirring of the electrolyte (bringing more O_2 to the perovskite surface) was increased at each point annotated by arrows. For absolute currents $\leq$ 0.04 mA cm^{-2}_{ox}, an increased supply of O_2 did not result in greater measured current. The activity measured below this current value is thus not significantly influenced by the diffusion of reactants and is representative of the intrinsic catalytic activity of the film.

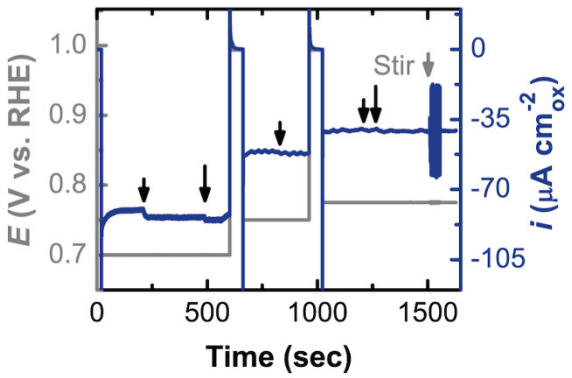

Figure D-8. *Plot of the applied voltage (left axis, gray) and current (right axis, navy) vs. time, where the flow of O_2 or stir rate of the O_2–saturated 0.1 M KOH electrolyte was increased at each time annotated by arrows.*

The investigation of well-defined, nanometer-thin films has allowed us to show Mn^{3+} not Mn^{4+} is the active valence state for the ORR. The oxygen reduction currents of LMO, CMO, and LSMO films of 5 nm from cyclic voltammetry are presented in **Figure D-7A**, and specific ORR activities obtained from CV and chronoamperometry measurements are shown in **Figure D-7B**. All observed ORR currents were attributed to the manganite thin films as verified by the negligible activity of NSTO above 0.4 V vs. RHE. We found that LMO and LSMO exhibited significantly higher ORR current compared to CMO, which suggests that Mn^{3+} is more active than Mn^{4+} and is responsible for the high ORR activity of LMO-based catalysts. LSMO with nominal Mn oxidation of 3.33+ (67% Mn^{3+} and 33% Mn^{4+}) also showed an ORR activity comparable to that of LMO with nominal Mn valence of 3+. Although activity is not linearly correlated with the amount of Mn^{3+}, the comparably high ORR activities of LMO and LSMO imply that Mn^{4+} has negligible activity on the perovskite surface.

The lower ORR activity of CMO with nominal Mn^{4+} (e_g occupancy of 0) compared to LMO with nominal Mn^{3+} (e_g occupancy of 1) is consistent with the previously proposed design principle for a range of perovskite catalysts,[4] whereby the ORR activity is governed by the e_g occupancy of transition metal ions in the perovskite structure, yielding a volcano trend, centered approximately at e_g close to unity for high activity (**Figure D-9**). LSMO with an average e_g occupancy of ~0.7, assuming a high-spin state for Mn^{3+} (**Figure D-10**) has an ORR activity comparable to LMO. Our result, using the well-defined (001) surfaces of epitaxial films, therefore shows that Mn^{3+} with e_g occupancy of unity is responsible for the high ORR activities of Mn-based perovskites (**Figure D-9**). The high ORR activities found for other Mn-based oxides, including MnO_2 with nominal Mn^{4+} in octahedral coordination,[13,23] are thus postulated to be a result of the surface nonstoichiometry and the presence of surface Mn^{3+}, which we and others[10,24]

have identified as responsible for the high ORR activity. We believe that the link between surface stoichiometry and structure with ORR activity[9] is one of the reasons behind the significant activity variations in nanostructured MnO_2 catalysts with different surface morphologies.[13,23]

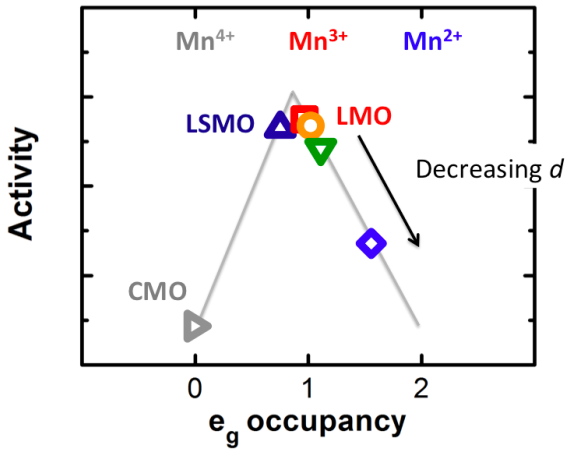

Figure D-9. *Schematic of the volcano relationship for ORR activity of d = 5 nm $CaMnO_3$ (CMO), 5 nm $La_{0.67}Sr_{0.33}MnO_3$ (LSMO), and $LaMnO_3$ (LMO) films of 10 (red), 5 (orange), 2 (green) and 1 nm (blue) thickness. The activity can be described by e_g orbital occupancy, as found previously by Suntivich et al.,[4] which is estimated from the Mn valence state (assuming high spin in all cases).*

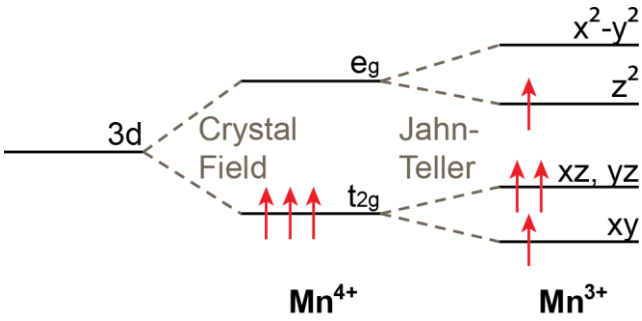

Figure D-10. *Energy splitting of the 3d-electron states in an octahedral crystal field (Mn^{4+}, as in $CaMn(IV)O_3$) and due to the Jahn-Teller effect (Mn^{3+}, as in $LaMn(III)O_3$). For Mn^{3+}, both the occupied z^2 and unoccupied x^2-y^2 orbital are of e_g parentage.*

The oxygen reduction currents of LMO films with 1, 2, 5, and 10 nm thickness from cyclic voltammetry are shown in **Figure D-11A**. The voltage to achieve a given oxygen reduction current was found to shift negatively with decreasing thickness. In other words, the ORR activity decreases with decreasing thickness. The trend was further confirmed by chronoamperometry measurements in **Figure D-11B**, where comparable specific ORR activities were found for these two measurement methods (**Figure D-7**). For reference, we also include the activity of the micron-sized LMO powder reported previously.[4] We found that the activity of an (001)-oriented

10-nm film is comparable to that of the micron-sized particles, which suggests that the (001) facet may dominate activity, and that the ORR activity decreases by over one order of magnitude with decreasing thickness from 10 to 1 nm. Electrochemical measurements of additional LMO films show the observed trend is repeatable (**Figure D-4B**). It is interesting that the activity measured for films grown on as-purchased substrates is comparable to that for films grown on annealed, terraced surfaces (**Figure D-12**), suggesting that topological differences do not influence this trend.

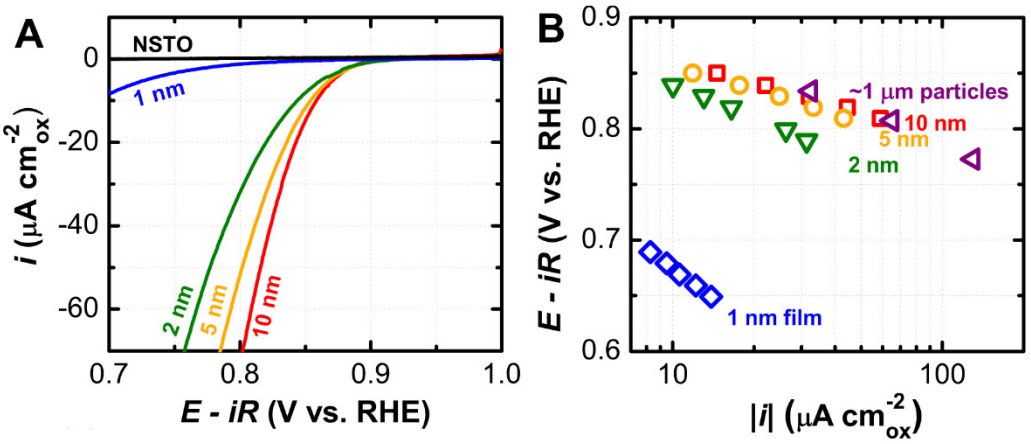

Figure D-11. *(A) Cyclic voltammetry (CV) in O_2–saturated 0.1 M KOH at 10 mV/s showing the capacitance-corrected ORR current per surface area (i) vs. the ohmic corrected applied voltage (E-iR) for a blank NSTO substrate and LMO films of 1, 2, 5, and 10 nm thickness. (B) Tafel plot from chronoamperometry showing E-iR vs. |i| on a logarithmic scale, comparing to previously reported micron-sized powder.*[4]

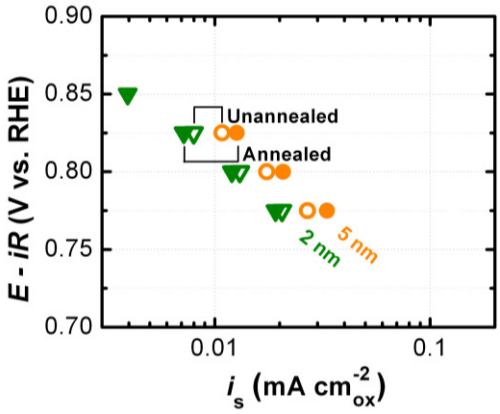

Figure D-12. *ORR activity for LMO films deposited at Oak Ridge National Labs on as-received (open) and annealed, terraced NSTO substrates (solid). A Tafel plot from chronoamperometry*

shows the ohmic corrected applied voltage (E-iR) vs. absolute current ($|i_s|$) on a logarithmic scale.

We propose that the differences in the catalytic activity among LMO films of different thicknesses originate from the proximity of the surface to the NSTO/LMO interface. While the 10-nm film behaves similar to bulk LMO powder, thinner films behave more like the NSTO substrate. In contrast to metals, where charge-transfer or ligand effects,[25,26] are limited to adjacent planes of atoms due to free electron screening, semiconductors such as LMO can support charge transfer over multiple unit cells, which could influence the ORR activities of LMO films only a few nanometers in thickness.

In order to probe the electronic structure at the surface and the possible physical origin of the reduced ORR activities of very thin LMO films, we utilize the redox couple ferri/ferrocyanide, $[Fe(CN)_6]^{3-/4-}$, where this outer sphere redox reaction with facile kinetics can measure the ease of electron transfer from the electrode surface to the redox couple in the electrolyte. The ease of a given electron transfer to or from the electrode surface is reflected qualitatively by the proximity of the peak maximum to the equilibrium voltage, 1.2 V vs. RHE. **Figure D-13A** shows the CV curves of LMO films of different thicknesses immersed in a 0.1 M KOH electrolyte with equal molarity of both oxidized and reduced forms of the redox couple. The redox of $[Fe(CN)_6]^{3-/4-}$ occurs readily on the 10 nm film, with comparable oxidation and reduction current peak intensities, similar to the result on metallic surfaces. However, the charge transfer becomes increasingly sluggish for thinner films; the oxidation and reduction currents were found to diminish and approach that of the NSTO substrate (**Figure D-13B**) with decreasing thickness from 5 to 1 nm, which was accompanied with negative shifts in the reduction potential. Remarkably, the oxidation currents became rectified for films of 2 and 1 nm.

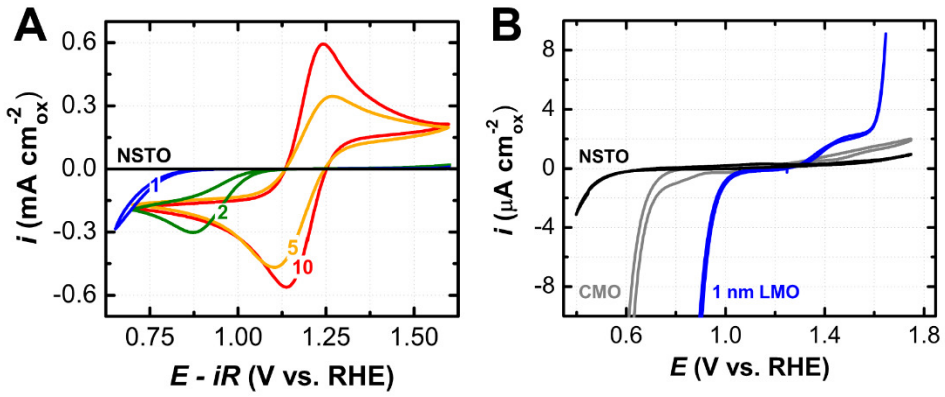

Figure D-13. *Cyclic voltammetry (CV) plot at 10 mV/s in Ar–saturated 0.1 M KOH for the* $[Fe(CN)_6]^{3-/4-}$ *redox couple. (A) LMO films of 1, 2, 5, and 10 nm thickness, in addition to a blank NSTO substrate (black). (B) NSTO, a 5 nm CMO film (gray) and 1 nm LMO film (blue).*

To explain the physical origin of the observed redox behaviors of $[Fe(CN)_6]^{3-/4-}$, we first consider a bare NSTO/$[Fe(CN)_6]^{3-/4-}$ solid/liquid junction. In this configuration, the difference between the surface Fermi level, E_F, and that of the redox couple determines band bending at the interface. This difference can be estimated by the difference in the work function, ϕ, of n-type NSTO, which is 4.1 eV[27] as shown in **Figure D-14A**, and the equilibrium potential for $[Fe(CN)_6]^{3-/4-}$ (equal concentrations of Fe(II)and Fe(III) species in 0.1 M KOH), which is at 4.9 eV (measured experimental value of 1.2 V vs. RHE, converted to vacuum using H_2/H^+ at 4.5 eV[28]). Once contacted, the electrochemical potential difference between the NSTO and the electrolyte will drive electrons away from the surface, consequently forming a depletion layer inside NSTO. From the charge transfer viewpoint, this will cause the bands to bend up, which presents an electron transfer barrier, as shown in **Figure D-14B**. The effective resistance of the junction is then much greater than the electrolyte resistance of ~45 Ω cm^{-2}. Therefore, conducting electrochemistry of the $[Fe(CN)_6]^{3-/4-}$ redox on NSTO will require significant overpotential in order to overcome the depletion layer barrier ($\phi_{NSTO} - \phi_{Fe(CN)6} \approx 0.8$ eV). This is qualitatively reflected in the overpotential (~0.7 V, negative potential shift relative to the equilibrium redox potential) needed to obtain appreciable reduction current in the $[Fe(CN)_6]^{3-/4-}$ reaction (**Figure D-13**).

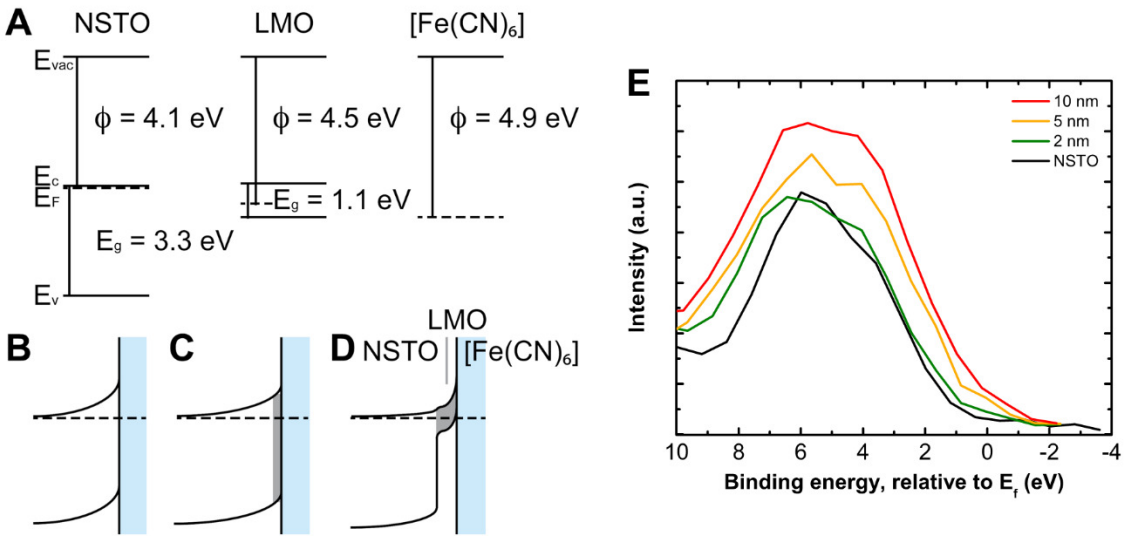

Figure D-14. *(A) Band diagrams for NSTO[27] and LMO[18,29] measured in the bulk, and the electrolyte used in the $[Fe(CN)_6]^{3-/4-}$ reaction. (B) For an NSTO substrate in electrolyte, the surface will be depleted of electrons. (C) When covered by a thin (~2 nm) LMO film, the surface depletion will be lessened. (D) With a 10 nm LMO film, the p-type LMO is effectively degenerate. (E) XPS of LMO films of 2 (green), 5 (orange), and 10 nm (red) thickness, as well as a blank NSTO substrate (black). The binding energy is calibrated to the Fermi level, E_F, by defining the binding energy of adventitious carbon to 285 eV.[17]*

With the framework to understand the difficulty in redox of the $[Fe(CN)_6]^{3-/4-}$ at a bare NSTO substrate, we now discuss the role of the LMO films. In the case of a 10 nm LMO film, the E_F of this film is assumed be well approximated by the bulk value (4.5 eV),[18,29,30] which is higher than that of the electrolyte (4.9 eV), as shown in **Figure D-14D**. In the NSTO/LMO/$[Fe(CN)_6]^{3-/4-}$ configuration, the incipient p-type LMO would donate electrons to the electrolyte, and form a depletion layer near the surface while the n-type NSTO substrate could donate its electrons to LMO. Because the E_F of the LMO lies between that of the NSTO and $[Fe(CN)_6]^{3-/4-}$, the presence of the film reduces the barrier associated with electron depletion seen by NSTO, allowing charge to transfer in and out of the electrode surface more efficiently. Thus, the layer next to the substrate is electron-rich, whereas that at the surface has the bulk electron concentration or less, depending on the degree of charge transfer to the electrolyte. As the traditional rigid band approach has shown that the depletion width of LMO on NSTO is estimated to be < 6 nm,[30] the LMO-10-nm/electrolyte interface is not influenced by the NSTO/LMO interface, effectively making a degenerately doped layer for the $[Fe(CN)_6]^{3-/4-}$ redox (**Figure D-14D**) at the

LMO/electrolyte interface. We propose this as the reason why LMO of 10 nm exhibits reversible redox of $[Fe(CN)_6]^{3-/4-}$, in contrast to bare NSTO.

To understand the sluggish redox kinetics of $[Fe(CN)_6]^{3-/4-}$ on LMO films thinner than 10 nm, we discuss the influence of thickness on the interaction between NSTO and LMO. Considering the NSTO/LMO junction in the absence of an electrolyte, electrons will be transferred from the high Nb 4d donor state into LMO, thus raising E_F relative to bulk because ϕ_{NSTO} (4.1 eV) is less than ϕ_{LMO} (4.5 eV). As the physical dimension of the film encroaches on the space charge layer, the behavior of the film becomes dominated by the NSTO/LMO interface, which results in the LMO becoming more negatively charged. Such a change is in agreement with XPS data, which shows that the valence band becomes more narrow and moves farther from E_F with decreasing film thickness from 10 nm (**Figure D-14E**). The lack of sufficient thickness required to establish a space charge as a result of this geometric limitation results in the fact that LMO is unable to form two junctions below 10 nm.[30] As a result, the thin LMO films become less effective in reducing the electrode/electrolyte barrier (**Figure D-14C**), which is in agreement with increasing sluggishness of the redox of $[Fe(CN)_6]^{3-/4-}$. This change is supported by EIS data, which show a dominant capacitor-like behavior for the NSTO substrate and films of 1 and 2 nm, but a dominant resistor-like behavior for LMO of 5 and 10 nm (**Figure D-15A**). The impedance intercept projected from the linear regime gives a capacitance of 1.7 μF for the NSTO, increasing to 3.5 μF for the 2 nm film.

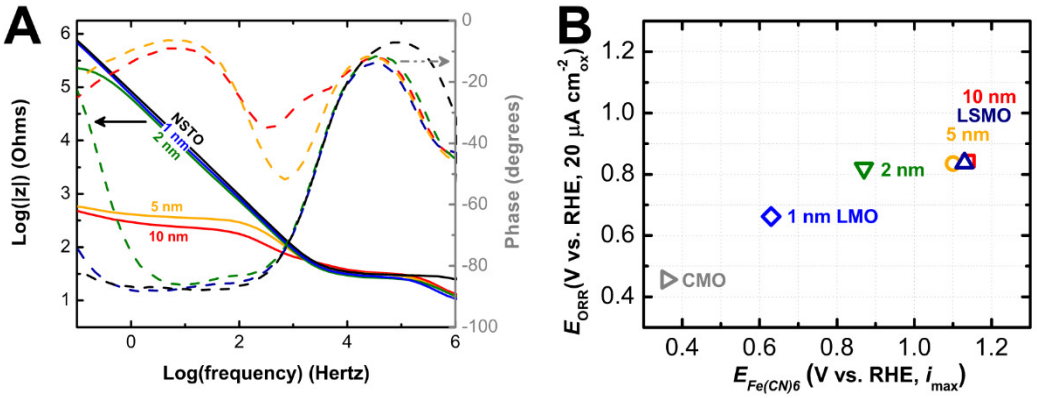

Figure D-15. *(A) Electrical impedance spectroscopy (EIS) presented as a Bode plot: solid lines (left axis) show the magnitude of impedance, |z|, on a log scale vs. frequency on a log scale, and dashed lines (right axis) plot the phase against the same abscissa. EIS was taken at the open circuit voltage (1.2 V vs. RHE) in 0.1 M KOH with the* $[Fe(CN)_6]^{3-/4-}$ *redox couple for LMO films of 10 (red), 5 (orange), 2 (green), and 1 nm (blue) thickness, as well as a blank NSTO substrate (black). (B) Plot of the potential required to achieve 20* $\mu A/cm^2_{ox}$ *of oxygen reduction current*

from capacitance-corrected CVs, E_{ORR}, vs. the potential corresponding to the maximum reduction current of $[Fe(CN)_6]^{3-}$, $E_{Fe(CN)6}$.

While the trend in the ORR activities with thinner films can be explained in part by the barrier of the electro-reduction as revealed by the $[Fe(CN)_6]^{3-/4-}$ reaction studies, the role of catalysts in stabilizing adsorbed intermediates requires us to additionally consider the electronic state of the Mn at the surface. As a result of the increasing E_F of LMO with decreasing thickness, the e_g orbital occupation for thinner films would also increase from one toward two as the content of Mn^{2+} increases, provided that Mn^{2+} remains in a high spin state. Thus, the reduced activity measured on these films is likely a result of (1) the barrier arising from band bending at the electrode/electrolyte interface, which indiscriminately reduces both $[Fe(CN)_6]^{3-/4-}$ and ORR electro-kinetics (**Figure D-15B**), and (2) reduction in Mn^{3+} character, which negatively affects the intrinsic catalytic activity of the thin LMO films by affecting the surface's ability to stabilize intermediate species.[4] Reduction in Mn^{3+} character of LMO films of 1, 2 and 5 nm is further supported by reduction in the Mn valence state with decreasing thickness, as revealed from XAS data of the Mn L-edges, shown in **Figure D-16**. The spectrum of the 10 nm film is characteristic of that for the Mn^{3+} state, which is distinct from reference spectra for Mn(II)O, and $Sr_4Mn(IV)_2CoO_9$. With decreasing thickness, we observed an increase in the peak amplitude of the low-energy feature at ~641.5 eV, which is characteristic of electron doping of LMO.[31,32] The reduction of Mn valence state with decreasing thickness can be considered analogous to the space-charge layer in a semiconductor p-n junction, where the extent of charge donation (and reduction to Mn^{2+}) increases drastically as the film is thinner and terminated closer to the substrate. Our spectroscopic result thus confirms the earlier suggestion of the raising of E_F from interaction with NSTO, manifested as the conversion of Mn^{3+} to Mn^{2+} for thinner films.

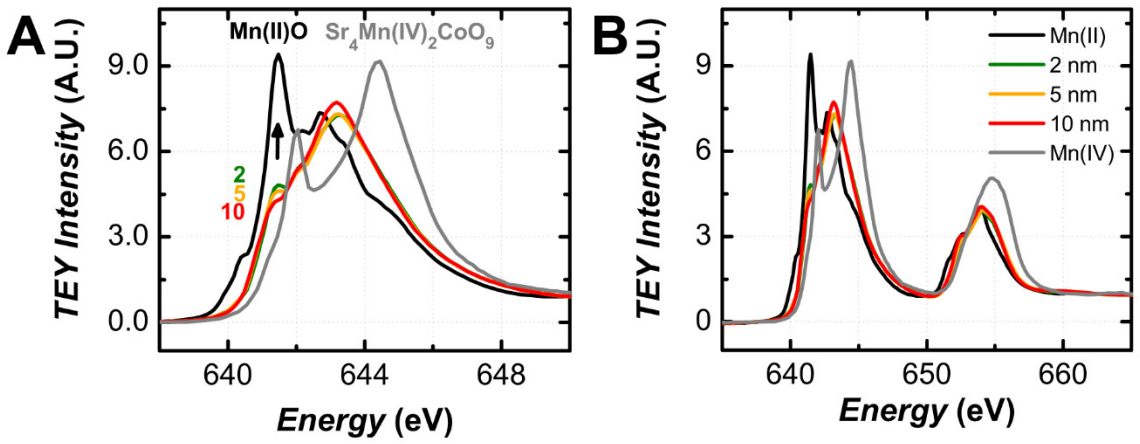

Figure D-16. *X-ray absorption spectra (XAS) acquired in total electron yield (TEY) mode at the Mn L_3-edge. (A) LMO films of 2, 5, and 10 nm thickness are compared to references of Mn(II)O and $Sr_4Mn(IV)_2CoO_9$. The increase in amplitude at ~641.5 eV indicates that thinner films are characterized by conversion of Mn^{3+} to Mn^{2+}. (B) Extended range. Electrochemical measurements for this set of films are presented in Figure D-4.*

We note that electron donation from NSTO to LMO as found in this study is opposite of that reported for LMO grown on undoped $SrTiO_3$ (STO), where a polar discontinuity results in electron doping of the TiO_2 layer to form Ti^{3+} at the interface[33] and an accumulation of holes in the LMO layer.[34,35] The difference in electron transfer between LMO/NSTO thin films and LMO/STO heterostructures may arise from the less effective pinning of the lattice parameter for single layer, uncapped films compared to superlattices and the ability of energetic Nb 4d states to serve as an electron donor. Our view is that superlattice structuring can provide a further avenue to manipulate the charge transfer between the titanate and the manganite layers. For example, it was found the direction of charge transfer between STO and LMO could be modulated by controlling the thickness of the STO layer, where 17 unit cells (~7 nm) of LMO were hole-doped when alternated with 2 unit cells (~1 nm) of STO but electron-doped with thicker STO layers (12 unit cells, ~5 nm).[36] Identifying more active ORR electrocatalysts via superlatticing is the subject of our current pursuit and will be discussed in a future communication.

D.4. Conclusions

This appendix has shown that (001)-oriented LMO perovskite films have intrinsic activities comparable to that of high-surface-area LMO powder catalysts, which suggests the (001) surface may be the activity-dominant facet. By tuning the Mn valence state via A-site

substitution, we clearly demonstrate that Mn^{3+} is the active valence state for ORR, in agreement with the requirement of single e_g occupancy for high ORR activity as previously reported for particles.[4] ORR activities of LMO films grown on NSTO decrease with decreasing thickness. Using $[Fe(CN)_6]^{3-/4-}$ redox to probe electron transfer kinetics and synchrotron X-ray techniques to reveal Mn valence state changes, we determine that this trend can be attributed to the barrier associated with interfacial band bending that impedes electron transfer at the electrode/electrolyte junction, and increased e_g orbital occupancy compared to that of Mn^{3+} by proximity to an electron-rich substrate, which affects the ability of the surface to stabilize ORR intermediates. This new insight demonstrates the importance of charge transfer at support/catalyst and catalyst/electrolyte interfaces in influencing oxygen electrocatalysis, and provides an important framework for future design of thin-film oxide catalysts, whose activity and selectivity for energy conversion reactions can benefit from further tuning of the electronic structure of well-defined oxide surfaces.

References

1 Suntivich, J., Gasteiger, H. A., Yabuuchi, N. & Shao-Horn, Y. Electrocatalytic Measurement Methodology of Oxide Catalysts Using a Thin-Film Rotating Disk Electrode. *Journal of The Electrochemical Society* **157**, B1263-B1268, (2010).

2 Poux, T. *et al.* Dual role of carbon in the catalytic layers of perovskite/carbon composites for the electrocatalytic oxygen reduction reaction. *Catalysis Today* **189**, 83-92, (2012).

3 Sunarso, J., Torriero, A. A. J., Zhou, W., Howlett, P. C. & Forsyth, M. Oxygen Reduction Reaction Activity of La-Based Perovskite Oxides in Alkaline Medium: A Thin-Film Rotating Ring-Disk Electrode Study. *The Journal of Physical Chemistry C* **116**, 5827-5834, (2012).

4 Suntivich, J. *et al.* Design principles for oxygen-reduction activity on perovskite oxide catalysts for fuel cells and metal–air batteries. *Nat Chem* **3**, 546-550, (2011).

5 Matsumoto, Y., Yoneyama, H. & Tamura, H. Catalytic activity for electrochemical reduction of oxygen of lanthanum nickel oxide and related oxides. *Journal of Electroanalytical Chemistry and Interfacial Electrochemistry* **79**, 319-326, (1977).

6 Han, X., Zhang, T., Du, J., Cheng, F. & Chen, J. Porous calcium-manganese oxide microspheres for electrocatalytic oxygen reduction with high activity. *Chemical Science* **4**, 368-376, (2013).

7 Tulloch, J. & Donne, S. W. Activity of perovskite $La_{1-x}Sr_xMnO_3$ catalysts towards oxygen reduction in alkaline electrolytes. *Journal of Power Sources* **188**, 359-366, (2009).

8 Débart, A., Paterson, A. J., Bao, J. & Bruce, P. G. α-MnO_2 Nanowires: A Catalyst for the O_2 Electrode in Rechargeable Lithium Batteries. *Angewandte Chemie International Edition* **47**, 4521-4524, (2008).

9 Valim, R. B. *et al.* Oxygen reduction reaction catalyzed by ε-MnO_2: Influence of the crystalline structure on the reaction mechanism. *Electrochimica Acta* **85**, 423-431, (2012).

10 Pickrahn, K. L. *et al.* Active MnO_x Electrocatalysts Prepared by Atomic Layer Deposition for Oxygen Evolution and Oxygen Reduction Reactions. *Advanced Energy Materials* **2**, 1269-1277, (2012).

11 Gorlin, Y., Chung, C.-J., Nordlund, D., Clemens, B. M. & Jaramillo, T. F. Mn_3O_4 Supported on Glassy Carbon: An Active Non-Precious Metal Catalyst for the Oxygen Reduction Reaction. *ACS Catalysis* **2**, 2687-2694, (2012).

12 Lee, J.-S. *et al.* Ketjenblack Carbon Supported Amorphous Manganese Oxides Nanowires as Highly Efficient Electrocatalyst for Oxygen Reduction Reaction in Alkaline Solutions. *Nano Letters* **11**, 5362-5366, (2011).

13 Cheng, F., Su, Y., Liang, J., Tao, Z. & Chen, J. MnO_2-Based Nanostructures as Catalysts for Electrochemical Oxygen Reduction in Alkaline Media†. *Chemistry of Materials* **22**, 898-905, (2009).

14 Komo, M., Hagiwara, A., Taminato, S., Hirayama, M. & Kanno, R. Oxygen Evolution and Reduction Reactions on $La_{0.8}Sr_{0.2}CoO_3$ (001), (110), and (111) Surfaces in an Alkaline Solution. *Electrochemistry* **80**, 834-838, (2012).

15 Wang, J. *et al.* Epitaxial $BiFeO_3$ Multiferroic Thin Film Heterostructures. *Science* **299**, 1719-1722, (2003).

16 Garcia-Barriocanal, J. *et al.* Colossal Ionic Conductivity at Interfaces of Epitaxial ZrO_2:Y_2O_3/$SrTiO_3$ Heterostructures. *Science* **321**, 676-680, (2008).

17 Johansson, G., Hedman, J., Berndtsson, A., Klasson, M. & Nilsson, R. Calibration of electron spectra. *Journal of Electron Spectroscopy and Related Phenomena* **2**, 295-317, (1973).

18 Kida, T., Guan, G. & Yoshida, A. $LaMnO_3$/CdS nanocomposite: a new photocatalyst for hydrogen production from water under visible light irradiation. *Chemical Physics Letters* **371**, 563-567, (2003).

19 Karczewski, J., Riegel, B., Gazda, M., Jasinski, P. & Kusz, B. Electrical and structural properties of Nb-doped $SrTiO_3$ ceramics. *Journal of Electroceramics* **24**, 326-330, (2010).

20 Thole, B. T. & van der Laan, G. Branching ratio in x-ray absorption spectroscopy. *Physical Review B* **38**, 3158-3171, (1988).

21 Qiao, R., Chin, T., Harris, S. J., Yan, S. & Yang, W. Spectroscopic fingerprints of valence and spin states in manganese oxides and fluorides. *Current Applied Physics* **13**, 544-548, (2013).

22 Boulahya, K., Parras, M., González-Calbet, J. M. & Martínez, J. L. Synthesis, Structural Characterization, and Magnetic Study of $Sr_4Mn_2CoO_9$. *Chemistry of Materials* **15**, 3537-3542, (2003).

23 Xiao, W., Wang, D. & Lou, X. W. Shape-Controlled Synthesis of MnO_2 Nanostructures with Enhanced Electrocatalytic Activity for Oxygen Reduction. *The Journal of Physical Chemistry C* **114**, 1694-1700, (2009).

24 Su, H.-Y. *et al.* Identifying active surface phases for metal oxide electrocatalysts: a study of manganese oxide bi-functional catalysts for oxygen reduction and water oxidation catalysis. *Physical Chemistry Chemical Physics* **14**, 14010-14022, (2012).

25 Hyman, M. P. & Medlin, J. W. Effects of Electronic Structure Modifications on the Adsorption of Oxygen Reduction Reaction Intermediates on Model Pt(111)-Alloy Surfaces. *The Journal of Physical Chemistry C* **111**, 17052-17060, (2007).

26 Kitchin, J. R., Norskov, J. K., Barteau, M. A. & Chen, J. G. Modification of the surface electronic and chemical properties of Pt(111) by subsurface 3d transition metals. *The Journal of Chemical Physics* **120**, 10240-10246, (2004).

27 Zagonel, L. F. *et al.* Orientation-dependent work function of in situ annealed strontium titanate. *Journal of Physics: Condensed Matter* **21**, 314013, (2009).

28 Gratzel, M. Photoelectrochemical cells. *Nature* **414**, 338-344, (2001).

29 Horiba, K. *et al.* In vacuo photoemission study of atomically controlled $La_{1-x}Sr_xMnO_3$ thin films: Composition dependence of the electronic structure. *Physical Review B* **71**, 155420, (2005).

30 Nakamura, M., Sawa, A., Fujioka, J., Kawasaki, M. & Tokura, Y. Interface band profiles of Mott-insulator/Nb:$SrTiO_3$ heterojunctions as investigated by optical spectroscopy. *Physical Review B* **82**, 201101, (2010).

31 Mitra, C. *et al.* Direct observation of electron doping in $La_{0.7}Ce_{0.3}MnO_3$ using x-ray absorption spectroscopy. *Physical Review B* **67**, 092404, (2003).

32 Han, S. W. *et al.* Photoemission and x-ray absorption spectroscopy study of electron-doped colossal magnetoresistive manganite $La_{0.7}Ce_{0.3}MnO_3$ films. *Physical Review B* **69**, 104406, (2004).

33 Garcia-Barriocanal, J. *et al.* Spin and orbital Ti magnetism at $LaMnO_3/SrTiO_3$ interfaces. *Nat Commun* **1**, 82, (2010).

34 Shah, A. B. *et al.* Probing Interfacial Electronic Structures in Atomic Layer $LaMnO_3$ and $SrTiO_3$ Superlattices. *Advanced Materials* **22**, 1156-1160, (2010).

35 Yamada, H. *et al.* Engineered Interface of Magnetic Oxides. *Science* **305**, 646-648, (2004).

36 Garcia-Barriocanal, J. *et al.* "Charge Leakage" at $LaMnO_3/SrTiO_3$ Interfaces. *Advanced Materials* **22**, 627-632, (2010).

E. The effect of strain: epitaxial strain in $LaCoO_3$ films

E.1. Introduction

In alkaline fuel cells, cost-effective transition metal oxides can catalyze oxygen electrocatalysis with comparable activities to precious metal-based catalysts such as Pt for the ORR and RuO_2 for the OER.[1-4] Fundamental research is needed to understand rate-limiting processes and the physical parameters of catalysts that govern the activity in order to develop catalysts with enhanced activities.[5-7]

In investigations of the roles of elemental composition, and electronic and crystal structure on oxide electrocatalytic activity, many studies have focused on powder-based measurements.[2,5,6] Recently, studies have considered the activity of dense polycrystalline[8] or epitaxial perovskite films, the latter providing a new knob to tune oxide crystallographic orientation,[9,10] charge transport,[11] and potentially strain. Strain has proven a useful means to improve the ORR activity of metal surfaces by changing the binding energy of adsorbed intermediates,[12-14] and can alter the defect formation energy and surface oxygen exchange kinetics in solid oxide fuel cells.[15-19] In the case of oxides, strain is also known to impact charge transport properties due to changes in orbital overlap.[20] Variation in orbital overlap can alternatively be induced by cationic substitution, where perovskites with a σ^* conduction band[6] and low resistivity[21] are more active for the ORR. Thus, epitaxial strain in thin films may influence the activity for oxygen electrocatalysis via the adsorption energy of reaction intermediates, the charge transport properties, or a combination thereof.

In order to probe the role of strain and electronic conductivity in oxide materials for oxygen electrocatalysis, we investigated the catalytic activity of $LaCoO_3$ (LCO) thin films, as LCO is reasonably active for both the ORR and OER.[3,22] Recently, several authors have demonstrated that strain can be used to tune the magnetic properties of LCO thin films by increasing the fractional occupancy of higher spin states of Co in the ground state,[20,23-25] expected to affect the strength of the metal-oxygen bond.[26-28] To this end, we conducted a systematic study of epitaxial LCO films with different thicknesses and lattice mismatch with substrates in order to elucidate the effect on oxygen electrocatalysis, as well as asymmetries in the mechanism of the ORR and OER.

E.2. Experimental

Film Fabrication and Characterization. High-quality LCO thin films and LCO/LSMO heterostructures were fabricated by using pulsed laser epitaxy (PLE) on STO (cubic, a = 3.905 Å), LSAT (pseudocubic, a = 3.868 Å), and LAO (pseudocubic, a = 3.79 Å) substrates (CrysTec GmbH). PLE was performed using a KrF excimer laser (λ = 248 nm) with a laser fluence of ~1 J/cm^2 at a repetition rate of 10 Hz. Sintered $La_{0.67}Sr_{0.33}MnO_3$ (LSMO) and $LaCoO_3$ (LCO) targets were used for ablation. The heterostructures were fabricated at 700 °C in 100 mTorr of O_2, and cooled to room temperature in 100 Torr of O_2.

The crystal structure of the heterostructures was examined using x-ray diffraction (XRD) (X'Pert, Panalytical Inc.). LCO films deposited directly onto the chosen substrate, without the LSMO contact layer, show similar strain states (**Figure E-1**), although the precise peak locations are difficult to extract due to thin film interference effects in the LCO/LSMO/substrate case. The nominal strain presented in the main text is from lattice mismatch according to Fuchs:[29] $(a_{SUB} - a_{LCO})/a_{LCO}$, where the pseudo-cubic $a_{LCO} \approx 3.80$ Å.

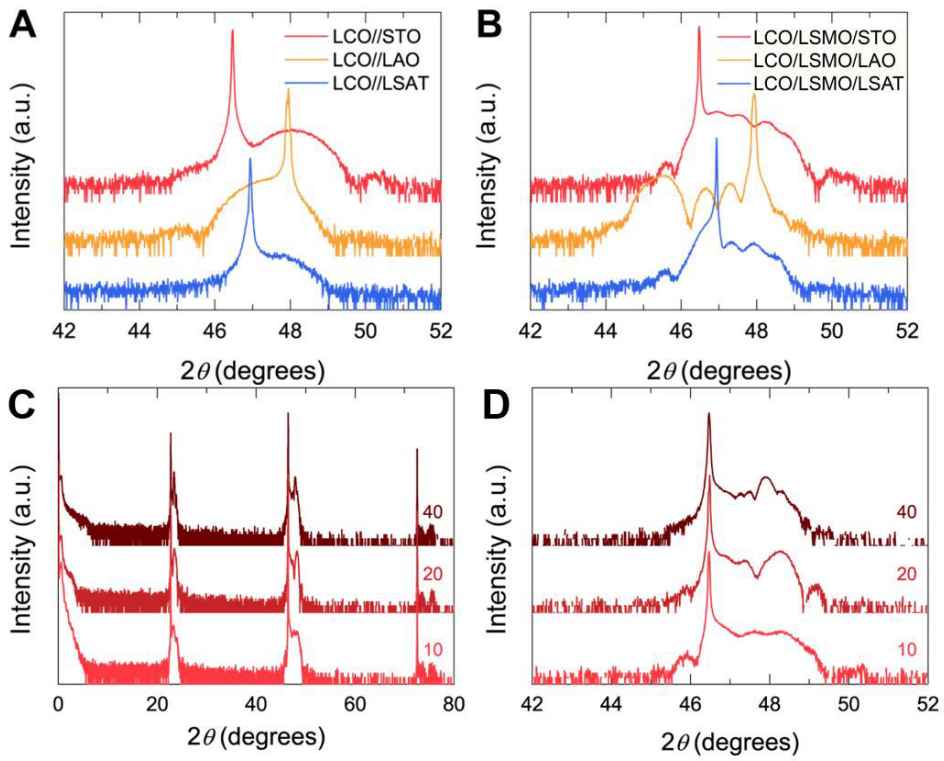

Figure E-1. *Coupled x-ray diffraction 2θ-ω scan at the (002) reflection of strained LCO films (A) grown directly on the insulating substrates of different lattice parameters, and (B) with the use of*

the conductive LSMO interlayer. (C) LCO films of different thicknesses grown on LSMO/STO over a wide range of angles illustrating phase purity, and (D) at the (002) reflection illustrating the relaxation of strain with increased film thickness (shifting to lower angles).

Film surface morphologies were examined by atomic force microscopy (AFM, see **Figure E-2, E-3**) (EnviroScope and Nanoscope IV, Veeco Metrology). Although films exhibit some roughness, the maximum heights were comparable with root-mean-squared (RMS) roughness at ~1 nm (**Table E-1**), projected to modulate the surface area by <1 %, obtained from the Nanoscope analysis software.

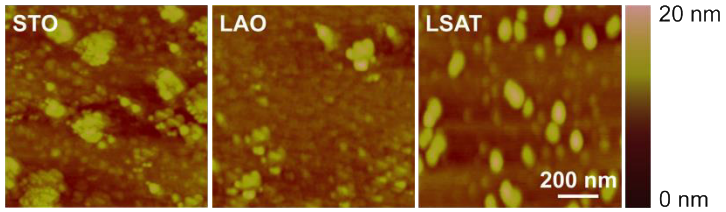

Figure E-2. *Atomic force microscopy (AFM) images of LCO grown on different substrates with conductive LSMO interlayer.*

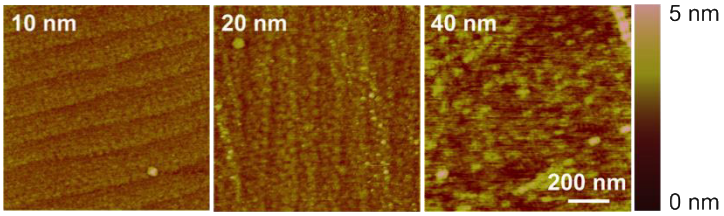

Figure E-3. *AFM images of LCO of different thicknesses grown on STO with conductive LSMO interlayer. The 10 nm LCO film is smoother than that shown in Figure E-2 yet has the same catalytic activity.*

Table E-1. *Roughness and projected difference in surface area for LCO films grown on noted substrates and for LCO films of different thickness grown on LSMO/STO.*

LCO thickness	Substrate	Z_{max} (nm)	RMS (nm)	SA diff (%)
10 nm	LSMO/STO	11.195	1.7	0.729
10 nm	LSMO/LAO	12.169	1.172	0.424
10 nm	LSMO/LSAT	12.795	1.808	0.596
10 nm	LSMO/STO	5.31	0.217	0.402
20 nm	LSMO/STO	4.29	0.291	0.612

40 nm	LSMO/STO	6.23	0.531	1.13

*Electrochemical Measurements***.** In order to affix electrical contacts, gallium–indium eutectic (Sigma-Aldrich, 99.99%) was scratched into a small corner of the film to reach the LSMO layer, and a Ti wire (Sigma-Aldrich, 99.99%) was affixed with silver paint (Ted Pella, Leitsilber 200). The back and sides of the electrode, as well as the wire, were covered with a non-conductive, chemically resistant epoxy (Omegabond 101), so only the catalyst surface was exposed to the electrolyte.

Electrochemical measurements were conducted with a Biologic SP-300 potentiostat in an ~120 mL solution of 0.1 M KOH, prepared from deionized water (Millipore, >18.2 MΩ cm) and KOH pellets (Sigma-Aldrich, 99.99%). Potentials were referenced to a saturated Ag/AgCl or saturated calomel electrode (Pine), both calibrated to the reversible hydrogen electrode (RHE) scale in 0.1 M KOH. Electrical impedance spectroscopy (EIS) was performed at the open circuit voltage with an amplitude of 10 mV. Potentials were corrected for the electrolyte/cell resistance from the high frequency intercept of the real impedance (~45 Ω).

Measurements of the oxygen reduction and evolution reactions (ORR, OER) were carried out in 0.1 M KOH electrolyte pre-saturated by bubbling O_2 for ~30 minutes and under continuous O_2 bubbling (Airgas, ultrahigh-grade purity) to fix the equilibrium potential. Cyclic voltammetry (CV) scans were performed at a sweep rate of 10 mV/s, starting and finishing at open circuit voltage, sweeping from 1.0 down to 0.7 and up to 1.7 V vs RHE for the ORR and OER, respectively. Discrete points on the Tafel plot were obtained from potentiostatic measurements. Measurements of the $[Fe(CN)_6]^{3-/4-}$ reaction were carried out after performing the OER, in an Ar-saturated (Airgas, ultrahigh-grade purity) solution of 0.1 M KOH, to which 5 mM each of $K_4Fe(CN)_6$-$3H_2O$ (Sigma-Aldrich, 99.99%) and $K_3Fe(CN)_6$ (Sigma-Aldrich, 99%) were added. The potential was swept from 0.7 to 1.55 or 1.6 V vs. RHE at a rate of 10 mV/s, starting and finishing at open circuit voltage.

E.3. Results and discussion

LCO thin films (10 nm in thickness) were grown by pulsed laser deposition on a 10 nm conductive interlayer of $La_{0.67}Sr_{0.33}MnO_3$ (LSMO) on insulating (001)-oriented $SrTiO_3$ (STO), $(LaAlO_3)_{0.3}(Sr_2AlTaO_6)_{0.7}$ (LSAT), and $LaAlO_3$ (LAO) substrates. For electrochemical measurements, a wire was affixed to the LSMO interlayer; this contact and the back and sides of the electrode were then coated with epoxy to define the catalyst surface area (**Figure E-4**). X-ray diffraction (XRD) confirms good crystallinity and matching orientation with the substrate,

illustrating strain-induced lattice elongation along the out-of-plane direction by the shifts in diffraction peak location, marked with a * in **Figure E-4C**. Note that XRD reciprocal space mapping confirms all films are epitaxially strained with the in-plane lattice constants coherently matched with those of the substrate. Similar catalytic activity was found for an LCO/Nb:$SrTiO_3$ film in which the conductive substrate was contacted at the back, suggesting that use of the LSMO layer does not affect the measured catalytic activity of the LCO film (**Figure E-5**). X-ray photoelectron spectroscopy (XPS) confirms complete coverage of the substrate by LCO and no discernable change from nominal valence state of 3+ from the Co 2*p* core level[30,31] (**Figure E-6**).

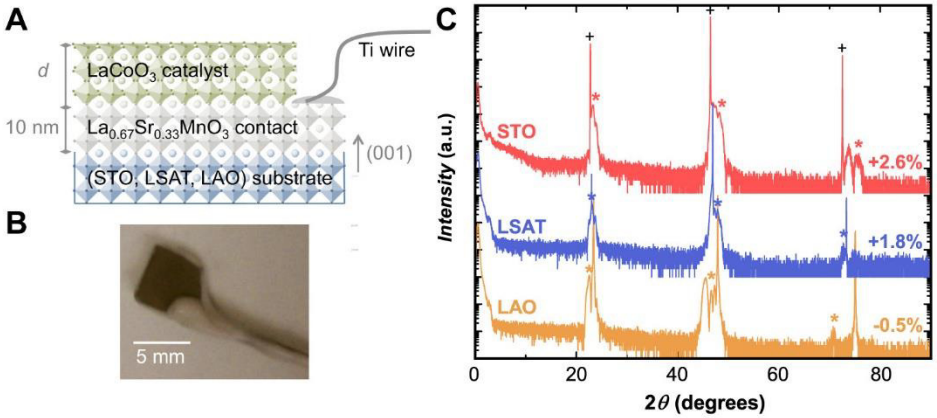

Figure E-4. *(A) Cross-sectional schematic of the samples. For electrical contact, a 10 nm layer of $La_{0.67}Sr_{0.33}MnO_3$ (LSMO) was grown on top of insulating substrates with different lattice constants (STO, LSAT, and LAO). The d = 10 nm $LaCoO_3$ (LCO) catalysts were then grown on top of the electrically conducting layer. (B) Photograph of a prepared electrode with the contact to the LSMO layer and sample sides covered with an inert epoxy, isolating the catalyst surface. (C) XRD 2θ-ω scans for 10 nm LCO films with 10 nm LSMO interlayers grown on the noted substrates with corresponding nominal strain: STO (+2.6%, red), LSAT (+1.8%, blue), and LAO (-0.5%, yellow), with substrate peaks marked by a +. The systematic shifts of the Bragg peaks from the LCO films are marked with a *, illustrating the change in out-of-plane lattice constant, and thereby, the biaxial strain in the films.*

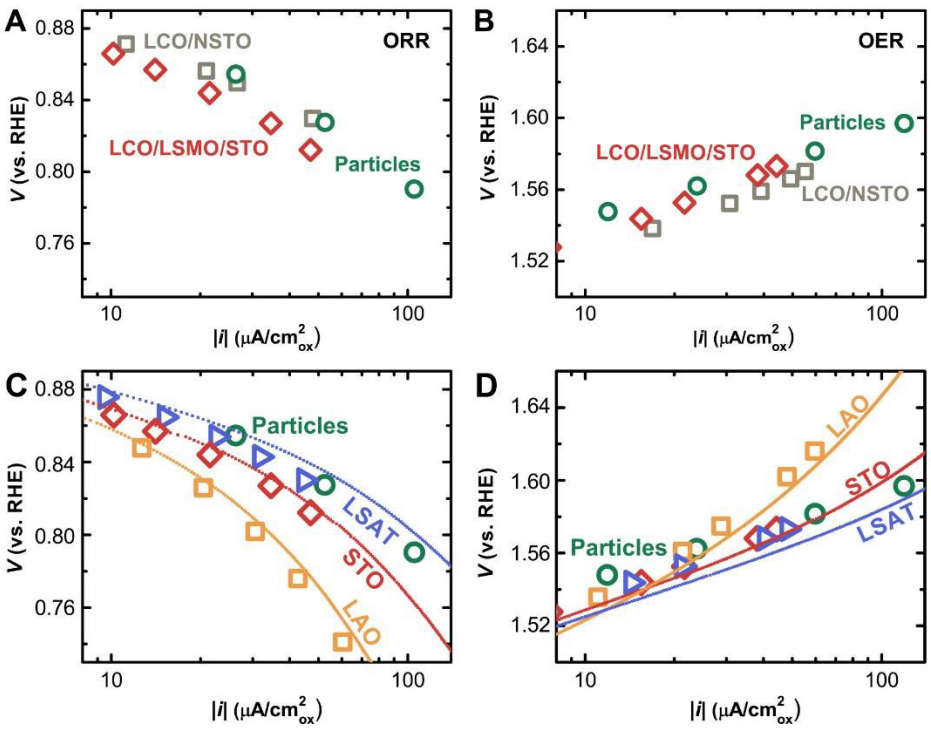

Figure E-5. *Comparison of (A) ORR activity and (B) OER activity for LCO in different electrode configurations: LCO grown on STO on top of a conductive layer of LSMO used for contacting (red diamonds), LCO grown on conductive Nb-doped $SrTiO_3$ (NSTO), contacting the backside of the NSTO substrate (gray squares),[32] and LCO particles interspersed with high surface area carbon and Nafion, where the surface area was quantified by scanning electron microscopy (green circles).[22,33] (C) Capacitance corrected cyclic voltammetry (CV), taking the average of forward and backward sweeps at a scan rate of 10 mV/s for 10-nm-LCO/10-nm-LSMO films grown on the noted substrate of STO (red line), LSAT (blue line), and LAO (yellow line). Overlayed are potentiostatic measurements (constant applied voltage) of ORR (points in corresponding color), with particles[33] in green. (D) CV and potentiostatic measurements as above, but for OER, with particles[22] in green.*

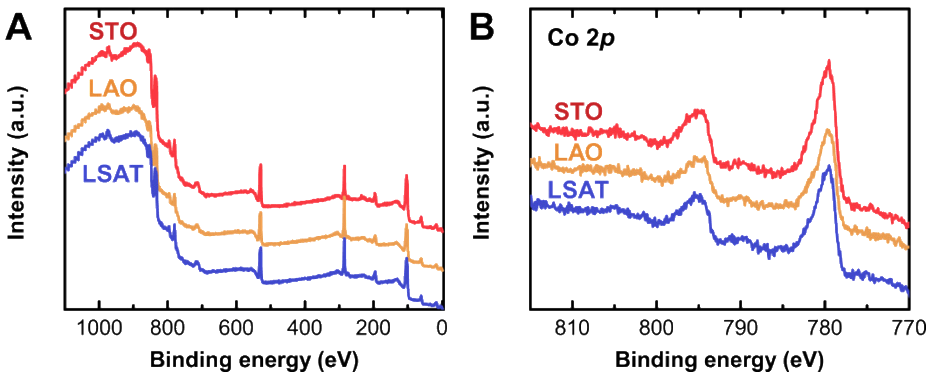

Figure E-6. *X-ray photoelectron spectroscopy (XPS) of strained LCO films confirming (A) complete coverage from the lack of Sr and Mn in survey spectrum and (B) identical Co 2p spectra, suggesting no notable change in surface valence state from nominal 3+*[30,31] *for LCO films grown on the noted substrates with LSMO interlayer: STO (red), LAO (yellow), LSAT (blue).*

Tensile strain was found to increase the ORR activity measured in O_2-saturated 0.1 M KOH from cyclic voltammetry (**Figure E-7A, E-8**) and potentiostatic measurements (**Figure E-7B**). Both measurements yield comparable activities, which are similar to that found in powder[3,22] (**Figure E-5**) with surface area of mixed orientations estimated from scanning electron micrographic images of representative particles. The activity of compressively strained LCO grown on LAO was the lowest while that of moderate tensile strain grown on LSAT was the most active. A similar trend was found for the OER (**Figure E-7C, D**), where the activity of LCO increased in the order of the substrates LAO < STO < LSAT, although the effect was smaller in magnitude. The increase in magnitude of the Tafel slope for the less active LCO film grown on LAO suggests poorer charge transfer kinetics compared to other films.[34,35] Given low current densities where kinetics are rate limiting, the greater change in voltage required to obtain a given increment of current is expected to correlate to increased resistance of charge transport through the film and/or charge transfer to adsorbates.

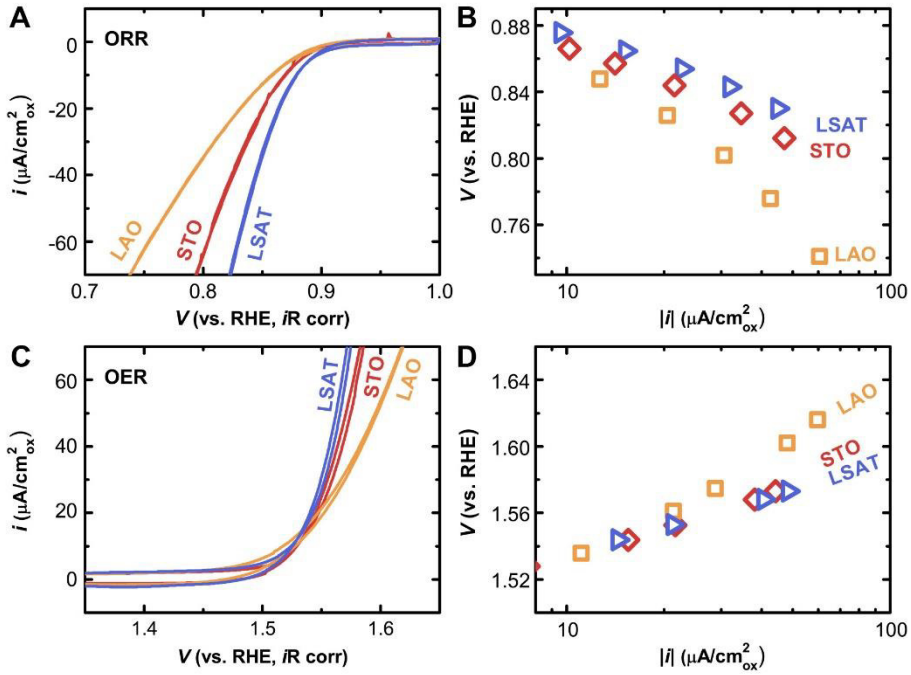

Figure E-7. *(A) Cyclic voltammetry (CV) for the ORR at a scan rate of 10 mV/s in O_2-saturated 0.1 M KOH, showing the current per surface area (i) vs. the applied voltage corrected for electrolyte resistance (E-iR) for 10-nm-LCO films grown on the noted substrate of STO (red), LSAT (blue), and LAO (yellow). (B) Tafel plot from potentiostatic measurements of the ORR (constant applied voltage, points) showing E-iR vs. |i| on a logarithmic scale for films grown on the noted substrates of STO (red, diamonds), LSAT (blue, triangle), and LAO (yellow, square). (C) CV for the OER as above. (D) Tafel plot from potentiostatic measurements of the OER as above.*

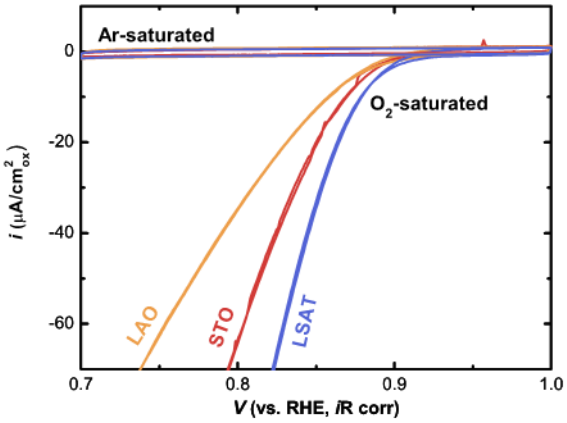

Figure E-8. *Comparison of the current measured under ORR conditions, where 0.1 M KOH is saturated with O_2 gas, to the background capacitance measured in Ar-saturated electrolyte. All films show comparable capacitance without notable features.*

To further investigate the role of strain via relaxation within the catalyst layer, LCO films 10, 20, and 40 nm in thickness were grown on LSMO contact layer covered STO substrates (**Figure E-1, E-3**). Thicker films were less active, again with the effect being greater on the ORR (**Figure E-9A**) than the OER (**Figure E-9B**). Interestingly, the activities of the 20 and 40 nm films grown on STO were lower than the compressively strained 10-nm-LCO film grown on LAO (**Figure E-7**), despite the expected relaxation of strain with increased film thickness, evident by the shift to lower out-of-plane 2θ values by XRD (**Figure E-1**). This result suggests that the effect of LCO thickness on catalysis is not solely due to changing the lattice constant. To this end, we probe electronic transport within the film and subsequent charge transfer to adsorbed intermediates, where film thickness may have a notable effect on out-of-plane resistance and thus activity.

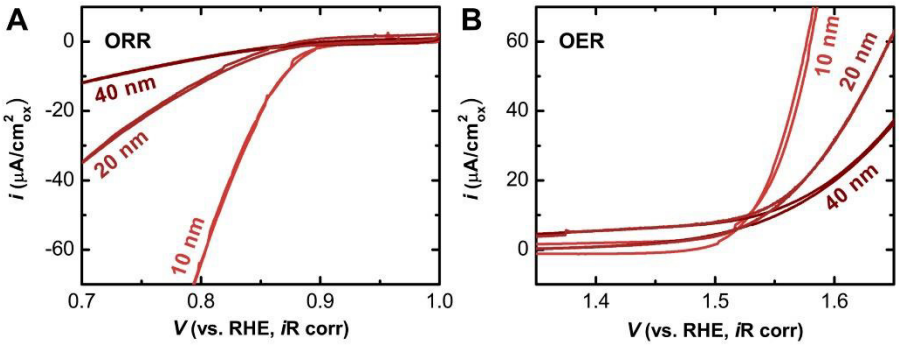

Figure E-9. *(A) Cyclic voltammetry (CV) for the ORR at a scan rate of 10 mV/s in O_2-saturated 0.1 M KOH, showing the current per surface area (i) vs. the applied voltage corrected for*

electrolyte resistance (E-iR) for films grown on LSMO/STO, with thickness of 10 nm (light red), 20 nm (medium red), and 40 nm (dark red).

We hypothesize that thicker LCO films hinder bulk electronic transport (characterized by resistance R_{trans}) from the LSMO interlayer used for contact to the film surface. In the simplest case, this could be considered a voltage drop ($V=iR_{trans}$) which occurs throughout the film, resulting in a reduced potential to promote catalysis. To characterize electron transfer within the electrode and at the film-electrolyte interface, we utilized the facile outer sphere redox couple ferri/ferrocyanide, $[Fe(CN)_6]^{3-/4-}$. For the strained LCO films grown on different substrates (**Figure E-10A**), all can pass notable current at the voltages corresponding to the ORR and OER (0.9 and 1.5 V vs. RHE) and exhibit symmetric redox behavior around the $[Fe(CN)_6]^{3-/4-}$ equilibrium voltage of ~1.2 V vs. RHE. Spreading of the redox peaks away from the equilibrium voltage is characteristic of higher resistance in the system (**Figure E-10, E-11, Table E-2**). Performing electrochemical impedance spectroscopy (EIS) at open circuit enabled the different origins of resistance to be isolated and quantified by their frequency dependence.[36] The resistances associated with charge transport to the surface through the film (R_{trans}) at medium frequencies and that with charge transfer to the electrolyte (R_{CT}) at low frequencies change notably with film strain and thickness.

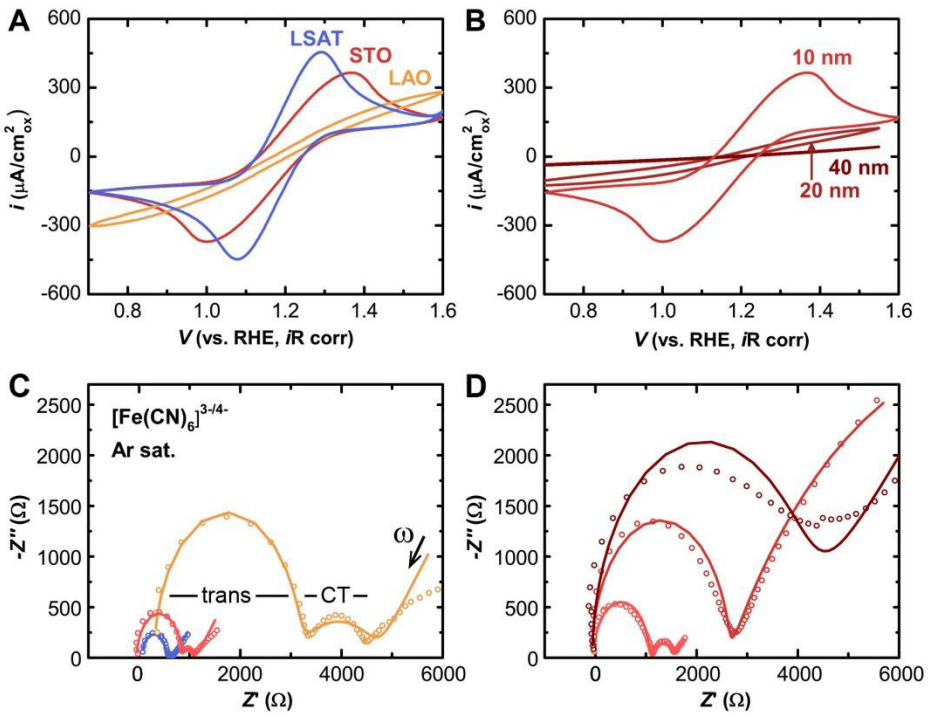

Figure E-10. *(A) Cyclic voltammetry (CV) at a scan rate of 10 mV/s in 0.1 M KOH, Ar-saturated with 5 mM each* $[Fe(CN)_6]^{3-/4-}$ *showing the current per surface area (i) vs. the applied voltage corrected for electrolyte resistance (E-iR) for 10-nm films grown on LSMO on the noted substrate of STO (red), LSAT (blue), and LAO (yellow). (B) CV as above for films grown on LSMO/STO, with thickness of 10 nm (light red), 20 nm (medium red), and 40 nm (dark red). (C) Electrochemical impedance spectroscopy (EIS) at the open circuit voltage (~1.2 V vs. RHE), with an arrow indicates the direction of increasing frequency, ω. Raw data are shown as circles, and solid lines are fits from the representative circuit in* ***Figure E-11****. (D) EIS at the open circuit voltage as above for films of different thickness.*

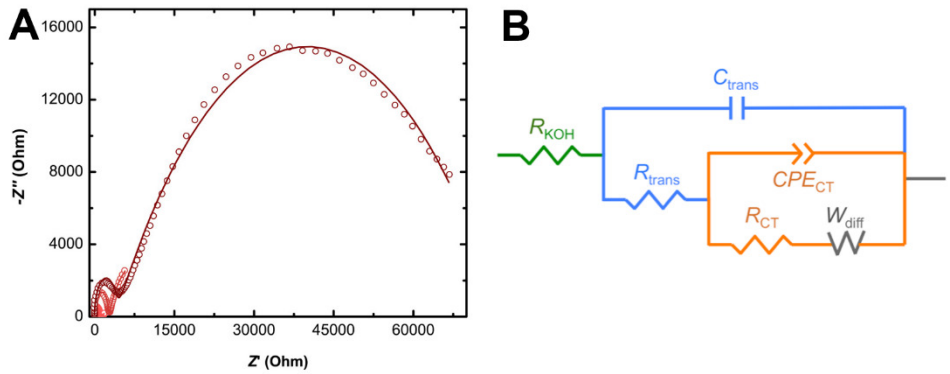

Figure E-11. *(A) Larger range of Figure E-10D. (B) Schematic of the model used for fitting EIS in Figure E-10. Fits were obtained with the EC-Lab® tool "Z Fit", and in all cases* $\chi^2 < 0.8$*. The high frequency impedance from the electrolyte (*R_{KOH}*) is ~45 Ω. The resistance at medium frequencies is attributed to transport through the multilayer film electrode (*R_{trans}*), with associated transport capacitance (*C_{trans}*). At low frequencies, charge transport at the interface contributes a resistance (*R_{CT}*), non-ideal capacitance modeled as a constant phase element (*CPE_{CT}*), and diffusive element (*W_{diff}*).*[36]

Table E-2. *Fitted transport resistance (*R_{trans}*), associated* iR_{trans} *correction, and charge transfer resistance (*R_{CT}*) for LCO films grown on different substrates and LCO films of different thickness grown on LSMO/STO.*

Thickness	Substrate	R_{trans} (Ω)	R_{trans}/t (Ω/nm)	iR_{trans} @ 40 μA cm^{-2} (V)	R_{CT} (Ω)
10nm	LSMO/STO	1099	110	0.01(1)	526
20nm	LSMO/STO	2703 8596	135 430	0.01(5) 0.05(1)	11126 17007
40nm	LSMO/STO	3949 12813	99 320	0.02(3) 0.08(6)	78523 9695
10 nm	LSMO/STO	881 778	88 78	0.00(7) 0.00(6)	306 376
10 nm	LSMO/LAO	3008 1683	301 168	0.01(8) 0.00(7)	1598 1067
10 nm	LSMO/LSAT	496 1170	50 117	0.00(3) 0.00(8)	262 196

The trend in transport resistance (R_{trans}) scales inversely with that of catalytic activity of strained films (LCO on LSAT < STO < LAO from ~400 to ~3000 Ω). Although LSMO resistance can change with strain,[37] the reported resistivities (<1 mΩ-cm for LSMO on LSAT, STO versus 20 mΩ-cm on LAO) are small across the 5 mm sample width studied in this work. Comparing LCO films of different thicknesses grown on LSMO/STO (**Figure E-10, E-11**), R_{trans} scales directly with film thickness (**Table E-2**), suggesting that electronic transport through the LCO film thickness is a notable source of resistance to the $[Fe(CN)_6]^{3-/4-}$. The conductive behavior of LCO grown on LSMO/LSAT illustrates the extent to which characteristics of thin films such as strain can manipulate charge transport, where intermediate or high spin Co resulting from tensile strain can yield metallic LCO.[38]

The charge transport resistance through the film (R_{trans}) can be accounted for in the ORR and OER measurements by an iR_{trans} correction of the applied voltage (in addition to the smaller correction for electrolyte resistance) in the region where currents are small. The iR_{trans}-corrected overpotential required to achieve 40 μA/cm^2 is shown in **Figure E-12**. Although film resistance contributes to the differences in measured activity (correcting for this reduces the effect of both strain and thickness on activity), notable differences remain between films that cannot be explained by bulk electronic transport. Despite the limited surface interactions and singular electron transfer in the facile redox couple $[Fe(CN)_6]^{3-/4-}$, we find correlation between the charge-transfer resistance (R_{CT}) of this reaction and the overpotential for the ORR and OER corrected for transport through the film (**Figure E-12B**). In contrast to the symmetric $[Fe(CN)_6]^{3-/4-}$ reaction, the ORR shows a stronger dependence on R_{CT} compared to the OER (**Figure E-13**), suggesting a difference in the role of charge transfer in the rate-determining step.

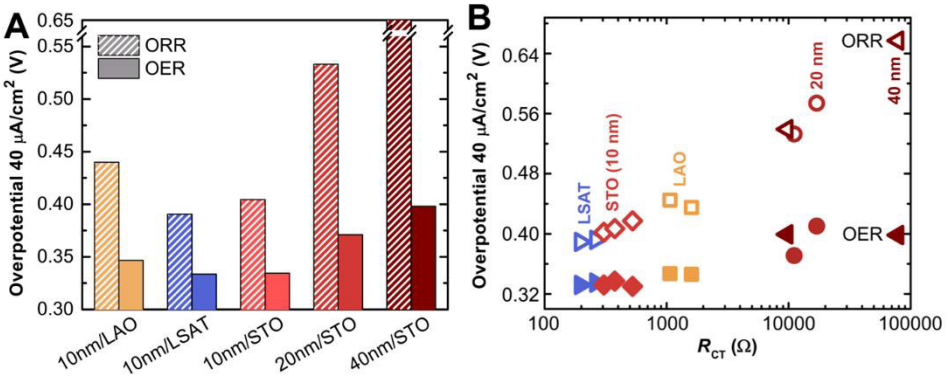

Figure E-12. *(A) Overpotential in Volts required to achieve 40 μA/cm^2 for the ORR (striped/open) and OER (solid). The voltage was corrected for the charge transport resistance (V-iR_{trans}) measured at open circuit in an electrolyte with $[Fe(CN)_6]^{3-/4-}$. (B) The overpotential*

correlates with the charge transfer resistance, R_{CT}, measured at open circuit via $[Fe(CN)_6]^{3-/4-}$, plotted on a log scale to encompass the spread.

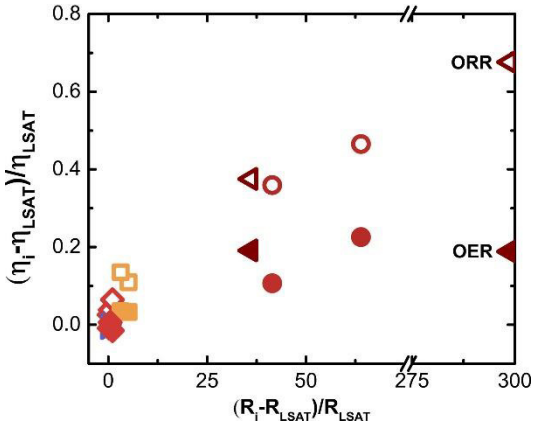

Figure E-13. *Correlations between the overpotential corrected for transport losses (R_{trans}) through the film, η, relative to 1.23 V vs. RHE for ORR (open) and OER (solid) relative to the charge transfer resistance, R_{CT}, measured at open circuit via $[Fe(CN)_6]^{3-/4-}$. For 10-nm-LCO/10-nm-LSMO on the following substrates, colors are: LSAT (blue triangles), STO (red diamonds), and LAO (yellow squares). LCO films of different thicknesses are in shades of red, where dark corresponds with thicker films (circle for 20 nm, left pointing arrow for 40 nm). For the case of three independent measurements of 10 nm LCO films on LSMO/STO, the standard deviation in η was 8 mV for ORR and 4 mV for OER.*

In contrast to previously measured relations in powders, which probe the role of e_g occupancy only by changing chemistry, this study marks the first aiming to tune e_g for a fixed oxide chemistry in alkaline oxygen electrocatalysis using strain. In order to understand the implications of strain on catalysis, the effect on LCO electronic structure must be considered. For bulk powders, the dependence of magnetism on surface area suggests the anion coordination at surface Co^{3+} ions is capable of stabilizing higher spin states;[39] intermediate spin is consistent with the current understanding of the role of the e_g orbital occupation in the ORR[3] and OER.[22] However, studies of the rich physics of LCO show that the application of tensile strain in epitaxial films leads to ferromagnetic behavior at low temperatures,[20,23,24] with an unconventional lattice modulation in thin LCO films under tensile strain observed by scanning transmission electron microscopy (STEM) at room temperature.[24] The activity measured for films of all strain states in this study (nominally -0.5% to 2.6%) are similar to that measured in powders (**Figure E-5**), suggesting that the surface spin state changes little from the proposed intermediate spin on the surface of powders. Calculations have shown both suppression of octahedral rotation and

constraints on the lattice constant act together in determining spin state,[20] both of which differ from bulk due to reduced symmetry at the surface.

It is possible that the changes in activity with strain in fact arise from deviations in the local symmetry. Calculations of tensile strained LCO report a reduction in symmetry from tetragonal for the nonmagnetic case compared to orthorhombic for the intermediate spin case.[40] The decrease predicted in the Co-O bond distance perpendicular to the surface upon application of tensile strain would increase the strength of the adsorbed oxygen bond. As LCO (e_g = 1) is on the weak-bonding side of the ORR activity volcano determined by e_g filling,[3] the maximum activity for moderate tensile strain is consistent with such a change in bond strength. Strain at the surface may also affect the number of defect sites, which could in turn influence charge transfer resistance.

The asymmetry in catalysis of the ORR and OER observed when changing the strain by modifying substrate lattice and film thickness can provide insight into details of the reaction mechanisms of oxygen electrocatalysis. The stronger dependence of the ORR on strain could arise from a difference in surface reconstruction or involved redox couples for reducing versus oxidizing conditions. However, the stronger dependence on thickness in turn suggests the role of charge transport (R_{trans}) and transfer (R_{CT}) may contribute to different extents for the ORR and OER.

E.4. Conclusions

In this work, we report the use of epitaxial strain via lattice mismatch as a means to tune the activity toward oxygen electrocatalysis on $LaCoO_3$ in alkaline environments. The reduced activity observed in compressively strained and thicker films, corrected for changes in electronic transport through the film, trends with increased charge transfer resistance measured by the facile redox couple $[Fe(CN)_6]^{3-/4-}$. Thus, a balance between tensile strain and electronic conductivity must be achieved to maximize catalytic activity. This study points to an asymmetry in oxygen electrocatalysis, where the rate limiting step in the ORR is influenced more strongly by charge transfer resistance than the OER. This key insight into the reaction mechanism will guide the design of highly active catalysts, where strain can be incorporated chemically or using core-shell particles to obtain high surface area for technical applications.

References

1 Dau, H. *et al.* The Mechanism of Water Oxidation: From Electrolysis via Homogeneous to Biological Catalysis. *ChemCatChem* **2**, 724-761, (2010).

2 Suntivich, J., Gasteiger, H. A., Yabuuchi, N. & Shao-Horn, Y. Electrocatalytic Measurement Methodology of Oxide Catalysts Using a Thin-Film Rotating Disk Electrode. *J. Electrochem. Soc.* **157**, B1263-B1268, (2010).

3 Suntivich, J. *et al.* Design principles for oxygen-reduction activity on perovskite oxide catalysts for fuel cells and metal–air batteries. *Nat. Chem.* **3**, 546-550, (2011).

4 Gorlin, Y., Chung, C.-J., Nordlund, D., Clemens, B. M. & Jaramillo, T. F. Mn_3O_4 Supported on Glassy Carbon: An Active Non-Precious Metal Catalyst for the Oxygen Reduction Reaction. *ACS Catalysis* **2**, 2687-2694, (2012).

5 Bockris, J. O. & Otagawa, T. Mechanism of oxygen evolution on perovskites. *J. Phys. Chem.* **87**, 2960-2971, (1983).

6 Matsumoto, Y., Yoneyama, H. & Tamura, H. Influence of the nature of the conduction band of transition metal oxides on catalytic activity for oxygen reduction. *J. Electroanal. Chem. Interfacial Electrochem.* **83**, 237-243, (1977).

7 Vesborg, P. C. K. & Jaramillo, T. F. Addressing the terawatt challenge: scalability in the supply of chemical elements for renewable energy. *RSC Advances* **2**, 7933-7947, (2012).

8 Miyahara, Y., Miyazaki, K., Fukutsuka, T. & Abe, T. Catalytic Roles of Perovskite Oxides in Electrochemical Oxygen Reactions in Alkaline Media. *J. Electrochem. Soc.* **161**, F694-F697, (2014).

9 Komo, M., Hagiwara, A., Taminato, S., Hirayama, M. & Kanno, R. Oxygen Evolution and Reduction Reactions on $La_{0.8}Sr_{0.2}CoO_3$ (001), (110), and (111) Surfaces in an Alkaline Solution. *Electrochemistry* **80**, 834-838, (2012).

10 Jeen, H. *et al.* Orienting Oxygen Vacancies for Fast Catalytic Reaction. *Adv. Mater.* **25**, 6459-6463, (2013).

11 Stoerzinger, K. A. *et al.* Oxygen electrocatalysis on (001)-oriented manganese perovskite films: Mn valency and charge transfer at the nanoscale. *Energy Environ. Sci.* **6**, 1582-1588, (2013).

12 Strasser, P. *et al.* Lattice-strain control of the activity in dealloyed core–shell fuel cell catalysts. *Nat. Chem.* **2**, 454-460, (2010).

13 Stephens, I. E. L., Bondarenko, A. S., Gronbjerg, U., Rossmeisl, J. & Chorkendorff, I. Understanding the electrocatalysis of oxygen reduction on platinum and its alloys. *Energy Environ. Sci.* **5**, 6744-6762, (2012).

14 Stephens, I. E. L., Bondarenko, A. S., Bech, L. & Chorkendorff, I. Oxygen Electroreduction Activity and X-Ray Photoelectron Spectroscopy of Platinum and Early Transition Metal Alloys. *ChemCatChem* **4**, 341-349, (2012).

15 Lee, D. *et al.* Strain Influence on the Oxygen Electrocatalysis of the (100)-Oriented Epitaxial $La_2NiO_{4+\delta}$ Thin Films at Elevated Temperatures. *J. Phys. Chem. C* **117**, 18789-18795, (2013).

16 Yamada, A. *et al.* Ruddlesden-Popper-Type Epitaxial Film as Oxygen Electrode for Solid-Oxide Fuel Cells. *Adv. Mater.* **20**, 4124-4128, (2008).

17 Kubicek, M. *et al.* Tensile Lattice Strain Accelerates Oxygen Surface Exchange and Diffusion in $La_{1-x}Sr_xCoO_{3-\delta}$ Thin Films. *ACS Nano* **7**, 3276-3286, (2013).

18 Han, J. W. & Yildiz, B. Enhanced one dimensional mobility of oxygen on strained $LaCoO_3$(001) surface. *J. Mater. Chem.* **21**, 18983-18990, (2011).

19 Kushima, A., Yip, S. & Yildiz, B. Competing strain effects in reactivity of $LaCoO_3$ with oxygen. *Phys. Rev. B* **82**, 115435, (2010).

20 Rondinelli, J. M. & Spaldin, N. A. Structural effects on the spin-state transition in epitaxially strained $LaCoO_3$. *Phys. Rev. B* **79**, 054409, (2009).

21 Matsumoto, Y., Yoneyama, H. & Tamura, H. Dependence of the exchange current density of oxygen reduction on the resistivities of $La_{1-x}Sr_xMnO_3$ and $LaNi_{1-x}M_xO_3$ electrodes. *J. Electroanal. Chem. Interfacial Electrochem.* **83**, 245-249, (1977).

22 Suntivich, J., May, K. J., Gasteiger, H. A., Goodenough, J. B. & Shao-Horn, Y. A Perovskite Oxide Optimized for Oxygen Evolution Catalysis from Molecular Orbital Principles. *Science* **334**, 1383-1385, (2011).

23 Fuchs, D. *et al.* Tuning the magnetic properties of $LaCoO_3$ thin films by epitaxial strain. *Phys. Rev. B* **77**, 014434, (2008).

24 Choi, W. S. *et al.* Strain-Induced Spin States in Atomically Ordered Cobaltites. *Nano Lett.* **12**, 4966-4970, (2012).

25 Kwon, J.-H. *et al.* Nanoscale Spin-State Ordering in $LaCoO_3$ Epitaxial Thin Films. *Chem. Mater.* **26**, 2496-2501, (2014).

26 Pavone, M., Ritzmann, A. M. & Carter, E. A. Quantum-mechanics-based design principles for solid oxide fuel cell cathode materials. *Energy Environ. Sci.* **4**, 4933-4937, (2011).

27 Křápek, V. *et al.* Spin state transition and covalent bonding in $LaCoO_3$. *Phys. Rev. B* **86**, 195104, (2012).

28 Hong, W. T. *et al.* Tuning the Spin State in $LaCoO_3$ Thin Films for Enhanced High-Temperature Oxygen Electrocatalysis. *J. Phys. Chem. Lett.* **4**, 2493-2499, (2013).

29 Fuchs, D., Arac, E., Schwarz, T. & Schneider, R. Tuning the Strain in $LaCoO_3$ Thin Films by the Heteroepitaxial Growth on Single Crystal Substrates. *Adv. in Solid State Phys.* **47**, 271–275, (2008).

30 Biesinger, M. C. *et al.* Resolving surface chemical states in XPS analysis of first row transition metals, oxides and hydroxides: Cr, Mn, Fe, Co and Ni. *Applied Surface Science* **257**, 2717-2730, (2011).

31 Dupin, J. C., Gonbeau, D., Benqlilou-Moudden, H., Vinatier, P. & Levasseur, A. XPS analysis of new lithium cobalt oxide thin-films before and after lithium deintercalation. *Thin Solid Films* **384**, 23-32, (2001).

32 Stoerzinger, K. A. *et al.* Reactivity of perovskites with water: role of hydroxylation in wetting and implications for oxygen electrocatalysis. *Submitted*, (2014).

33 Suntivich, J. *et al.* Design principles for oxygen-reduction activity on perovskite oxide catalysts for fuel cells and metal–air batteries. *Nat Chem* **3**, 546-550, (2011).

34 Fang, Y.-H. & Liu, Z.-P. Tafel Kinetics of Electrocatalytic Reactions: From Experiment to First-Principles. *ACS Catalysis* **4**, 4364-4376, (2014).

35 Kear, G. & Walsh, F. C. The characteristics of a true Tafel slope. *Corrosion and Materials* **30**, 51-55, (2005).

36 Lopes, T. *et al.* Hematite photoelectrodes for water splitting: evaluation of the role of film thickness by impedance spectroscopy. *Physical Chemistry Chemical Physics* **16**, 16515-16523, (2014).

37 Adamo, C. *et al.* Effect of biaxial strain on the electrical and magnetic properties of (001) $La_{0.7}Sr_{0.3}MnO_3$ thin films. *Appl. Phys. Lett.* **95**, 112504, (2009).

38 Korotin, M. *et al.* Intermediate-spin state and properties of $LaCoO_3$. *Phys. Rev. B* **54**, 5309-5316, (1996).

39 Yan, J. Q., Zhou, J. S. & Goodenough, J. B. Ferromagnetism in $LaCoO_3$. *Phys. Rev. B* **70**, 014402, (2004).

40 Posadas, A. *et al.* Strain-induced ferromagnetism in $LaCoO_3$: Theory and growth on Si (1 0 0). *Microelectron. Eng.* **88**, 1444-1447, (2011).